INTERNATIONAL RELATIVISTIC ASTROPHYSICS DOCTORATE PROGRAM
IRAP PHD

PH.D. THESIS

LONG GAMMA-RAY BURSTS AS BINARY-DRIVEN HYPERNOVAE

ANALYSIS WITHIN THE INDUCED GRAVITATIONAL COLLAPSE PARADIGM

PH.D. CANDIDATE
Daria Primorac

THESIS ADVISORS
Prof. Remo Ruffini
Prof. Carlo Luciano Bianco

SAPIENZA
UNIVERSITÀ DI ROMA

"Sapienza" University of Rome

February 2020

I thank Francesco and my parents for their unconditional support

ABSTRACT

The central engine of long gamma-ray bursts (GRBs) is still under debate. The (currently) prevailing theoretical understanding is referred to as the standard fireball model. Here, the prompt emission is attributed to the internal shocks and the afterglow emission is attributed to the external shocks. The GRB outflow contains a wide range of bulk Lorentz factors. When a fast-moving portion overtakes the slower one, an internal shock is generated. On the other hand, the external shocks are caused by the interaction between the outflow and the circum-burst medium. However, data that was accumulated in the last 25 years challenges the overall picture. Some of the observed properties can not be explained within the standard framework. For example, the immense isotropic energy requirements of GRBs can be considerably reduced if one assumes the outflow is collimated. As a consequence, an achromatic break should appear in the afterglow light-curves. However, for the majority of GRBs the break is not achromatic, if present at all. In addition, the model itself does not deal with the exact mechanism of this initial energy release, but only its consequences.

One of the alternatives to the fireball model is the fireshell model. Its origins can be traced back to the idea which revolves around the energy extraction from a charged black hole. During the years, with the implementation of new available data, the fireshell model evolved into the induced gravitational collapse (IGC) paradigm. This theory emphasizes the importance of binary system interaction for the GRB production mechanism, offering additional channels to study the role these systems have in GRB formation. In it, all GRBs originate from binary systems. Different observational properties are a direct consequence of a wide spectrum of acceptable binary system parameters. According to these observational properties, long and short GRBs are divided into nine different sub-classes. GRBs belonging to the type-I binary driven hypernova (BdHNe-I) class are of main interest in this thesis. The name is referring to GRBs with energies above $\sim 10^{52}$ erg that originate from a collapse of a neutron star into a black hole. This collapse is initiated by the supernova explosion of its binary companion.

In the work presented here, the theoretical framework of the IGC paradigm was tested on twelve GRBs. From these, only GRB 160829A is a member of the short GRB class. The remaining ones are long bursts, classified as BdHNe-I on the account of their energetics and GeV emission. Two main tools were put to use in order to analyze and interpret the data: the `rmfit` software and the simulation of the fireshell propagation that is available on our group's server. All of the GRBs were detected with the GBM detector onboard the *Fermi* satellite. Time-integrated and time-resolved analysis was carried out for each GRB in order to determine their isotropic equivalent energy and to possibly identify the P-GRB signature. The latter is expected to occur in the beginning of the prompt emission and to have a spectrum that shows a presence of thermal signatures. From 11 BdHNe-I, five had an identified P-GRB associated emission: GRB 100728A, GRB151027A, GRB 090618, GRB 110731A and GRB 141028A. A black body component was found in six GRBs. For three of them, the component did not exhibit the expected P-GRB spectral and temporal properties and it was therefore rejected as a possible P-GRB. GRB 110731A, GRB151027A and GRB 090618 were further interpreted within the fireshell model. Average values of circum-burst medium density inferred from the simulations are ~ 0.03 cm^{-3}, ~ 15 cm^{-3} and ~ 1 cm^{-3}, respectively. Therefore, these bursts occurred in different environments. The averaged value of this sample, $\sim$1 baryon per cm^3, is consistent with previous findings. Baryon load and the relativistic Lorentz gamma factor at transparency

point were also consistent with long GRBs, although we find that GRB 110731A shared some of these values with short bursts. In the case of short GRB 160829A, the fireshell simulation up to the transparency point was used in order to evaluate the redshift. Poor S/N ratio constrained its redshift to $z < 5$. This is not particularly helpful considering it is true for all of the short GRBs observed so far. That is, if one does not take into account GRB 080913 at $z = 6.7$, which was observed to last longer than 2 s due to its high redshift, but it may be intrinsically short. The difficulties encountered during the analyses played a role in the further development of the IGC paradigm. The ongoing work is also discussed. It was devised with a goal to enable a more consistent and faster analysis. Then, a more complete BdHNe-I catalog with all of the fireshell parameters included would be easier to produce.

INTRODUCTION

In the simplest manner, gamma-ray bursts can be described as distant and energetic transient sources that, approximately once per day, signal the deaths of massive stars. However, even though half of the century has passed since its discovery, the scientific community is still putting an enormous amount of effort to answer many of the questions that remained unresolved. This is because gamma-ray bursts (GRBs hereafter) are nothing but simple. Their behavior can all-inclusively be described only by a wide spectrum of different properties. GRB light-curves can be erratic or plain and show no (or very little) evident patterns. Their duration can last from milliseconds to several minutes. Sometimes, high-energy GeV emission can be observed long after the GRB has ended. The burst of gamma-rays is usually followed by an emission at longer wavelengths, whose peak emission shifts from X-ray to radio-waves with time, called the *afterglow*. But this is not a rule. In short, a single GRB may or may not be accompanied by an X-ray, optical, radio or GeV emission. The first three of these may or may not exhibit breaks in the light-curve from which some may or may not be simultaneous. The X-ray light-curve can also contain a plateau and flares, from which the last one may or may not be seen in the prompt emission, thus influencing the burst duration. As a consequence of these inconsistent properties, one may talk about short, long or ultra-long GRBs, about dark, X-ray rich and SN-less GRBs or about Norris-Bonnell sources. One may say that it is hard to see the forest for the trees.

The question worth answering is: what does all this data imply and does it provide any helpful constraints for the current models? In addition, are these constraints realistic or a product of instrumental biases of numerous observatories that monitor the sky? As it was said, GRBs are nothing but simple. However, a general consensus has been reached regarding the twofold nature of their progenitors. Long GRBs (> 2 s) are associated with, in one way or another, the collapse of massive stars while short GRBs (< 2 s) originate from the compact binary mergers. Although, the separation value of 2 s is still debated due to time dilatation effects and instrument sensitivity. The *fireshell* model and its extension, the induced gravitational collapse paradigm, represent an effort to unify all of these observed properties under a single theory. Within it, both short and long bursts originate from binary systems. Different observational properties of GRBs are then a direct consequence of the wide range of parameters that describe binary systems. In this work, spectral analyses of twelve GRBs put this model to the test.

This thesis is divided in four chapters. First two chapters build the theoretical framework needed for understanding the GRB phenomena. An up-to-date view is needed in order to understand the differences between the fireball and the fireshell model and their caveats. Chapter 1 is focused on the observational properties of GRBs. Section 1.1 outlines the first two decades of progress starting with their discovery and on the way mentioning some of their main spectral and temporal features. Section 1.2 focuses on the role of observatories that monitor the sky in other energy bands. Spectral models, needed in order to quantitatively describe the prompt emission, are listed in Section 1.3. This section also revolves around the peculiarities often found in GRB spectra. It illustrates how the consequently derived correlations represented an attempt to utilize GRBs as standard candles. Theoretical explanation of these features and the phenomena itself, at least the generally accepted one (i.e., the *fireball* model), is given in Section 1.4. This entire chapter emphasizes the technological advances and shows how the newly collected data continues to spark (or eliminate) numerous ideas within the scientific community. The shortcomings of these ideas are also carefully described.

The fireshell model with all of its recent developments is explained in Chapter 2. Sections 2.6 to 2.9 are devoted to the induced gravitational paradigm, which is the main focus of this work. All of the performed analyses are presented in Chapter 3. The methodology is summarized in Section 3.1 in order to avoid its repetition throughout the chapter. Section 3.2 introduces 11 long GRBs and their prompt emission analysis. A full treatment within the fireshell model was applied to three of those bursts, as described in Section 3.3 and Section 3.4. Section 3.5 illustrates how the fireshell model can be utilized in order to determine the redshift of a given burst. Conclusions and future prospects are outlined in Chapter 4.

LIST OF PUBLICATIONS

REFEREED JOURNALS

1. R. Ruffini, Y. Aimuratov, L. Becerra, C. L. Bianco, M. Karlica, M. Kovačević, J. D. Melon Fuksman,R. Moradi, M. Muccino, A. V. Penacchioni, G. B. Pisani, D. Primorac, J. A. Rueda, S. Shakeri, G. V. Vereshchagin, Y. Wang, and S. S. Xue. The cosmic matrix in the 50th anniversary of relativistic astrophysics. *International Journal of Modern Physics D*, 26(10):1730019–367, Jan 2017

2. Jorge A. Rueda, Y. Aimuratov, U. Barres de Almeida, L. Becerra, C. L. Bianco, C. Cherubini, S. Filippi, M. Karlica, M. Kovačević, J. D. Melon Fuksman, R. Moradi, M. Muccino, A. V. Penacchioni, G. B. Pisani, D. Primorac, R. Ruffini, N. Sahakyan, S. Shakeri, and Y. Wang. The binary systems associated with short and long gamma-ray bursts and their detectability. *International Journal of Modern Physics D*, 26(9):1730016–309, Jan 2017

3. Y. Aimuratov, R. Ruffini, M. Muccino, C. L. Bianco, A. V. Penacchioni, G. B. Pisani, D. Primorac, J. A. Rueda, and Y. Wang. GRB 081024B and GRB 140402A: Two Additional Short GRBs from Binary Neutron Star Mergers. *The Astrophysical Journal*, 844(1):83, Jul 2017

4. R. Ruffini, Y. Wang, Y. Aimuratov, U. Barres de Almeida, L. Becerra, C. L. Bianco, Y. C. Chen,M. Karlica, M. Kovačević, L. Li, J. D. Melon Fuksman, R. Moradi, M. Muccino, A. V. Penacchioni, G. B. Pisani, D. Primorac, J. A. Rueda, S. Shakeri, G. V. Vereshchagin, and S. S. Xue. Early X-Ray Flares in GRBs. *The Astrophysical Journal*, 852(1):53, Jan 2018

5. R. Ruffini, Y. Wang, Y. Aimuratov, U. B. de Almeida, L. Becerra, C. L. Bianco, Y. C. Chen, M. Karlica, M. Kovačević, L. Li, J. D. M. Fuksman, R. Moradi, M. Muccino, A. V. Penacchioni, G. B. Pisani, D. Primorac, J. A. Rueda, S. Shakeri, G. V. Vereshchagin, and S. S. Xue. VizieR Online Data Catalog: Early X-ray flares in GRBs (Ruffini+, 2018). *VizieR Online Data Catalog*, page J/ApJ/852/53, Sep 2018

6. J. A. Rueda, R. Ruffini, Y. Wang, Y. Aimuratov, U. Barres de Almeida, C. L. Bianco, Y. C. Chen, R. V. Lobato, C. Maia, D. Primorac, R. Moradi, and J. F. Rodriguez. GRB 170817A-GW170817-AT2017gfo and the observations of NS-NS, NS-WD and WD-WD mergers. *Journal of Cosmology and Astro-Particle Physics*, 2018(10):006, Oct 2018

7. D. Primorac, M. Muccino, R. Moradi, Y. Wang, J. D. Melon Fuksman, R. Ruffini, C. L. Bianco, and J. A. Rueda. Structure of the Prompt Emission of GRB 151027A within the Fireshell Model. *Astronomy Reports*, 62(12):933–939, Dec 2018

8. R. Ruffini, L. Becerra, C. L. Bianco, Y. C. Chen, M. Karlica, M. Kovačević, J. D. Melon Fuksman,R. Moradi, M. Muccino, G. B. Pisani, D. Primorac, J. A. Rueda, G. V. Vereshchagin, Y. Wang, andS. S. Xue. On the Ultra-relativistic Prompt Emission, the Hard and Soft X-Ray Flares, and the Extended Thermal Emission in GRB 151027A. *The Astrophysical Journal*, 869(2):151, Dec 2018

9. R. Moradi, R. Ruffini, C. L. Bianco, Y. C. Chen, M. Karlica, J. D. Melon Fuksman, D. Primorac, J. A. Rueda, S. Shakeri, Y. Wang, and S. S. Xue. Relativistic Behavior and Equitemporal Surfaces in Ultra-Relativistic Prompt Emission Phase of Gamma-Ray Bursts. *Astronomy Reports*, 62(12):905–910, Dec 2018

PROCEEDINGS

1. Daria Primorac, Remo Ruffini, Giovanni Battista Pisani, Yerlan Aimuratov, Carlo Luciano Bianco, Mile Karlica, Julio David Melon Fuksman, Rahim Moradi, Marco Muccino, Ana Virginia Penacchioni, Jorge Armando Rueda, and Yu Wang. GRB 110731A within the IGC paradigm. *In European Physical Journal Web of Conferences*, volume 168, page 04008, Jan 2018

Acknowledgments

I am thankful to Marco Muccino and other members of the International Center for Relativistic Astrophysics Network for their guidance and support.

This thesis has made use of NASA's Astrophysics Data System. The work presented here made use of data supplied by the UK Swift Science Data Centre at the University of Leicester (UK), the use of the VizieR catalog access tool, CDS at Strasbourg (France), and the cross-match service it provides.

CONTENTS

LIST OF FIGURES

LIST OF TABLES

LIST OF ABBREVIATIONS

AGILE	Astro-rivelatore Gamma a Immagini Leggero
AGN	active galactic nucleus
ARR	Autonomous Repoint Request
BAT	Burst Alert Telescope
BATSE	Burst and Transient Source Experiment
BB	black body
BdHN	binary-driven hypernova
BG	background
BH	black hole
BHL	Bondi-Hoyle-Lyttleton
BM	binary merger
CBM	circum-burst medium
CGRO	Compton Gamma-Ray Observatory
C-STAT	Castor statistics
DOF	degree of freedom
EAC	effective area correction
EGRET	Energetic Gamma-Ray Experiment Telescope
EMBH	electromagnetic black hole
EQTS	equitemporal surface
ETE	extended thermal emission
EXE	extended X-ray emission
FB-KN	fallback-powered kilonova
FPA	flare-plateau-afterglow
FRED	fast rise, exponential decay
GBM	Gamma-ray Burst Monitor
GCN	Gamma-ray Coordinates Network
GRB	gamma-ray burst
GRBM	Gamma-Ray Burst Monitor
GRF	gamma-ray flash
GW	gravitational wave
HETE	High Energy Transient Explorer
HIT	hardness-intensity tracking
HN	hypernova
HR	hardness ratio
HTS	hard-to-soft
HXD	Hard X-ray Detector
IGC	induced gravitational collapse
IGM	intergalactic medium
INTEGRAL	International Gamma-Ray Astrophysics Laboratory
KN	kilonova
LAT	Large Area Telescope
LIGO	Laser Interferometer Gravitational Observatory
MNS	massive neutron star
NFI	Narrow Field Instrument
NS	neutron star
νNS	new neutron star
NuSTAR	Nuclear Spectroscopic Telescope Array
PEP	prompt emission phase
P-GRB	proper gamma-ray burst
PL	power-law
SAA	South Atlantic Anomaly
SDSS	Sloan Digital Sky Survey
SFR	star formation rate
S-GRB	short gamma-ray burst
S-GRF	short gamma-ray flash
S/N	signal to noise ratio
SN	supernova
SPH	smoothed-particle hydrodynamics
TOPCAT	Tool for OPerations on Catalogues And Tables
TTE	time-tagged event
U-GRB	ultra-short gamma-ray burst
UHE	ultra-high energy
UHECR	ultra-high energy cosmic ray
UPE	ultra-relativistic prompt emission
UV	ultraviolet
UVOT	Ultraviolet/Optical Telescope
VLA	Karl G. Jansky Very Large Array
WAM	Wide-band All-sky Monitor
WD	white dwarf
WFC	Wide Field Camera
WR	Wolf-Rayet
XMM	X-ray Multi-Mirror Mission
XRF	X-Ray flash
XRGRB	X-Ray rich gamma-ray burst
XRT	X-Ray Telescope

1

GAMMA-RAY BURST PHENOMENON (IN A NUTSHELL)

One can tell that gamma-ray burst literature is often packed with superlatives. Besides being the most luminous transient sources, they are beacons of one of the most distant population of formed objects in the Universe. As such, gamma-ray bursts present the greatest astrophysical phenomena since the discovery of quasars and pulsars. The motivation for this chapter is to provide the basic framework for understanding the gamma-ray burst phenomenology. While tracing the milestones achieved by the related space-missions, this chapter summarizes the observational properties of gamma-ray bursts and their afterglows, as well as the theoretical models of their progenitors.

1.1 DISCOVERY OF GRBs

The *Vela* military satellites

One would not expect that an environmental concern and radioactive fallout management could lead to the discovery of the most energetic phenomena in the Universe (Klebesadel et al. 1973). Therefore, when giving an introduction about gamma-ray bursts (GRBs), one must necessarily begin with a description of the USA military *Vela* satellites. A total of 6 pairs of satellites was launched between the 1963 and 1970 in order to monitor the compliance of the USSR with the 1963 nuclear test ban treaty. The concerns were directed both towards the possibilities of exo-atmospheric testing and the detonations within the Earth's atmosphere. Radiation signature emitted by a nuclear detonation in space comes in the form of an X-ray flash lasting less than a millisecond. On the other hand, if the tests were to be conducted within the atmosphere, prompt radiation would be hidden from the detectors. Nevertheless, the expanding fission debris would soon become visible in the form of delayed gamma-rays. Thus, while keeping in mind that the "prompt" caused by a nuclear event is short-lasting (< 1 ms), the detection mechanisms onboard *Vela* satellites included X-ray, gamma-ray and neutron detectors. With each new launch, there was an improvement in detector sensitivity, time resolution, and spectral response[1]. This laid a foundation for gamma-ray burst detection.

Soon, the first event was identified, now known as GRB 670702. The occurrence of the two peaks was too rapid to have been produced by a solar flare, especially in the absence of the solar activity at that time. The signature also did not correspond to a nuclear weapon test[2]. Upon the extent database search, more events were discovered. They were simultaneously observed by multiple satellites, which excluded the possibility of some local stimulation. From the crude locations of the bursts, it was established that they were not associated with any of the major members of the Solar System or with any known flaring stars.

[1] However, spectral resolution remained the same: a single energy channel in the range of 0.3–1.5 MeV.

[2] In the *Vela* mission history, no (certain) nuclear detonations were ever detected. One candidate exception was the signal detected in 1979 near Antarctica, but the explanations of the possible causes remained inconclusive.

Colgate (1968) proposed that a relativistic shock produced by a supernova (SN) explosion could generate a burst of gamma-rays (see also Colgate 1974). Still, a performed check for any temporal coincidences of gamma-ray emission with cataloged SNe did not yield results. The locations of GRBs were also not consistent with those of nearby galaxies. Their spatial distribution did not seem to favor the Galactic plane, but the number of the observed bursts was still too low to draw any statistically significant conclusion. It became evident that the detectors were responding to some new, unidentified, natural phenomena.

It was not until 1973 that this information was released to the public (Klebesadel et al. 1973). One year later, there were already 15 progenitor models proposed. By 1990's, more than a hundred. Proposed models included both cosmological and local (galactic) origins. With distances still unknown, it was not clear whether gamma-ray bursts originated in the Oort cloud (in the outermost reaches of the Solar System), somewhere else within our galaxy, or beyond. The main argument against the theories supporting the cosmological origin was the vast energy budget needed to reach the observed luminosities.

The consensus at the time was that GRBs were produced by nearby neutron stars (NSs). Several arguments were employed. Short rise-times of the bursts, when multiplied with the speed of light, result in a characteristic length comparable with the size of a NS. The observed non-thermal spectra indicated an optically thin emission region at gamma-ray energies (Schmidt 1978). With emission region being limited in size, $\gamma - \gamma$ interactions at high photon densities limit the luminosity of the burst. Schmidt concluded that (unbeamed, non-relativistic) sources cannot be further away than a few kpc from the Sun and therefore must be galactic. Spectral features in the 50–70 keV and 350–500 keV energy range detected by other satellites further strengthened this idea (see, e.g., Mazets et al. 1981a). The low-energy features had been identified as cyclotron lines due to a 10^{12} Gs magnetic field (typical of pulsars). The latter was thought to be due to the 511 keV annihilation line[3]. The apparent isotropic distribution was thought to be due to the relative sensitivity of the gamma-ray detectors onboard *Vela* satellites. It was argued that these instruments were unable to observe sources beyond our local disk of stars. This in return made the burst distribution appear isotropic. The observed isotropy was expected to change with the future missions, employing more sensitive detectors.

BATSE and the duration bimodality

In April 1991, Burst and Transient Source Experiment (BATSE) was launched into the low Earth's orbit, as part of the *Compton Gamma-Ray Observatory* (*CGRO*). As stated above, prior to this date many other spacecrafts made considerable observational progress in the field of GRBs (see, e.g., Mazets et al. 1981b or Metzger et al. 1974 for the *Venera* and *Appolo 16* contribution, respectably). Hence, many observational characteristics were known prior to the BATSE era. However, BATSE was the first large, comprehensive experiment specifically designed to study the bursts (the remaining three instruments on *CGRO* were not optimized for this purpose). The BATSE confirmed the GRB properties that were up to then only indicated by prior observations. Namely, the isotropic but inhomogeneous GRB distribution and the duration bimodality of GRBs. It also allowed the burst characteristics to be studied like never before[4]. The detection would occur about once per day at a random location in the sky. The observed light-curves showed diversity that was hard to classify (single or multiple peaks, smooth or erratic). The spatial distribution of GRBs (Figure 1.1 - left panel) was found to be isotropic, even for the faintest bursts in the sky.

[3] The energy of the photons reduces by as much as 24% as they climb out of the potential well of the NS.

[4] The extent of the BATSE contribution and the imprint it left on the scientific community is reflected in the sheer number of papers with "BATSE" in the abstract; almost 1000 papers in refereed journals and as trice as much when counting the numerous proceedings. Over 50 Ph.D. thesis at that time used BATSE as their main data source.

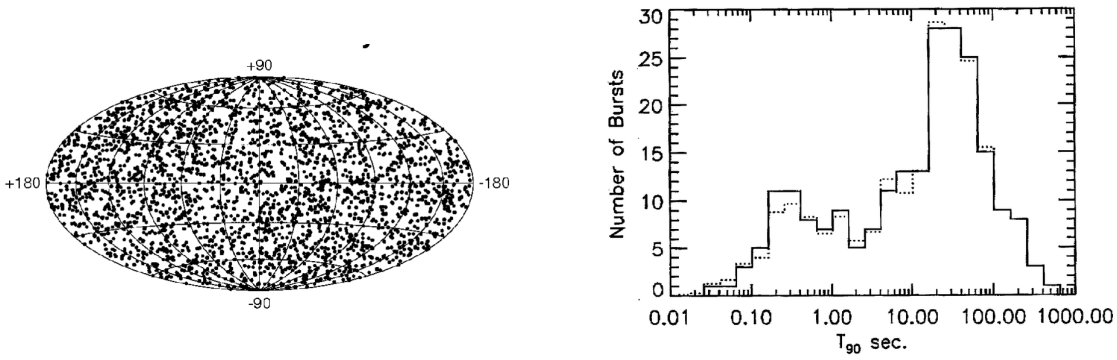

Figure 1.1. *Left panel:* Locations of 2704 BATSE bursts recorded during the nine-year mission. The distribution is shown in Galactic coordinates using an equal-area Aitoff projection. Credits: *CGRO* BATSE team. *Right panel:* T_{90} distribution for the 222 GRBs listed in the first BATSE catalog. Figure reproduced from Kouveliotou et al. (1993).

However, bursts did not appear to be distributed homogeneously throughout space. In other words, the number density of sources was not distance-independent. Fluence S of a GRB with an energy E, located at distance r from Earth is given by $S = E/4\pi r^2$, assuming an isotropic burst. It follows that $r(S) = (E/4\pi S)^{1/2}$. The number of bursts observed with a fluence greater than some value S should then be proportional to $S^{-3/2}$. The proportionality is easily obtained by assuming that all bursts have the same intrinsic energy E. All of the sources within a sphere of radius $r(S)$ will then be observed to have a fluence bigger or equal to S. The number of observed sources is then given by

$$N(S) = \frac{4}{3}\pi\, n\, r^3(S) = \frac{4}{3}\pi\, n\, \left(\frac{E}{4\pi S}\right)^{3/2} \tag{1.1}$$

where n is the number of bursts per unit volume[5]. Meegan et al. (1992) analyzed 153 gamma-ray bursts detected by BATSE. The proportionality was violated for fluence small enough to include more distant, fainter sources (see Figure 1.2). The bursts did not extend forward without the limit. There was an edge to the distribution. This evidence of inhomogeneity has also been seen in several other experiments with sufficient sensitivity (e.g., Ogasaka et al. 1991; Higdon et al. 1992).

Perhaps the most important contribution to the GRB field made by BATSE instruments is summarized in the work of Kouveliotou et al. (1993). For the first time, the duration bimodality was linked with the GRB hardness-duration correlation. Only suggestive evidence of this bimodal nature was reported in former studies (Mazets et al. 1981b; Norris et al. 1984). Better temporal resolution and instrument sensitivity were needed in order to constrain the separation beyond the 0.5–4 s interval. There was also no existing agreement on how the GRB duration should be calculated in the first place (consequently, there was a variety of different criteria for determining a burst duration). Kouveliotou et al. (1993) was the one to initially introduce the duration parameter T_{90}, an unbiased and reproducible way of estimating the duration. Using the sum of the triggering detector counts > 25 keV, T_{90} was defined as the time interval during which the cumulative, background-subtracted counts increase from 5% to 95%, thus enclosing 90% of the total observed burst counts. Right panel in Figure 1.1 shows the T_{90} distribution for the 222 GRBs within the first BATSE catalog (Fishman et al. 1994). Duration bimodality was thus confirmed, with the separation at ≈ 2 s. Both groups also had different hardness ratio (HR), usually defined as the ratio of the hard and soft observed counts. In Figure 1.3 hardness ratio HR_{32} is plotted together with the burst duration, where HR_{32} is the ratio of the total counts in the 100–300 keV and 50–100 keV energy band.

[5] If there are different populations of bursts with respect to the intrinsic energy, the argument would still be valid for each population separately.

It was observed that, in average, short events have a higher HR values (with a mean of 1.49 ± 0.08) than the long ones (with a mean of 0.87 ± 0.03). The same trend was seen in other energy channels. While the duration was found to be correlated to the HR for the entire set of BATSE data, it was not correlated at all for either of the two observed classes of GRBs. Both sets had, however, isotropic and inhomogeneous spatial distribution, suggesting that they originated from the same type of objects (Kouveliotou et al. 1993). Since then, GRBs are classified into two types according to their duration: the long (soft) bursts with $T_{90} > 2$ s and short (hard) bursts with $T_{90} < 2$ s.

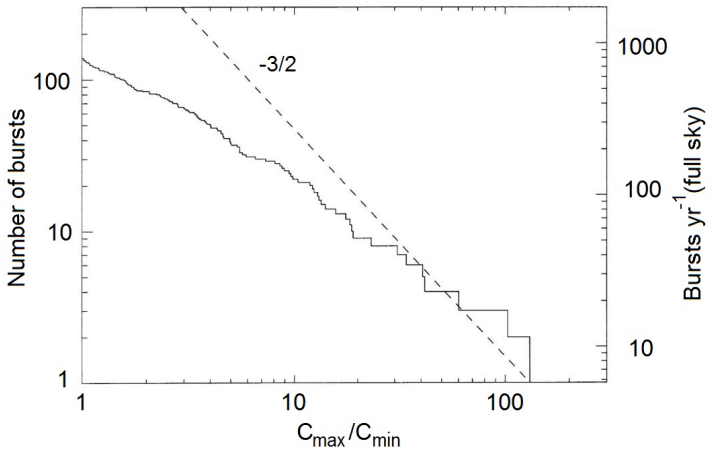

Figure 1.2. Number vs. intensity distribution for the 153 GRBs detected by BATSE. The violation of the $N \propto S^{-3/2}$ proportionality indicates an edge to the distribution. Instead of fluence S, $C_{\max}/C_{\min}$ is plotted, where $C_{\max}$ and $C_{\min}$ are the maximum and the minimum gamma-ray count rate, with $C_{\min}$ being the weakest burst *CGRO* could confidently detect (see also Schmidt et al. 1988). Figure reproduced from Meegan et al. (1992).

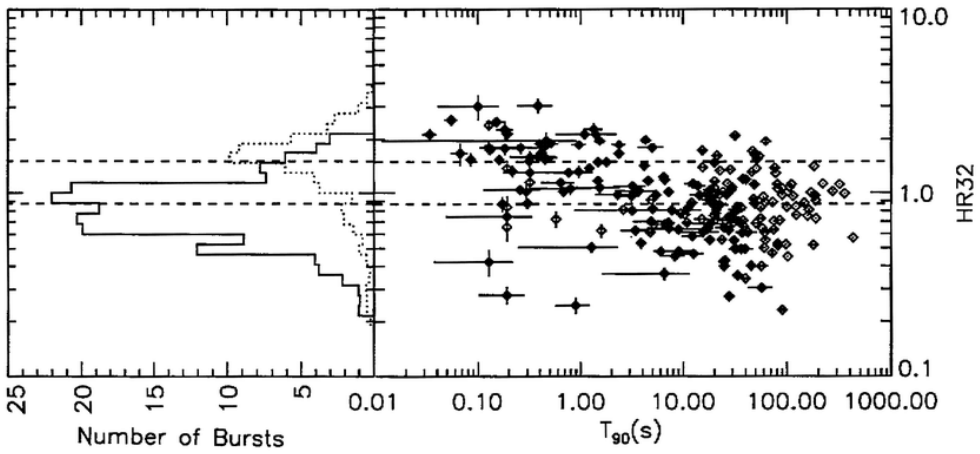

Figure 1.3. Hardness ratio HR_{32} vs. duration plot for the 222 GRBs from the first BATSE catalog. The mean hardness ratios for the short and long GRB class, marked by the dashed lines, are 1.49(±0.08) and 0.87(±0.03), respectively. Corresponding hardness ratio histograms for the two classes are shown on the left. Figure reproduced from Kouveliotou et al. (1993).

Are the sources of GRBs then galactic or extragalactic? More than 100 gamma-ray burst progenitor models were published at the time in the refereed journals, with locations ranging from the Solar System to the distant galaxies. The scientific community was not lacking ideas when it came to the question of GRB origin (see Nemiroff 1994 for a list of proposed progenitors capable of generating a GRB). With the arrival of the new BATSE results, the extragalactic origin theory gained more supporters. The lack of the excess concentration of sources towards the galactic center or the galactic plane was inconsistent with any Galactic disk progenitor model. At the same time, the observed number of weak bursts was well below the number one expected for the spatially extended homogeneous distribution of sources. The conclusion was straightforward; Earth is in the center of a spherically symmetric distribution of gamma-ray sources that do not extend indefinitely. On the account of the recent discovery that some NSs have velocities high enough to escape the Galactic disk (Frail et al. 1994; Lyne & Lorimer 1994), the Galactic disk theory was replaced with a spherical Galactic halo hypothesis. Here, the halo is populated with bursting NSs (e.g., Brainerd 1992; Podsiadlowski et al. 1995). The halo size requirement, imposed by the angular burst isotropy, meant that the halo should be large enough so that the Earth's offset from the Galactic center remains undetectable. That condition also implied that we should be able to see the bursts from the local Andromeda galaxy[6], as well as the bursts of the local Galactic NSs in the form of a separate component. The aftermath of these results did not point to any known galactic parent population for the phenomena or any known nearby extragalactic group association. These main setbacks further cast doubt on the galactic origin of GRBs.

The idea that GRBs could arise from cosmological sources naturally explained the isotropy and the shortage of faint sources in terms of redshift effects (e.g., Mao & Paczynski 1992). It also encountered few difficulties, such as already mentioned compactness problem and the required energetics of $\sim 10^{52}$ erg (see more in Section 1.4 about the consequent *fireball* model). For the debate to be settled, a direct measurement of distance was needed. Locating the host galaxy or a progenitor star required precise GRB locations and fast follow-up observations in longer wavelengths. An interaction of high-velocity ejecta with a medium surrounding the GRB progenitor should be detectable in X-ray and other, less-energetic, energy bands (i.e., the GRB *afterglow*). However, at the time it was unclear if these longer-lived counterparts existed. The burst positions located by BATSE were ill-determined. Locations of even the strongest bursts had error-boxes of a few degrees across and thus contained a large number of possible counterparts[7]. The earliest follow-up observations could also only take place several days after the burst detection, which was another shortcoming of BATSE. No follow-up observations were therefore possible and the investigation of the GRB phenomenology remained limited to gamma-rays alone.

BeppoSAX and the cosmological origin of GRBs

Faster and more precise localizations were made possible in 1996 with the launch of *BeppoSAX* X-ray satellite (Boella et al. 1997), a product of collaboration between the Italian Space Agency and the Netherlands. Its key objective was to study the transient X-ray sources over a wide area of the sky. Approximately 5% of GRB energy is emitted in the form of X-rays (Yoshida et al. 1989). Although *BeppoSAX* was not specifically designed for GRB studies, it was therefore able to provide faster and more precise burst localization. Scientific payload onboard the *BeppoSAX* was divided into two classes: the Narrow Field Instruments (NFIs, e.g., Parmar et al. 1997), covering an energy range of 0.1–300 keV with a 30" accuracy, and the Wide Field Cameras (WFCs, Jager et al. 1997), with an energy window of 2–30 keV and the positional accuracy of about 2'. The third instrument, Gamma-Ray Burst Monitor

[6] Brainerd (1992) notes that the isotropy can be achieved if the halo extends out beyond 100 kpc. For comparison, Andromeda galaxy is located approximately 780 kpc from Earth.

[7] For a typical GRB redshift of ~ 1 there can be hundreds of galaxies within an arcminute error-box.

(GRBM, Frontera et al. 1997), had limited positional accuracy and, in principle, no imaging capability. Operating in 40–700 keV band, it served as a temporal trigger and as a provider the hard X-ray spectral information. Positioning limitations were evaded by coupling the GRBM with the WFCs. This produced a localization with error-boxes of 2–3' across. The 600 km equatorial orbit of the satellite, with a period of 96 minutes, had multiple advantages. The cosmic-ray background at this altitude was reduced due to the Earth's magnetic field, which thus shielded the important high-energy instruments. The passage time over the South Atlantic Anomaly[8] (SAA) was also reduced. Finally, the short orbital period meant frequent communication with the ground station in Malindi (Kenya) and the consequent data exchange with the Science Operation Center in Rome. The typical delay between a GRB and the follow-up observation was reduced to ~ 8 h, with a minimum of 5 h. More accurate NFI observations could then be scheduled and uplinked during the next available spacecraft passage.

Fast and precise burst localizations, wide spectral coverage and rapidly scheduled follow-up observations soon resulted in the first detection of an X-ray afterglow from a GRB 970228 (Costa et al. 1997). Due to the rapid knowledge of the burst position, other ground-based optical telescopes were now able to probe that area of the sky as well. This facilitated the detection of an optical counterpart at the same location (van Paradijs et al. 1997). Subsequent deep images of the region taken with the *Hubble Space Telescope* revealed a nebula like structure (Sahu et al. 1997). It was unclear if it was a distant host galaxy or a local explosion remnant. The final resolution of the distance question came with the detection of GRB 970508 and, soon following, GRB 971214. The early detection of the optical afterglow in GRB 970508 and its relative bright magnitude enabled the optical spectroscopy analysis. This revealed FeII and MgII absorption lines, produced by the gas in the galaxy on a distance of $z = 0.835$ (Metzger et al. 1997). Thus, the question of the galactic/cosmological origin of GRBs was finally settled. Further confirmation came in the same year with the detection of the GRB 970508 afterglow, which showed spectral features corresponding to the redshift of $z = 3.42$ (Kulkarni et al. 1998).

The connection between SNs and GRBs was long expected (Woosley 1993; Paczyński 1998b), even in the case of, now rejected, galactic progenitor models (Colgate 1974). A direct link between SNs and long GRBs was established with the observation of GRB 980425 and the SN1998bw (Galama et al. 1998). At the distance of just 40 Mpc, the energy of the burst was peculiarly low ($< 10^{48}$ erg). The fluence was observed to be orders of magnitude lower than one would expect for such a close burst. Soon after, the rebrightening of the optical light-curve revealed an underlying SN signature. In the following years, more evidence that support this connection were found (e.g., Bloom et al. 1999; Reichart 1999). A notable mention is the bright GRB 030329 at the redshift of $z = 0.167$ (Vanderspek et al. 2004) detected by *HETE-2* instruments (High Energy Transient Explorer Satellite, Ricker et al. 2002). The isotropic energy of this burst was more similar to the bulk of GRB population ($\sim 10^{52}$ erg). About two weeks after the burst, the spectroscopic signature of a type Ic SN emerged in the optical emission spectrum. The spectrum of this SN, named SN 2003dh, was incredibly similar to the one of SN1998bw (Hjorth et al. 2003), despite the fact that two GRBs had a 5 orders of magnitude difference in energy. This confirmed the connection between long GRBs and SNe, which is now generally accepted and plays an important role in the *fireshell* model (see Chapter 2). As for short GRBs, merger of two NSs or a NS and a black hole (BH), suggested by various authors (e.g., Narayan et al. 1992; Mochkovitch et al. 1994), remains the leading model up to this date (see Section 1.4). The observational differences between long and short bursts are described in more detail in Section 1.3.

[8] The South Atlantic Anomaly is an area of the increased flux of energetic particles coming from the Earth's inner Van Allen radiation belt. In order to reduce the exposure levels, satellites usually do not take observations while passing through it.

1.2 SWIFT OBSERVATORY AND THE AFTERGLOW ERA

As it was discussed in Section 1.1, the possibility to accurately pin-point GRB location came with the detection of their longer-lived counterparts. Wavelengths of these counterparts range from radio, optical to X-ray. These so-called *afterglows* are visible for several hours to weeks after the trigger, generally fading according to the power-law $F_\nu(t) \propto t^{-\alpha}\nu^{-\beta}$. They are described reasonably well with synchrotron emission from accelerated electrons and accordingly have a featureless power-law spectrum. In the standard *fireball* model (Section 1.4), the afterglow arises from the dissipation of kinetic energy in *external* shocks. This occurs when the relativistic outflow interacts with the circum-burst medium (CBM) surrounding the GRB (Mészáros & Rees 1997; Sari et al. 1998). As the flow slows down, the peak of the emission shifts to lower energies, from X-rays to radio wavelengths. The model differentiates between a forward and a reverse shock, although there are inconsistent observational evidence for the latter. A reverse shock propagates back into the ejecta and should be detectable in optical and radio wavelengths at early times of the emission. Therefore, GRB afterglows can provide insights into the burst energy and CBM properties (e.g., see Schulze et al. 2011).

The next step towards was the *Swift* mission (Gehrels et al. 2004), built by an international team of US, UK, Italy, Japan, and Germany. Launched in 2004, its purpose was to investigate the GRBs and their afterglows. The temporal gap between the prompt emission and the observations of the fading afterglow was considerably shortened due to, now well-established, strategy involving the three instruments onboard the *Swift* spacecraft. The wide-field Burst Alert Telescope (BAT, Barthelmy et al. 2005b) detects GRBs in the 15–350 keV band. In about 20 seconds, it can provide a crude burst localization with a 1–4 arcminute accuracy. Within the next two minutes, the X-Ray Telescope (XRT, Burrows et al. 2005b) slews into position and pinpoints the afterglow in the 0.2–10 keV energy range, with a typical accuracy of 5 arcseconds. Utilizing the new refined position, ultraviolet (UV) and optical observations can be carried out by the Ultraviolet/Optical Telescope (UVOT, Roming et al. 2004) onboard the *Swift* spacecraft, or by any other ground-based telescope.

With an annual average rate of about 100 detections, the last published BAT GRB catalog (Lien et al. 2016) counted ~ 1000 GRBs of which ~ 360 had redshift measurements, ranging from $z = 0.03$[9] (Mirabal & Halpern 2006) to $z = 9.38$[10] (Cucchiara et al. 2011). From the redshift distribution, it was seen that *Swift* was detecting GRBs at higher redshifts than any other previous mission. The average redshift of long GRBs increased from $\bar{z} = 1.2$ to $\bar{z} = 2.4$. It was found that the distribution is consistent with the models in which the GRB rate is proportional to the star formation rate (SFR, e.g. Jakobsson et al. 2006). The *Swift* detections of distant GRBs with $z > 8$ (Salvaterra et al. 2009; Ruffini et al. 2014b) opened a new era of high-redshift Universe exploration. It remains to be seen if the GRB rate follows the SFR up to these distances (e.g., Wanderman & Piran 2010). GRBs are also expected to answer other open questions in cosmology, providing a better view of the reionization and metallicity history of the Universe (see Section 1.5). Detection of GRB 050509B provided the first localization of the short GRB X-ray afterglow (Gehrels et al. 2005a). The *Swift* observatory also contributed to the detection of the first radio counterpart (GRB 050724, Barthelmy et al. 2005a) of a short GRB. Due to its higher sensitivity in the low energy range, it also revealed the existence of ultra-long GRBs as well as the unexpected, soft, extended emission in few short GRBs, challenging the standard twofold classification (Norris & Bonnell 2006). Other notable contributions of the *Swift* observatory that involve transient events include: the first evidence

[9] Unfortunately, GRB 170817A with $z = 0.0095$ at the time was outside BAT field of view, but it was later observed by *Swift* in longer wavelengths.

[10] The inferred redshift of GRB 090429B was photometric, with the 90% likelihood range for the $9.06 < z < 9.52$ (although there is a low-probability tail to somewhat closer redshifts).

of a kilonova[11] (KN) in a short GRB (Tanvir et al. 2013), observations of a SN shock breakout (Soderberg et al. 2008), and detection of tidal disruption events (Bloom et al. 2011). For a more complete picture of the achieved observational milestones, see Gehrels & Cannizzo (2015).

X-ray afterglow

In 2004, with new XRT data starting only seconds after the burst, an unexpected X-ray afterglow picture began to emerge. Early X-ray afterglow showed canonical behaviour, involving one or more of the following five components, as labeled in Figure 1.4 (Zhang et al. 2006a; Nousek et al. 2006; Bernardini et al. 2012):

I **The initial steep decay** is associated with the tail of the prompt emission (0). Typically it extends up to 300–500 seconds, with a temporal index $\alpha \lesssim 3$, where $F \propto t^{-\alpha}$ (Tagliaferri et al. 2005). The spectral slope is usually different from the later afterglow phases. The most widely considered explanation involves the prompt phase photons that are radiated at large angles relative to our line of sight. This off-axis emission from $\theta > 1/\Gamma$ is then observed once the line-of-sight gamma emission had ceased (*high-altitude emission* model, Kumar & Panaitescu 2000). Here, the combined effect of the delay in the off-axis photon arrival ($\Delta t \approx R\theta^2/2c$) and the Doppler factor ($\propto t^{-1}$), which shifts the energies into the X-ray observer band, is thought to produce the observed steep decay (e.g., Panaitescu et al. 2006b). The flux decay (more or less) satisfies a simple relation in the form of $\alpha = 2 + \beta$, where $F_\nu(t) \propto t^{-\alpha}\nu^{-\beta}$ (Zhang et al. 2006a, also see Section 1.4 for closure relations). Although, some steep decays show spectral evolution which can not be interpreted within this model (Zhang et al. 2007b, also see O'Brien et al. 2006).

II **The plateau/shallow decay phase** begins within the first hour and lasts up to 10^3–10^4 seconds. It is characterized by a slope of $0.2 \lesssim \alpha \lesssim 0.8$, or sometimes even a flat profile. Both out of the two suggested explanations involve a continuous energy injection into the external shock. In the first one, flattening is the result of a broken power-law Γ distribution in the initial ejecta (Granot & Kumar 2006), where Γ is the Lorentz factor. When the initial afterglow, produced by the high-Γ end of the ejecta starts to decline, a slower portion catches up and provides an additional energy injection to the shock (Rees & Mészáros 1998). The alternative considers a prolong central-engine activity, possibly due to the continued fall back of the material into the BH (Woosley & Heger 2006).

III **The standard afterglow phase** with $1.1 \lesssim \alpha \lesssim 1.7$ can last up to 10^5 or even longer for some cases.

IV **A late time steep decay** has been seen in less than $\sim 10\%$ of the afterglows followed-up by *Swift*, and usually but not always in long bursts. In that case, the decay steepens ($2 \lesssim \alpha \lesssim 3$) after $\sim 10^5$ s. It was also observed in pre-*Swift* optical afterglows. Achromatic steepening of the light-curve is expected after ~ 1 day if the relativistic outflow is collimated (Sari et al. 1999, see Section 1.4). Once the Lorentz factor has decreased enough for the light-cone angle to become larger than the jet opening angle ($\Gamma^{-1} \gtrsim \theta_j$), the observer misses a part of the emission (Sari et al. 1999). However, only a handful of GRBs with achromatic jet break in both X-ray and optical bands has been observed (e.g., Dai et al. 2007; Mangano et al. 2007). There is a lack of evidence for jet breaks in the XRT afterglows (Sato et al. 2007; Willingale et al. 2007): the number of bursts with achromatic break detection is small (e.g., Liang et al. 2008a) and, although there are a few possible jet break candidates,

[11] Kilonova, or Li-Paczyński macronova, manifests itself as a bump in the optical and near-infrared late afterglow of short GRBs (Li & Paczyński 1998; Kulkarni 2005; Metzger et al. 2010). The merger of two NSs ejects a neutron-rich matter, where heavy elements are synthesized by the r-process (the rapid neutron-capture process). The produced elements are unstable and radioactively decay, heating up the ejecta along the way. This is believed to be the origin of the macronova emission, which exhibits weak luminosities on the order of 10^{41} erg s^{-1} (e.g., Tanvir et al. 2013; Berger et al. 2013; Yang et al. 2015). However, the discussion regarding the process which powers this emission is still ongoing (e.g., Matsumoto et al. 2018).

there are many examples in which the late decay for days proceeds as a single power-law, therefore not satisfying the tight Ghirlanda relation (see Section 1.3). Still, there is a doubt that the poor data quality is responsible for the absence of break detections (Curran et al. 2008).

V **X-ray flares** are seen in $\sim 33\%$ of the X-ray afterglows (Chincarini et al. 2010). One or multiple flares can be superimposed to any segment of the light-curve (starting as early as 100 s after trigger or as late as $\sim 10^5$ s), although they are known to occur predominantly during the steep declining phase. No correlation was found between the number of flares of a single event and the number of detected prompt pulses (Chincarini et al. 2007; Falcone et al. 2007). They are portrayed by a rapid rise and decay with $3 \lesssim \alpha \lesssim 6$ and, in some cases, an extreme fluence comparable with the prompt emission (e.g., GRB 050502B, see Burrows et al. 2005a; Falcone et al. 2006). Their average fluence, however, is about 10% of the prompt emission fluence observed by BAT (Chincarini et al. 2007; Falcone et al. 2007). The flux level after the flare usually decays to the value extrapolated from the earlier times, suggesting a presence of two emission processes that overlap in time (Willingale et al. 2007). While their $E_{\rm p}$ is typically in the soft X-rays, there is no apparent agreement within the scientific community regarding the prevalent spectral evolution pattern (see Section 1.3). Both hard-to-soft evolution and intensity tracking are said to be the one that is commonly observed (Chincarini et al. 2007; Falcone et al. 2007; Butler & Kocevski 2007; Margutti et al. 2011). The flare intensity was also observed to decrease with time while the flare duration was seen to increase with time.

The extrapolation of flux levels prior to the flare, in addition to their extreme steepness and the vast energy budget, relates them to the late central-engine activity rather than to an afterglow-effect (Nousek et al. 2006; Panaitescu et al. 2006b; Sonbas et al. 2013). Still, a notable fraction of flares can not be related to the external shock mechanism (Chincarini et al. 2007; Falcone et al. 2007). In addition, there is still an ongoing debate on how does one exactly restart the central engine (e.g., Proga & Zhang 2006; King et al. 2005). The matter becomes more complicated when one recalls that the progenitors of short and long GRBs differ, while the flares are said to occur in all kinds of GRBs (Chincarini et al. 2007; Falcone et al. 2007). Several mechanisms were suggested as an explanation of the flaring activity in short GRBs (e.g., see Fox et al. 2005; La Parola et al. 2006), including the fragmentation of the accretion disk (Perna et al. 2006), magnetic halting (Proga & Zhang 2006) and long-term evolution of the debris (Lee et al. 2009). The occurrence of energetic flares, especially hours after the trigger time, therefore remains difficult to understand.

The above-described I–IV components are visible in less than half GRBs and mainly in long bursts (Evans et al. 2009), although some short bursts manifested similar afterglow behavior. Phases I–III were not anticipated in the pre-*Swift* era (with one misinterpreted exception, e.g. see Piro et al. 2005). Apart from the large prompt fluence that is usually followed by a large afterglow fluence (Nysewander et al. 2009), there is no tight correlation between the prompt and afterglow component parameters (with few claimed exceptions, see Section 1.3). A review of the observational progress on the GRB afterglow and subsequent theoretical implications can be found in Zhang (2007a). Margutti et al. (2011) offers an extensive comparison of short and long GRB flares.

Thermal component in the early X-ray afterglow

Once in a while, an additional thermal component is identified in the early X-ray afterglows (in about 5% of long GRBs, Valan et al. 2018). Because the detection usually happens when the X-ray luminosity is low, the thermal component might occur in a larger number of GRBs but remain hidden due to their bright afterglows. Prompt emission properties of these GRBs appear to be unexceptional in every way. This includes their spectral parameters, total energy, duration and, the light-curve behavior (Valan et al. 2018).

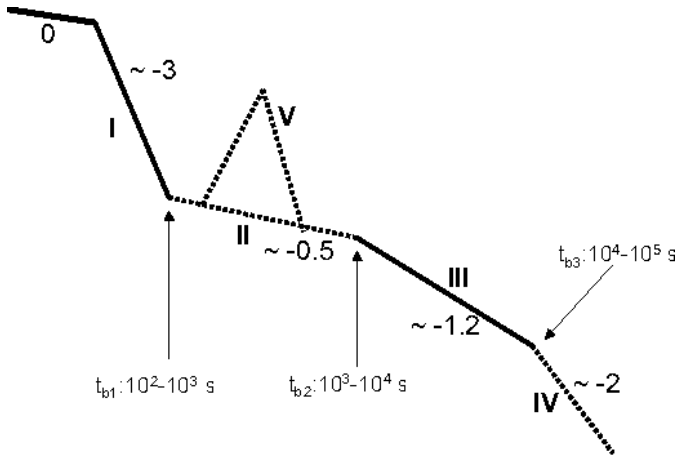

Figure 1.4. The log flux-log time schematics of the canonical X-ray afterglow. Five components observed by *Swift* are shown: a steep decline in the afterglow (I) following the prompt phase (0), shallower decline/plateau phase (II), a standard afterglow phase (III) and possibly, a final steepening (IV) with flaring activity (V) superimposed on the plateau phase. Decay indices and typical observed phase times are also indicated. Figure reproduced from Zhang et al. (2006a).

Due to the limited GRB sample, the origin of the thermal component is still debated. The narrow range of black body (BB) radii ($\sim 2\times10^{12}$ cm), paired with a large range of luminosities ($L_{\rm p} \sim 10^{47}$–10^{51} erg/s), points towards the progenitor star. Origin of the thermal component is usually explained by invoking one of the two leading models: the SN shock breakout and the emission from the cocoon surrounding the jet (Mészáros & Rees 2001; Starling et al. 2012, see also Friis & Watson 2013).

A flash of UV/X-ray radiation with a BB spectrum is produced when photons from the expanding SN shock wave start escaping the star (Waxman & Katz 2017). This SN *shock-breakout* can last from seconds to tens of minutes. Optical emission on a longer timescale is subsequently produced by the cooling envelope. The timescale of a shock-breakout is expected to be around few seconds[12], with energies $\sim 10^{44}$ erg and spectrum peaking in the range of few keV. Campana et al. (2006) favored this explanation in the case of GRB 060218, which was the first detected burst with a BB component observed within the spectrum of the X-ray afterglow. However, this scenario was ruled out for most of the following detections. The BB energies well-exceed the 10^{44} erg order of magnitude (e.g., Nappo et al. 2017). The second case invokes a hot, mildly relativistic *cocoon* which forms around the jet as it propagates through the star and interacts with its material (Ramirez-Ruiz et al. 2002, see Section 1.4). While emerging from the star together with the jet, it starts to spherically expand, producing a signal similar to but more energetic than SN shock breakout (e.g., Izzo et al. 2019).

X-ray flashes

X-ray flashes (XRFs, Heise et al. 2001), not to be confused with the X-ray flares or the X-ray afterglow, make up about 1/3 of the total GRB population (Heise 2003). In standard GRBs, the X-ray fluence is of order of 10–20% of the gamma-ray fluence. XRFs and an intermediate class called the X-ray rich gamma-ray bursts (XRGRBs) are transient events distinguished by a faint signal in the gamma-energy range (or a complete lack of it), where the X-ray fluence is comparable to or larger than the gamma-ray

[12]The timescale of a shock-breakout is assumed to be close to R/c, where $R \sim 10^{11}$ cm is the radius of a Wolf-Rayet star, an assumed progenitor of GRBs (e.g., Sander et al. 2012).

one. Their duration, ranging from few tens to $\sim 10^3$ seconds, together with the fulfillment of the Amati relation (Amati et al. 2002), suggests a common cosmological origin with standard long GRBs. Their spectra are also similar to the ones of long GRBs (Section 1.3), with the exception being the lower values of $E_{\rm iso}$ and $E_{\rm p}$[13] (typically less than $\sim$ 15 keV for the majority of XRFs, see Kippen et al. 2003; Sakamoto et al. 2005). The observed X-ray luminosities are a factor of two lower than those of typical long GRBs (D'Alessio et al. 2006). Overall, XRFs, XRGRBs, and long GRBs seem to form a smooth continuum.

A straightforward explanation would include a regular long GRB at the redshift of $z \sim$7–8, observed as an XRF due to the shift in the $E_{\rm p}$ (Heise 2003). This was dismissed as a universal explanation soon after the detection of the first XRF host galaxy at $z < 3.5$ (Bloom et al. 2003a). Another possibility is that the long GRBs are being observed off-axis (Yamazaki et al. 2002; Dado et al. 2004). In that case, the luminosity should depend on the off-axis viewing angle and be significantly fainter. Because of it, the model suffers severe problems (e.g., D'Alessio et al. 2006), although it is not completely excluded. The final option revolves around an intrinsic property of the source due to which most of the energy is radiated in the X-ray range (e.g., Dermer et al. 1999). The real nature of XRFs remains a riddle, with a possibility of all three scenarios contributing to the answer.

Optical afterglow and the SN connection

The brightest optical burst ever observed was GRB 080319B (Racusin et al. 2008). With the peak apparent magnitude of 5.3, it was brighter than the faintest naked-eye star. Fast follow-up observations revealed three different optical components. The emission during $t < 50$ s possibly originated in the same region as the gamma-ray emission as they shared a common shape. The excess above the time-reversed extrapolation from the later optical decay was observed at 50 s $<$ t $<$ 800 s, correlating the second optical component with a reverse shock (also see Section 1.4). Within this model, the emission becomes detectable only when the prompt phase fades away. Also, the high peak optical luminosity observed so soon after the prompt phase suggests that the reversed shock was at least mildly relativistic. Finally, the time interval $t > 800$ s corresponded to the external forward shock propagating into the surrounding medium. Still, although the rapid response of the *Swift* satellite enabled early optical follow-ups, there are only several GRB afterglows which can be generally interpreted within the reverse shock model (e.g., see Japelj et al. 2014). In addition, there have been few cases with a clear lack of the reverse shock component despite the early observation of a bright optical afterglow (e.g., Schady et al. 2006; Mundell et al. 2007).

Twenty years ago, the association of GRB 980425 with SN1998bw provided the first direct link between long GRBs and deaths of massive stars (also see Section 1.1). A mounting observational evidence emerged in the following years. Bumps, superimposed on the otherwise featureless power-law decay, would emerge after $\sim$ 10 days in the optical afterglow light-curves (Figure 1.5). In 2006, this association was extended to XRFs with the *Swift* detection of GRB 060218/SN 2006aj at z = 0.033 (Campana et al. 2006). This was also the first GRB with a directly observed SN shock breakout, inferred from the evolution of a soft thermal component through X-ray and UV spectra. The burst was underluminous, making its detection a rare event, possible only due to its proximity[14]. On the other hand, the *Swift* observatory also added GRB 130427 to the list of bursts with accompanied SN detection (Maselli et al. 2014; Melandri et al. 2014). At redshift $z = 0.340$ (Levan et al. 2013) and with energy $E_{\rm iso} =\sim 10^{54}$ erg, it falls within the 5% of the most luminous bursts observed with *Swift*. Hence, these observations imply that similar progenitors can create GRBs with $E_{\rm iso}$ spanning over six orders of magnitude.

[13] $E_{\rm iso}$ stands for the isotropic-equivalent radiated energy, calculated in the 1–10, 000 keV range in the rest-frame of the source. $E_{\rm p}$, or $E_{\rm peak}$, is the peak energy of the $\nu F(\nu)$ spectrum, where $\nu F(\nu) \propto E^2 N(E)$.

[14] Although rarely detected, these events should be 5–10 times more common than normal GRBs (Soderberg et al. 2006).

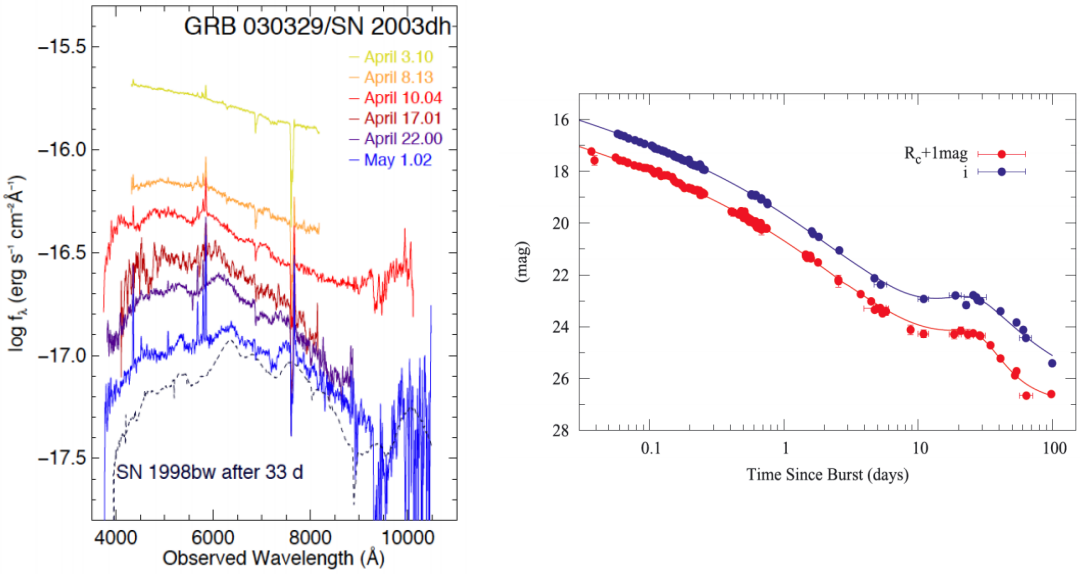

Figure 1.5. *Left panel:* Spectral evolution of the optical flux density observed in the afterglow of GRB 030329/SN2003dh. It transitions from a featureless power-law (upper spectrum) to a SN-like dominated spectrum (lower spectrum). Dashed line outlines the spectrum of SN1998bw after 33 days, shifted to the GRB 030329 redshift. Superimposed strong emission lines come from the underlying host galaxy. Figure reproduced from Hjorth et al. (2003). *Right panel:* Optical light-curve of GRB 090618 in blue and red filters. A late SN bump starts to emerge ~ 20 days after the trigger. Figure reproduced from Cano et al. (2011).

When compared to previous SNe associated with GRBs, SN 2006aj was dimmer by a factor ~ 2 yet 2–3 times brighter than a regular SN/Ic (Pian et al. 2006). All of the SNe associated with GRBs up to date are of type Ic: broad-lined with signatures of neither H nor He. Even (well) before the afterglow era, it was noted that the energy release of a GRB would be comparable to a typical SN explosion if they lie at cosmological distances (Paczynski 1986). Indeed, the total energies emitted are roughly of the same order of magnitude with an important difference in the timescale during which the radiation is released. In a GRB (SN), energy is emitted in a matter of seconds (months) in the form of a (non-) relativistic outflow with non-thermal (thermal) emission.

Although the *Swift* observatory dramatically changed the way we study GRBs and their association with SNe, the detection of the first optical counterpart was a result of a joined effort of *HETE-2* and *Chandra* (Weisskopf et al. 2000) satellites (GRB 050709, Villasenor et al. 2005; Fox et al. 2005). Deep follow-up observations of the host galaxies of these three GRBs revealed no presence of a SN, despite their proximity ($z < 0.26$, Gehrels et al. 2005b; Fox et al. 2005; Berger et al. 2005). This showed that short GRBs are cosmological sources with a progenitor that is not associated with deaths of massive stars. Still, not all nearby ($z \lesssim 1$) long GRBs have an accompanying SN detection. *Swift* annually discoveries around 6–8 long GRBs at $z < 1$. The detection rate of the GRB-associated SNe is around 2–3 per year (Klose et al. 2019). Up to this date, around 50 GRBs have a photometrically identified SN in their optical afterglows, 50% of which have an additional spectroscopic confirmation (Cano et al. 2017). GRB 060505 (Fynbo et al. 2006), GRB 060614 (Della Valle et al. 2006; Fynbo et al. 2006), and GRB 111005A (Tanga et al. 2018) are examples of nearby long GRBs with no SN detection. If the possibility of a chance projection of some foreground galaxy is excluded, the long-lasting bright optical afterglow could be responsible for the lack of detection as it can hide the rising SN component. Still, SN-less bursts pose a challenge to current

models and the classification scheme. An excellent review of GRBs and the photometric and spectroscopic properties of their accompanying SNe can be found in Cano et al. (2017).

Taking into account the combined effort of ground-based optical observatories, about 60% of *Swift*-GRBs have optical afterglow detection. The remaining part is dubbed as "dark" GRBs (Fynbo et al. 2001). Bromm & Loeb (2002) estimate that 20–30% of GRBs should lie at $z > 5$. At these redshifts, the Lyα absorption in the R band could be accountable for the lack of optical detections (see Section 1.5). This was dismissed as the only explanation when dark GRB host galaxies were observed at $z \approx 1$ (Djorgovski et al. 2001; Piro et al. 2002). The next suspected culprits were the dusty, star-forming regions, expected to obscure the optical afterglow by the means of strong absorption. Both scenarios could introduce a problem in terms of selection bias and sample completeness when it comes to statistical studies of long GRB host galaxies (Section 1.5). On the other hand, rapidly fading optical afterglow of GRB 021211 (Fox et al. 2003), which would otherwise be missed if not delivered by the fast detection of HETE-2, pointed to a possibility of intrinsically subluminous events (e.g., low-density environment or low-explosion energy). According to Fynbo et al. (2001), about 75% of dark GRBs could also be characterized as dim bursts. Indeed, dark GRBs are on average six times fainter in X-rays than bursts with optical detection (De Pasquale et al. 2003). More precisely, 75% of dark bursts have an optical-to-X-ray flux ratio consistent with the ones of optically bright GRBs (i.e., achromatic dimming effect). The remaining 25%, for which the optical band is effected more than the X-ray band, could be explained by the first and second scenario.

From radio waves to GeV emission

High-energy emission (>100 MeV) was first detected in five GRBs (Dingus 1995) observed by the Energetic Gamma-Ray Experiment Telescope (EGRET, Kanbach et al. 1988) onboard CGRO. The high-energy emission of GRB 930131, lasting more than 200 s, manifested a different temporal behavior when compared to the low-energy emission. It also required an additional spectral component. On the other hand, for GRB 930131, high energy emission was consistent with an extrapolation from its BATSE spectrum in the 25 keV–4 MeV band (Sommer et al. 1994). The prolonged emission lasting ~ 90 minutes was also observed in GRB 940217, with an 18 GeV photon arriving ~ 75 minutes post-trigger (Hurley et al. 1994). *Fermi Gamma-Ray Space Telescope* (*Fermi*, see also Section 3.1) was launched in 2008. Within the first year of operation, the Large Area Telescope (LAT, Atwood et al. 2009) onboard *Fermi* had more than doubled the number of GRBs detected above 100 MeV. LAT is a pair conversion telescope, covering the energy range from 20 MeV up to more than 300 GeV. By the time the first catalog was published (Ackermann et al. 2013b), 28 GRBs (both long and short) have been detected above 100 MeV. The *Fermi* observation of GRB 090926A (Ackermann et al. 2011) clearly showed an extra high-energy component in addition to the Band function (Band et al. 1993, also see Section 1.3). The additional component was found in both time-integrated and time-resolved analysis, similar to GRB 090510 and GRB 090902B (Ackermann et al. 2010a; Abdo et al. 2009b). The exception was GRB 080916C (Abdo et al. 2009c), where adding an additional component did not improve the fits. A common pattern started to emerge:

THE DELAYED ONSET The delay observed in high energy emission is common to almost all LAT GRBs, with few exceptions (e.g., GRB 090217A, Ackermann et al. 2010b). It may arise due to the flux increase or hardening of the Band component or, on the other hand, due to the flux increase within the additional component, depending on the model.

TEMPORARY EXTENDED EMISSION The GeV emission lasts longer than the prompt MeV emission. The flux shows a power-law decay: $F_\nu \propto (T - T_0)^\alpha$ where $\alpha \sim -1.5$ (e.g., Abdo et al. 2009b; Ackermann et al. 2010a). The peak count rates may coincide with the ones in prompt emission observed in the lower energy range.

ADDITIONAL HIGH-ENERGY COMPONENT The origin of the additional power-law component is not yet fully understood in both external and internal emission scenarios. In internal shock models, both spectral components arise within the ejecta. The extra component can arise either due to the Compton scattering of soft target photons by relativistic electrons (Gao et al. 2009; Bošnjak et al. 2009) or via hadronic processes (e.g., see Asano et al. 2009). In the former alternative, which invokes the broadband afterglow emission, the external forward shock that propagates into the CBM can produce a significant amount of gamma-ray emission from the high energy tail of synchrotron radiation (Kumar & Barniol Duran 2009; Ghisellini et al. 2010). Here, the delayed onset of the LAT emission is explained as the time required for the forward shock emission to sweep up enough material and become detectable. Still, afterglow contributions to the gamma-ray flux at these early times would indicate a significantly earlier onset of the interaction between the GRB blast wave and the CBM. Also, a rapid variability observed in GRB 090926A is not expected within the external shock model (Ackermann et al. 2011). High temporal variability introduces some strong constrains, including the one that the external medium needs to be highly clumpy. More recently, Acciari et al. (2019) reported an observation of 0.2–1 TeV emission coming from GRB 190114C, thought to originate from the inverse Compton upscattering. Further study of the GRBs in the GeV energy range is needed to resolve these issues. It will also provide the possibility of further explaining the nature of the progenitors and the ultra-relativistic outflows (Band et al. 2009).

At the other end of the afterglow spectra, the number of radio observations has been fairly constant before and after the launch of *Swift*. From 1997 to 2011, 304 afterglows in radio bands were observed, constituting a detection rate of $\approx 31\%$ (Chandra & Frail 2012). This changed with an upgrade of the Karl G. Jansky Very Large Array (VLA). A significantly better VLA sensitivity resulted in an increase of the radio detected GRBs to 60% (Hancock et al. 2013). Still, GRB radio flux densities are typically at the sub-mJy level and remain accessible only to the largest telescopes in the world. In radio wavelengths, the afterglow emission is long-lasting: light-curves rise during the first hours or days, peak on a timescale of days to weeks and remain detectable for months, even years (e.g., GRB 030329, Berger et al. 2003; Frail et al. 2005; Mesler et al. 2012). The importance of the radio afterglow comes from an independent and direct confirmation of the relativistic expansion (e.g., Frail et al. 1997). Scintillations, erratic variations in flux by a factor of ~ 2, will be suppressed once the angular size of the source becomes larger than the electron fluctuation scale in the interstellar medium. Knowing the distribution of plasma clouds in our Galaxy, one can then infer the evolving size of the source. The analysis of the nearby GRB 030329 showed that the expansion with the Lorentz factor of $\Gamma \approx 7$ was still ongoing one month after the GRB (Taylor et al. 2004). Also, high-redshift, bright radio afterglows could excite the spin doublet fundamental state of the neutral hydrogen, producing a characteristic forest of 21-cm absorption lines. This would help to constrain the gas distribution and the reionization history (Ciardi et al. 2015, also see Section 1.5).

The ongoing study of both the prompt and the afterglow emission is required for a more complete picture of the central engine and emission process of GRBs. In the end, our progress in understanding the GRBs will always remain highly dependent on the capabilities of the observatories that carry out the measurements. Many other missions contributed to our progress and overall knowledge of this phenomena. Another Italian X- and γ-ray satellite, the AGILE (*Astro-rivelatore Gamma a Immagini Leggero,* Tavani et al. 2009), has been observing the sky since 2007. With its three detectors, it covers a wide energy range of 18–60 keV in hard X-rays and a range of 30 MeV–50 GeV in the gamma-ray energy window. The X-ray satellite *Suzaku* (Mitsuda et al. 2007) also contributed to the GRB research field through the afterglow follow-ups by its two narrow field instruments, covering the 0.3–600 keV range. The prompt GRB emission, on the other hand, was also observed in the 50–5000 keV by the *Suzaku*/WAM (Wide-band All-sky Monitor, Yamaoka et al. 2009), primarily used as a shield for the HXD (Hard X-ray Detector, Takahashi et al. 2007), rejecting its background. Thanks to its large effective area and a wide field of

view, WAM detected more than 1400 GRBs in 10 years of operation, a number comparable to that of other, GRB-specialized observatories. Many other X-ray or gamma-ray instruments participate in the GRB observations and follow-ups of their afterglows, such as *INTEGRAL* (International Gamma-ray Astrophysics Laboratory, Winkler et al. 2003), XMM-*Newton* (X-ray Multi-Mirror Mission, Jansen et al. 2001) and *NuSTAR* (Nuclear Spectroscopic Telescope Array, Harrison et al. 2013). A good way to conclude this mission-list would be with the mention of the KONUS/*Wind* (Aptekar et al. 1995), the first Russian experiment onboard a NASA science mission, mainly devoted to the study of the solar wind. As a result, the spacecraft is located in the interplanetary space and the KONUS experiment does not suffer from the SAA effects, nor the Earth's occultation.

Other ground-based observatories are complementing the afterglow observations throughout the rapid data distribution. This is accomplished by using the Gamma-ray Coordinates Network[15] (GCN, Barthelmy et al. 1995; 1998), which includes real-time GRB locations and reports of the follow-up observations. In the *Swift* era, exploitation of the GCN network reached its full potential. Some telescopes have the whole follow-up process completely automatized (e.g., Guidorzi et al. 2006). Deep optical spectroscopy, IR coverage, radio observations, and HST deep imaging are all included in this information exchange and thus form a backbone of the multiwavelength GRB observations.

1.3 NATURE OF LONG (AND SHORT) GAMMA-RAY EMISSION

Temporal and spectral properties of prompt emission

So far we have seen that GRBs are extremely energetic transient sources, observed across the entire spectral range. Their isotropic energy $E_{\rm iso}$ can range from $\sim 10^{54}$ erg down to $\sim 10^{49}$ erg, with XRFs included. Short bursts are typically less energetic than the long ones. While an average X-ray temporal behaviour can be represented with a five-component schematics (Figure 1.4), prompt gamma-ray emission does not seem to follow any pattern (Fishman & Meegan 1995, see Figure 1.6). A light-curve can contain a single or multiple pulses which in return can be smooth or erratic/spiky. A single pulse can also have a FRED-like structure (fast rise, exponential decay). The distinct pulses may or may not be well separated by gaps of no detectable emission (this can lead to T_{90} overestimation). The shape of the light-curve is also influenced by the energy band: wider pulse profiles will be seen in lower energy bands following a power-law $\Delta t \propto \nu^{-0.4}$ (Figure 1.7 - left panel, Fenimore et al. 1995; Norris et al. 1996). In addition, bursts at higher redshifts are expected, on average, to be longer and more energetic (Woosley & Heger 2006; Graziani et al. 2004, see Figure 1.7 - right panel).

The prompt phase is occasionally preceded by a well-separated and less intense episode, called a precursor. There are mixed reports on their occurrence rate and spectral properties, possibly due to the operational definition and instrumental biases. The first systematic search for precursors showed they occur in 3% of bursts with properties that do not differ from the rest of the prompt emission (Koshut et al. 1995). Lazzati (2005) found a spectrally softer precursor in ∼20% of long BATSE GRBs. On the other hand, Burlon et al. (2009) found that 12% of BATSE observed GRBs have one or more precursors, with spectral properties similar to the main emission. This also included the spectral evolution trends in the time-resolved analysis, such as $E_{\rm p}$-intensity tracking (see below). Similar results were obtained for the *Swift* sample (Burlon et al. 2008), within which precursor properties did not depend on the quiescent period duration. This suggests that the phenomenon is not distinct from the main emission. Short GRB precursors exhibit similar properties (Troja et al. 2010) and similar conflicting reports (Minaev & Pozanenko 2017).

[15] https://gcn.gsfc.nasa.gov/gcn/

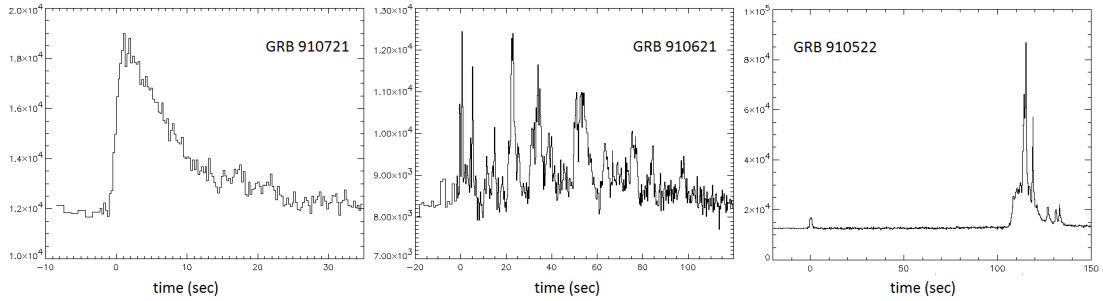

Figure 1.6. Sample of prompt emission temporal variety observed in BATSE light-curves (in units counts/s, Fishman et al. 1994). Figures retrieved from `https://gammaray.msfc.nasa.gov/batse/grb/lightcurve/`.

All studies do agree that the spectrum is typically a non-thermal power-law, with only a few thermal exceptions (e.g., Murakami et al. 1991). A photospheric thermal emission is expected at the moment the fireball transitions to an optically thin regime (Paczynski 1986; Ruffini et al. 2008), Still, the quiescent periods can extend up to ~ 100 seconds. Long delays and non-thermal spectra make it hard to settle the debate about the origin of this early emission.

In contrast to the their temporal profile diversity, most of GRB spectra are well-fitted by the empirical Band function (Band et al. 1993), featuring two smoothly connected power-laws:

$$BAND(E) = \begin{cases} A\left(\frac{E}{100\,\mathrm{keV}}\right)^{\alpha} \exp(-E(2+\alpha)/E_{\mathrm{p}}), & E \leq \left(\frac{\alpha-\beta}{2+\alpha}\right) E_{\mathrm{p}} \\ A\left[\frac{(\alpha-\beta)E_{\mathrm{p}})}{(2+\alpha)100\,\mathrm{keV}}\right]^{\alpha-\beta} \left(\frac{E}{100\,\mathrm{keV}}\right)^{\beta} \exp(\beta-\alpha), & \text{otherwise.} \end{cases} \tag{1.2}$$

The four parameters in the Band function are: the amplitude (A), the low- and high-energy photon indices (α and β, respectively), and the peak of the $\nu F(\nu)$ spectrum (E_{p}). The cut-off energy E_0 is expressed using E_{p}, where $E_{\mathrm{p}} = (2+\alpha)E_0$. It is valid only for well behave parameters of $\alpha > -2.0$ and $\beta < -2.0$. Values of the photon indices usually revolve around $\alpha \sim -1$ and $\beta \sim -2.3$ (Ghirlanda et al. 2002; Kaneko et al. 2006). E_{p} is widely spread over three orders of magnitude as a single distribution, ranging from a few keV to the MeV range (e.g., Kippen et al. 2003). Nava et al. (2011b) showed that long bursts have a typical observed peak energy of ~ 160 keV and low spectral index $\alpha \sim -0.9$ while for short bursts these values are harder, with $E_{\mathrm{p}} \sim 490$ keV and $\alpha \sim -0.5$. Still, the measured E_{p} distribution can be strongly affected by the adopted cuts in the fluence or the peak flux (i.e., selecting only the brightest bursts Kaneko et al. 2006) since these quantities are related (Lloyd et al. 2000; Nava et al. 2008). Ghirlanda et al. (2009) compared a sample of long and short GRBs selected with the same limit on the peak flux and found a similar E_{p} distributions for the two classes. In addition, they find that the spectra of long bursts are similar to the ones found during the first 1–2 seconds of the short GRB emission. Nava et al. (2011a) offers a more detailed comparison between long and short GRBs detected by *Fermi* and BATSE satellites.

Band fit is phenomenological; there is no particular theoretical model that predicts this spectral shape. It also fits well to smaller sections of data within the time-resolved analysis, although the spectral parameters vary within the burst (Kaneko et al. 2006). The high-energy power-law index does not vary as much within a single burst, or between different bursts, as the low-energy one does (Preece et al. 1998b). The peak-emission spectra, on average, have harder low-energy spectral indices but similar peak energies when compared to time-integrated spectra (Nava et al. 2011b).

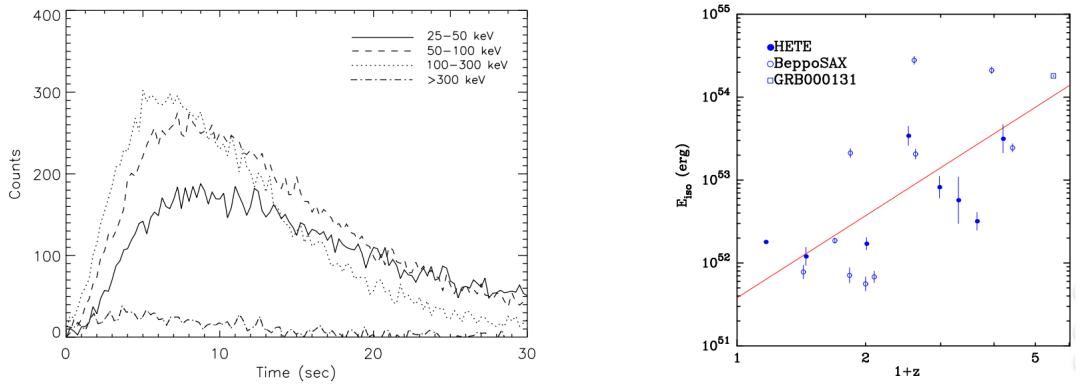

Figure 1.7. *Left panel:* GRB 930612 light-curve profile in different energy bands, demonstrating a significant time delay for the soft energy photons as well as the slower decay of lower energy pulses. Figure reproduced from Kocevski & Liang (2003). *Right panel:* $E_{\rm iso} - z$ plane showing GRBs observed by *BeppoSAX* and *HETE-2*. The correlation implies that GRBs evolve with redshift, with distant GRBs being more luminous. Figure reproduced from Lamb et al. (2004).

Equally well-fitting is the cut-off power-law function (named also Compton -COMP- model), obtained for the case when $\beta \rightarrow -\infty$:

$$COMP(E) = A\left(\frac{E}{100\,\mathrm{keV}}\right)^{\alpha} \exp(-E(2+\alpha)/E_{\rm p}). \tag{1.3}$$

The COMP model has one free parameter less than the Band model and provides a sharper decrease at high (~ MeV) energies. Ghirlanda et al. (2009) note that the majority of short, BATSE-observed GRB spectra are reproduced more accurately with a COMP model, while this was true for 43% of long GRB. In their sample of 432 *Fermi*-detected GRBs, Nava et al. (2011b) found that most of the long and short GRB spectra are adequately fitted by the COMP model. Finally, in the $\alpha \rightarrow \beta$ limit, a simple power-law model is recovered:

$$PL(E) = A\left(\frac{E}{100\,\mathrm{keV}}\right)^{\Gamma}, \tag{1.4}$$

where the power-law index is denoted with Γ. About 80% of BAT detected GRBs are best fitted with a simple power-law due to its relatively narrow energy range (e.g., Butler et al. 2007; Cabrera et al. 2007)[16]. Still, $E_{\rm p}$ can usually be estimated using the $E_{\rm p} - \Gamma^{\rm BAT}$ relation for cases where $1.2 < \Gamma^{\rm BAT} < 2.3$ (Zhang et al. 2007a; Sakamoto et al. 2009b). For reviews on the prompt phase temporal structure and spectral properties see Kumar & Zhang (2015) or Gehrels et al. (2009).

Spectral evolution and gamma-ray burst lag

GRB spectra evolve with time in two distinctive ways. First, the spectrum (in general) softens with time. Second, the pulse peak migrates to later times in lower energies (Figure 1.7 - left panel). Two different evolution patterns of $E_{\rm p}$ have been observed in GRBs, i.e., the"hard-to-soft" (HTS) evolution and the "hardness-intensity tracking" (HIT), which are seemingly incompatible with each other (Ford et al. 1995; Liang & Kargatis 1996; Kaneko et al. 2006; Lu et al. 2010). Liang & Kargatis (1996) were first to quantify

[16]BAT measurement of $E_{\rm p}$ becomes difficult for values below 30 keV or above 100 keV (Sakamoto et al. 2009b). For comparison, a simple power-law provides the best spectral fit to the data for around ~25% of *Fermi* observed burst (Nava et al. 2011b).

the HTS trend as an exponential decay of the maximum of the $\nu F(\nu)$ spectrum: $E_{\rm p} = E_0 e^{\Phi/\Phi_0}$, where Φ is the photon fluence integrated from the start of the burst and Φ_0 is the decay constant. Pulses with HTS evolution tend to be more asymmetric when compared to the HIT ones, with a steeper rise than the fall. Most of the smooth, long GRB pulses show HTS behavior (Lu et al. 2010) while the trend reverses for short GRBs (Lu et al. 2012). Lu et al. (2012) also showed that, although the majority (5/8 in the study sample) of single-pulse GRBs exhibit HTS evolution, the pattern gets complicated for bursts with multiple peaks. From 43 multi-pulse bursts, 17 showed intensity-tracking, 3 HTS evolution and the rest a mix of the two (see Figure 1.8). Intensity-tracking was observed to be predominant after the first pulse. The latter may be explained by a superposition of HTS pulses, where the intensity-tracking is merely its effective outcome (Hakkila & Preece 2011). However, while this can explain the $E_{\rm p}$ behavior in some, highly-overlapping pulses, it can not account for all of them. Since the intensity-tracking is also observed within single-pulse GRBs and in first or well-separated pulses of multi-pulse GRBs, it should be regarded as an independent component (Lu et al. 2012).

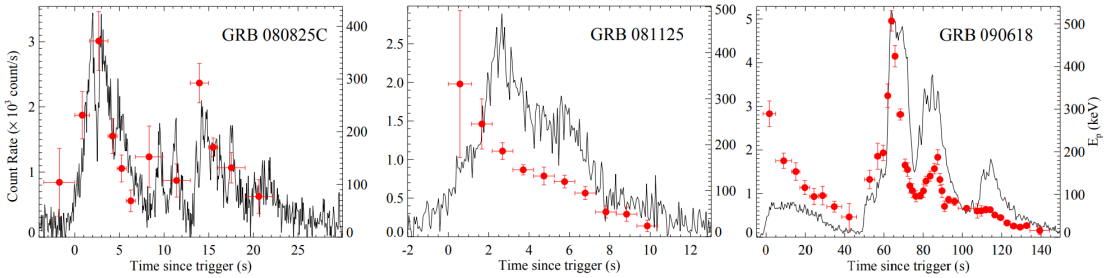

Figure 1.8. Examples of $E_{\rm p}$-evolution patterns superimposed to GRB light-curves: HIT (left panel), HTS (middle panel) and a HTS evolution followed by a HIT (right panel). Figure reproduced from Lu et al. (2012).

The migration of the pulse peak to later times in lower energy channels (i.e., the arrival delay of low energy photons) was found to be a common feature among GRBs (Cheng et al. 1995; Norris et al. 1996; Band 1997). This so-called *spectral lag* is defined as the difference between the time of arrival of high- and low-energy photons, where an earlier onset of high-energy photons equals to a positive lag. Short burst give relatively small lags (Zhang et al. 2006b; Bernardini et al. 2015) while long bursts give large lags (with few exceptions, e.g., Gehrels et al. 2006). An attempt has been made to utilize the spectral lag as an alternative classification method (e.g., see Zhang et al. 2009). Regardless of their light-curve properties, around $\sim 17\%$ of short GRBs have a negative spectral lag (with the hard photons arriving later, Yi et al. 2006). The lag is usually measured between the two given energy bands, with three known ways of extraction (e.g., see Li et al. 2004; Norris et al. 2005; Hakkila et al. 2008; Ukwatta et al. 2010b). From these three methods, the utilization of the modified cross-correlation function[17] is the most efficient one (Cheng et al. 1995; Band 1997). Still, the obtained value can be highly sensitive to the choice of the selected energy channels. The lag was found to be well (anti)correlated with the peak luminosity: $L_{\rm iso} = 2.51 \times 10^{51} (\Delta t_{\rm lag})^{-1.14}$, meaning that the fainter bursts exhibit the largest time delay (Figure 1.9, Norris et al. 2000a; Schaefer 2001). Later inquiries employing larger GRB samples confirmed the lag-luminosity relation (Norris 2002; Ukwatta et al. 2010b), making it one of the first prompt-emission-only distance indicators and a useful cosmological tool (Murakami et al. 2003; Schaefer 2007; Liang et al. 2008b, see also Mochkovitch et al. 2016). Furthermore, Norris et al. (2005) found that pulses in long-lag bursts are few in number and ~ 100 times wider than

[17]The Pearson cross-correlation function, in the limits of $-1 \leq CCF(d,x,y) \leq 1$ is a standard method to estimate the degree to which two series x_i and y_i are correlated. The value of 1(-1) indicates a maximum (inverse) correlation and the value of 0 indicates no correlation. The spectral lag is then a time delay corresponding to the global maximum of the $CCF(d,x,y)$.

those in bright bursts, with systematically lower $E_{\rm p}$. Lags in short GRBs do not appear to be correlated with the pulse duration (Yi et al. 2006). Other studies also connected the spectral lag with the jet break times in the afterglow light-curves (Salmonson & Galama 2002).

One can not discuss the spectral lag without considering the evolution of the $E_{\rm p}$ to lower energies. The observed lag and the broadening of GRB pulses with lower energies should produce the HTS pattern. Consequently, the timescale of spectral decay ought to correlate with the burst's lag and luminosity. Assuming that bursts with the largest lag would have the longest $E_{\rm p}$ decay, the lowest luminosity should then correspond to the largest Φ_0. Kocevski & Liang (2003) did find that the $L_{\rm iso} - \Phi_0$ (anti)correlation is satisfied, implying that more luminous bursts tend to have faster rates of spectral evolution. The perfect HTS scenario would result in a positive lag values for all channel combinations (e.g., $lag_{41} > lag_{42} > lag_{43}$). Still, not all bursts exhibit this behavior (e.g., see Ukwatta et al. 2010b). These results were confirmed in later studies; Shao et al. (2017) found that $E_{\rm p}$ in GRBs with negligible lag usually follows the HIT pattern, while the pulses with a significant lag exhibit HTS behavior.

In conclusion, $E_{\rm p}$ which shows HIT is commonly paired with a negligible lag while HTS evolution is paired with a significant lag. Most short GRBs were observed to have small or not existent lag and $E_{\rm p}$ that follows HIT. Pulses in long bursts have (usually) a HTS evolution and a significant lag that is correlated with luminosity and the light-curve properties: fainter bursts have larger lag, and long-lag bursts have fewer and wider pulses, with lower $E_{\rm p}$. As in most of the GRB observed properties, there is no unanimous consensus on the lag origin. Proposed genesis mechanisms include spectral evolution in the radiation processes (Dermer 1998; Ryde 2005a), geometric effects (Lu et al. 2006) and pulse confusion of different components (Eichler & Manis 2008).

GRB spectral and temporal correlations

Realization that the GRB variability correlates with its absolute luminosity, where smooth bursts are less luminous (Fenimore & Ramirez-Ruiz 2000), was one of the first discovered relations proposed to be used as a redshift indicator (in addition to already mentioned spectral lag correlations). Since then, numerous studies have been conducted in order to see how a variety of parameters that characterize the prompt (and afterglow) emission correlate with one another. Most of the attempts share a common goal: estimation of the intrinsic brightness and redshift from the observed characteristics of the GRB emission. The delivered results are also somewhat repetitive, forming by now a well-established pattern. With the new, ever-growing sample of detected GRBs, old correlations are revisited and the new, tighter correlations are claimed to be found (employing the same or different parameters). The results are then utilized to assess the redshifts of a large number of GRBs and consequently derive the GRB luminosity evolution, their formation rate as a function of z or constrain the cosmological parameters (e.g., Lloyd-Ronning et al. 2002; Zitouni et al. 2016). However, these relations are often largely dispersed and based on a statistical analysis of quantities which physical causes are poorly understood. Therefore, their utilization as a proxy for standard candles is under intense discussion (Bloom et al. 2003b; Schaefer 2003; Friedman & Bloom 2005). A selected sample of prompt emission correlations is showed in Figure 1.9. A few of them are further summarized in the text below.

The most widely studied and debated correlation must be the one between the $E_{\rm p}$ (in the GRB rest-frame) and the isotropic radiated energy $E_{\rm iso}$, so-called $E_{\rm p} - E_{\rm iso}$ (Amati) relation (Amati et al. 2002; Amati 2006). It was first predicted by Lloyd et al. (2000) on the base of the connection between the total fluence and the observed $E_{\rm p}$ within a sample of BATSE bursts. Using a limited sample of 12 long *BeppoSAX* GRBs, Amati et al. (2002) demonstrated that $E_{\rm p} \propto E_{\rm iso}^{\alpha}$, where $\alpha \sim 0.5$. Later revisits confirmed this relation using a larger sample of bursts (e.g., Nava et al. 2006). extending it further to XRFs (e.g., Sakamoto et al. 2004; 2006). Short GRBs form an outlier group (see Figure 1.9). There is still no unanimous consensus on

the physical interpretation of Amati relation (e.g., see Eichler & Levinson 2004; Thompson et al. 2007). According to Ghirlanda et al. (2004), a much tighter correlation is obtained if the isotropic energy is collimation corrected: $E_\gamma = (1 - cos\theta)E_{\rm iso}$. Here, the opening half-angle of the jet θ (or otherwise θ_j) was assessed through the breaks in the afterglow light-curves of 16 long GRBs[18]. The Ghirlanda relation, taking form of $E_{\rm p} \propto 480(E_\gamma/10^{51}{\rm erg})^{0.7}$, implies that GRBs are characterized by a universal energy reservoir. Namely, after the application of the $(1 - cos\theta)$ correction, it was found that the large range of isotropic energies $E_{\rm iso}$ is reduced to the span of 2 orders of magnitude, clustering around $\sim 10^{51}$ erg (Frail et al. 2001a). Still, the used sample was limited in terms of the isotropic energy span, where among the GRBs with $E_{\rm iso} < 10^{52}$ erg only two had θ that was not given in terms of the upper/lower limit estimation.

Liang & Zhang (2005) bypassed the use of E_γ (which heavily depends on the jet opening angle estimation, see Sari et al. 1999 and Section 1.4) by directly employing the achromatic light-curve break time (t_{jet}). They found that it also correlates with $E_{\rm iso}$ and $E_{\rm p}$ in the form of a single function. Other authors also found correlations between the parameters of the prompt phase and the afterglow. Izzo et al. (2015) formulated the so-called Combo-relation which makes practical use of four parameters: prompt intristic peak energy $E_{\rm p,i}$, the X-ray afterglow initial luminosity L_0, the rest-frame duration τ of the X-ray afterglow shallow phase, and the index of the late PL decay $\alpha_{\rm X}$. There are other correlation utilizing the afterglow properties alone. For example, the $T_a^{\rm RF}$-L_a relation anti-correlates the rest-frame end time of the plateau phase in the X-ray afterglow (T_a) with its isotropic X-ray luminosity (Dainotti et al. 2008; 2010). Dainotti et al. (2017) extended this correlation to include the peak luminosity of the prompt emission. Namely, they showed that the relation between T_a, L_a, and the peak luminosity define a GRB fundamental plane.

Although Ghirlanda relation appears to be tighter, it suffers a few difficulties when compared to the Amati one. For bursts with measured redshifts and consequently with an estimated $E_{\rm iso}$, the jet opening angle (and hence the jet break time, Sari et al. 1999) can be predicted by inverting the Ghirlanda relation. Sato et al. (2007) found that the X-ray afterglows of the examined GRBs, although lasting up to 10–70 days, show no sign of the predicted jet break. On the other hand, their energetics and $E_{\rm p}$ were consistent with the Amati relation. The breaks could be masked by some additional source of the X-ray emission or by a continuous injection of energy into the external shock, yielding a separate X-ray component. However, in both cases the break should be observed in the optical band, which is not always the case (e.g., GRB 050401, Panaitescu et al. 2006a).

As with $E_{\rm iso}$, spectral peak energy also correlates with the luminosity of the brightest peak in the form of Yonetoku relation: $L_{\rm iso}^{\rm p} \propto E_{\rm p}^{p}$, where $p \sim 2$ (Yonetoku et al. 2004, see also Schaefer 2003). It covers the energy range of 50–2000 keV and luminosity range of 10^{50}–10^{54} erg/s. This relation also holds for any segment within the same GRB and among different GRBs, as demonstrated by Liang et al. (2004) on a sample of 92 time-resolved BATSE GRB spectra. In a similar manner, Firmani et al. (2006) used a duration-corrected peak luminosity and found that $L_{\rm iso} \propto E_{\rm p}^{1.62}T_{0.45}^{-0.49}$, where $T_{0.45}$ is the timescale of the brightest, background-subtracted light-curve counts in the reference frame of the source. The Yonetoku correlation also holds between the observed quantities, namely $E_{\rm p}^{\rm obs}$ and P, where P is the peak flux (Nava et al. 2008). Ghirlanda et al. (2009) reached a similar conclusion: short GRBs populate the same region of the $E_{\rm p}^{\rm obs} - P$ plane as the long bursts and could therefore follow the $E_{\rm p} - L_{\rm iso}$ relation. Furthermore, both studies agreed that the Amati relation is also valid when moved to the observed plane (i.e., $E_{\rm p}^{\rm obs} - F$, where F is the burst fluence). However, due to the higher/similar peak energies and lower fluences, short GRBs populate different regions of the $E_{\rm p}^{\rm obs} - F$ plane and, as it was observed before, should not follow the Amati relation. Furthermore, within the time-resolved analysis, Yonetoku relation appears to be tighter for the decaying phase of the pulse in comparison with the rise time (Lu & Liang 2010).

[18] For additional 7 GRBs used by Ghirlanda et al. (2004), only the upper/lower limits could be estimated.

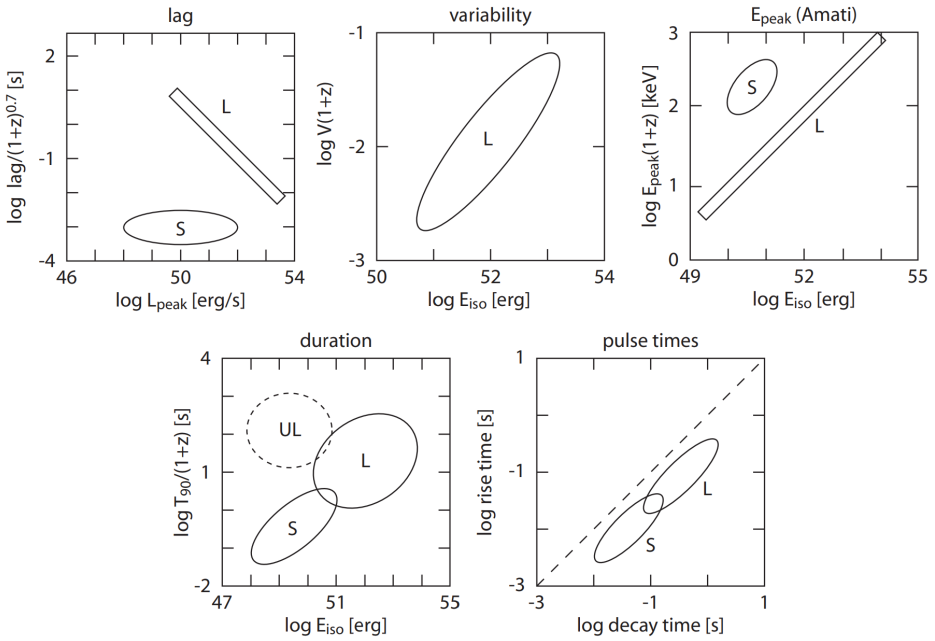

Figure 1.9. Examples of GRB prompt emission correlations reproduced from Gehrels et al. (2009), summarizing the observational differences between long (L), short (S) and under-luminous (UL) gamma-ray bursts. From left to right: spectral lag in the source frame versus luminosity (Norris et al. 2000b), variability in the source frame versus $E_{\rm iso}$ (Fenimore & Ramirez-Ruiz 2000; Reichart et al. 2001), $E_{\rm p}$ in the source frame versus $E_{\rm iso}$ (Amati et al. 2002; Amati 2006), source-frame duration versus $E_{\rm iso}$ and pulse rise time versus its decay time (Norris et al. 1996).

1.4 FIREBALL - THE STANDARD MODEL

Since the discovery of GRBs, every following mission provided new data that put the existing models on trial. The *fireball* model soon became the leading one, surviving (most of) the tests introduced by new observations. The fireball model assumes that GRBs are the result of a catastrophic event that injects a SN-like amount of energy into a small volume. This in return generates an ultra-relativistic outflow (Piran 2004; Mészáros 2006). The progenitor itself is not specified. Evidence collected during the first ~ 30 years of observations (Section 1.1) pointed toward two different progenitors for short and long GRBs. Today, it is well accepted that the *collapsar* is the progenitor of long GRBs (Woosley 1993; MacFadyen & Woosley 1999) while a compact binary mergers produce short GRBs (Eichler et al. 1989; Narayan et al. 1992).

Collapsars and compact binary mergers

A starting point for the *collapsar* model is a Wolf-Rayet star (WR, Wolf & Rayet 1867; Abbott & Conti 1987): hot (> 30,000 K), evolved and massive, with M initially exceeding 20 $M_\odot$ (Crowther 2007). WR stars are also characterized by a rapid mass loss due to the strong stellar wind ($\approx 10^{-5}\ M_\odot/y$). It eventually strips away the hydrogen envelope, leaving behind a 10–25 $M_\odot$ core. For cases in which the progenitor has a sufficient mass, the cease of nuclear fusion inside the core will be accompanied by a catastrophic

collapse into a stellar BH. The new BH will be surrounded by a massive accretion disk formed out of the surrounding stellar material. Large angular momentum can halt the accretion process. However, around the rotation axis, it can almost undergo a free-fall, creating a low-density funnel within the envelope. This allows the outflow to eventually break through the overlying material of the infalling stellar envelope, assuming enough energy was injected into this region in the first place. This leads to a burst of gamma-rays. The pressure of the stellar mantle will cause the outflow to be collimated and highly relativistic, forming a so-called *jet*. The jet would appear to be further collimated due to its high Lorentz factor[19].

The collapsar model does not specify how the jet is launched. It assumes that it happens one way or another. Among the suggested mechanisms are the neutrino/anti-neutrino annihilation along the rotational axis (e.g., Popham et al. 1999; Liu et al. 2008) and the magneto-hydrodynamic processes, such as Blandford-Zanjek process[20] (e.g., Di Matteo et al. 2002; Kawanaka et al. 2013). Regardless of the mechanism, the star needs to be depleted of the hydrogen envelope in order for the jet to escape (hence the WR origin model). Even the most compact SNe progenitors with hydrogen in their spectrum have the radius of ~ 100 light seconds. This is too long for the jet to escape, considering the time interval characteristic for long GRBs. Lack of hydrogen and helium lines observed in the GRB associated SNe, in addition to their connection with the star-forming regions (see Section 1.5), further favors the WR progenitor. However, there are some contradictions. Low metallicity in stars is connected to a higher angular momentum and lower rate of mass loss (Maeder & Meynet 2001; Meynet et al. 2006). Heavier stars are more prone to end up as BHs and high angular momentum is needed in order to form an accretion disk. Therefore, long GRBs should be created more easily when metallicity is low. Nevertheless, as a result of stronger mass-loss during earlier evolutionary phases, WR stars are more common at higher metallicity (Crowther 2006).

What happens when the jet fails to break out from the stellar envelope and it is chocked within it? Do these hidden jets exist in type Ib/c SNe that do not harbour a GRB? Piran et al. (2019) found evidence of hidden jets in the early spectrum of multiple SNe, including those that did not power a GRB. As relativistic jet makes an attempt to escape the stellar envelope, forward and reverse shock forms at its head. Since the head speed is lower than the one of the jet, the material will spill sideways, forming a cocoon. The cocoon collimates the jet. As long as the jet is propagating through the envelope, it will dissipate its energy at the head which will then flow into the cocoon. From this point, two scenarios can happen depending on how long the central engine operates. If it operates for too short, the jet will transfer all of its energy into the cocoon. The jet is then labeled as *chocked*. Otherwise, a GRB will be produced. In both cases the fast cocoon expands and eventually breaks out. It will leave a signature in the early days of the emission. An additional, high-velocity component ($0.1c$) will be visible in the optical spectrum. Such component was recently observed in the afterglow of GRB 171205A (Izzo et al. 2019).

A competing model invokes a rapidly spinning, highly magnetized NS, i.e., the magnetar (Narayan & Popham 1989; Duncan & Thompson 1992). They are found in young SN remnants and may be surrounded by a disk of fallback explosion debris but they are not powered by these disks (Wang et al. 2006). Magnetars are an expected outcome for a fraction of collapsing massive stars, as well as for the merger of white dwarfs (WDs) or two NSs, providing that the final mass is below the maximum NS mass. Their birthrate is comparable with that of ordinary SNe (Kouveliotou et al. 1998), implying that only a fraction of magnetars may be responsible for long GRBs. The total rotational energy of a millisecond magnetar depends on its initial period, mass, and radius. A NS born with an initial rotation rate of ~ 1 ms can contain a large

[19]This so-called *headlight* effect plays an important role in astrophysics. Lorentz velocity transformations reveal that the isotropic radiation of the source moving with respect to the observer at speed $\boldsymbol{u}$ will appear collimated. The light ray traveling perpendicular to $\boldsymbol{u}$ will be observed to have a component in the direction of motion as well. Combined with the finite speed of light, the aftermath leads to the collimation effect where the light appears beamed with a half opening angle of $\theta = 1/\Gamma$. For example, the synchrotron emission, emitted by relativistic electrons that spiral around the magnetic field lines, will be concentrated in the direction of the electron's motion and strongly plane-polarized.

[20]An extraction of the rotational energy of a BH through strong magnetic fields in the accretion disc (Blandford & Znajek 1977).

amount of energy. Namely, $E_{\rm rot} = 0.5 I \Omega^2 \sim 1.5 \times 10^{52}$ erg. This places an upper limit on the total energy budget of a single GRB. Magnetars can only power GRBs whose energy is below this value. This imposed condition still encompasses the majority of GRBs if their energy is collimation-corrected. Consequently, it was proposed that this model can explain a large number of short and long GRB light-curves (e.g., Usov 1992; Duncan & Thompson 1992; Lü et al. 2015). However, one of the predictions of this model is a strong radio afterglow, which is not always observed (Fong et al. 2016).

The most popular central engine model of short GRBs is the merger of a compact binary system, namely a NS-NS or a NS-BH binary (Eichler et al. 1989; Narayan et al. 1992). The merger starts with the slow inspiral ($\sim 10^6$–10^9 y). As the orbital period and the separation between the compact objects decreases, the system emits gravitational waves (GW). Right before the merger, tidal interactions rip apart the NSs. Two spiral arms that are consequently formed carry out the excess angular momentum. The final stage, depending on the initial masses of the two NSs, resembles the central region of the collapsar: a BH surrounded by an accretion disk. Emitted GWs are a consequence of the theory of General Relativity: ripples in the fabric of space-time that propagate at the speed of light. They are produced in many astrophysical scenarios in which huge masses are accelerated or deformed, including the compact binary mergers. The first indirect evidence of GWs came with the (Nobel prize-winning) discovery of the binary pulsar PSR B1913+16 (Hulse & Taylor 1975). The observed evolution of the system's orbital period was in excellent agreement with general relativity predictions in which the binary will lose energy through the emission of GW (Weisberg & Taylor 1981). One hundred years after Einstein's prediction, the advanced[21] LIGO-Virgo global network of interferometers (Laser Interferometer Gravitational Observatory, LIGO Scientific Collaboration et al. 2015; Acernese et al. 2015) detected the first GW from a binary BH merger (GW150914, Abbott et al. 2016a). With it, the long-held promise finally materialized and opened a new era for the observational astrophysics. The association of short GRBs with the NS-NS mergers, although predicted several decades ago, was confirmed with the detection of GW 170817 (Goldstein et al. 2017; Abbott et al. 2017; 2019). The observed NS-NS inspiral therefore presents the first event ever to be observed in both gravitational and electromagnetic waves.

Compactness problem

The compactness problem refers to a compact source with a large luminosity in gamma-rays that would be opaque to its own radiation due to the e^+e^- pair production. This problem was realized very early on by Ruderman (1975) and Schmidt (1978). The shortest time variability measured in an astrophysical source constrains its size R. All fluctuations within the source shorter than the time light needs to cross it will be smeared out by propagation delays within the source. For GRBs, the fastest observed variations of $\Delta t \approx 1$ ms suggest the source to be compact, with $R \lesssim c\Delta t \approx 300$ km. Optical depth of these compact and energetic sources can be estimated as $\tau_{\gamma\gamma} \sim n_e \sigma_T R$, where σ_T is the Thompson cross-section for the photon-photon interaction producing e^+e^- pairs, R is the escape distance of the high-energy photon and n_e is the number density of free electrons, namely $n_e = f_e n_\gamma$. Here, n_γ is the photon number density at the source and factor f_e takes into account that not all photons will produce e^+e^- pairs. The photon number

[21] The advanced LIGO-Virgo are the second-generation gravitational interferometers. The upgrade is expected to boost the sensitivity in a way that GW detections will become a routine occurrence. The original observations before the enhancement could mainly establish the upper limits on the GW flux. For example, the NS-NS merger detection rate of Virgo is expected to increase from 1 detection in every 20–50 years to 1 detection per week or month.

density can be evaluated as $n_\gamma \sim \frac{E_{\rm iso}}{\overline{E}_\gamma D^3}$, where $\overline{E}_\gamma \sim 1$ MeV is the typical observed photon energy. The optical depth expression can then be written as (Guilbert et al. 1983; Piran & Shemi 1993):

$$\tau_{\gamma\gamma} \sim 10^{13} f_e \left(\frac{E_{\rm iso}}{10^{42}\ {\rm J}}\right)\left(\frac{1\ {\rm MeV}}{\overline{E}_\gamma}\right)\left(\frac{0.01\ {\rm s}}{\Delta t}\right)^2. \tag{1.5}$$

For any reasonable set of parameters, the source is optically thick (Piran 2004). Even if there are no pairs in the beginning, they will form rapidly and Compton scatter the lower energy photons, again producing a great optical depth for all photons. However, if the motion of the source is relativistic, the emitting material will closely follow the emitted light and the observed time interval between the two successive photons will be compressed. This relaxes the requirement on $\tau_{\gamma\gamma}$ in a twofold way. First, the observed and the proper time interval are consequently related as $\Delta t^{\rm obs} = \Delta t/2\Gamma^2$. The estimated size of the compact source is now larger for a factor of Γ^2, namely $R \lesssim \Gamma^2 c\Delta t$, relaxing by that the size constraint[22]. Secondly, the energy of the photon emitted in the source frame will be *blueshifted* for the observer as $E_\gamma^{\rm obs} = \Gamma E_\gamma$. The number of photons that carry enough energy for the pair production is therefore reduced (i.e., the observed fraction f_e of the pair-producing photons does not correspond to the fraction at the source). The fraction of these photons is consequently decreased by a factor of $\Gamma^{-2\beta}$, where β is the high energy spectral index (Piran 1999). All together, a Lorentz factor of $\Gamma \approx 100$ is needed in order for the compactness problem to be resolved. Lorentz factors observed in GRBs are well above this limit (Fenimore et al. 1993; Lithwick & Sari 2001 give a more detailed discussion on Γ limits).

General picture

The fireball model is a result of an effort to answer two main questions regarding the creation of GRBs and their afterglows: how does one accelerate particles to relativistic velocities and how is the kinetic energy of the relativistic flow converted into radiation? The theoretical framework starts with a stellar mass object undergoing a catastrophic event which releases a large amount of energy into a small region of space. This leads to an opaque photon-electron fireball expanding with highly relativistic velocities. Far away from the central engine, the system becomes optically thin and the photons escape, carrying out only a fraction of energy. The rest is carried on, producing along the way the prompt GRB emission and its afterglow by means of internal and external energy dissipation. This general theoretical framework was found to successfully interpret the broad GRB phenomenology (Rees & Meszaros 1992; 1994; Meszaros & Rees 1993b; Mészáros & Rees 1997). Different stages of the fireball evolution (showed in Figure 1.10) can be summarized as:

FIREBALL A cataclysmic stellar event is followed by an enormous release of energy in different forms (neutrinos, GWs, radiation, etc.) into a small region of space. Neutrinos and GWs escape to infinity with almost no interaction, leaving behind a *fireball*. The term refers to a radiation-plasma composed of electrons, positrons, gamma-rays and a small amount of baryons (mostly protons, with a total mass of $M_0 \sim 10^{-5} M_\odot$). The value of the released energy E_0 is much greater than the rest energy of baryons. The amount of baryons is usually expressed with $\eta \equiv E_0/M_0c^2$ (i.e., the fireball energy per baryon, Shemi & Piran 1990). The involved area is compact, with a radius smaller than a light-second ($r_0 \sim 10^6$–10^7 cm). The energy density is high enough that collisions of high-energy photons create e^+e^- pairs. These in return annihilate into gamma-rays and so on. In other words, the fireball is opaque to its own radiation. The initial temperature is $kT_0 \sim 1$ Mev, with particles having

[22] The $1/2\Gamma^2$ factor follows from the transformations of the arrival times of two photons between the comoving frame of the emitting gas, the stellar frame (i.e., the origin of the explosion) and the observers frame (Earth). The schematic is similar to the one of the apparent velocity in super-luminal motion. For the step-by-step derivation, see Mészáros (2006).

a bulk Lorentz factor of $\Gamma \sim 1$. The idea that the e^+e^- could provide an energy source for GRBs was not new. In 1975, Damour & Ruffini proposed that the e^+e^- pair plasma, created during the formation of a Kerr-Newman BH, could act as a sufficient energy source for GRBs at cosmological distances (see Section 2.2). Three years after, Cavallo & Rees (1978) proposed that the e^+e^- pairs, produced by a cataclysmic event, instantaneously annihilate. By doing so they would release a vast amount of energy which pushes onto the CBM (the original concept of the fireball). This concept was further examined by Goodman (1986) and Paczynski (1986). Both of them considered a pure radiation fireball, i.e. a large concentration of gamma-rays confined in a small region of space. The models differed in time during which the energy was released (sudden and prolonged injection) but exhibited the same qualitative behavior: even for the pure radiation fireball, if the initial temperature is high enough, the pairs will form and the radiation will not be able to escape. The system description exhibits a prominent analogy with the Early Universe. Further progress was made by Shemi & Piran (1990), Meszaros & Rees (1993b), Piran et al. (1993) and Katz (1994).

RADIATION DOMINATED ADIABATIC EXPANSION The fireball undergoes expansion under its own internal pressure. The observed width remains the same due to the Lorentz length contraction. Since $E_0 \gg M_0c^2$, the pressure is radiation-dominated. Because of the high optical depth, the expansion may be considered adiabatic: $TV^{1-\gamma_\alpha} = const$, where T and V are the fireball temperature and volume and $\gamma_\alpha = 4/3$ is the adiabatic index. It follows that the expanding fireball cools down with $T \propto V^{\gamma_\alpha - 1} = r^{3(\gamma_\alpha - 1)} = 1/r$ (Meszaros et al. 1993). The density of pairs and hence the opacity decreases exponentially with temperature. When the temperature drops below the pair production threshold (around 20 keV) the pairs annihilate and the plasma in a very abruptly manner becomes transparent. However, the addition of an amount of baryonic matter (either injected by the explosion or present on the site from the beginning) affects the fireball evolution in two ways (e.g., Shemi & Piran 1990; Paczynski 1990). First, the optical depth of electrons associated with baryons (τ_b) decreases with radius as $1/r^2$. The optical depth associated with pair production decreases exponentially with temperature and therefore also with increasing r ($T \propto 1/r$). As a consequence, the final transparency condition ($\tau = 1$) is delayed. The second outcome of even a small baryon load is the (eventual) transfer of the fireball energy into the kinetic energy of the baryons (i.e., the baryons are accelerated). The bulk Lorentz factor increases linearly with r up to $\Gamma \sim E_0/M_0c^2 \approx 100$. Saturation radius $r_S \sim 10^9$ cm is the distance at which the Lorentz factor reaches its maximum value. It marks the transition from the radiation-dominated phase ($\Gamma \propto 1/r$) to the matter-dominated phase where most of the fireball energy is contained in the bulk energy of protons.

PHOTOSPHERIC EMISSION The delay of transparency means that the fireball becomes matter-dominated before it becomes optically thin. The photospheric radius r_{PH} for which the optical depth reaches value of $\tau = 1$ is $\sim 10^{11}$–10^{12} cm, well beyond the saturation radius. At this point, the photons can escape to infinity. A fraction of the initial thermal energy is radiated at the photosphere. However, the observed (nearly-thermal) spectra and the timescales over which the photons escape (milliseconds) are not consistent with the emission typically observed in GRBs. Goodman (1986) computed the energy distribution of the photon flux at the moment of transparency as seen by a remote observer. The obtained spectrum was nearly thermal, with a broader peak and the slope at low energies slightly shallower. Still, the observed geometric broadening of the BB could not account for (now known to follow Eq. 1.2) GRB spectra[23]. Some mechanism was needed for the system in order to recover its energy back to radiation. The solution was introduced in the form of the two new versions of the

[23] Recently, a BB component has been identified in the time-resolved spectrum of several GRBs. The temperature evolution agrees with the predictions of the fireball model (e.g., see Ghirlanda et al. 2003; 2013a; Ryde et al. 2010; Guiriec et al. 2011). It was observed not to be correlated with the peak energy nor with the underlying non-thermal component.

fireball model which implemented external (Rees & Meszaros 1992) and internal (Rees & Meszaros 1994) shocks.

INTERNAL SHOCKS From this point, the fireball continues to expand at a constant speed. The outflow is not completely homogeneous. It is structured as several mini-shells with a wide range of bulk Lorentz factors. When a fast-moving shell overtakes the slower one, a shock is generated in a collision-less manner. The density of matter is too low for a significant number of direct collisions. Instead, the interaction is mediated via magnetic fields which enable energy and momentum transfer. A part of this energy will be transferred to electrons, which will accelerate by means of multiple reflections of the magnetic field (first-order Fermi acceleration). The radiation then comes from the synchrotron emission of accelerated electrons (Sari & Piran 1997). Energetic photons can also be produced by the inverse Compton scattering of keV-photons by accelerated electrons. These mechanisms are generally believed to be the emission sites of the observed prompt GRB phase. They are likely developed before the fireball is decelerated by the ambient medium, at radial distances $r_{IS} \sim 10^{14}$–10^{15} cm. This scenario can easily reproduce highly variable temporal profiles observed in prompt emission (Piran 1999). The observed temporal structure simply reflects the temporal behavior of the internal engine that is responsible for shell production. On the other hand, the relative velocity between the shells is limited: conversion efficiency from kinetic to radiation energy is low, ranging from the maximum of 50% under favorable conditions to only a few percent otherwise (Kobayashi et al. 1997; Katz & Piran 1997).

EXTERNAL SHOCKS After internal shocks, the Lorentz factor remains highly relativistic. As stated before, the internal shocks arise within the flow when the fast-moving particles catch up with the slow ones. The external shock, however, refers to the interaction between the fast-moving shell and the CBM. Its formation starts as soon as the outflow starts, with the initial Lorentz factor similar to the one of the ejecta. The radiation will initially be negligible. The fireball starts to decelerate at radius r_{ES}, which is defined as the distance at which the Lorentz factor has dropped to half of its initial value. This happens when the mass of the swept-out external matter equals $\sim 1/\Gamma$, where Γ is the bulk Lorentz factor before the deceleration. It usually takes place at distances $r_{ES} \sim 10^{16}$ cm. Before this point, the amount of matter that has been swept up is too small to convert a significant amount of kinetic energy into radiation. Beyond this point, the shock will continue to advance with continually decreasing speed as it encounters more external material (Blandford & McKee 1976; Rees & Meszaros 1992). Its evolution is affected by the CBM profile, which can be either constant or $\propto 1/r^2$. Typical densities are on the order of 1 cm^{-3}. The radiation comes in the form of the synchrotron emission from a power-law distribution of electrons. The spectral energy distribution has several power-law segments with related indices (Sari et al. 1998). The peak of the emission shifts to lower energies as the flow slows down. Similar as in SN remnants, the external shock comes in pairs: one forward shock propagates into the external medium and one reverse shock propagates back into the ejecta (Meszaros & Rees 1993b). The forward shock is responsible for the long-lasting broad-band afterglow (Mészáros & Rees 1997). The reverse shock is short-lived and only mildly relativistic. It is thought to be the origin of an additional component sometimes observed in the early optical afterglow (Sari & Piran 1999, also see Section 1.2). An extensive review of the external shock model can be found in Gao et al. (2013a).

In-depth review of the fireball model end emission mechanisms that power GRBs can be found in Piran (1999), Zhang & Mészáros (2004), and Kumar & Zhang (2015).

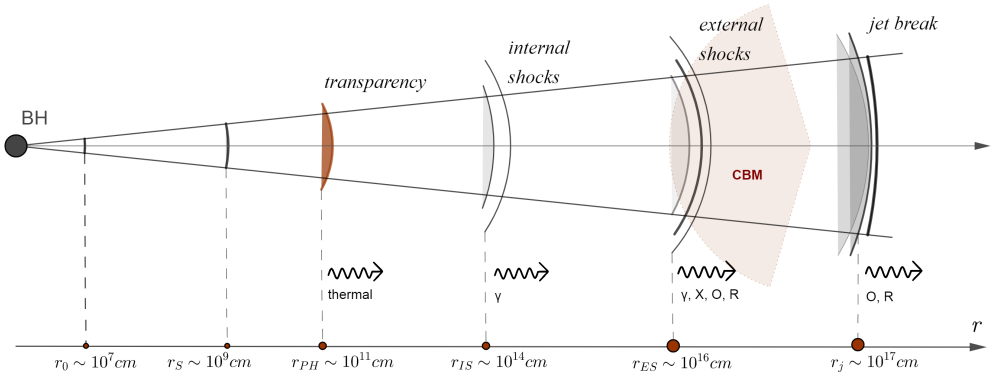

Figure 1.10. Scheme of the fireball model with indicated distances from the central engine for each phase. Here, r_0 marks the initial fireball radius, r_S is the saturation radius defining the end of the acceleration phase where $\Gamma \propto r$ and r_{PH} stands for the photospheric radius, a distance at which the transparency condition has been reached (with a thermal emission as a consequence). Internal shock phase begins at $r_{IS} \sim 10^{14}$. It is here where the prompt GRB emission is generated. The beginning of the external shock phase is marked by $r_{ES} \sim 10^{16}$ cm, also called the deceleration radius. This is the distance at which the inertia of the swept-up CBM becomes noticeable and the GRB afterglow begins. In the case of a collimated outflow, at $r_j \sim 10^{17}$ the flow velocity is expected to decrease such that $\Gamma \simeq 1/\theta_j$, where θ_j is the half-opening angle of the jet (thus producing a break in the afterglow light-curves).

Synchrotron spectrum

Due to the presence of accelerated electrons and magnetic fields within the expanding fireball, synchrotron radiation is expected to play a key role in the prompt and afterglow GRB emission. Polarization, an important feature of the synchrotron emission, was detected both in the prompt and the afterglow phase, further supporting this idea (e.g., Bersier et al. 2003; Wiersema et al. 2014; Sharma et al. 2019). Piran (2004) reviews some of the key aspects of the synchrotron emission in GRBs while a more detailed analysis of the mechanisms involved can be found in Rybicki & Lightman (1979).

Three quantities essential to characterize the synchrotron emission are: the Lorentz factor of relativistic electron (γ_e), the magnetic field strength (B) and the Lorentz factor of the emitting material (Γ). The characteristic synchrotron frequency for an electron of mass m_e and charge q_e depends on all three of these quantities: $\nu_{syn}^{\rm obs}(\gamma_e) = (q_e B/2\pi m_e c)\gamma_e^2\Gamma$ (in the observer frame). Therefore, the typical observed energy of a synchrotron photon also depends on γ_e, Γ and B. The power in the observed frame, emitted by a single electron, is $P_{syn}^{\rm obs} = P_{syn}\,\Gamma^2 = \frac{4}{3}\sigma_T c U_B \gamma_e \Gamma^2$, where σ_T is the Thompson cross-section and $U_B = B^2/8\pi$ is the magnetic field density (e.g., Rybicki & Lightman 1979). Electrons that emit radiation are loosing energy, i.e., are cooling down. Electron energy, divided by the rate at which they are radiating it away, gives the electron cooling time t_{syn}, where $t_{syn}^{\rm obs} = t_{syn}/\Gamma$:

$$t_{syn}^{\rm obs} = \frac{1}{\Gamma}\frac{\gamma_e m_e c^2}{P_{syn}} = \frac{3 m_e c}{4\sigma_T U_B \Gamma}\gamma_e^{-1} = \frac{3}{\sigma_T}\sqrt{\frac{2\pi m_e q_e c}{\Gamma B^3}}\nu^{-1/2}. \tag{1.6}$$

Here, the dependence of t_{syn} on γ_e was bypassed by inverting the equation for the observed photon frequency $\nu_{syn}^{\rm obs}(\gamma_e)$. This suggests that the electron cooling time is universal: $t_{syn}^{\rm obs} \propto \Gamma^{-1/2}\nu_{syn}^{-1/2}$ at a given frequency does not depend on the electron energy distribution as long as γ_e is large enough to produce synchrotron radiation in the first place.

It has been observed that many GRB light-curves consist of fast rise - slow decay spikes (Section 1.3). The short rise time can be interpreted to be a consequence of a rapid heating time of electrons via shock episodes. The decay width should then correspond to the electron cooling time. The dependence $t_{syn}^{\rm obs} \propto \nu_{syn}^{-1/2}$ also resembles the observed connection between the frequency and pulse width: $\Delta t \propto \nu^{-0.4}$ (Fenimore et al. 1995, see Section 1.3). However, $t_{syn}^{\rm obs}$ is much shorter than the observed pulse width for any reasonable set of parameters, making these associations highly unlikely (Piran 2004). Integration over the Lorentz factor distribution of electrons is required in order to calculate the overall spectrum. Electrons receive their random motions through shock-heating. Therefore, the electron energies are expected to follow a power-law distribution with an index p for velocities above the minimal Lorentz factor γ_m (Sari et al. 1998):

$$N(\gamma_e) \sim \gamma_e^{-p}, \quad \text{for } \gamma_e > \gamma_m \cong 610\, \epsilon_e \Gamma. \tag{1.7}$$

Here, m_p is the proton mass and index p needs to be > 2 so that the electron energy distribution is finite for large γ_e. The upper energy cutoff does not play a role here since it happens at the high energy tail far away from the peak energy. Value of the minimum Lorentz factor $\gamma_m \cong 610\epsilon_e\Gamma$ is obtained for the standard choice[24] of $p = 2.5$. Parameter ϵ_e, assumed constant, measures the fraction of total thermal energy that goes into the random motion of electrons. Distribution in the form of a power-law means that the energy of the majority of electrons will be near $E_{\rm min} = \gamma_m m_e c^2$. Therefore, γ_m ($\nu_m = \nu_{snc}(\gamma_m)$) can be labeled as the *typical* Lorentz factor (frequency) of the electron population.

The synchrotron spectrum of a single electron with the initial energy $\gamma_e m_e c^2$ can be represented as a power-law $F_\nu \propto \nu^{1/3}$ (up to $\nu_{syn}(\gamma_e)$) followed by an exponential decay at larger frequencies. The lowest part of the spectrum will then always be a sum of the tail contributions of all the electron's emission, i.e., $F(\nu) \propto \nu^{1/3}$ (a characteristic synchrotron radiation, Meszaros & Rees 1993a; Cohen et al. 1997). It does not depend on the shape of electron distribution. The uppermost part of the spectrum will have a power-law dependence. The most energetic electrons cool rapidly and emit practically all their energy at their synchrotron frequency. The number of electrons (Eq. 1.7) with energy $\gamma m_e c^2$ is proportional to γ^{1-p}. As these electrons cool, their energy ($\propto \gamma^{1-p} m_e c^2 \gamma \propto \gamma^{2-p}$) will be emitted in a frequency range $\sim \nu_{syn}(\gamma) \propto \gamma^2$. This energy can then be expressed using $\nu_{syn}(\gamma)$ as $E(\gamma) \propto \gamma^{2-p} \propto \nu^{1-\frac{p}{2}}$. Thus, the uppermost part of the spectrum will satisfy $F_\nu = dE/d\nu \propto \nu^{-p/2}$. Energetic electron will cool rapidly until it reaches γ_c, defined as the Lorentz factor of an electron that cools down on a hydrodynamic timescale. It is a critical parameter which determines if the cooling is rapid or slow. Using the Eq. 1.6, substituting t_{syn} for t_{hyd} and solving for γ leads to

$$\gamma_c = \frac{6\pi m_e c}{\sigma_T B^2 t_{hyd} \Gamma} \text{ (in the observer's rest-frame).} \tag{1.8}$$

For intermediate frequencies, the spectrum can be characterized as *slow cooling* or *fast cooling*, depending on the value of typical electron frequency γ_m with respect to γ_c. All of the presented cases can be summarized by two functions (Sari et al. 1998). For $\gamma_m > \gamma_c$ all of the electrons will cool rapidly. Let $F_{\nu,\,\rm max} = N_e P_{\nu,\,\rm max}/(4\pi d_l^2)$ be the observed peak flux, where N_e is the number of electrons in the post-

[24] Sari et al. (1996) fixed the power-law index under the requirement that the synchrotron model should be able to explain the high energy spectra of GRBs. They assumed that the radiation observed in the BATSE window is due to the synchrotron cooling, therefore directly relating parameter p with the high energy power-law index β of the Band function (Eq. 1.2). Numerical modelling of electron acceleration also showed to be consistent with p >2 (Achterberg et al. 2001; Eichler & Waxman 2005).

shock region and $P_{\nu,\,\max} = P(\gamma_e)/\nu_{syn}(\gamma_e)$ is the peak spectral power. Then, the observed flux F_ν for the total electron distribution in the *fast-cooling* regime is given by

$$F(\nu) = F_{\nu,\max} \begin{cases} (\nu/\nu_c)^{1/3} & \text{for } \nu < \nu_c \\ (\nu/\nu_c)^{-1/2} & \text{for } \nu_c < \nu < \nu_m \\ (\nu_m/\nu_c)^{-1/2}(\nu/\nu_m)^{-p/2} & \text{for } \nu > \nu_m. \end{cases} \tag{1.9}$$

For the *slow-cooling* regime, when $\gamma_m < \gamma_c$, the observed flux is

$$F(\nu) = F_{\nu,\max} \begin{cases} (\nu/\nu_m)^{1/3} & \text{for } \nu < \nu_m \\ (\nu/\nu_m)^{-(p-1)/2} & \text{for } \nu_m < \nu < \nu_c \\ (\nu_c/\nu_m)^{-(p-1)/2}(\nu/\nu_c)^{-p/2} & \text{for } \nu > \nu_c. \end{cases} \tag{1.10}$$

Spectrum is thus composed of broken power-laws (Figure 1.11). In reality, these breaks are likely smooth (Granot & Sari 2002). Fast cooling is expected during the prompt phase due to the requirement that the energy is emitted with high efficiency. Also, due to the high variability observed in the GRB light-curves, the cooling time can not be too long (assuming that the cooling time is connected with the width of the pulse). A transition to the slow cooling regime is expected at the beginning of the afterglow phase (Waxman 1997a;b; Mészáros & Rees 1997; Katz 1997).

Two additional mechanisms can also take place, impacting the shape of the observed spectrum. An electron with substantial kinetic energy can transfer a part of it to a photon, which results in the scattered photon having a higher frequency (inverse Compton scattering, or equivalently, synchrotron self-Compton, Sari et al. 1996; Dermer et al. 2000). Here, the very same electrons that produce synchrotron photons Compton-scatter them to high energies. This can increase the cooling rate of the electron propagating within the reverse shock. Panaitescu & Mészáros (2000) suggested that inverse Compton can be responsible for the hard spectra observed by BATSE (in the 20–1000 keV range) if electrons emit in the slow cooling regime. At lower frequencies, synchrotron self-absorption may cause a steep cutoff of in the spectrum (Granot et al. 1999b). This reabsorption of the photons by the synchrotron electrons occurs when the intensity of synchrotron radiation is sufficiently high (e.g., Rybicki & Lightman 1979; Piran 2004). It remains difficult to identify the correct (combination) of radiation mechanism as all of them suffer from several weaknesses (Ghisellini et al. 2000). The synchrotron shock model makes a testable prediction: for low energies $F(\nu) \propto \nu^{1/3}$. In a similar manner, the photon number spectrum N should follow $N \propto \nu^{-2/3}$. The low-energy power-law spectral index was indeed observed to be harder in about ~30% of the bursts (Preece et al. 1998a; 2000; 2002). Violation of this spectral limit poses a serious challenge to the model: the synchrotron spectrum of cooling electrons is too soft to account for the observed spectral slopes (Imamura & Epstein 1987; Stern & Poutanen 2004).

Evolution of the temporal and spectral properties of GRB afterglows that fireball model predicts can be characterized by so-called *closure relations*: a set of equations that relate temporal and spectral indices α and β for different portions of the afterglow light-curve (for $F_\nu \propto t^{-\alpha}\nu^{-\beta}$). They depend on the surrounding medium, electron spectral index, cooling regime and physical processes relevant for a portion of the light-curve under consideration (Sari et al. 1998; Dai & Cheng 2001). For example, as it was mentioned in Section 1.2, the steep decline of segment-I in the canonical X-ray light-curve is a result of the emission from high latitude and light propagation effects (Dermer 2004; Dyks et al. 2005; Fan & Wei 2005; Zhang et al. 2006a). For this segment, the relationship between the temporal and spectral indices is $\alpha = 2 + \beta$. It can be used to discriminate segment-I from other segments in the light-curve, but it provides no further information on any environmental or electron parameters. Racusin et al. (2009) found that around 60% of segments-I is not consistent with this relation. An extensive list of closure relations, including those for different CBM profiles, electron spectral indices and cooling regimes, can be found in Racusin et al.

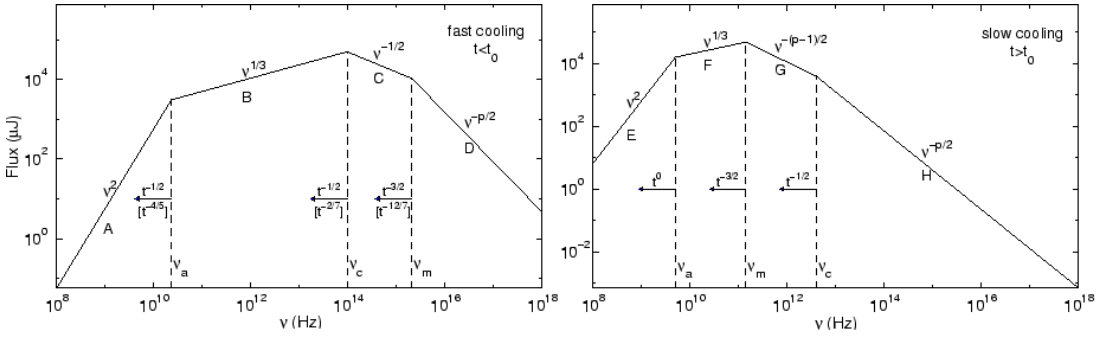

Figure 1.11. Synchrotron spectrum of a relativistic shock with a power-law electron distribution in a fast cooling (left panel) and a slow cooling (right panel) regime. The spectrum resembles a broken power-law with four segments separated by three frequencies: ν_a, the synchrotron self-absorption frequency; ν_m, the typical synchrotron electron frequency; and ν_c, a frequency of an electron with critical Lorentz factor γ_c. The way these frequencies evolve with time changes with regard to the evolution being adiabatic or fully radiative. Figure reproduced from Sari et al. (1998).

(2009). Still, some GRBs do not satisfy the closure relations for the afterglow emission (e.g., Liang et al. 2008a; Evans et al. 2009; Wang et al. 2015b).

In conclusion, the emission mechanism of the gamma-ray bursts is still a matter of debate. There is a variety of different models devised in order to interpret the spectral shape (e.g., Piran 1999; Stern & Poutanen 2004; Ryde et al. 2011; Lazzati et al. 2013; Uhm & Zhang 2014; Burgess et al. 2014; Yu et al. 2015; Guiriec et al. 2016). Zhang (2011) summarizes a vast number of open questions in GRB physics, including the ones relevant for the radiation and particle acceleration mechanisms.

Furthermore on jets

Prompt emission in GRBs was observed to have energies up to $E_{\rm iso} \sim 10^{55}$ erg. That GRB fireballs are likely to be collimated was proposed in order to explain these extraordinarily large isotropic energies (Waxman et al. 1998; Fruchter et al. 1999; Rhoads 1999). However, this does not influence any main results derived for the spherical case. The physics that dominates the system's behavior and the consequent treatment remain the same. The deviations only become noticeable once the ejecta and the shock slow down to speeds for which the half-opening angle of the outflow is smaller than the Lorentz factor of the shock. This tends to happen only one or several days after the GRB. Jet related relations and model caveats are discussed in more detail in Section 1.2 and Section 1.3. As it was mentioned before, the relativistic motion beams the radiation into a cone with a half-opening angle $\sim 1/\Gamma$, smaller than the jet opening angle θ_j due to the high velocities involved. As the jet slows down, the break in the light-curve should be observed at the point where $\Gamma \simeq 1/\theta_j$. This prediction of the collimated scenario takes the form of (Sari et al. 1999):

$$\theta_j = 0.161 \left(\frac{t_{jet,\,d}}{1+z}\right)^{3/8} \left(\frac{n\eta_\gamma}{E_{\rm iso,\,52}}\right)^{1/8}, \tag{1.11}$$

where n is CBM a density in cm^{-3} (assumed constant), η_γ is a fraction of the kinetic energy of the fireball emitted during the prompt phase, $t_{jet,\,d}$ is the break time in days and $E_{\rm iso,\,52}$ is the isotropic energy in 10^{52} erg. The energy conversion efficiency η_γ is usually assumed to be 20% (Frail et al. 2001a). The CBM density can be measured from the broadband modeling of the afterglow emission (e.g., Panaitescu & Kumar 2001). However, this is rarely the case and a median value of $\simeq 3$ cm^{-3} is often used instead. This

may introduce uncertainties as values of n can be widely spread from 0.1 cm^{-3} to 30 cm^{-3} (e.g., Harrison et al. 2001; Frail et al. 2001a; Yost et al. 2002; Bloom et al. 2003b; Frail et al. 2003). For long GRBs in which the break is observed, a typical half-opening angle lies in the $3^\circ \lesssim \theta_j \lesssim 10^\circ$ range. For short GRBs, only a lower limit of $\theta_j \gtrsim 3^\circ$ is known due to their faint afterglows (Berger 2014a). After the break, the ejecta starts to expand sideways. For an off-axis observer, an orphan afterglow (i.e., an afterglow which was not preceded by the prompt emission) may in principle be detected (e.g., Nakar et al. 2002; Totani & Panaitescu 2002).

The majority of GRB afterglows do not comply to these predictions, as it can be seen from the literature listed in Section 1.2. Besides, Eq.1.11 computes the arrival time of the photons at the detector assuming that all radiation is emitted on the line of sight. On the other side, an alternative expression proposed afterwards by Panaitescu (2006) assumes that all of the radiation is emitted from the boundary of the visible region. Both of these approaches neglect the fact that the visible area must be computed over equitemporal surfaces (see Section 2.4); areas which emit radiation that reaches the observer at the same arrival time. These surfaces do not correspond to the spherical surface of the shell. Bianco & Ruffini (2006) computed the value of the detector arrival time at which the sides of the jet become visible using equitemporal surfaces. While the expression of Sari et al. (1999) overestimates these values, the result obtained by Panaitescu (2006) slightly underestimates it.

1.5 GRB HOST GALAXIES, ENVIRONMENTS AND COSMOLOGY PROSPECTS

Gamma-ray burst host galaxies

Soon after detection of the first optical afterglow, long GRB hosts were found to be predominantly blue, star-forming galaxies (e.g., Paczyński 1998a; Savaglio et al. 2009). At the time, this suggested a young star population origin. With the sample growing in size, it was realized that GRB hosts were fainter and bluer than expected (Le Floc'h et al. 2003), indicating that GRBs may be related only to the massive stars with metallicity below a certain threshold. This was anticipated by most models at the time since they invoked a rapidly rotating NS or a BH. The Fe abundance was unfavorable as it removes the much needed angular momentum by increasing strength of the stellar wind. During this period, among 10 GRBs with provided redshift, Lyα emission was detected in five of them (while not being excluded for the remaining half). Only around 25% of the observed starbursts at these redshifts were Lyα emitters. Since the Lyα emission is more common for metal-poor starbursts (Charlot & Fall 1993), this data also favored the low metallicity bias of GRB progenitors. Massive, short-lived progenitors were also supported by the fact that long GRBs appear to coincide with the most bright regions of their hosts (Fruchter et al. 2006). The difference between the environments of GRBs and core-collapse SNe was noted as well, where GRBs tended to appear in the brighter regions of their host galaxies when compared to the core-collapse SNe (e.g., see Fruchter et al. 2006). Furthermore, the host galaxies of long GRBs at $z < 1$ differed from the core-collapse SN ones, being fainter and more irregular (e.g., Vreeswijk et al. 2004). Modjaz et al. (2008) also compared the environments of broad-lined SNe type Ic that were accompanied by a GRB with those which were not. Environments that hosted a GRB were more metal poor than the environments of broad-lined SNe type Ic that lacked GRB detection (Figure 1.12). This difference supported the claim that low metallicity drives massive stars to end their life with a GRB.

Most of these conclusions were based on the pre-*Swift* samples and might have been affected by the observational biases. Sample completeness is needed in order to derive meaningful conclusions from the statistical study of the GRB hosts. Incompleteness can be caused by various factors. While the GRB detection does not depend on the host galaxy properties, the longer wavelength emission, critical for the

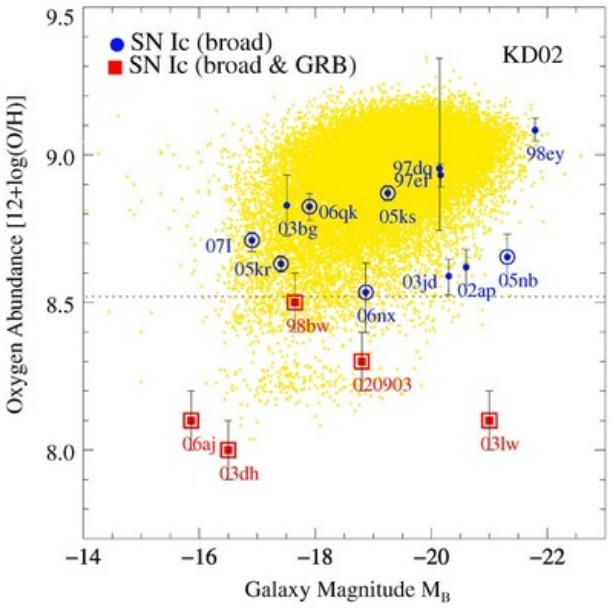

Figure 1.12. Host-galaxy luminosity (M_B) and host-galaxy metallicity (in terms of oxygen abundance) at the sites of broad-lined SNe type Ic (blue filled circles) and GRB-associated broad-lined SNe type Ic (red filled squares). Yellow points are values for local star-forming galaxies that illustrate the luminosity-metallicity relation for galaxies. Host environments of GRBs are more metal poor than the ones where no GRB was observed. Figure reproduced from Modjaz et al. (2008).

precise localization and redshift measurements, strongly depends on the dust column density in the host galaxy along the line of sight (e.g., Fiore et al. 2007). Weather and inadequate GRB positions in the sky can also contribute to the lack of optical counterparts, although these do not produce biased samples. Some sample contamination is expected in the form of Galactic high-energy transients misclassified as GRBs (Castro-Tirado et al. 2008). In addition, if the host galaxy is defined as the one closest to the line of sight there is a possibility of a chance projection, depending on the magnitude and angular size of the galaxy. Conflicting redshifts of GRBs and their host galaxies, which help eliminate the bogus associations, paired with a large galaxy sample located with high precision, should form a set of a desired cleanness (e.g., see Jakobsson et al. 2004b; Fruchter et al. 2006). The biggest concern regards the possible systematic bias against the dust-obscured hosts. Galaxies hosting GRBs located in high-metallicity will be underrepresented due to their faint or non-existent optical afterglows (Groot et al. 1998; Jakobsson et al. 2004a).

The *Swift* mission, with its unique multiwavelength capabilities (Section 1.2), opened the possibility to build a more complete sample of GRB host galaxies, unbiased in terms of the optical properties of their afterglows. This was achieved by introducing constrains both on the optical afterglow and the consequent GRBs included in the sample, such as favorable declination, small foreground Galactic extinction, and swift X-ray detection (Jakobsson et al. 2006). From 69 GRBs that fulfilled the selection criteria, the host was located for 80% of them. New results were in agreement with the previous indications: long GRB hosts are predominantly subluminous (0.01 to 1 L^*), blue, star-forming (0.2–50 $M_\odot$ yr^{-1}) galaxies. Long GRBs are therefore mostly found in dwarf, irregular galaxies or in star-forming regions of spiral galaxies (Bloom et al. 2002; Hjorth et al. 2012; Graham & Fruchter 2013; Izzo et al. 2017). In other words, the type of burst is determined by the local environment rather than the general properties of the host galaxy. For example, superluminous SN 2017egm was found in the low-metallicity, star-forming region of a

high-metallicity, non-starburst spiral galaxy (Izzo et al. 2018). In addition, long GRB 100316D, associated with SN 2010bh, occurred in the environment that is lower in metallicity and has a higher SFR than the other areas of the host (Izzo et al. 2017).

Compact binary merger scenario implies that short GRBs should be observed in both elliptical galaxies (which tend to consist of older stars) and younger galaxies where the star formation still takes place. This is due to the broad distribution of time delays expected between the stellar birth and spiraling death, during which the initial kick velocity caused by the SN explosions can create a significant distance between the star-forming region and the compact objects (Fryer et al. 1999b). From the *Swift* sample it was observed that around 20% short GRBs explode in early-type galaxies. *Swift* localization of GRB 050509B revealed a non-star-forming elliptical galaxy at $z = 0.225$ (Gehrels et al. 2005b), strongly relating them to an older stellar population (e.g., Berger 2014a). Short GRBs also occur on average five times further from the center than long GRBs (Fong et al. 2010), with the SFR ranging from 0.2 to 6 $M_\odot$ yr^{-1}. Short bursts that are associated with late-type galaxies are usually not located in the star-forming regions (e.g. GRB 050709, Fox et al. 2005). Belczynski et al. (2006) explained this diversity with two distinct populations of binary compact objects, set apart by their different evolutionary history. One population consists of wide, long-lived binaries with merger times of 100 Myr–15 Gyr. Other consists of tight, short-lived binaries with merger times of 0.001–0.2 Myr. This bimodality of merger times has an observable consequence. Mergers (and associated short GRBs) of short-lived compact binaries will be more frequently observed in galaxies that have a young stellar population. Short GRBs originating from mergers of long-lived compact binaries are expected to be found in elliptical galaxies with little or no star formation. The location of the merger within the galaxy is then a function of the merger time and the size of the host. For massive host galaxies and short merger times, the merger is expected to take place within the host. See Berger (2009; 2011) for further information on short GRB host galaxies and their differences when compared to the long GRB ones. More detailed review can also be found in van Paradijs et al. (2000) and Djorgovski et al. (2003).

Probing the high-redshift Universe

After almost three decades of GRB specialized missions, a question imposes itself: what can we learn from GRBs? As it turns out, plenty. Due to their extreme luminosities, they can be observed over a wide range of redshifts, covering more than 13 billion years of history of the Universe. With a spectroscopic redshift of $z \sim 8.2$, translating roughly to ~ 625 million years after the Big Bang, GRB 090423 was a distant record holder up to 2015[25] (Tanvir et al. 2009). It still remains the most distant transient event ever to be observed, near the very beginning of the reionization era. Figure 1.13 shows GRBs within a cosmological context.

The first stars (Pop III) had a key role in transforming the simple, homogeneous Universe into a state we see today. Their formation is expected to have started as early as $z > 20$ (Tegmark et al. 1997; Yoshida et al. 2003), much earlier then the predicted formation of the first quasars at $z \gtrsim 10$ (e.g., Haiman & Loeb 2001; Bromm & Loeb 2003). With their predominantly high mass ($M > 100\ M_\odot$) and short lifetime of several Myr (e.g., Bromm et al. 2002), they were quite possibly the dominant source of ionizing UV photons while rapidly enriching the IGM with heavy elements through the first SN explosions. By the redshift of $z \sim 10$, a substantial fraction of the intergalactic hydrogen was already ionized (e.g., Cen 2003). However, there is still a rather small number of observational constraints, much needed for understanding their formation, impact on the surrounding environment, and the emerging structure formations. As a consequence of their high mass, creation of a BH may be the end result for a significant fraction of Pop III stars, potentially leading to a large number of GRBs at high redshift[26]. The theoretical (long) GRB

[25] The current distant record holder is GN-z11, an irregular small galaxy with a redshift of $z \sim 11.1$ (Oesch et al. 2016). This corresponds to approximately 400,000 years after the Big Bang.

[26] It it suggested that GRBs would be theoretically detectable to $z \sim 15$ and beyond (Lamb & Reichart 2000).

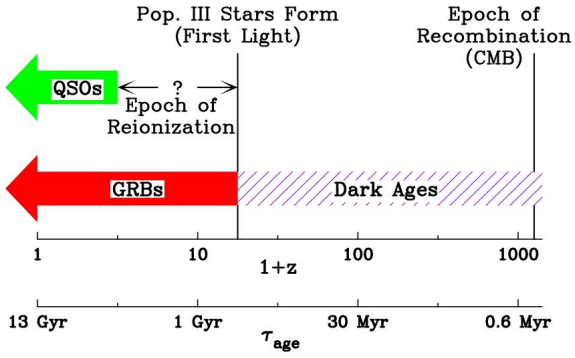

Figure 1.13. Cosmological context for high-redshift GRBs showed together with different epochs. The Universe became transparent at $z \sim 1100$ during the epoch of reionization (the origin of the cosmic background radiation). The temperature drop corresponds to the "dark ages", lasting until the birth of the first stars ($z \sim 20$). Light from these stars reionized the Universe. Figure reproduced from Lamb (2003).

redshift distribution can be derived from the current SFR models, which employ a set of free parameters. These parameters can then be calibrated and adjusted by comparing the expected GRB distribution at high redshift with the one observed by the *Swift* satellite. This has a potential to further constrain the reionization and metal enrichment of the IGM, one Pop III star at the time. However, the expected number of GRBs at high redshift heavily depends on the GRB progenitor metallicity (Salvaterra et al. 2007). This introduces additional problems because although long GRBs tend to be associated with low metallicity regions (Fruchter et al. 2006), there are hints of this trend reversing for redshifts of $z > 5$ (Savaglio et al. 2003). Further information regarding the primordial star formation can be found in the reviews of Bromm & Larson (2004) and Bromm (2013).

The metal enrichment is important as it allowed the formation of the lower-mass, Pop II stars, once the critical metallicity of $z_{\rm crit} \sim 10^{-3.5} z_\odot$ had been reached (Omukai 2000). Similar to the reionization process, the metal enrichment was not homogeneous. The effort is still needed in order to explore its topology by finding particular regions of the Universe that went critical (e.g. Mackey et al. 2003). The existence of the early metal-enriched pockets means that different models of star formation can occur simultaneously for redshifts $z > 5$. Around 50% of GRBs are presumed to originate at these distances (which differs from the presumed 25% of the *detected* GRBs at the same redshift, see Bromm & Loeb 2002), making them a useful tool for the observational cosmology. Still, Pop III stars are expected to form a majority of the GRB population only at redshifts higher than $\sim$ 10–15 (Campisi et al. 2011). For example, in addition to the isotropic equivalent energy of $E_{\rm iso} = 1.0(\pm 0.3) \times 10^{53}$ erg (von Kienlin 2009), spectral and temporal properties of GRB 090423 were consistent with the bulk of the population, suggesting there is no evidence of exceptional behavior indicating a Pop III progenitor[27]. However, it might be possible to isolate the Pop III GRB progenitors and put constraints on the Pop III star formation. They are thought to produce longer and more energetic GRBs (Bromm & Loeb 2006), that is if one assumes that the energy and duration linearly depend on the BH mass. Even so, the Pop III GRB progenitors are expected to be rare events, with the upper limit close to 0.03 Gpc^{-3} y^{-1}, considering *Swift* detector sensitivity (Salvaterra et al. 2007).

Stellar origin of long GRBs offers additional advantages. In contrast to quasars, their intrinsic luminosity is tied to the progenitor star and they tend to originate in star-forming galaxies regardless of the host galaxy mass. Therefore, a GRB can outshine its host galaxy by a factor that gets larger with the increasing redshift (e.g., Ciardi & Loeb 2000), since the first galaxies are expected to have lower masses

[27]Similar conclusions were reached for GRB 090429B with a photometric redshift of $z \simeq 9.4$.

and lower luminosities (Barkana & Loeb 2000). Once the afterglow fades away, the observed high-redshift galaxy, which would otherwise be too faint and rare to find, can be studied in more detail. This is also true for any random galaxy located on the line-of-sight. All of this enables the location and consequent unbiased study of the population of distant galaxies that are not selected for their brightness. Even if the host remains undetected, the upper limits on the unobscured and obscured SFR can still be derived. For example, the fruitless search for the host galaxy of GRB 090423 yielded the SFRs of 0.38 $M_\odot$ yr^{-1} (unobscured, Tanvir et al. 2012) and 5 $M_\odot$ yr^{-1} (obscured, Berger et al. 2014).

The Universe was largely neutral and transparent to photons from around $\sim 400,000$ years after the Big Bang, with the exception being wavelengths shorter than the ionization wavelength of hydrogen (912 Å) and the wavelengths corresponding to the transitions in neutral hydrogen, of which Lyα is by far the strongest. The reionization of the IGM, a state which remained to the present day, began at least as early as $z \sim 11$. It started as a small-bubble structure, gradually expanding around the first stars, and was neither smooth nor homogeneous (e.g., see Kitayama et al. 2004 or Dijkstra 2014). Tracing the evolution of this structure throughout the time-line of the Universe is a key goal for observational and theoretical cosmology. As it impacted almost every baryon in the Universe, understanding it is vital for developing a complete picture of the Universe's history, addressing a broad range of open questions on the way. Discoveries of high-redshift quasars, acting as a distant torch, allowed the first quantitative studies of the IGM and the history of reionization at redshifts near 6 (Fan et al. 2000).

The UV light traveling from a background source through the intergalactic space is continuously redshifted until it reaches the observer. This also includes the Lyα absorption features, caused by the neutral hydrogen transitions within the IGM[28]. All light bluewards of Lyα that encounters these residual hydrogen pockets is then continually redshifted into absorption, eventually creating a drop in the spectrum called the Gunn-Peterson trough (Gunn & Peterson 1965; Scheuer 1965). The Lyα forest, growing more dense with increasing redshift, can then be used to trace the reionization process by mapping the wavelength of each absorption feature. This reveals the distance along the line of sight at which the absorption took place (Miralda-Escudé 1998; Barkana & Loeb 2004). Therefore, the Lyα absorption presents a prominent cosmological tool for probing both galactic halos and the IGM at high redshift. Comparison of the optical spectra of quasars lying on different high-redshift distances revealed that Lyα absorption in their spectrum evolves highly with z (Becker et al. 2001), indicating a systematic change of the IGM nature. Zero flux seen in the spectrum of SDSSp J103027.10+052455.0 at $z = 6.28$, immediately blueward of the Lyα emission line, is a clear detection of a Gunn-Peterson trough (Figure 1.14 - top panel). This observation does not indicate that the quasar is observed prior to the reionization epoch, as even a small neutral hydrogen fraction would result in an undetectable flux in the Lyα forest region. Completely saturated absorption only gives a weak lower bound on the neutral fraction of IGM hydrogen ($f_{\mathrm{H_I}} = n_{\mathrm{H_I}}/n_{\mathrm{H}} \gtrsim 10^{-4}$). It does suggest, however, that $z > 7$ quasars will only be detectable at wavelengths longer than 1 micron. On the other hand, a drop in the flux by a factor of ~ 10, seen in the quasar spectra up to $z \sim 5.7$, is consistent with the extrapolation from lower redshifts. The absence of Gunn-Peterson trough observed in these sources indicates that the ionization process finalized by $z \approx 6$ (e.g., see Malhotra & Rhoads 2004; Becker et al. 2007).

Still, quasars are generally found in the highest density peaks in large-scale structure, making them a strongly biased tracers. In addition, they may alter the ionization status of the surrounding IGM by means of their strong radiation. All of this puts the reionization completion by $z \sim 5-6$ in question (Mesinger 2010). Similar to quasars, GRBs can act as UV light sources, while offering additional advantages. Besides being detectable at redshifts currently exceeding the ones of quasars (Figure 1.13), their short-duration emission releases ~ 10 orders of magnitude less energy into the surrounding IGM, hardly affecting its ionization status. Unlike the smooth power-law spectrum of the GRB afterglows, complicated quasar

[28]Transition between the ground state and the first excited state occurs at a wavelength of 1216 Å.

spectra with emission and broad absorption lines makes the detection of the IGM absorption features more demanding. Association of GRBs with star formation sites may lead to the less biased distribution, where they would act as signal posts of lower mass galaxies (Tanvir et al. 2012). As such, they should not be localized in over-ionized regions relative to the average. The afterglow flux is also not expected to fade significantly with increasing redshift. The cosmological time-stretching effect translates the observation to the earlier times in the source frame, during which the afterglow is intrinsically brighter (Ciardi & Loeb 2000; Barkana & Loeb 2004). All of the above makes GRBs the cleanest sources for mapping the reionization of neutral hydrogen fraction through time (see Barkana & Loeb 2004 for quantitative comparison of the Lyα absorption profile between quasars and GRB afterglows).

That promise started to realize with the spectral analysis of the exceptionally bright optical afterglow of GRB 130606A (Figure 1.14 - bottom panel). Located at $z = 5.913$, it provided new evidence that the reionization is not as yet complete at $z \sim 6$. A minimal model considering only a host galaxy absorption did not provide a good fit. A fit to a simple, uniform IGM model extending up to the host redshift gave $f_{\rm H_I} = 0.086$ (Totani et al. 2014, but also see Chornock et al. 2013). Previous afterglow analysis of high-redshift GRBs were only able to place weak upper-limit constrains of $f_{\rm H_I} < 0.73$ and $f_{\rm H_I} < 0.6$ at $z \sim 6$ due to the insufficient signal to noise ratio of the data (Totani et al. 2006; Patel et al. 2010). A similar spectrum was observed in the afterglow of GRB 140515A at $z = 6.33$, where a well-detected continuum is cut by a steep decline to zero flux blueward of 8915 Å (Chornock et al. 2014).

By observing the absorption profile in the afterglow spectra, GRBs can provide information on the host metallicity and the metal enrichment level of the intervening IGM, (theoretically) out to $z > 10$ (e.g., Furlanetto & Loeb 2003). The afterglow spectrum of GRB 140515A did not contain any narrow absorption lines from the host galaxy, indicating a host metallicity of $[{\rm Z/H}] \lesssim -0.8$. Early afterglow can also modify the gas properties close to the source as it travels through the interstellar environment, causing a time-dependent spectral features in the afterglow. From these, properties of the gas cloud such as its density, size and metal abundance can be derived. In contrast to GRB 140515A, spectrum of GRB 130606A exhibited a presence of many metal elements.

The missing neutrinos

Next to active galactic nuclei (AGNs), GRBs have been proposed as promising accelerators of even the most energetic segment of ultra-high energy cosmic rays (UHECRs, Vietri 1995), capable of accelerating them to energies higher than 10^{19} eV (e.g., Waxman 1995; Wick et al. 2004). On the other hand, the lack of detection of the consequent neutrino flux challenges current models and the role of GRBs as UHECR accelerators. Neutrinos are regarded as an unambiguous signature of proton acceleration. In proton-gamma interactions, neutrinos are expected as a final outcome of the decay of charged particles. Namely, through the Δ^+ resonance, the resulting charged pions decay into muons and muon neutrinos (Equation 1.12) while neutral pions decay into gamma-rays:

$$p + \gamma \xrightarrow{\Delta^+} n + \pi^+ \rightarrow n + \mu^+ + \nu_\mu \rightarrow n + e^+ + \nu_e + \overline{\nu}_\mu + \nu_\mu. \tag{1.12}$$

The fireball model (Piran 2004; Mészáros 2006, see Section 1.4) involves the release of photons, electrons and hadrons induced by a cataclysmic stellar collapse. Therefore, on sites of proton acceleration such as GRBs, neutrino and gamma-ray detection should coincide. Relativistic electrons, accelerated to high energies by shock waves, contribute to the observable prompt gamma-ray emission once the transparency condition has been reached. If protons are accelerated in the same manner, GRBs should account for the

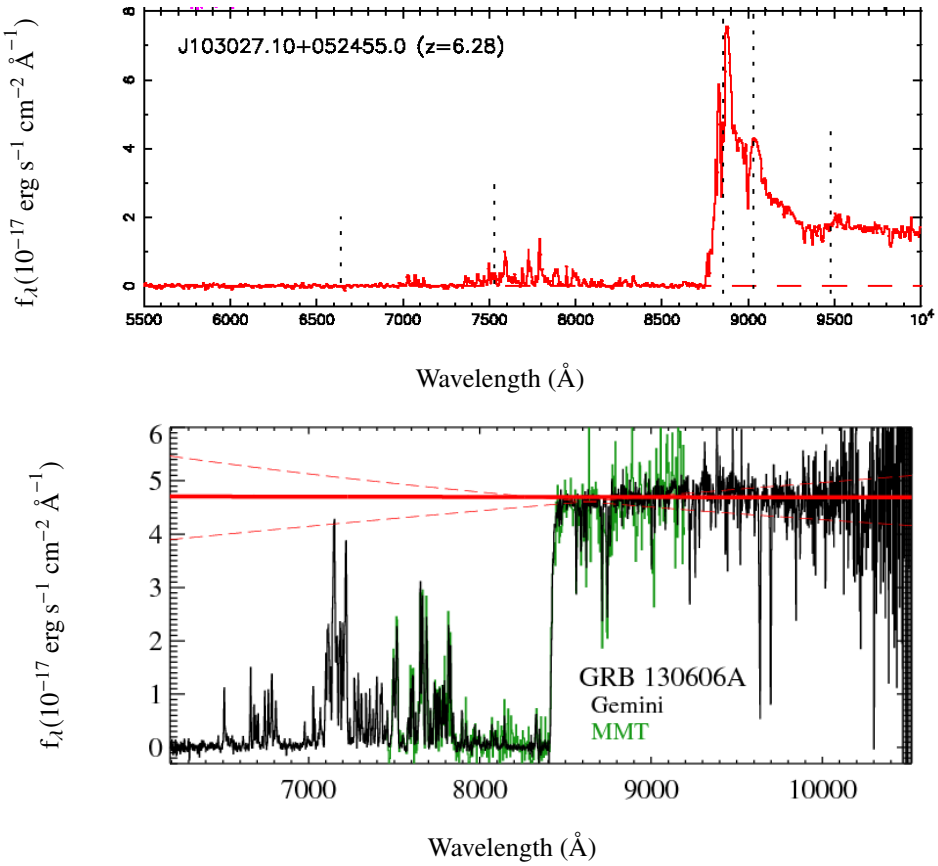

Figure 1.14. *Top panel:* Optical spectrum (observed frame) of $z = 6.28$ quasar. Drop in the flux level by a factor > 150, immediately blueward of Lyα emission line, is consistent with zero flux. This represents a clear detection of a complete Gun-Peterson trough, caused by a neutral hydrogen in the IGM. Figure reproduced from Becker et al. (2001). *Bottom panel:* Spectrum of the optical afterglow of GRB 130606A at $z = 5.913$, with a cut-off blueward of 8410 Å due to absorption from Lyα. Some flux is transmitted through the Lyαforest between 7000–7800 Å. The solid red line shows a best-fit power-law to the line-free regions of the continuum. The two dashed red lines show hypothetical extreme systematic variations around the best-fit value. Figure reproduced from Chornock et al. (2013).

measured UHECR flux[29]. The accelerated protons would interact with the ambient photon field, thus producing the *prompt* neutrinos (Equation 1.12), observable in both temporal and spatial coincidence with the gamma-ray emission.

The IceCube neutrino detector (Aartsen et al. 2017b), with its current configuration of 60 string modules, is well within the sensitivity at which the GRB-triggered neutrino detection is anticipated by current theoretical models (e.g., Aartsen et al. 2015; 2019; 2017a; Turley et al. 2018). Hence, the lack of coinciding neutrino detection came as a surprise. These results are consistent with other neutrino detectors in operation (Adrián-Martínez et al. 2013a;b). This implies either that GRBs are not the sources of cosmic rays with energies exceeding 10^{18} eV or that the efficiency of neutrino production is much lower than has been predicted. The absence of neutrinos is then usually used as a constraining method of the bulk Lorentz

[29]The sources of UHECRs with energies greater than 10^{18} eV remain unknown as intergalactic magnetic fields deflect the rays while they propagate through the Universe.

factor Γ and the baryon loading for the various fireball scenarios (e.g., photospheric scenario, see Gao et al. 2013b). At the same time, a purely-electron jet model was also suggested (Fargion & Oliva 2016).

Chocked jets, mentioned in Section 1.4, may act as an additional source of high energy neutrinos. They may also explain the lack of association between the observed GRBs and IceCube neutrinos, since gamma-ray photons will not escape the stellar envelope. Guetta et al. (2020) calculated the expected high-enery neutrino flux from chocked jets and their detectability with IceCube and other neutrino detecting facilities. If most of type Ib/c SNe harbour a chocked jet, the number of detected neutrinos will be larger than in the standard case of GRB-only associated jets. The future follow-ups may then provide a way to limit the fraction of SNe that produce jets.

Further prospects of GRB exploitation

Observations of GRBs can give much more constrains and implications regarding cosmology, from which only some will be briefly mentioned here. Efforts were made regarding the prospects of utilizing the $E_{\rm p} - E_{\rm iso}$ correlation (Amati et al. 2002) in order to obtain the independent estimate on $\Omega_{\rm M}$ (Amati & Della Valle 2013, but also see Li 2007). The same was done for the parameter $w(z)$ of the dark energy equation of state, which relates the dark energy pressure with the dark energy density (Chevallier & Polarski 2001; Linder 2003), while exploring its possible dependence with redshift (Demianski et al. 2012; 2017). As distant, rapidly variable sources of high energy photons, GRBs could also offer ways to investigate the Lorentz-violating effects for photons. The coefficients of the Taylor expansion for the energy-dependence of the speed of light in vacuum (Amelino-Camelia et al. 1998) are specified by a given theory of quantum gravity. GRB observation can provide limits on these coefficients (e.g., see Abdo et al. 2009a).

As it was mentioned in Section 1.4, Advanced LIGO and Advanced Virgo have confidently detected GWs from ten stellar-mass binary BH mergers and one binary NS inspiral (Abbott et al. 2018). From these, the last one was accompanied by an electromagnetic counterpart (GRB 170817A, Goldstein et al. 2017). This marked the dawn of a new era of scientific exploration where compact binaries formation, growth and evolution models can be tested, together with the models of GW generation and propagation. Detection of GWs emitted by merging BHs can probe the BH binary environment, and the consequent analysis will allow for precise tests of general relativity. The first detections already put constraints on the compact binary populations and expected merger rates (see, e.g., Abbott et al. 2016b;c;d). Assuming the fixed population distribution, the current inferred merger rates at the 90% confidence intervals are $110 - 3840\,{\rm Gpc^{-3}\ y^{-1}}$ for the binary NSs and $9.7 - 101\,{\rm Gpc^{-3}\ y^{-1}}$ for the binary BHs. An upper limit of $610\,{\rm Gpc^{-3}\ y^{-1}}$ for a NS-BH merger rate was also determined (see Abbott et al. 2018 for more detailed astrophysical implications of these results). Della Valle et al. (2018) used GRB 170817A and the accompanied KN detection (e.g., Arcavi et al. 2017) to constrain the rate of such sources. The rate, assuming that the emission was isotropic, was $352^{+810}_{-281}\,{\rm Gpc^{-3}\ yr^{-1}}$ (much smaller than the upper limits of the KN occurrence rates set by several sky surveys, e.g., Doctor et al. 2017; Smartt et al. 2017). This rate is also much larger than most of the short GRB rates approximated so far (e.g., Guetta & Piran 2005; 2006) and much lower than the density of binary NS mergers. This means that either only a fraction of binary NS mergers produce short GRBs or that the short GRB emission is beamed and can be observed under angles as large as 40°. Well-constrained KN and binary NS merger rates will help to assess if the mergers are the dominant contributors to the heavy element production via r-processes (e.g., see Kasen et al. 2017).

As for long GRBs, SN event rate can be used in order to acquire new insights into the properties of the GRB population. Not all nearby long GRBs have an associated SN (see Section 1.2). Guetta & Della Valle (2007) calculated the local rates of low-luminosity ($\leq 10^{49}\,{\rm erg\ s^{-1}}$) GRBs by considering two nearby, long, subluminous bursts: GRB 980425 and GRB 060218. After taking into account the detector sensitivity, its sky coverage, and its operating years, the derived low-luminosity GRB rate was in agreement with

the one inferred from the BATSE and *Swift* peak flux distribution, namely 380^{+620}_{-225} Gpc^{-3} yr^{-1}. Since the afterglows of the two bursts showed no evidence of a jet break, the rate was not corrected for beaming. High-luminosity GRB rate ($\geq 10^{49}$ erg s^{-1}) of 100–550 Gpc^{-3} yr^{-1} was obtained by taking the rate of ~ 1.1 Gpc^{-3} yr^{-1} (Guetta et al. 2005) and correcting it for the range of jet beaming angles (4°–10°, Frail et al. 2001b; Guetta et al. 2005). Ratios of $\sim$ 1%–9% (low-luminosity GRBs) and $\sim$ 0.4%–3% (high-luminosity GRBs) were obtained when these rates where compared to the ones of SNe type Ib/c. These data point to two interesting possibilities. Either two distinct classes of GRBs exist that differ in frequency of occurrence, or a single GRB population gives rise to both low-luminous isotropic component and highly-luminous beamed emission, detectable over a different range of redshifts.

And finally, there have been numerous studies of the effect GRBs have on the life-hospitality of their host galaxies, including our own Milky Way. Nearby GRBs ($\sim$ kpc) have been proposed as a possible cause of mass extinctions on Earth during the last billion years (e.g., the Ordovician-Silurian mass extinction event, see Melott et al. 2004; Dermer & Holmes 2005; Thomas 2009). Li & Zhang (2015) estimate that the Earth would be affected by roughly one long GRB every 500 million years. The predictions regarding the effects of radiation on the Earth's biosphere need to consider the differences between the present and the prehistoric atmospheres (e.g., see Galante & Horvath 2007). It is expected that the incoming gamma radiation would quickly deplete much of the Earth's ozone layer, allowing an increase in solar UV radiation reaching the surface. Still, the expected impact depends on the type of organism under consideration and it is therefore complicated (Thomas et al. 2005; 2015). The endangerment also comes in the form of long-lasting nitrogen oxides (see, e.g., Melott et al. 2005). Once gamma-rays dissociate nitrogen molecules in the upper atmosphere, they are prone to recombine with oxygen atoms. Nitrogen dioxide is opaque, and can thus cause a fast global cooling accompanied by a mass extinction event (Reid et al. 1978; Gehrels et al. 2003).

While the habitability of the Milky Way received by far the most attention, consideration of other galaxies is necessary in order to characterize the habitability of the wider Universe. Presuming that the timescale of 500 Myr is enough for advanced life to develop, Li & Zhang (2015) conclude that approximately 50% of galaxies at $z \approx 1.5$ and as many as 99% of local ones may be benign. The examined environments included the solar neighborhood, SDSS galaxies (Sloan Digital Sky Survey, York et al. 2000) and GRB host galaxies while keeping in mind the dependence of the long GRB rate on star formation and metallicity. The obtained increase in lethal GRBs with redshift is therefore a consequence of the increasing SFR and decreasing metallicity in high redshift galaxies. This result differs from the one obtained by Piran & Jimenez (2014), which conclude that terrestrial form of life could not have existed in galaxies at $z > 0.5$. However, the adopted timescale to re-develop advance life was not the same as in Li & Zhang (2015).

2

FIRESHELL MODEL AND THE IGC PARADIGM

That a vast amount of energy can be extracted from a charged (or rotating) BH in the moment of its formation and that the majority of type Ic SNs occur in binary systems are the two starting points that make up a core of the alternative fireshell model and its extension, the induced gravitational collapse paradigm. This chapter briefly reviews the relevant properties of the fireshell model in Section 2.1 that has been developed in the last 20 years, followed by a more detailed description in the following sections. The evolution of binary system, its effect on the GRB formation, and the consequent observational signatures predicted by the binary-driven hypernova model are summarized in Section 2.8. Special attention is devoted to modifications that were introduced with each published work, which include the emission mechanism responsible for GRB observational properties, sub-classification of GRBs and the nomenclature. Therefore, Sections 2.6–2.9 familiarize the reader with the model's development up to its present form.

2.1 INTRODUCTION TO FIRESHELL MODEL

In 1971, Christodoulou & Ruffini devised a BH mass-energy formula for a Kerr-Newman BH as a function of its irreducible mass[1], angular momentum, and its charge. The result indicated that up to 50% of the mass can be converted to energy (while for the extreme Kerr BH this portion is 29%, see Section 2.2). This opened a new window of possibilities regarding the high-energy phenomena in the Universe: a BH formation can be accompanied by an energy release on the order of $10^{54}(M_{\rm BH}/M_{\odot})$ erg (Damour & Ruffini 1975). Soon after, the discovery of GRBs was announced (Klebesadel et al. 1973; Strong et al. 1975). Taking side with the so-called "cosmophiles", Damour & Ruffini (1975) recognized that the order of magnitude of the energies involved coincides with the ones that can be extracted from a BH, i.e., the BH formation could provide the sufficient energy reservoir to explain the bursts of gamma-rays at cosmological distances. Confirmation of cosmological origin of GRBs motivated a revisit of the model proposed in the '70s and its further development (e.g., Ruffini 1998; Preparata et al. 1998). From that point onward, the focus was directed towards the fundamental physical processes occurring outside the horizon in the moment of the Reissner-Nordstrom BH formation and to the possible detection of this system as it evolves with time. The fireshell model was thus formed (Ruffini et al. 2010; Ruffini 2011), based on the extractable energy of a charged BH through the vacuum polarization process[2] (Ruffini 2002). This process can also

[1] Irreducible mass is the equivalent of energy that can not be extracted from a BH using classical means (e.g., the Penrose process). Rotational and Coulomb fractions of the total energy represent the reducible parts of the mass. Mass of the Schwarzschild black hole is therefore 100% irreducible if one does not consider Hawking radiation.

[2] Within the framework of quantum electrodynamics, the presence of a critical electric field can polarize the vacuum. This yields the spontaneous creation of e^+e^- pairs that reposition themselves in a way that reduces the initial electric field (analogous to the way a dielectric is polarized). Sauter (1931) understood that Dirac's theory of the electron predicts that, for a sufficiently strong electric field, the e^+e^- pairs will be spontaneously created from the vacuum. The pair with far-enough separation will draw its rest mass energy from the field. These virtual particles can then acquire the threshold pair creation energy $2mc^2$ and become real

occur in the vicinity of a rotating BH immersed in the magnetic field of a NS; a possibility that was recently invoked in the work of Ruffini et al. (2018h) and Ruffini et al. (2019c).

The vacuum polarization and the consequent pair creation (Section 2.2) is fully reversible. This makes it a very efficient energy extraction mechanism. It occurs in a region called the dyadosphere (for a Reissner-Nordstrom BH, Preparata et al. 1998) or dyadotorus (for a Kerr-Newman BH, Cherubini et al. 2009). Formed e^+e^- pairs, with total energy of $E^{\rm tot}_{e^+e^-}$, reach the thermal equilibrium (Aksenov et al. 2007) and self-accelerate up to ultra-relativistic velocities under their own internal pressure (Ruffini et al. 1999, Section 2.3). The expanding plasma, named *fireshell*, slows down upon encountering and engulfing the baryons, which remain from the star-collapse. The baryonic matter, quantified with a parameter $B = M_{\rm B}c^2/E^{\rm tot}_{e^+e^-}$, where $M_{\rm B}$ is the mass of the baryons, thermalizes with the pairs due to the large optical depth and continues to accelerate together with the fireshell (Ruffini et al. 2000). Parameters B and $E^{\rm tot}_{e^+e^-}$ completely describe the dynamics of the optically thick phase. When the transparency condition is reached, the flash of thermal radiation is emitted, called the proper GRB (P-GRB, Ruffini et al. 2001a). Lorentz factor at the transparency can vary over a wide range of values, between $10^2 \lesssim \Gamma \lesssim 10^4$. The final Lorentz factor value, the final distance at which the transparency occurs, and the amount of energy emitted in the P-GRB are all functions of B and $E^{\rm tot}_{e^+e^-}$. The model is valid for $B \lesssim 10^{-2}$, after which the constant-thickness approximation (used throughout the model) breaks down. Baryons, together with residual leptons, continue to expand under a fully-radiative regime until they reach the CBM at distances around 10^{16} cm (Ruffini et al. 2001a, Section 2.4). These collisions result in a gamma-ray emission, which allows the CBM profile and its inhomogeneities to be estimated (see Section 3.1). Therefore, within the fireshell model, the prompt emission light-curve is divided in two parts based on the mechanisms in question: the P-GRB and the emission after it. The description of both phases requires an appropriate relative space-time transformations which relate the observed GRB signal to its past light-cone, introduced in Ruffini et al. (2001b). Events that are correctly placed on the worldline of the source are imperative for the correct interpretation of the data. In the most recent version of the induced gravitational paradigm, the prompt emission is divided in several episodes. In addition to P-GRB and e^+e^- plasma interaction with the CBM, these episodes account for the possibility of a precursor and fireshell's reflection. The fireshell model, further described in following sections, was first applied to GRB 991216 (Ruffini et al. 2001a), and since then has correspondingly evolved to incorporate new data provided by following missions.

Fireshell versus fireball

The fireball model (Rees & Meszaros 1992; 1994; Piran 2004; Mészáros 2006, see Section 1.4) assumes a sudden release of a large amount of energy in a compact region of space, which results in an optically thick photon-lepton plasma. However, the model itself does not deal with the exact mechanism of this initial energy release, only its consequences. On the contrary, the foundation of the fireshell model is the extraction mechanism of a BHs energy by the means of vacuum polarization. The magnitude of the involved energies in this process also makes the introduced requirement of the collimated outflow (i.e., the jet, Sari et al. 1999) redundant.

In the fireball scenario, the prompt phase and its duration is defined as the time interval during which the emission is observed in gamma-rays. It is associated with the internal shocks, while the collisions with the external CBM are believed to be the source of the afterglow (Section 1.4). The observed temporal structure of the prompt emission then simply reflects the temporal behavior of the inner engine that is

electron-positron pairs. The phenomena was further investigated by Euler & Kockel (1935) and Heisenberg & Euler (1936). It was later formalized by Schwinger (1951), giving it a complete theoretical description and its name (the Schwinger effect). The Schwinger pair production in a constant electric field takes place at a constant rate per unit volume. However, this effect has not as yet been directly observed due to its required magnitude for the critical electric field: $\sim 10^{16}$ V/cm.

responsible for the production of shells with different Lorentz factors. On the other hand, the fireshell model divides the GRB light-curve into the P-GRB and the ultra-relativistic prompt phase [3]. After the transparency condition has been reached, the accelerated baryonic matter starts to slow down only when it encounters the CBM. This interaction is considered to be the origin of the gamma-ray emission following the P-GRB (Section 2.4). Evolution of the CBM density with distance is therefore reflected in the shape of the prompt emission light-curve. For example, for a constant CBM the resulting light-curve would contain a single peak. The prolonged central engine activity is often required in the fireball model in order to explain many of the observed properties (see Section 1.2). The prolonged activity of the inner engine in the fireshell model (see Section 2.8) is invoked as a possibility only for the high energy photons (> 100 MeV) that are sometimes observed to coincide with the prompt emission.

In both internal and external shocks, the synchrotron emission of the relativistic electrons is widely accepted to be the main conversion mechanism of the fireball energy to radiation (Section 1.4). The interactions within the fireball model are collision-less, i.e. mediated via chaotic electric and magnetic fields. Additional spectral modifications are possible at low energies (synchrotron self-absorption, Meszaros & Rees 1993a; Granot et al. 1999b), or at high energies (inverse Compton scattering, Meszaros et al. 1994; Dermer et al. 2000). In the fireshell model, the collisions between the plasma and the baryons, and between the baryons and the CBM, are modeled as inelastic. The latter has been assumed to produce a modified BB spectrum (Patricelli et al. 2012), while the observed non-thermal shape is a result of the convolution of a very large number of these spectra with different Lorentz and Doppler factors, and different temperatures. Multiple Compton scattering can also modify the spectrum (Bianco et al. 2001). Recently, a synchrotron emission of relativistic electrons, injected into the magnetized plasma of a hypernova (Section 2.8), has been suggested in order to explain the X-ray and optical afterglow of GRB 130427A (Ruffini et al. 2018a).

The adopted mathematical treatment of the problem also differs between the two models. In the fireshell model, the analytic solution of the equations of motion for the baryonic shell was obtained by integrating them in a self-consistent way once the initial conditions were set (Ruffini et al. 2002; Bianco & Ruffini 2004; 2005b). The fireball model uses the approach of Blandford & McKee (1976), where the dependence of the Lorentz gamma factor with distance is approximated with a power-law. This also affects the derivation of the equitemporal surfaces, which are essential in order to calculate the expected observed spectra, as predicted by the model (see Section 2.4).

The fireshell concept can be applied in total generality to any source of the optically thick, baryon-loaded pair plasma. Plasma evolution is fully determined by $E^{\rm tot}_{e^+e^-}$ and B and independent of the process that created it. This encompasses the hyper-accretion disk described in Woosley (1993) as well as the pair plasma created via $\nu\bar{\nu} \leftrightarrow e^+e^-$ mechanism in a NS merger (Narayan et al. 1992; Salmonson & Wilson 2002; Rosswog et al. 2003). Thus, the fireshell model applies to both long and short GRBs.

2.2 CENTRAL ENGINE

Development of the fireshell model started with the Christodoulou-Ruffini mass formula for a Reissner-Nordstrom BH (abbreviated to EMBH for "electromagnetic black hole", Reissner 1916; Nordström 1918), for which this model was fully developed (Christodoulou & Ruffini 1971). Namely,

$$E = Mc^2 = M_{\rm ir}c^2 + \frac{Q^2}{2r_+} = M_{\rm ir}c^2 + \frac{Q^2c^2}{4GM_{\rm ir}}, \tag{2.1}$$

[3] Initially, the emission was divided into the P-GRB and the extended afterglow, which encompassed the entire following multi-wavelength radiation (Bianco et al. 2008).

where Q is the charge of the BH (or equivalently, the previous charge of the non-rotating collapsing shell, e.g., see Cherubini et al. 2002), $M_{\rm ir}$ is its irreducible mass and $r_+ = 2GM_{\rm ir}/c^2$ is the horizon radius with the surface of

$$S = 4\pi r_+^2 = 16\pi \left(\frac{G^2}{c^4}\right) M_{\rm ir}^2 \qquad \text{(in the c.g.s. units)}. \tag{2.2}$$

Limited by the cosmic censorship conjecture, the energy associated with the charge Q can not exceed the one associated with the irreducible mass. This leads to the expression for a maximally charged BH[4]:

$$\frac{Q^2}{2r_+} \leq M_{\rm ir}c^2 \quad \rightarrow \quad Q_{\rm max} = 2\sqrt{G}M_{\rm ir}. \tag{2.3}$$

In reality, BHs should be characterized by all three fundamental parameters: mass, angular momentum, and charge (Ruffini & Wheeler 1971). However, only the charge Q can be responsible for a large energy extraction on a short time scale. The mass and the momentum evolve on a much larger time-scales (e.g., Penrose & Floyd 1971; Hawking 1974; 1975). Additionally, the Eq. 2.3 shows that up to 50% of the total EMBH mass-energy can be stored in the electromagnetic form[5], when compared to the 29% for the (rotating) Kerr BH (Kerr 1963), as stated before. This energy can be swiftly extracted by pair creation induced by vacuum polarization, all the way up to EMBH with $M_{\rm ir} < 10^6 M_\odot$ (Heisenberg & Euler 1936; Schwinger 1951; Damour & Ruffini 1975). A concept of *dyadosphere* was introduced by Preparata et al. (1998) and Ruffini (1998) in order to avoid the final absorption of pairs by the EMBH. The term refers to the region outside the horizon where the electric field exceeds the critical value for spontaneous e^+e^- pair production, $\mathcal{E}_{\rm c} = \frac{m^2c^3}{\hbar e}$ (Schwinger 1951), where e and m are the charge and the mass of the electron. The EMBH electromagnetic energy is distributed throughout the entire region of space, starting from the horizon, where it reaches its maximum value of $\mathcal{E}_+ = Q/r_+^2$, to infinity. Therefore, the dyadosphere will occupy the region around the EMBH that extends from the horizon at r_+ to $r_{\rm ds}$, which is the distance where $\mathcal{E} = \mathcal{E}_{\rm c}$. The dyadosphere is expected to form only during the collapse, in the region that is depleted of charge. Both r_+ and $r_{\rm ds}$ can be expressed via dimensionless parameters μ and ξ, where $\mu = \frac{M}{M_\odot} > 3.2$ and $\xi = Q/Q_{\rm max} \leq 1$. Then, the dyadosphere expands over $r_+ \leq r \leq r_{\rm ds}$ (Preparata et al. 1998), where

$$r_+ = 1.47\times10^5 \mu \left(1+\sqrt{1-\xi^2}\right) \text{ cm} \quad \text{and} \quad r_{\rm ds} = 1.12\times10^8\sqrt{\mu\xi} \text{ cm}. \tag{2.4}$$

Typical values of these parameters in the case of the stellar-mass BH are $r_+ \sim 10^6$ cm and $r_{\rm ds} \sim 10^8$ cm. Parameter μ also has an indirect upper limit of 6×10^5. Electromagnetic field decreases with radius as $\sim 1/r^2$ starting from the BH horizon, which in return is mass dependent. For a supermassive BH, with mass exceeding this limit, the electromagnetic field will never become critical (e.g., see Figure 1 in Preparata et al. 1998).

The creation of pairs will in an exponential manner come to a halt as the electric field proceeds to fall below the critical value $\mathcal{E}_{\rm c}$. Time-scale during which this happens is very short ($\sim 10^{-19}$ s). The density and energy of pairs can be modeled by a sequence of concentric thin-shell capacitors, as shown by the left panel in Figure 2.1. Pair energy within a certain shell will then be equal to the difference between

[4] It is often noted in the literature that BHs with a significant charge are not expected to form in nature. However, for a maximally charged BH, it would be enough to have a difference of one quantum of charge per 10^{18} nucleons in the collapsing stellar matter (Preparata et al. 1998).

[5] In other words, the irreducible mass $M_{\rm ir}$ is not a function of electromagnetic energy (Bekenstein 1971; Ruffini & Vitagliano 2002).

the initial and critical energy of the electromagnetic field. The total energy of pairs deposited within the dyadosphere is given by (Preparata et al. 1998; Ruffini et al. 1999; Ruffini 1999)

$$E^{\rm tot}_{e^+e^-} = \frac{Q^2}{2r_+}\left(1-\frac{r_+}{r_{\rm ds}}\right)\left[1-\left(\frac{r_+}{r_{\rm ds}}\right)^2\right]. \tag{2.5}$$

Since r_+ and $r_{\rm ds}$ depend on the irreducible mass $M_{\rm ir}$ and charge Q, $E^{\rm tot}_{e^+e^-}$ is completely determined by these two parameters as well. The energy stored in the dyadosphere of a maximally charged EMBH will depend on the BH total mass as $E^{\rm tot}_{e^+e^-} \simeq \frac{M}{M_\odot}\times 10^{54}$ erg (Damour & Ruffini 1975). For more general scenarios, the range of energies spans over few orders of magnitude, namely 10^{49}–10^{54} erg. Large pair densities with respect to the size of cross-sections for the $e^+e^- \rightarrow \gamma+\gamma$ process will result in a thermal equilibrium characterized with $N_{e^+} = N_{e^-} \sim N_\gamma \sim N_{\rm pair}$ and an average temperature of $kT \sim$ MeV where

$$kT_\circ = \frac{E^{\rm tot}_{e^+e^-}}{3N_{\rm pair}\times 2.7}. \tag{2.6}$$

Here, $N_{\rm pair}$ is the number of e^+e^- pairs composed of N_{e^+} number of positrons and N_{e^-} number of electrons, where k is Boltzmann's constant. The plasma described by the equations above is termed fireshell. Additionally, the processes occurring for the case of $\mathcal{E} < \mathcal{E}_{\rm c}$ are believed to be the origin of a prolonged high-energy emission and, as such, a possible source of UHECR. Cherubini et al. (2002) and Ruffini & Vitagliano (2002) offer more details on this subject, including on the collapse of a non-rotating charged shell and a further clarification regarding the consequences of the mass-energy formula.

2.3 EXPANSION OF THE FIRESHELL

Preparata et al. (1998) gave details on the e^+e^- pair creation and their distribution within the dyadosphere. Determining the pair densities as functions of the radial coordinate and the average energy per pair as a function of the EMBH mass sets the initial conditions for their subsequent relativistic expansion. Building on this work, Ruffini et al. (1999) studied the temporal evolution of this plasma by using a simplified quasi-analytic approach which led to ordinary differential equations. Within these equations, the plasma was assumed to be optically thick, since the radiation energy that escapes during the expansion is very small when compared to the total energy of the fireshell (until the transparency condition is reached). This means that the expansion can be considered adiabatic. Gravitational interactions are also not considered as their effect on plasma expansion is negligible. The aftermath can be summed with the equation expressing the change of the electron-positron number-density as the plasma fluid infinitesimally expands from $V'_\circ$ to V' in the time interval $t_\circ - t$, where "$\circ$" refers to the initial value of the quantity in question and where V' and t are the coordinate volume of the plasma fluid and the coordinate time. Two additional equations,

$$\epsilon_\circ = \epsilon\left(\frac{V}{V_\circ}\right)^{\Gamma_{\rm T}} \quad \text{and} \quad \Gamma = \Gamma_\circ\sqrt{\frac{\epsilon_\circ V'}{\epsilon V'}}, \tag{2.7}$$

form a complete set needed for numerical integration. Here, $V = \gamma V'$ is the proper volume of the plasma, ϵ is the proper internal energy density, Γ is Lorentz factor and $\Gamma_{\rm T}$ is the thermal index.

Three possible relativistic expansion patterns were analyzed: the one with the constant shell thickness in the laboratory frame, the one with the constant thickness in the rest frame and the one where a uniform time-decreasing density is assumed (Ruffini et al. 1999). The way the relativistic gamma factor is increasing with radius (or time) differs among these models. Ruffini et al. (1999) compared these three different results

(obtained by the simplified models) with the one acquired by numerically integrating the (general) analytic relativistic hydrodynamic equations, presented in Wilson et al. (1998). The comparison validated the case of the constant-thickness approximation, while the other two expansion patterns did not match with the numerical solutions. As in many things in physics, the results were obtained for vacuum, the assumption that is here justified since the local environment has been depleted of matter due to its gravitational collapse into a BH.

In other words, the plasma quickly reaches thermal equilibrium ($\lesssim 10^{-12}$ s, Aksenov et al. 2007) and starts to expand under its own internal radiation pressure. The expansion is in the form of a shell of constant thickness[6] (in the laboratory frame). The internal energy is transferred into the outward kinetic energy of the positrons and electrons. As it expands and accelerates (e.g., see the right panel in Figure 2.1), the plasma cools down up to the transparency point. Its dynamics in a matter-free space is therefore determined by only two parameters, the EMBH mass and charge, which set the initial conditions for its expansion.

Reaching the baryons

The e^+e^- plasma considered so far was baryon free. Baryons, the remnants of the progenitor star, are expected to lie at rest beyond the dyadosphere in the form of a spherical shell. The baryon number density is assumed to be constant. The shell should be close enough so that the expanding plasma reaches it before it turns transparent. Its geometry is described by thickness Δ, assumed to be $\Delta \sim 10^9$ cm $(10\,\mathrm{r_{ds}})$, starting at a distance of $r_{\rm in} \sim 10^{10}$ cm $(100\,\mathrm{r_{ds}}$, Ruffini et al. 2000). Here, $r_{\rm ir}$ is the inner radius of the baryon shell. Parameter B, termed baryon load, was introduced in order to express the mass of the remnant as a fraction of the energy stored in the dyadosphere:

$$B = \frac{M_{\rm B}c^2}{E^{\rm tot}_{e^+e^-}}, \tag{2.8}$$

where $M_{\rm B} = N_{\rm B}m_p$ is the mass of the baryons in which $N_{\rm B}$ is the number of baryons and m_p is the proton mass. Ruffini et al. (2000) examined the collision of the expanding fireshell plasma with the baryonic matter for a range of baryonic load values lying well outside the EMBH. The analysis was done by adopting the constant-thickness approximation in the moment of the collision and after. As it was mentioned before, this approximation was previously confirmed for the expansion in the absence of baryonic matter (Ruffini et al. 1999), and in Ruffini et al. (2000) it was generalized and validated for baryon load values of $B \leq 10^{-2}$.

The plasma will start to interact with the baryon shell once it reaches $r_{\rm in}$. The collision process considered in Ruffini et al. (2000) happens between the two radii r_1 and r_2, where $r_{\rm in} + \Delta > r_2 > r_1 > r_{\rm in}$. The mass acquired by the plasma is then the one enclosed by these two radii. This interaction is described using the following assumptions: the geometry of the plasma does not change during the interaction, the collision is inelastic and the baryonic matter reaches thermal equilibrium with the photons and pairs within the plasma. These assumptions are generally valid for a certain range of parameters: Lorentz factor needs to be high ($\gtrsim 100$), baryon load needs to be low ($B < 10^{-2}$) and the ratio between the comoving number density of pairs and that of baryons needs to be greater than 10^6. For $B \geq 10^{-2}$, the expansion after collision becomes much more complex and the constant-thickness approximation can no longer be applied.

After the collision, for distances larger than $r_{\rm in} + \Delta$, the baryons are a part of the fireshell. Further adiabatic expansion is described by the total baryon number, energy, and conversation of entropy (using a generalized set of equations derived in Ruffini et al. 1999). Pulse evolution depends only on $E^{\rm tot}_{e^+e^-}$ and B,

[6] This highly relativistic and sharply defined expansion of electromagnetic radiation is often termed as pair-electromagnetic (PEM) pulse (Ruffini et al. 1999; 2000; Bianco et al. 2001).

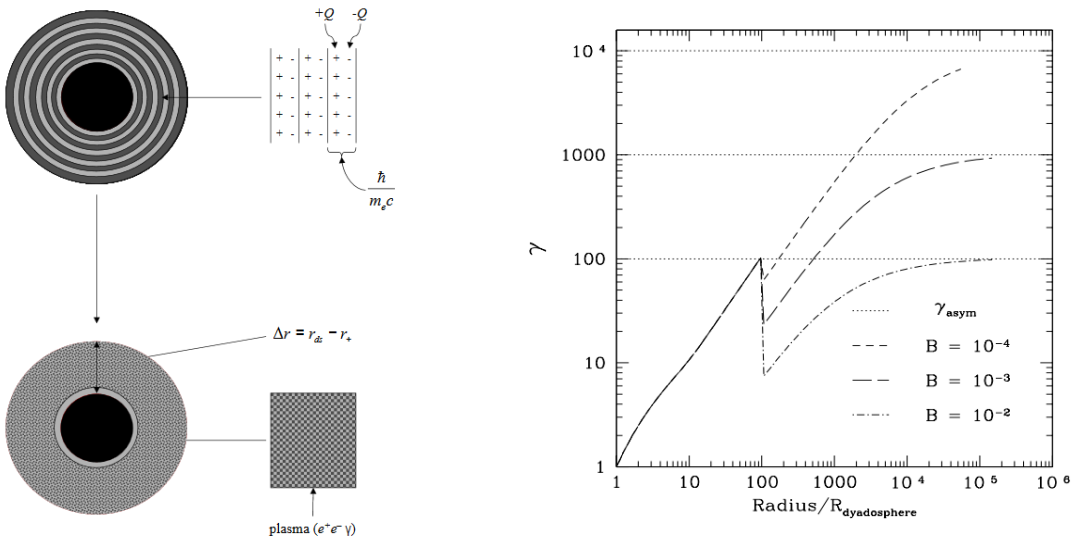

Figure 2.1. *Left panel:* Vacuum polarization process and e^+e^- pair creation within the indicated area of dyadosphere, which is modeled as a series of thin capacitors. Figure reproduced from Ruffini & Vitagliano (2002). *Right panel:* The evolution of the Lorentz factor Γ (γ on the plot) as a function of radius (in units of $r_{\rm ds}$) for a typical case of EMBH of $M = 10^3 M_\odot$). The three examples are plotted for different values of the baryon load B. The starting point corresponds to the initial free expansion of the plasma while the end point marks the moment when the transparency condition has been reached. The asymptotic values of $\gamma_{\rm asym}$ for each baryon load are also indicated. Figure reproduced from Ruffini et al. (2000).

and is reasonably independent on the exact location of the baryonic remnant (Ruffini et al. 2003). As a consequence of the plasma-baryon interaction, the comoving internal energy will rise. This will lead to an increase of opacity due to the increased number of pairs (Ruffini et al. 2000; 2003). The system will reach the thermal equilibrium in a very short time $\lesssim 10^{-12}$ s (Aksenov et al. 2007). Right panel in Figure 2.1 depicts the Lorentz factor evolution as a function of radius (in $r_{\rm ds}$ units) up to the transparency point. It can be seen that the Lorentz factor suddenly decreases at the moment in which the plasma encounters the baryons. The drop depends on B. For $B < 10^{-5}$, the influence of baryons on the expansion dynamics is negligible (e.g., see Aksenov et al. 2008). After the collision, the Lorentz factor Γ will continue to rise as the plasma energy is transferred to the bulk kinetic energy of the baryons. The Lorentz factor corresponding to a complete energy transfer is also plotted in Figure 2.1 on the right, with a value of

$$\gamma_{\rm asym} = \frac{E^{\rm tot}_{e^+e^-}}{M_{\rm B}c^2}. \tag{2.9}$$

Proper GRB emission

Baryons and the e^+e^- plasma will continue to expand until the transparency condition is reached. However, at the point of transparency, the closer the value of Γ is to the asymptotic value $\gamma_{\rm asym}$, the smaller is the intensity of the radiation emitted by the burst (due to the larger amount of energy transferred to the baryons). For a given EMBH mass, Γ at the point of transparency has a maximum value for a certain

amount of baryonic mass. For a larger mass, it starts to decline, getting closer to its asymptotic value. This means that the energy available to escape at the transparency point is also declining with the increase of the baryon load (e.g., see Figure 9 in Ruffini et al. 2000). For baryon loads exceeding the 10^{-2} limit, the amount of energy released at the transparency is very small, meaning that the constant-thickness approximation is valid for the majority of relevant situations (Ruffini et al. 2000).

When the expanding plasma cools down enough, the $2\gamma \rightarrow e^+e^-$ processes will stop. The last of the pairs will then annihilate and the plasma will become transparent. The transparency condition is

$$\int_R dr\,(n_{e^\pm} + \bar{Z}_{N_B})\,\sigma_T \approx 1, \tag{2.10}$$

where $\bar{Z}$ is the average number of electrons per baryon. For a smaller baryon load, there will be less baryon associated electrons and the transparency will be reached earlier (with a larger amount of energy released via escaping photons). One way or another, once this condition is fulfilled, the escaping photons will carry away all the "leftover" energy given by the difference between the Lorentz factor at the transparency and its asymptotic value given by Eq. 2.9. The escaped flash of radiation is called the P-GRB (proper GRB Ruffini et al. 1999; 2000; Bianco et al. 2001; Ruffini et al. 2003). Since the plasma was in thermal equilibrium, the spectrum is generally described by a single thermal component.

These expectations apply in the case of a simplified assumption that has been used so far, the one of a spherically symmetric dyadosphere. However, a different spectrum can be observed due to the geometrical effects of the radiating region, the fireshell, which shape is in return dictated by the geometry of the pair-creating region, the dyadotorus. The dyadotorus emerges when Kerr-Newman geometry is considered, instead of the non-rotating, charged BH. Cherubini et al. (2009) showed that the pair-creating region of a Kerr-Newman BH becomes axially symmetric, in a similar manner the ergosphere does (e.g., see Wiltshire et al. 2009). This region is characterized with a specific distribution of e^+e^- pairs, its own magnetic field, and can be described in terms of the polar angle. Instead of a purely thermal spectrum, as in the case of the dyadosphere, the spectrum of an axially symmetric dyadotorus is a convolution of thermal spectra of different temperatures. The expected temperatures are then a function of the polar angle. Final spectral shape resembles a power-law energy distribution with an exponential cutoff (i.e., COMP(E), see Section 1.3). In this case, the evolution of the baryon-load plasma is governed by three parameters: the e^-e^+ plasma energy, the baryon load, and the angular momentum of the newly formed BH (e.g., see Ruffini et al. 2016a). In addition, a multiple inverse Compton scattering (e.g., Felten & Rees 1972) can modify the spectrum (for details, see Bianco et al. 2001).

Therefore, without disregarding the BH case in question (or the way it initiates the vacuum polarization), the initial energy of the fireshell is now divided between the energy of the P-GRB and baryons, which will continue to expand in a ballistic manner and collide with the CBM. The larger the baryon load, the larger is the portion of $E^{\rm tot}_{e^+e^-}$ that gets carried away by the baryons instead of the photons, and vice versa.

2.4 EQUITEMPORAL SURFACES AND INTERACTION WITH THE CBM

After P-GRB, the expanding shell of baryons and remaining leptons will encounter the CBM at $r \sim 10^{17}$ cm. This interaction will slow down the shell and produce the classical, prompt emission. Since the emitting region is expanding at ultra-relativistic speeds, the photons with the same detector-arrival time will come from different times and different positions on the expanding fireshell sphere. This has to be taken into account when modeling the light-curve and the spectrum as seen by the detector. Thus, the process of obtaining the observable quantities of GRBs, from their prompt radiation properties to their spectral

distribution, essentially depends on the definition and calculation of equitemporal surfaces (EQTSs); areas of fireshell which emit photons with the same detector-arrival time (e.g., Ruffini et al. 2002). In 2004, Bianco & Ruffini numerically computed the exact EQTSs for GRB afterglows by integrating Taub equations.

Relativistic hydrodynamic equations introduced by Taub (1948) are now generally accepted as a tool for describing the GRB phenomena. More precisely, Taub equations have been used to describe the adiabatic, optically thick expansion phase in GRBs (Meszaros et al. 1993; Bisnovatyi-Kogan & Murzina 1995; Ruffini et al. 1999) and can be used to describe the ultra-relativistic baryonic matter and its interaction with the CBM. Therefore, these equations provide a framework within which the GRB emission can be explained. In this context, they are in the form of (Blandford & McKee 1976; Piran 1999; Ruffini et al. 2003):

$$dE_{\rm int} = (\gamma - 1)\, dM_{\rm CBM} c^{2,} \tag{2.11}$$

$$d\gamma = -\frac{\gamma^2 - 1}{M}\, dM_{\rm CBM}, \tag{2.12}$$

$$dM = \frac{1-\epsilon}{c^2}\, dE_{\rm int} + dM_{\rm CBM} \tag{2.13}$$

$$dM_{\rm CBM} = 4\pi m_p n_{\rm CBM} r^2 dr, \tag{2.14}$$

where $E_{\rm int}$ is the internal energy of the shell, γ is the Lorentz factor, M is the mass-energy of the expanding pulse, $n_{\rm CBM}$ is the CBM density, m_p is proton mass and $M_{\rm CBM}$ corresponds to the amount of CBM swept up within the radius r: $M_{\rm CBM} = \frac{4}{3}\pi(r^3 - r_\circ^3) m_p n_{\rm CBM}$, where $r_\circ$ is the initial radius of the shock front. The emitted fraction of energy from the collision with the CBM is labeled ϵ and assumed constant[7].

Bianco & Ruffini (2004) used Eqs.2.11–2.14 in order to compute EQTSs. The profile of the EQTS surface for some time t_a at which the photons arrive at the detector can be expressed as $\vartheta = \vartheta(r)$. It can be found by using the equation

$$c\, t_a = ct(r) - r\, cos\vartheta + r^\star, \tag{2.15}$$

where $r^\star$ is the initial size of the expanding source and ϑ is the angle between the radial expansion velocity of a surface point and the line of sight. Function $t(r)$ is the equation of motion in the laboratory frame and is obtained by integrating Eqs.2.11–2.14. These equations are also used to evaluate the dependence of the Lorentz gamma factor on radius, $\gamma(r)$, so that following equation can be used

$$c\, t = \int_0^r dr\, [1 - \gamma^{-2}(r)]^{-1/2}, \tag{2.16}$$

which is derived from the definition of the Lorentz gamma factor $\gamma^{-2} = 1 - (dr/cdt)^2$.

Blandford & McKee (1976) also solved Taub equations by using the so-called "ultrarelativistic" approximation: $\gamma_\circ \gg \gamma \gg 1$, where $\gamma_\circ$ is the initial value of the Lorentz gamma factor of the shock front. A simple power-law relation follows from this approximation and it has been used in the current literature: $\gamma \propto r^{-\alpha}$, where $\alpha = 3$ ($\alpha = 3/2$) corresponds to the fully radiative (adiabatic) case, with $\epsilon = 1$ ($\epsilon = 0$). However, Bianco & Ruffini (2004) compared these results with their own, obtained by integrating the Taub equations, as explained above. They found that the power-law solution does not hold for any finite region of the afterglow, i.e., α reduces to 0 for the early and late phases of the afterglow. Additionally, the values in-between were found to be smaller than values predicted for a fully radiative and adiabatic case, $\alpha = 3$ and $\alpha = 3/2$, respectively.

[7] Generally, additional conditions are needed to determine ϵ since it is a function of radial coordinate: $\epsilon(r)$.

This affects the calculation of EQTS, where $\gamma \propto r^{-\alpha}$ is commonly used to evaluate Eq. 2.16 (with some further approximations which neglect the earliest parts of the afterglow, e.g., see Ruffini et al. 2001b; 2002). Bianco & Ruffini (2004) found that both of the current approximate treatments of adiabatic and fully radiative expansion currently available in literature (Sari 1998; Panaitescu & Mészáros 1998; Granot et al. 1999a) overestimate the size of the EQTS for the early times of the afterglow, and underestimate it for the late times. A short time after, Bianco & Ruffini (2005b) derived exact analytic expressions of the EQTS that could be applied to any value of the Lorentz factor[8]. The expressions were compared both to the previous numerical integration in Bianco & Ruffini (2004) (which they validate) and to the current expressions used by Sari (1998) and Panaitescu & Mészáros (1998) (reaching the same conclusion as in Bianco & Ruffini 2004). These conclusions were again validated and re-examined in more detail in Bianco & Ruffini (2005a).

Similar basic assumptions as in Section 2.3 were adopted in order to describe the collisions with the CBM (Ruffini et al. 2003): the width of the baryonic shell does not change in the laboratory frame, the energy is emitted instantaneously (fully radiative regime with $\epsilon = 1$), collisions are inelastic, and lastly, CBM shells are cold (have negligible internal energy) and at rest with respect to the EMBH. The interaction is modeled with a large number of thin CBM shells of thickness Δr ($\sim 10^{15}$ cm) and mass $M_{\rm CBM}$, located between r_1 and r_2, where $r_2 - r_1 = \Delta r \ll r_1$. In the limit of infinitesimally thin shells, one obtains Eqs. 2.11–2.14. The dynamics of the system is given by the following solution:

$$\gamma = \frac{1 + (M_{\rm CBM}/M_{\rm B})(1+\gamma_\circ^1)[1 + (1/2)(M_{\rm CBM}/M_{\rm B})]}{\gamma_\circ^{-1} + (M_{\rm CBM}/M_{\rm B})(1+\gamma_\circ^1)[1 + (1/2)(M_{\rm CBM}/M_{\rm B})]} \tag{2.17}$$

which precisely governs the shell's dynamics, depending on engulfed CBM mass, baryon mass $M_{\rm B}$ and the initial Lorentz factor $\gamma_\circ$. Each peak in the prompt light-curve is produces by an interaction with one shell. Evolution of the Lorentz factor, from the beginning of the fireshell expansion, is showed in Figure 2.2.

The observed spectrum at any point in time will then be a convolution of all the spectra produced at the corresponding EQTS. Emission in the fireshell model, caused by the increase of internal energy due to collisions, is assumed to be thermal, radiated away instantly and isotropically (opposed to the synchrotron emission in the fireball model, e.g., see Piran 2004). Spectrum is then modeled while keeping in mind the CBM distribution (obtainable from the light-curve, see Section 3.1), evolution of the temperature with time, and EQTSs. The final product is a non-thermal, COMP-like spectrum (Ruffini et al. 2004; Bernardini et al. 2005), similar to the ones usually observed in GRBs (Section 1.3). However, the theoretically predicted, pure-thermal emission in the comoving frame could not explain the intensity of the low-energy spectral region observed in some GRBs (e.g., GRB 080319B and GRB 050904). For this reason, a modified thermal spectrum was introduced, characterized by a phenomenological parameter α which changes the lower-energy slope of the BB spectrum (Patricelli et al. 2012), such that

$$\frac{1}{h}\frac{dN_\gamma}{dV\,d\nu} = \left(\frac{8\pi}{c^3 h}\right)\left(\frac{h\nu}{kT}\right)^\alpha \frac{\nu^2}{\exp(h\nu/kT) - 1}. \tag{2.18}$$

where h is the Planck constant and N_γ is the photon number density per unit energy. The value of α, determined in the fitting process, remains constant throughout the burst (see Section 3.1). This means that changing the spectrum integration time (or equivalently, changing the number of different comoving spectra which are convolved into the observed one), while keeping α constant, still produces the correct time-resolved spectrum (Patricelli et al. 2012). The observed HTS $E_{\rm p}$ evolution (Section 1.3) can then be explained as a consequence of the comoving temperature that decreases with time and the bulk Lorentz factor. The curvature effect, originating in EQTSs, amplifies this effect by producing the observed time lag

[8] However, the thin-shell approximation, used when deriving these formulas, is no longer correct as the shell approaches a non-relativistic (Newtonian) phase.

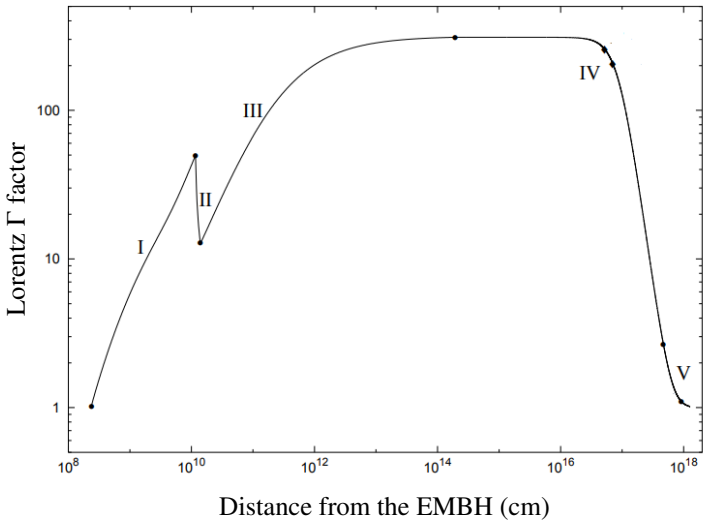

Figure 2.2. Theoretically computed Lorentz gamma factor for GRB 991216 (here marked as Γ) as a function of radial coordinate in the laboratory frame, assuming $E^{\rm tot}_{e^+e^-} = 4.83 \times 10^{53}$ erg and $B = 3 \times 10^3$. The points mark the beginning and the end of each stage of the fireshell expansion, which are: free e^+e^- plasma expansion (I), baryon encounter (II), further expansion and P-GRB emission at the point of transparency at $\sim 10^{14}$ cm (III), interaction with CBM (IV) and deceleration of baryons to a non-relativistic regime with emission in longer wavelengths (V). Figure reproduced from Ruffini et al. (2003).

in the majority of GRBs. For $\alpha = 0$, the Eq. 2.18 reverts back to the pure thermal case. This emission is different from the photospheric one (see Section 1.4), caused by the e^+e^- plasma annihilation. Here, the emission originates in an optically thin regime, from the interactions between the baryons and the CBM. It is also important to note that the extra power-law component is not necessarily related to the low-energy extrapolation of the high-energy component (> 100 MeV) discussed in Section 1.2 (e.g., Hurley et al. 1994; Abdo et al. 2009b; Ackermann et al. 2010a; 2011), since a non-zero value of α was also found in GRBs with no evidence of high-energy emission (e.g., Izzo et al. 2012b; Penacchioni et al. 2012).

The same mechanisms were believed to be responsible for the afterglow at longer wavelengths. When the Lorentz factor drops to relativistic speeds (see Figure 2.2), the peak of the spectrum will shift to lower energies. The light-curve will no longer have the erratic, spiky behavior it had in the gamma-ray band. However, recent results of Ruffini et al. (2018a) and Wang et al. (2019) suggest that X-ray and optical afterglows of long GRB 130427A and GRB 180728A originate from the synchrotron emission of relativistic electrons injected into the magnetized plasma of the hypernova. Synchrotron emission of CBM electrons, accelerated by the SN shockwave, was also used to explain the precursor that can sometimes be seen in the GRB light-curves. Accelerated protons emitting synchrotron radiation were also later invoked in order to explain the high GeV emission and UHECRs. These considerations have been used within the context of the binary-driven hypernova model, which is the central topic of the following Sections 2.6–2.9.

2.5 LONG AND SHORT BURSTS WITHIN THE FIRESHELL MODEL

As it was explained in Section 1.1, GRBs are phenomenologically classified on long (> 2 s) and short (< 2 s) bursts based on their duration in gamma-rays (Kouveliotou et al. 1993). In Section 1.2, the third class with hybrid properties was mentioned, the so-called Norris-Bonnell sources (Norris & Bonnell 2006). Their observed gamma-ray emission consists of an initial hard pulse, characteristic for short GRBs, followed by a long-duration soft tail (~ 100 s).

The fireshell model attributes the observed prompt-emission properties, including the duration, to values of the baryon load B and the average CBM density $\langle n_{\rm CBM}\rangle$ (Ruffini et al. 2002; 2004; 2005b, see Figure 2.3). Here, all bursts originate from the same inner engine. the dyadosphere (dyadotorus), created by a newly formed BH. That the most of short GRBs, in general, have weaker afterglows is explained by the high ratio of the P-GRB to total energy, caused by the low amount of baryons surrounding the central engine. Accordingly, gamma-ray bursts were initially divided into three[9] classes:

LONG GRBs The canonical long GRBs are characterized with the values of baryon load in the $10^{-4} \lesssim B \lesssim 10^{-2}$ range. The average values of CBM density $\langle n_{\rm CBM}\rangle$ are the ones typically found in inner-galaxy regions, namely 1 particle/cm^3 or more. Emission following the P-GRB is the dominant one in these bursts, which correspond to the typical long GRBs.

GENUINE SHORT GRBs On the other end of the baryon load scale ($B \lesssim 10^{-5}$), a genuine short GRBs will occur. In this case, the P-GRB will be the predominant part of the emission during which most of the energy will be emitted (characterized with a significant thermal-like emission). In the limit of $B \to 0$, only the P-GRB emission is expected. Still, since the baryon load is small but non-zero, a low-intensity non-thermal component from the baryon-CBM interaction can be observed. The typical separation between these two components is expected to be $\sim 10^{-3}$–10^{-2} s. Because of the low baryon load, the CBM densities do not play a significant role here. Bursts with these properties correspond to typical short GRBs. The search for short GRBs without a prominent afterglow emission yielded the discovery of GRB 090227B within *Fermi* catalog data (Muccino et al. 2013a). The spectral analysis identified this source as a genuine short GRB with some mixed properties in terms of its position on plot showed in Figure 2.3 (left panel).

DISGUISED SHORT GRBs The disguised short bursts have the same baryon load as the long ones but they occur in environments far less dense, with values of $\langle n_{\rm CBM}\rangle \approx 10^{-5}$–$10^{-2}$ particle/cm^3 (typical of galactic halos). As a consequence, their prompt emission, instead of being compact and energetic, is spread over a much longer period of time. Therefore, it can be often exceeded by the P-GRB emission (peak-luminosity vise), which leads to the already mentioned behavior in the form of the initial hard pulse followed by a long duration soft tail, as seen in the Norris-Bonnell sources (Bernardini et al. 2007; 2008; Caito et al. 2009; 2010).

If $10^{-5} \lesssim B \lesssim 10^{-4}$, the classification depends on the value of $E^{\rm tot}_{e^+e^-}$. Due to the origin of the explosion, both short and disguised short GRBs were perceived as ones originating from binary mergers. From this, it followed that the long and the disguised short GRBs should also be observed in different galactic environments: long GRBs in galactic disks and short GRBs in the outskirt of their host galaxies. This prediction has been directly supported by optical observations (e.g., Sahu et al. 1997; Bloom et al. 2006; Fong et al. 2010; Kopač et al. 2012). A more extensive sub-classification that was developed in the following years (both for long and short GRBs, e.g., Ruffini et al. 2016b; Rueda et al. 2018; Wang et al. 2019; Rueda et al. 2019a;b) is presented in the following section.

[9] The induced gravitational collapse paradigm extends this division to multiple subclasses, see Section 2.6 and after.

2.6 SN CONNECTION AND THE IGC PARADIGM

The association between long GRBs and energetic type Ic SNe, already discussed in Section 1.2 and Section 1.5, has been known for more than 20 years (Galama et al. 1998). In the collapsar model, these two events originate from a single star. The induced gravitational collapse (IGC, Izzo et al. 2012a;b) paradigm was introduced as an extension to the fireshell model. In contrast to the standard fireball/collapsar model, it takes into account that type Ic SNe mostly occur in double systems (Panagia & Laidler 1988; Smartt 2009; Smith et al. 2011) and investigates the effects of this interaction on the GRB emission mechanism. The starting point of the IGC scenario is a binary system composed of a NS and a carbon-oxygen core (CO_{core}) on the verge of a SN explosion[10] (e.g., see Nomoto et al. 1994; 1995; Fryer et al. 1999a). The CO_{core} (with $R_{core} \sim 10^7$–10^9 cm, Becerra et al. 2015; 2016; 2019) undergoing SN will leave behind a new NS (νNS) and trigger the hypercritical accretion of the SN ejecta onto its companion (the primary NS). While the fireball model considers the accretion on the newly formed BH, in the IGC model the accretion onto a companion NS is the process that (possibly) leads to a BH formation. Properties of the observed emission, and thus the type of GRB that will be detected, depend on the binary system parameters. These in return dictate the accretion rate and the out-states of the system. As a result, long GRBs were divided into the following binary-driven hypernova (BdHN) subclasses (Ruffini et al. 2006; Izzo et al. 2012a; Rueda & Ruffini 2012; Becerra et al. 2015; Wang et al. 2019):

X-RAY FLASHES If the accretion rate of the SN ejecta is not high enough to bring the NS mass to its critical value ($< 10^{-2}\ M_\odot\ s^{-1}$), no BH will be formed. This usually occurs for CO_{core}-NS binaries with a relatively large separation ($a \gtrsim 10^{11}$ cm). For typical NS masses considered in Becerra et al. (2015) and Becerra et al. (2016), this separation translates to orbital periods larger than $P \sim 5$ min. The value of P_{max} increases for lower values of the critical mass of the NS, i.e., it depends on the adopted equation of state. The out-state of the binary will consist of two NSs that may or may not remain bound, depending if the system was disrupted or not. The radiated energy E_{iso} will be $\sim 10^{52}$ erg or less, leading to the detection of a low-luminous X-ray flash (XRF, see Section 1.2 and Figure 2.3 - right panel). In the work of Wang et al. (2019), this subclass was renominated and further divided into BdHNe-II and BdHNe-III, based on the observed energy (see Table 1). The rest-frame spectral peak energy is soft, in the range of $2 \lesssim E_{p,i} \lesssim 200$ keV. They are observed to be in the relative proximity, up to redshifts of $z \lesssim 1$.

BINARY-DRIVEN HYPERNOVAE If the binary separation a is instead $\lesssim 10^{11}$ cm ($P \lesssim 5$ min), the SN explosion will trigger a large accretion rate onto the NS companion ($\gtrsim 10^{-2}$–$10^{-1}\ M_\odot\ s^{-1}$, Becerra et al. 2015; 2016) and bring the NS to the point of gravitational collapse. This system and the described process, which results in a νNS and a BH with observed energies $E_{iso} \gtrsim 10^{52}$ erg, is termed BdHN-I (see Figure 2.3 - right panel). The BdHNe-I energetics will depend on the initial mass of the NS (Becerra et al. 2016). Peak spectral energies are higher than XRFs and are detected in the range of $0.2 \lesssim E_{p,i} \lesssim 2$ MeV. The structure of the prompt and afterglow emission is also more complex than the one found in XRFs (see Section 2.8). Ultra-long GRBs (Levan et al. 2014; Boër et al. 2015) exhibit the same structure and are therefore considered to belong within the BdHNe-I subclass. BdHNe-I have been detected all the way up to $z = 9.3$ (GRB 090429B, Cucchiara et al. 2011).

Fryer et al. (2015) showed that due to their high compactness, a majority of type I BdHNe will remain bound. In typical systems, binaries become unbound due to the kick caused by the SN explosion. The number of systems that remain as binaries is thought to be low, up to 1% (Fryer et al. 1999a; Postnov & Yungelson 2014). If one adopts the instantaneous mass-loss assumption, the

[10] Due to the lack of both the hydrogen and the helium shell of the secondary star, these systems are also called the *ultra-stripped* binaries. They make up < 1% of the total SNe (Tauris et al. 2013; 2015).

system will become disrupted if it loses 50% of its initial mass (for circular orbits). With the ejected mass, the orbit of the system becomes too wide and eccentric to remain sustainable. However, two effects come into play for the case of BdHNe-I. For normal binaries, which have much wider orbit, the instantaneous mass-loss assumption is valid. The accretion peaks when the slow-moving part of the ejecta (10^2 km/s) passes the NS companion. The time needed for this to happen is around 10–1000 s. In the BdHNe-I, the accretion process can form a BH within a time period as short as the orbital period. In that case, the instantaneous mass-loss assumption is no longer valid. The system will remain bound as long as the explosion time is comparable with the orbital period, even in the case where 70% of the mass has been lost (Fryer et al. 2015). In addition, efficient accretion due to the tight BdHNe-I orbit reduces the mass and momentum loss.

BH-SN BINARIES Considering other possible combinations that can occur in compact object systems, a CO_{core}-BH binary can also exist. In this case, the accretion process will only result in a more massive BH. The end state composed of a νNS and a BH (named BdHN-IV) was first considered in Ruffini et al. (2016b) as a subset of BdHNe, with energies $E_{iso} \gtrsim 10^{54}$ erg.

Therefore, in the IGC/BdHNe model, the SN explosion does not directly result in a BH creation as it does in the collapsar model. It only provides the means for a possible collapse of its binary NS companion. This means that the IGC paradigm does not suffer from the metallicity problem regarding the BH formation as the collapsar model does (see Section 1.4). Although this sequence of events may seem unlikely due to the initial conditions that need to be fulfilled, it is consistent with the population synthesis presented by Fryer et al. (1999a) and Fryer et al. (2015). This model also supports the conclusion outlined in Section 1.2: XRFs, XRGRBs, and long GRBs form a smooth continuum and are a part of the same population (Sakamoto et al. 2005). The shorter the binary period is, the larger is the accretion rate, which is correlated with E_{iso} and E_p.

The hypercritical accretion rates discussed above refer to the accretion rates which are highly super-Eddington[11]. The accretion rates which exceed the Eddington limit are allowed due to a very efficient neutrino emission (triggered by a very hot NS atmosphere) which acts as the main energy sink (Zel'dovich et al. 1972; Fryer et al. 2014). Becerra et al. (2016) showed that for the accretion rate of $\sim 10^{-4}$–$10^{-2}\ M_\odot\ s^{-1}$ (characteristic for the IGC paradigm), pair annihilation dominates the neutrino emission out of all other production processes. The neutrino mean energy can reach values up to $\sim$ 20–30 MeV, depending on the accretion rate. Neutrinos, emitted above the NS surface, will then remove most of the gravitational energy gained by accretion and allow the material to be incorporated to the NS (see also Becerra et al. 2018).

That short GRBs originate from binary systems is not a novelty among the GRB community (e.g., see Eichler et al. 1989; Narayan et al. 1992; Berger 2014a). However, when it is considered with the IGC paradigm, it follows that the characteristics of both long and short GRBs can be attributed to their binary system properties. In Ruffini et al. (2016b), and later in Rueda et al. (2018) and Rueda et al. (2019b), short GRBs were divided into five different binary merger (BM) subclasses based on their initial components and the final outcome of their inspiral:

SHORT GAMMA-RAY FLASHES If a post-merger core of two NSs does not surpass the NS critical mass, a short gamma-ray flash (S-GRFs) is expected to occur, with $10^{48} \lesssim E_{iso} \lesssim 10^{52}$ erg (Zhang et al. 2012; Calderone et al. 2015; Ruffini et al. 2015b). These bursts are also termed BM-I bursts. The result will be a massive NS (MNS) and, possibly, an orbiting disk-like structure due to the energy and angular momentum conversation (e.g., also see Berger 2014b). The prompt emission duration is expected to be a function of the NS masses. Although energies of S-GRFs are similar to those of XRFs, their spectra are much harder, with $0.2 \lesssim E_{p,i} \lesssim 2$ MeV. There is no BH formation, but still the creation of pair plasma occurs via $\nu\bar{\nu} \rightarrow e^+e^-$ process (Salmonson & Wilson 2002;

[11]Above the Eddington limit, the radiation pressure forces exceed the gravitational attraction, blowing away the accreting gas.

Rosswog et al. 2003). The maximum extractable energy is $\approx 10^{52}$ erg, which sets the upper energy limit for this subclass. Therefore, a general treatment introduced in the fireshell model can still be applied. Ruffini et al. (2015b) demonstrated that S-GRFs fulfill the $E_{\rm p,i}$-$E_{\rm iso}$ relation introduced by Zhang et al. (2012) and Calderone et al. (2015).

AUTHENTIC SHORT GAMMA-RAY BURSTS If a post-merger core of the NS-NS inspiral reaches or surpasses the critical NS mass, the Kerr-Newman BH will be formed (e.g., Ruffini et al. 2015b). The energy of these authentic short GRBs (S-GRBs) is expected to be in the interval $10^{52} \lesssim E_{\rm iso} \lesssim 10^{53}$ erg (e.g., Muccino et al. 2013a; Calderone et al. 2015; Ruffini et al. 2015b). The observed spectra are the hardest among the given subclasses, with $2 \lesssim E_{\rm p,i} \lesssim 8$ Mev and it obeys the $E_{\rm p,i}$-$E_{\rm iso}$ relation as the S-GRFs. A faint precursor can sometimes be observed. It is believed to originate in the NS-NS merger activity that precedes the BH creation (Troja et al. 2010; Ruffini et al. 2016a). As in other short GRBs, the P-GRB and the prompt emission duration is expected to be correlated to the NS masses. These bursts were termed BM-II in the work of Wang et al. (2019).

GAMMA-RAY FLASHES In the work of Caito et al. (2009), a merger of a WD and a NS was considered. This inspiral should result in a MNS and a release of energy ($10^{51} \lesssim E_{\rm iso} \lesssim 10^{52}$ erg) in the form of a gamma-ray flash (GRF, or type BM-III). These flashes correspond to the disguised short GRBs described in Section 2.5 (the Norris-Bonnell sources, Norris & Bonnell 2006), which occur in a low-density CBM medium ($\sim 10^{-3}$ cm^{-3}). No SN was associated with these bursts in the literature, despite their observed proximity (e.g., Fynbo et al. 2006; Gal-Yam et al. 2006; Ofek et al. 2007). The prototype of these systems is GRB 060614 (Della Valle et al. 2006). The fireshell model can still be applied in the same manner as in the case of S-GRFs. The WD-NS systems and their mergers are fairly common (Tauris et al. 2000; Lazarus et al. 2014; Cadelano et al. 2015), but they can also be produced as an outcome of an inspiral that drives the S-GRFs (e.g., Bildsten & Cutler 1992). Although their initial spike also fulfills the $E_{\rm p,i}$-$E_{\rm iso}$ relation (with $0.2 \lesssim E_{\rm p,i} \lesssim 2$ MeV), they are separated from other short subclasses by their fairly high baryon load ($B \sim 10^{-3}$ cm^{-3}) and the possible presence of the macronova emission (e.g., GRB 060614, Jin et al. 2015).

FALLBACK-POWERED KILONOVAE This GRB subclass was introduced in Rueda et al. (2018) and Rueda et al. (2019b), characterized with energies $\lesssim 10^{51}$ erg and $E_{\rm p,i} \lesssim 0.2$ MeV. The progenitors of this class are the WD-WD mergers that lead to a massive, fast rotating, highly magnetized WD. Since the fallback of the expelled ejecta onto a newly-formed massive WD is expected to produce an infrared-optical transient, these sources are named fallback-powered kilonovae (FB-KNe, or BM-IV in the newer nomenclature). The optical/IR emission comes from the adiabatic cooling of the merger ejecta, heated by the fallback accretion. This mechanism therefore differs from the one responsible for the classical KNe originating from the NS-NS mergers.

ULTRA-SHORT GRBS Due to the compactness of their orbits, nearly 100% of BdHNe-I will remain bound (Fryer et al. 2014). An eventual merger of their out-states is therefore imminent (Fryer et al. 2015), with expected $E_{\rm iso} \gtrsim 10^{52}$ erg. It defines a new subclass of bursts, called ultra-short GRBs (U-GRBs, or equivalently, BM-V). The merger time is typically 10,000 years or less. For a particular set of parameters, namely long explosion times ($T_{\rm explosion}/T_{\rm orbit} = 2$) and a small ejected masses ($\leq 3.5 M_\odot$), the U-GRB may be observed in coincidence with BDHN-I within a human lifetime. Due to the prior evolution of the system within the IGC paradigm, the baryonic contamination is expected to be small. The U-GRBs can also be produced by a BdHN-IV merger.

Therefore, instead of a phenomenological GRB classification based on their duration, the IGC paradigm, together with Ruffini et al. (2015a;b; 2016b) and Rueda et al. (2018; 2019b), proposes a physical classification of GRBs based on the binary nature of their progenitors. Here, (some) short GRBs are produced during the late evolutionary stages of binary systems that, at one point in time, gave rise to long GRBs.

For example, the emission of gravitational waves will eventually lead to a merger of νNS-NS or νNS-BH binaries. Less than 4% of BdHNe-II/III is sufficient to explain the BM-I population (S-GRFs). This is consistent with the fact that many of these systems will not remain bound after the SN explosion. The full list of subclasses and their occurrence rates can be found in Table 1. Within this classification, the term *burst* is used for systems which result in a BH formation, and the term *flash* for systems which do not. The general description of all subclasses can be found in Ruffini et al. (2016b) and Rueda et al. (2019a).

GRB subclass	Number	In-state	Out-state	$E_{\rm iso}$ (erg)	$E_{\rm p,i}$ (MeV)	$\rho_{\rm GRB}$ ($\rm Gpc^{-3}yr^{-1}$)
BdHN-I (BdHN)	329	$\rm CO_{core}$-NS	νNS-BH	$\sim 10^{52}$–10^{54}	$\sim$ 0.2–2	$0.77^{+0.09}_{-0.08}$
BdHN-II (XRF)	(30)	$\rm CO_{core}$-NS	νNS-NS	$\sim 10^{50}$–10^{52}	$\sim$ 0.01–0.2	100^{+54}_{-34}
BdHN-III (HN)	(19)	$\rm CO_{core}$-NS	νNS-NS	$\sim 10^{48}$–10^{50}	$\sim$ 0.01	-
BdHN-IV (BH-SN)	5	$\rm CO_{core}$-BH	νNS-BH	$> 10^{54}$	$\gtrsim 2$	$\lesssim 0.77^{+0.09}_{-0.08}$
BM-I (S-GRF)	18	NS-NS	MNS	$\sim 10^{49}$–10^{52}	$\sim$ 0.2–2	$3.6^{+1.4}_{-1.0}$
BM-II (S-GRB)	6	NS-NS	BH	$\sim 10^{52}$–10^{53}	$\sim$ 2–8	$(1.9^{+1.8}_{-1.1})\times10^{-3}$
BM-III (GRF)	(1)	WD-NS	MNS	$\sim 10^{51}$–10^{52}	$\sim$ 0.2–2	$1.02^{+0.71}_{-0.46}$
BM-IV (FB-KN)	(1)	WD-WD	NS/MWD	$< 10^{51}$	< 0.2	$(3.7–6.7)\times10^{5}$
BM-V (U-GRB)	(0)	νNS-BH	BH	$> 10^{52}$	$\gtrsim 2$	$\approx 0.77^{+0.09}_{-0.08}$

Table 1. List of long (BdHNe) and short (MB) GRB subclasses, all of which originate from binary progenitors, The old nomenclature, used prior to Wang et al. (2019), is given within parentheses in column 1. For each subclass, the number of GRBs with known redshift up to the end of 2016 is given in column 2, where the value in the parentheses indicates the lower limit. Subclasses are differentiated by their in-states (column 3), out-states (column 4), energetics in the 1–10^4 keV rest-frame band (column 5) and $E_{\rm p,i}$ (column 6). Column 7 lists their occurrence rate, taken from Ruffini et al. (2016b), where the estimation was done assuming that no beaming is present. The occurrence rate for HN (BdHNe-III) subclass has not as yet been estimated. Taking into account their extreme luminosities, which can be as high as $\sim 10^{54}$ erg, GRBs can be detected in all 10^9 galaxies. Considering that in each galaxy they occur every $\sim$ 500 million years, this leads to the observed "once per day" rate. No member of the U-GRB subclass has been observed up to date. which is assumed to be due to the extremely short duration of these systems. Since they are thought to be an evolutionary outcome of BdHNe-I, their occurrence rate is approximated to be the same.

2.7 OVERVIEW OF THE IGC SIMULATIONS

Over the course of time, multiple simulations of the IGC process were performed. Each of them took a step further in order to realistically describe the binary system and its evolution. First 1D simulations of Fryer et al. (2014) can be described in three stages: the SN explosion of the $\rm CO_{core}$, the hypercritical accretion, and the evolution of the SN ejecta up to its incorporation into the NS. Here, the hypercritical accretion was computed within a spherically symmetric approximation. It confirmed the previous analytic results obtained by Rueda & Ruffini (2012): hypercritical accretion up to $10^{-1}\ M_\odot\ \rm s^{-1}$ is possible for tight binaries with orbital period on the order of 5 min. Planar simulations done by Becerra et al. (2015) implemented a series of additional refinements. For example, the angular momentum that is being transferred to the NS by the SN ejecta was estimated in order to see how it affects the evolution of the system. The pre-SN density profile of the $\rm CO_{core}$ envelope was introduced from numerical simulations, which followed a power-law with respect to radial distance. The expansion of the ejecta was assumed to be homologous. Homologous expansion can be described with the ejecta velocity that follows $v_{\rm ej}(r,t) = n\,r/t$, where r is the position of an ejecta layer from the SN center and n is the expansion parameter. For free expansion, adopted in

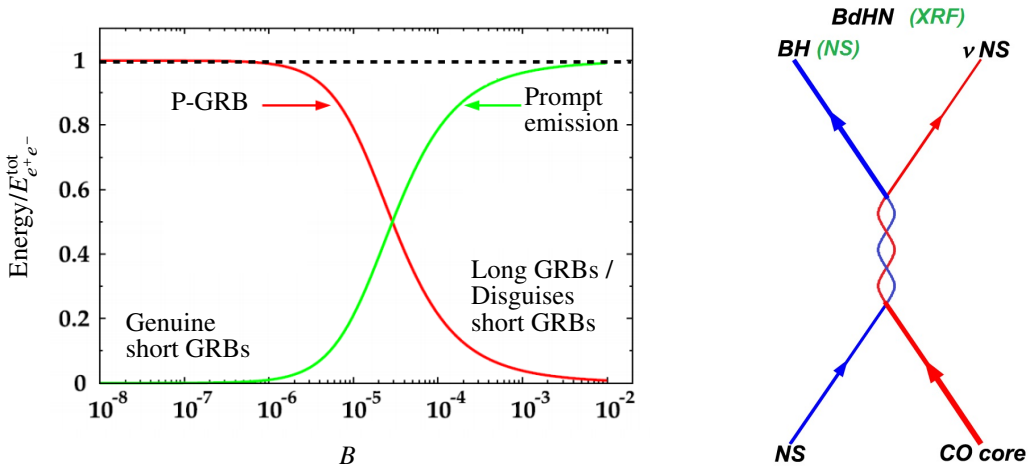

Figure 2.3. *Left panel:* The solid red line represents the energy emitted during the P-GRB phase while the solid green line shows the energy emitted in the emission following the P-GRB, with respect to the different values of baryon load B. The energy is in units of $E^{\rm tot}_{e^+e^-} = 1.77\times10^{53}$ erg (dashed horizontal line). GRBs at the crossing point will have their energy equally distributed between the P-GRB and the succeeding emission. Figure reproduced from Muccino et al. (2013a). *Right panel:* In- and out-states of binary systems for XRFs (green) and BdHNe. Figure reproduced from Ruffini et al. (2015a).

these simulations, $n = 1$. The consequent accretion rate was computed using the Bondi-Hoyle-Lyttleton[12] accretion formula. For typical initial conditions of the binary system (Fryer et al. 2014; Becerra et al. 2015), the obtained accretion rates were between 10^{-4} and 10^{-2} $M_\odot$ s^{-1}. The NS was assumed initially not to rotate, meaning that the space-time around it, at the beginning of the simulation, can be described with the Schwarzschild metric. For the parameters that describe the IGC system, the $r_{\rm st}/r_{\rm lso}$ was found to be $\sim$ 10–10^3, where $r_{\rm st}$ is the SN ejecta circularizing radius and $r_{\rm lso}$ is the last stable orbit. In other words, the ejecta has enough angular momentum to circularize for a short time and to form a disk around the NS. The viscous forces and other angular momentum losses will cause the matter in the disk to reach the $r_{\rm lso}$ and be accreted onto the NS. After this, the change in the NS central density and its spin-up can be calculated. The total angular momentum of the SN ejecta entering the Bondi-Hoyle region is much larger than the one that can be supported by a uniformly rotating NS ($\sim 10\, J_{\rm NS,max}$, Becerra et al. 2015), meaning that a part of it must be redistributed before the ejecta reaches the NS surface. Within the BdHNe, this leads to the creation of a BH with the initial dimensionless spin ~ 0.7 and the presence of a disk-like structure around the central object. This excess of the angular momentum can also lead to a jetted emission with a high-energy signature. Most importantly, the work of Becerra et al. (2015) demonstrated that there is a maximum orbital period $P_{\rm max}$ for which the accretion process is not high enough to result in a BH formation (consequently producing a BdHNe-II/III), as it was mentioned earlier.

[12]The accretion onto a point mass can be successfully modeled by the Bondi-Hoyle-Lyttleton solutions (BLH, Hoyle & Lyttleton 1939; Bondi & Hoyle 1944; Bondi 1952). The general picture of the BHL accretion consists of a point mass moving through a medium that is assumed to be uniform at infinity. The cloud is also considered to be free of self-gravity. Material passing within some critical radius will become bound and energetically obliged to the accretion by the star. Given the ejecta velocity relative to the NS $v_{\rm rel}$, and the sound speed $c_{\rm s,ej}$ of the SN ejecta, the critical (Bondi-Hoyle) radius can be calculated as $R_{\rm cap}(t) = \frac{2GM_{\rm NS}(t)}{v^2_{\rm rel}+c^2_{\rm s,ej}}$, where $M_{\rm NS}$ is the NS mass. The BLH solutions became widely used as a starting point for modeling accretion problems, with many numerical tests being available in the literature (e.g., Shima et al. 1985; Ruffert & Arnett 1994; Ruffert 1999). It had become fundamental for determining the final stellar mass (Bonnell et al. 1997; 2001). A historical review of the BHL accretion can be found in Edgar (2004).

The work of Becerra et al. (2016) introduced some further improvements. Parameter $P_{\rm max}$ was estimated for a variety of initial values of the NS mass and for different values of the angular momentum transfer efficiency. Different $CO_{\rm core}$ progenitors (leading to different masses of the SN ejecta) were also considered. An example of this simulation is shown in Figure 2.4. It can be seen that the presence of the NS is the cause of large asymmetries in the SN ejecta, which consequently lead to the observed characteristic signatures in X-rays and a possible obscuration of the prompt emission (see Section 2.8). Gravitational effects considered here include both the orbital motion and the changes in the NS mass as the accretion progresses with time. In order to represent the SN matter, these SPH-like (smoothed-particle hydrodynamics) simulations used point-like particles ($\sim 10^6$) with trajectories described by Newtonian equations of motions. The envelope had an initial power-law density profile, which was realized by populating the inner layers with more particles. This distribution was obtained assuming the homologous free expansion described earlier. Particles that reached the Bondi-Hoyle radius were removed from the system, since they would be captured and accreted by the NS. For highly efficient accretion rates, the random pressure exerted by the infalling material exceeds the magnetic field effects. Therefore, when describing the accretion process, the NS magnetic field effects were neglected. Here, the photons are trapped in the accretion flow and the gravitation energy is mainly radiated via electron-positron neutrino emission (e.g., see also Ruffini & Wilson 1973; Rueda & Ruffini 2012). In this way, a hypercritical accretion up to $10^{-1}\ M_\odot\ {\rm s}^{-1}$ can be achieved. The detection of these neutrinos is unlikely, due to the local BdHNe rate of $\sim 1\ {\rm Gpc}^{-3}\ {\rm yr}^{-1}$. A more detailed analysis of the neutrino emission was presented in Becerra et al. (2018). In addition, the material piling onto the NS and the atmosphere radius can create rising bubbles that emit a BB-shaped flux (Fryer 2009; Fryer et al. 2014). This can explain early thermal emission observed in some GRBs (see Episode 1 in Section 2.8). In that case, the temperature evolution can be used in order to determine how the radius of the bubble changes in time. Finally, a wide area of the binary parameter space was also explored in Becerra et al. (2019), by adapting the SPH code developed at Los Alamos (Fryer et al. 2006b).

The duration of the accretion process is determined by the flow time of the slowest (inner) layer of the SN ejecta. If $v_{\rm inner}$ is the velocity of these inner layers, then the accretion time Δt will be proportional to $a/v_{\rm inner}$. It was found that for small binary separations ($a \sim 10^{10}$ cm) the accretion process lasts around 100 seconds while for larger separations ($a \sim 10^{11}$ cm) it lasts around 1000 seconds (Becerra et al. 2015; 2016). The total energy released during this time is proportional to the rate at which the mass is accreted. More precisely, it is given by the difference of the accretion rate $\dot{M}_b$ and the NS mass gain $\dot{M}_{\rm NS}$, namely $L_{\rm acc} = (\dot{M}_b - \dot{M}_{\rm NS})\, c^2$ (Sibgatullin & Sunyaev 2000). Simulation showed that the BH collapse occurs for small binary separations ($\sim 10^{10}$ cm), as mention earlier. Energies released during this process were found to be larger than 10^{52} erg. This value separates the BdHNe-I from BdHNe-II/III (XRFs). It was obtained for a NS mass of 1.4 $M_\odot$ (typically observed in NS binaries, Zhang et al. 2011; Antoniadis 2015), which can reach a critical mass $M_{\rm crit}$ in the range of 2.2 $M_\odot$–3.4 $M_\odot$ (depending on the angular momentum and the equation of state). Since the same arguments can be applied to the NS-NS mergers, $E_{\rm iso} \approx 10^{52}$ erg also separates BM-I (S-GRFs) and BM-II (S-GRBs).

However, this limit is a function of the initial NS mass and the value of the critical mass it can reach (which in return depends on the particular equation of state). For example, if the NS mass is already near its critical value, the observed BdHNe-I binary outcome can be achieved for much lower energies. The maximum period for which the BdHNe-I occurs is therefore a function of the initial mass of the NS companion. It follows that the BdHNe-I and the BdHNe-II (XRFs) can be produced by binaries with similar $CO_{\rm core}$ and orbital periods. Here, a more massive ($\gtrsim 2\ M_\odot$) NS companion would lead to a BdHNe-I and a less massive ($\lesssim 1.4\ M_\odot$) NS would lead to a BdHNe-II. Therefore, long GRBs which exhibit different properties and different SN kinetic energies can have similar initial SNe and similar νNSs (e.g., see the two SNs described in Wang et al. 2019).

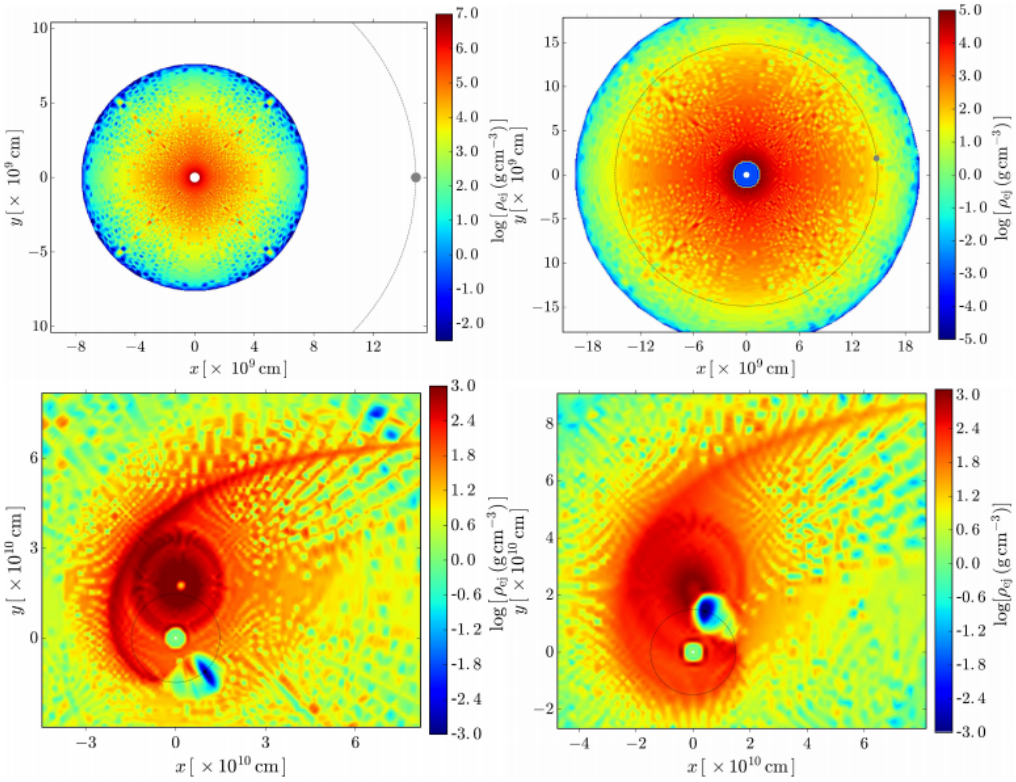

Figure 2.4. Orbital plane of a BdHNe binary with period $P \approx 5$ min ($a = 1.5 \times 10^{10}$ cm) at selected evolution times. The simulation starts with the CO_{core} which mass is divided between its ejecta (7.94 $M_\odot$) and the νNS remnant (1.5 $M_\odot$). The companion NS has an initial mass of 2.0 $M_\odot$ and it is represented with a gray-filled circle on a dashed line. The dashed line shows the NS circular trajectory (upper left panel). Colors indicate the density on a logarithmic scale. The accretion process starts after ≈ 7.7 s, when the first SN layers reach the Bondi-Hoyle region (upper right panel). After ≈ 250 s ($= 0.85\,P$) the NS reaches its critical mass and collapses into a BH of 3 $M_\odot$ (bottom left panel). Bottom right panel shows the binary system 100 s after the BH formation. Figure reproduced from Becerra et al. (2016).

The possibility that early X-ray flares (Section 1.2 and Section 2.8) originate from the interaction of the e^+e^- plasma with the dense medium of the SN ejecta ($10 \lesssim B \lesssim 10^2$) was initially examined by Ruffini et al. (2018b;g). The semi-analytic approach using a constant shell thickness (described in Section 2.3 and Section 2.4) breaks down for $B > 10^{-2}$. For this reason, the hydrodynamical simulations were performed using the PLUTO code (Mignone et al. 2012), which integrates the equations of an ideal relativistic fluid in the absence of gravity. First, the new code was validated for the parameter space where $B \lesssim 10^{-2}$ by comparing these results with the ones obtained with a semi-analytic approach. Then, the dynamics of an initially pure e^+e^- plasma was examined, which then impacts the SN ejecta. The plasma can be characterized with a negligible baryon load and a Lorentz factor of $\Gamma \sim 100$, while having a homogeneous distribution within a region of radii on the order of 10^8–10^9 cm. Building on the previous work of Becerra et al. (2016), the simulation takes into account the asymmetries of the SN ejecta created by the presence of the NS companion. The plasma engulfs different amounts of baryon mass along different directions of its propagation and slows down accordingly. The encounter of the plasma with the SN remnant leads to a shock formation and to its subsequent expansion until it reaches the outer parts of the remnant. The evolution along different directions (equivalently, different B values) will lead to different Lorentz factors

at the transparency radius, which were shown to be consistent with the ones inferred from observations ($\Gamma \lesssim 4$). Emissions with different Lorentz factors can be observed within the same GRB due to the system's rotation. An example of this emission is presented in Figure 2.5. Here, the ultra-relativistic prompt emission (C) of GRB 151027A (Ruffini et al. 2018g) occurs in a cone of 10° with low baryon contamination. Hard (F) and soft (G) X-ray flares result from the plasma interaction with the SN remnant. These are later observed as a part of the X-ray afterglow (see Section 2.9). A detailed 3D morphology of the SN remnant can be found in Becerra et al. (2018), where its asymmetry is described with clarity. There, new 3D SPH simulations were used to show that the hypercritical accretion also occurs on the νNS, leading to a possible formation of a BH-BH binary.

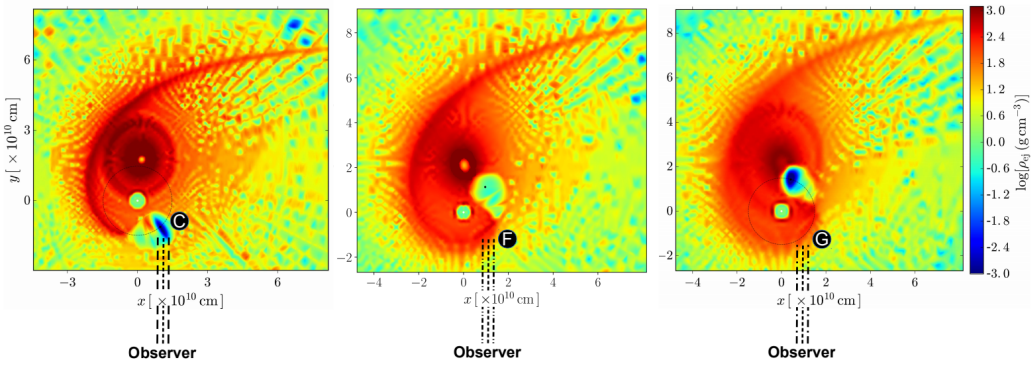

Figure 2.5. Density distribution of the SN ejecta in the equatorial plane showed at different times of the binary system evolution. It can be seen that the BH formation leaves behind a conical region of low density (C). As the system rotates, different portions of the ejecta will cross the line of sight of the detector. In the case of GRB 151027A showed here, this will first lead to the detection of the hard X-ray flare (F), followed by the soft X-ray flare (G). Figure reproduced from Ruffini et al. (2018g).

2.8 BINARY-DRIVEN HYPERNOVAE

After the SN explosion, the IGC/BdHNe paradigm implies a well-determined time sequence of events, with each stage having distinctive observational properties. This approach then also addresses multiple components often found within the time-resolved analysis of long GRBs. The asymmetry of the ejecta, caused by the binary interaction, plays a crucial role in this model. It includes a cavity of $\sim 10^{11}$ cm, lying in the orbital plane and pointing away from the CO_{core}. This is a region of low baryonic contamination (see Figure 2.4). In this section, the BdHNe-I evolution is outlined, as are their observational features which separate them from XRFs (BdHNe-II/III) and short GRBs (BM). Here, the X-ray afterglow and the high energy GeV emission play an important role in differentiating BdHNe-I and -II/III. In this work, the phenomena is structured in five different episodes:

EPISODE 1 (HYPERCRITICAL ACCRETION) After the $\sim 10\, M_\odot$ CO_{core} undergoes SN, the companion NS gains mass via hypercritical accretion of the ejected material. Both SN shock breakout as well as hypercritical accretion can be observed in the form of a soft precursor. Spectrum is described with an expanding thermal component plus an extra power-law. This episode was first observed in BATSE data (Ryde 2004; 2005b, but also see Campana et al. 2006) and later analyzed within the IGC paradigm for GRB 090618 (Izzo et al. 2012b), GRB 101023 (Penacchioni et al. 2012), GRB

110709B (Penacchioni et al. 2013), GRB 970828 (Ruffini et al. 2015d), and recently, GRB 180718A (Wang et al. 2019) and GRB 190114C (Ruffini et al. 2019c). The BB temperature decreases with time following a broken power-law. From the expanding thermal component, characteristic radii can be inferred[13]. They were found to be on the order of 10^9–10^{10} cm, with the average expansion speed of $\sim 10^8$–10^9 cm s^{-1}. The thermal component is believed to originate in the photosphere of convective outflows in the hypercritical accretion process, as mentioned in Section 2.6. The material that piles up onto the NS and the atmosphere radius causes convection instabilities in the atmosphere. These so-called bubbles rise faster than they are dragged inward by the accretion flow. They can accelerate above the escape velocity, causing relativistic outflows from the accreting NS. This process can eject up to 25% of the accreting material (Fryer et al. 2006a; Fryer 2009). For hypercritical accretion considered in the IGC/BdHNe model, the initial temperature of this bubble is ~ 5 MeV. As it adiabatically expands (in all dimensions), the temperature drops and reaches 5 keV at a radius of 10^9 cm. However, if it is ejected in the form of a jet, it will expand in the lateral direction (Fryer 2009; Fryer et al. 2014). The temperature of the bubble will evolve as $T \propto r^{-2/3}$, decreasing to ~ 50 keV when at 10^9 cm and ~ 15 keV when at 6×10^9 cm. For example, the time-resolved analysis of GRB 090618 (Izzo et al. 2012b) revealed that the BB temperature in Episode 1 evolves as $T \propto r^{-0.75\pm0.09}$, where the power-law index (within the provided error interval) agrees with the expected value. The differences between BdHNe-I and -II, observed in Episode 1, are outlined in Figure 2.6.

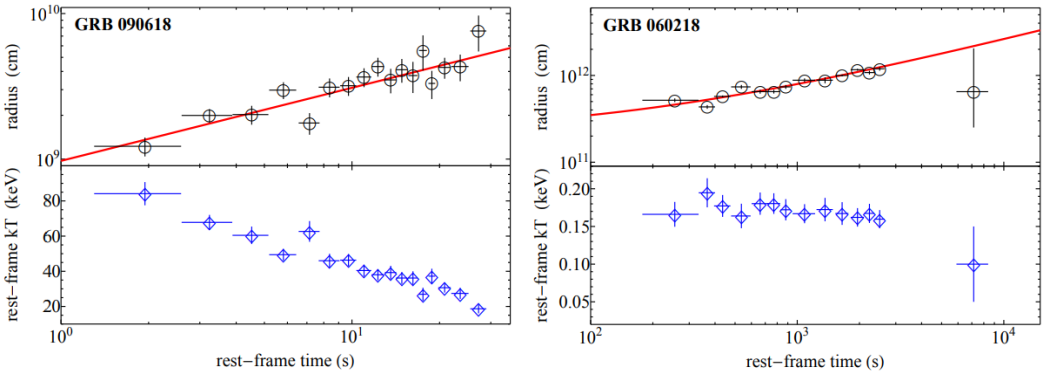

Figure 2.6. *Left panel:* Temperature (bottom panel) and radius (upper panel) evolution of the thermal component of GRB 090618, observed in Episode 1. A drop of temperature from ≈ 80 keV to ≈ 20 keV can be seen. Typical radii of the thermal emitter are found to be in the range of 10^9–10^{10} cm. Figure reproduced from Izzo et al. (2012b). *Right panel:* Temperature (bottom panel) and radius (upper panel) evolution of the thermal component of GRB 060218, observed in Episode 1. Radii of the thermal emitter usually found in BdHNe-II/III (XRFs) are in the range of 10^{10}–10^{12} cm. Temperatures can vary in the range of 0.1–2 keV. Figure reproduced from Campana et al. (2006).

For GRB 180728, classified as BdHNe-II with a longer orbital period of $a \gtrsim 10$ min, the observed temperature was ≈ 7 keV at $\sim 10^{10}$ cm (Wang et al. 2019). This was the first GRB whose emission evidenced both the emergence of the SN shockwave from the outermost layers of the CO_{core} (the first spike or a precursor) and the accretion with adiabatic expanding thermal outflow (second spike). A typical shockwave carries $\sim 10^{51}$ erg of kinetic energy (Arnett 1996), from which 10% is converted into electromagnetic radiation upon the interaction with the CBM (Bykov et al. 2012). Electrons from the CBM are accelerated and emit synchrotron radiation characterized with a power-law

[13]Calculation of radii from an evolving thermal component was initially done as described in Izzo et al. (2012b) for GRB 090618. Later, the treatment presented in Ruffini et al. (2018b) was adopted (e.g., see GRB 180728A in Wang et al. 2019).

behavior, as described in Section 1.4. GRB 180728 precursor had a power-law spectrum and energy $\approx 8\times10^{49}$ erg. The second spike was 84 times more energetic, which is explained by the accretion onto the NS companion (Becerra et al. 2016). In addition to Band/COMP models that fitted equally well, a BB component was found at the early times of emission. From its evolution, where the temperature decreased from ≈ 7.9 keV to ≈ 5.6 keV, a velocity of $0.53\,c$ was inferred. From the delay between two spikes, the binary separation of $\approx 3\times10^{10}$ cm was found.

EPISODE 2 (PROMPT EMISSION PHASE) At the end of Episode 1, the NS reaches its critical mass. Its collapse to a BH marks the beginning of Episode 2. The observed emission in BdHNE-I that follows the BH formation is explained within the framework of the fireshell model (Section 2.1–2.4). However, a new *inner engine* was recently introduced (Ruffini et al. 2018d;h; 2019a;c). The e^+e^- plasma is no longer created by vacuum polarization induced by an EMBH, as explained in Section 2.2. Instead, the plasma is created by the BH rotation, immersed in the magnetic field inherited from the NS. For a BH of mass M, this configuration induces the electric field via Wald's mechanism (Wald 1974) in the form of: $E_{r_+} \approx \frac{1}{2}\alpha B_0$, where E_{r_+} is the induced electric field at the BH horizon $r_+ = M(1+\sqrt{1-\alpha^2})$, $\alpha = J/M^2$ is the dimensionless angular momentum of the BH and B_0 is the magnetic field. The electric field is (initially) overcritical. It creates the pair-plasma through vacuum polarization, as explained before in Section 2.2. The creation of e+e- pairs will continue in cycles as long there is enough rotation energy to supply the process. As the energy is extracted, the BH will spin down. The induced electric field will eventually drop below the critical value and the pair production will come to a halt. The plasma self-accelerates to ultra-relativistic velocities along the direction where the baryon contamination is low, further depleting the cavity of baryons. This creates the necessary condition of low-baryon density needed in order to observe Episode 5. After the P-GRB, the ultra-relativistic fireshell interacts with CBM all the way up to $\sim 10^{15}$–10^{17} cm, which marks the end of Episode 2. The indicated size of the emitting region additionally emphasizes that this is a different process than the ones occurring in Episode 1 or Episode 3. This episode is a part of the extended afterglow emission initially considered in the fireshell model, here named prompt emission phase (PEP) or ultra-relativistic prompt emission (UPE) in previous works. The hydrodynamics of this episode refers to the processes occurring inside the opening of the low-density cavity mentioned earlier. Therefore, the detectability of this phase depends on the asymmetries of the SN ejecta (e.g., see Figure 2.4 and Becerra et al. 2018). Actually, for 90% of BdHNe-I which line of sight lies in the equatorial plane, *Swift* and *Fermi* instruments will not be triggered and the GRB will remain undetected. For the remaining 10%, the PEP will be detectable, as in GRB 151027 (Ruffini et al. 2018g). The ultra-relativistic emission of these sources lies within the allowed cone of $\sim 10^\circ$ of low baryon contamination. Baryon load B in BdHNe-I is usually found to be $\sim 10^{-3}$ (e.g., Izzo et al. 2012b; Ruffini et al. 2015d; 2018g) with the Lorentz factors at the transparency point ranging from $\Gamma \sim 10^2$ to $\Gamma \sim 10^3$. Depending on the galactic region, the average CBM densities (inferred from the fit of the prompt emission light-curve) can span over a wide range of 10^{-1}–10^2 cm^{-3}.

On the other hand, the average CBM densities in the vicinity of S-GRBs and GRFs (BM-II/III) were found to be $\approx 10^{-5}$ cm^{-3} (Caito et al. 2009; 2010; de Barros et al. 2011; Muccino et al. 2013a; Ruffini et al. 2015b; 2016a), a value typical of galactic halos where the compact binaries tend to migrate. There are few exceptions, where S-GRBs were found to explode in an over-dense galactic region (e.g., GRB 090510 Muccino et al. 2013b). While S-GRBs and GRFs have similar CBM environments, their baryons load differs. The subclass of S-GRBs is characterized with a low baryon load of $B \approx 10^{-5}$, which is consistent with the crustal masses of the NS-NS mergers (Belvedere et al. 2014). The baryon load of GRFs is higher (Caito et al. 2009; 2010).

In BdHNe-I, the BH formation leaves a cavity, as it is visualized in Figure 2.4. Ruffini et al. (2019a) investigated the possibility that a part of the e^+e^- plasma, after impacting onto the SN ejecta, reflects

off the walls of the cavity with velocity close to c. This should be observed as a featureless emission occurring after a delay with respect to the PEP (similar to the one seen in GRB 151027A Ruffini et al. 2018g). Inverse Compton scattering combined with the Doppler shift of the peak energies is thought to produce a spectrum that resembles a Comptonized BB. The study was done on GRB 190114C, although a similar delayed structure was also observed in two other GRBs: GRB 090926A and GRB 130427A (BdHNe-I). This episode is sometimes referred to as Episode 3, although here it is placed under Episode 2.

EPISODE 3 (EXTENDED X-RAY EMISSION) Interaction of the GRB outflow with the SN ejecta results in an additional emission with energies 10^{51}–10^{52} erg. This energy injection produces a flare at the beginning of Episode 3, which corresponds to the X-ray flares described in Section 1.2 (occurring after $\sim 10^2$ s in the rest-frame). An expanding thermal component can sometimes be found within the time-resolved analysis of the flare, with inferred radii of $\sim 10^{12}$–10^{13} cm. The expansion is mildly relativistic, with $\Gamma \lesssim 4$ (e.g., Ruffini et al. 2014c; 2015a; 2018g). The flare is followed, in a consequent order, by a steep decay. a plateau phase and finally by a late power-law decay. This canonical X-ray afterglow behavior that can sometimes (but not always) be seen among the GRB light-curves, was described in Section 1.2 (Zhang et al. 2006a). Within the fireshell model, this phase was a part of the extended afterglow while in the IGC/BdHNe paradigm it is also addressed as a flare-plateau-afterglow (FPA) phase, or recently, as extended X-ray emission (EXE). The late decay (starting between 10^4 and 10^5 s) exhibits a common power-law behaviour, with typical slopes of $-1.7 \lesssim \alpha_X \lesssim -1.3$ (Pisani et al. 2013). This commonality is found regardless of the values that characterize BdHNe-I prompt emission and their $E_{\rm iso}$, which can span over several orders of magnitude. This standardized behavior points away from the beamed emission, which is assumed in the fireball model. The late power-law also exhibits overlapping and nesting, if computed in the source cosmological rest-frame (Pisani et al. 2013; Ruffini et al. 2014c). It was shown that the duration of the plateau phase is inversely proportional to the energy of the source. Less energetic sources have longer plateau duration and vice versa. The luminosity of the plateau phase is also correlated with GRB energy, where more energetic sources have higher plateau luminosities. Penacchioni et al. (2012) and Penacchioni et al. (2013) explored the possibility of using the late X-ray emission as a distance indicator. However, this method was not universally successful (e.g., see Ruffini et al. 2013b; Varela et al. 2013; Ruffini et al. 2014a; Malesani et al. 2014a).

Out of all GRB subclasses, only BdHNe-I exhibit the FPA phase, characterized by a possible occurrence of flares, a common, late power-law behavior, and a nested structure. X-ray afterglows of BdHNe-II/III and BM subclasses (S-GRFs, S-GRBs, and GRFs) do not exhibit these commonalities. They are found to be less energetic and more chaotic. Figure 2.7 compares the rest-frame 0.3–10 keV luminosity light-curves of BdHNe-I (left panel) and BdHNe-II/III (XRFs, right panel). The origin of the X-ray emission in S-GRFs (BM-I) and GRFs (BM-III) is thought to be due to either the interaction of the accelerated baryons with the CBM or due to the r-processes which heat up the surrounding material.

Parts of the behavior that differentiates BdHNe-I and -II changed with the recent work of Ruffini et al. (2018a) and Wang et al. (2019). Here, the non-thermal component in the afterglow originates from the interaction between a νNS, created by the $CO_{\rm core}$ undergoing SN, and a mildly relativistic ejecta of the HN (*hypernova*, see Section 2.9). Two components contribute to the injected energy: synchrotron emission of relativistic electrons from the νNS, injected into the expanding magnetized HN ejecta, and later ($\sim 10^5$ s), the loss of rotational energy of the fast-spinning νNS via dipole and quadrupole emission. These give rise to the power-law observed in the optical and X-ray bands of

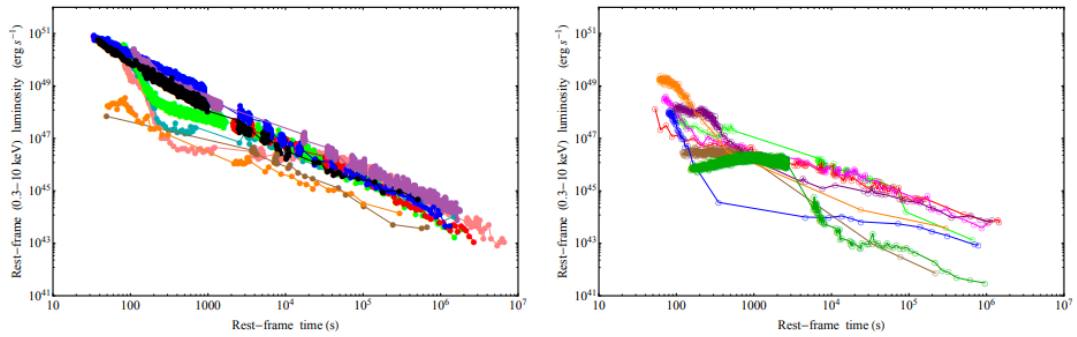

Figure 2.7. *Left panel:* X-ray luminosity light-curves of selected BdHNe-I in the 0.3–10 keV rest-frame energy band. These sources exhibit overlapping and a nested structure. BdHNe-I in the plot: GRB 050525 (brown), GRB 060729 (pink), GRB 061007 (black), GRB 080319B (blue), GRB 090618 (green), GRB 091127 (red), GRB 100816A (orange), GRB 111228A (light blue), and GRB 130427A (purple). *Right panel:* Rest-frame 0.3–10 keV luminosity light-curves of selected BdHNe-II/III (XRFs). Light-curves are generally more scattered, without a FPA pattern found in light-curves of BdHNe. BdHNe-II/III in the plot: GRB 050416A (red), GRB 060218 (dark green), GRB 070419A (orange), GRB 081007 (magenta), GRB 100316D (brown), GRB 101219B (purple), and GRB 130831A (green). Figures reproduced from Ruffini et al. (2018b).

the afterglow (Figure 2.8 - left panel). Therefore, in this recent development, the late X-ray emission of both BdHNe-I and BdHNe-II/III share a common power-law. Both GRB 130427A (BdHNe-I) and GRB 180728A (BdHNe-II) (e.g., Wang et al. 2019) were observed to have a power-law decaying index ~ -1.3 after 104 s, despite their different prompt and X-ray afterglow energy. Here, they assumed that the bolometric luminosity required by the synchrotron model is equal to the energy loss of the pulsar. The fitting results gave initial pulsar spin values of 2.5 ms (GRB 180728A) and 1 ms (GRB 130427A).

EPISODE 4 (OPTICAL SN EMISSION) For BdHNe (and XRFs) at $z \lesssim 1$, optical SN emission is expected after 10–15 days in the cosmological rest-frame, with luminosity similar to the one of SN 1998bw (SN 2010bh, see Galama et al. 1998; Bufano et al. 2012 and Section 1.2). The SN signature was confirmed, either spectroscopically or through the bump detection in the late optical light-curve, for many BdHNe (e.g., Kann et al. 2008; Cobb et al. 2010; Cano et al. 2011; Xu et al. 2013b) and XRFs (e.g., Malesani et al. 2004; Cobb et al. 2006; Mazzali et al. 2006; Fan et al. 2011). As one can assume, no SN signature is expected nor observed for any of the short GRB subclasses. The occurrence of a SN within the BdHNe model was predicted and confirmed by later observations for three GRBs, namely GRB 130427A (BdHNe-I), GRB 180728A (BdHNe-II) and GRB 190114C (BdHNe-I, Ruffini et al. 2013a; 2018c; 2019b). However, these predictions do not draw a distinction between the fireball and the BdHNe model, as the construction of both heavily relied on priorly observed GRB-SN connection.

EPISODE 5 (ULTRA-HIGH ENERGY EMISSION) The long-lived, ultra-high energy (UHE) emission (up to 100 GeV, see Section 1.2) is expected in the BdHNe-I scenario (or for any subclass where the BH is formed), with an onset starting after the P-GRB. The corresponding luminosity light-curve was observed to follow a power-law with index ≈ -1.2 (e.g., Nava et al. 2014). Similar power-law behavior of luminosity was also observed in the first spike of Episode 2 in some GRBs (e.g., GRB 190114C in Ruffini et al. 2019c), pointing towards the same inner engine that drives them. Within the IGC paradigm, GeV emission deterministically signalizes the birth of a BH. Therefore, *Fermi*/LAT observations have proven to be important as an additional tool for distinguishing

BdHNe-I and BdHNe-II (as well as BM subclasses). However, not all BdHNe-I are accompanied by GeV emission, despite being within the *Fermi*/LAT field of view (e.g., GRB 090516A and GRB 151027). In contrast, GeV emission in short GRBs is commonly observed if the conditions are favorable. In systems leading to short GRBs, the high-energy photons originating from the inner engine can freely reach the distant observer. This is due to the surrounding environment which is not as contaminated with the ejected material as the one surrounding the BdHNe. The material ejected from the CO_{core} explosion ($\approx M_\odot$) can be up to three orders of magnitude greater than the one ejected during the NS-NS or NS-BH mergers ($\lesssim 10^{-2}\ M_\odot$), thus obscuring the high-energy emission. In this case, when the inclination of the viewing angle is more than 60° from the normal to the plane of the binary system, the GeV radiation will become obscured (Ruffini et al. 2018g). Within the work of Ruffini et al. (2018e), a more general case of an arbitrary viewing angle was explored.

Ruffini et al. (2018e) showed that the rotational energy of a Kerr BH is sufficient to explain the GeV emission. The analysis of the GeV luminosity data indicated the Lorentz factor of $\Gamma \sim 1500$ at transparency radii of $\sim 10^{17}$ cm. More recently, the driving mechanism of the prompt emission and the high GeV emission was united under the same inner engine. The electric field around the BH, described in Episode 2, is also able to accelerate protons. When accelerated along the rotation axis, UHECRs (Section 1.5) with energies up to 10^{21} eV are expected to occur. In off-polar direction coinciding with the cavity, a proton-synchrotron emission is expected. This is currently considered to be the source of the high GeV emission (e.g., see the analysis of GRB 130427A and GRB 190114C in Ruffini et al. 2018d; 2019c). Details regarding the synchrotron emission of the accelerated protons can be found in the work of Ruffini et al. (2018d) and Ruffini et al. (2018h). This episode was made a part of Episode 2 in recent publications (e.g., Ruffini et al. 2019c).

Since the emission is associated with a newly formed BH, detection of high-energy photons is not expected for BdHNe-II/III and MB-I/III/IV (see Table 1), regardless of the position with respect to the LAT boresight (e.g., GRB 180728A, Wang et al. 2019). Ruffini et al. (2016a) note that although S-GRFs are approximately 100 times less energetic than S-GRBs, their GeV fluxes, if any, are necessary 10^5–10^6 times weaker (in order to remain below LAT detection threshold). However, there are few exceptions (e.g., GRB 130702A classified as an XRF with LAT detection, Cheung et al. 2013a). High-energy emission observed in S-GRBs (where a BH is formed from the NS-NS inspiral) differs from the BdHNe one: it occurs earlier and it is more energetic (Ruffini et al. 2016a).

To summarize, the SN outbreak and the accretion onto the companion NS can be seen in the form of a precursor. The accretion is hypercritical: the photons are trapped within the infalling material and the NS atmosphere is sufficiently hot to trigger the $\nu\bar{\nu}$ cooling emission. This emission releases the energy gained by the accretion. Regardless of the inner engine mechanism, once the BH is created, the resulting e^+e^- plasma propagates through the surrounding environment which contains different baryon densities. Differences in baryon densities are a result of the asymmetric morphology of the SN ejecta, caused by the accretion process onto a νNS (e.g., see Figure 2.4). The low-density region is necessary in order to observe high energy emission. Hence, the observable signatures of BdHNe-I are a function of the viewing angle. The self-acceleration of the plasma along the low-density cone gives rise to the prompt emission. A part of it can be reflected on the walls of the cavity that surrounds the BH, yielding a delayed, featureless emission as observed in the UPE/PEP phase of GRB 190114C. In the same direction, protons accelerated by the electric field give rise to the GeV emission via proton-synchrotron process. These same protons, when accelerated along the rotation axis, lead to UHECR detection. The observed emission does not depend only on the viewing angle with respect to the plane. The system is dynamical. Because of its rotation (~ 300 s period), viewing angle with respect to the SN remnant changes (e.g., see Ruffini et al. 2018g). The interaction of the e^+e^- plasma with the remnant produces X-ray flares observed at early times of the

afterglow (also see Section 2.9). The afterglow itself, on the other hand, is explained by the synchrotron emission of relativistic electrons originating from the νNS and the νNS pulsar emission. At first, the afterglow is powered by the kinetic energy of the mildly relativistic ejecta. Afterward, it is powered by the conversion of the νNS rotational energy to synchrotron emission. The precursor and X-ray flares in the early afterglow are mildly relativistic, while the prompt and high-energy emission are ultra-relativistic. Different Lorentz factors and radii of origin imply that these components do not form a causally connected sequence. Instead, they are a manifestation of the inner engine activity viewed from different angles.

2.9 EXTENDED THERMAL EMISSION AND HYPERNOVAE

In the BdHNe model, X-ray flares originate from a mildly relativistic expanding SN. The GRB onset in the form of e^+e^- plasma impacts the SN ejecta at $\sim 10^{10}$ cm. Here it engulfs a large amount of baryons until it reaches the transparency at radii $\sim 10^{12}$ cm, with $\Gamma \lesssim 4$. This additional energy injection leads to a broad-lined Ic SNe with luminosities beyond the ones traditionally observed in these sources, termed *hypernova* (HN, Maeda & Nomoto 2003; Lyman et al. 2016). The SN, which was originally expanding at $\approx 0.2\ c$, is now transformed via shock-heating into a HN, reaching expansion velocities up to $\approx 0.9\ c$. The expanding velocity can be directly inferred from the thermal emission observed in soft X-rays ~ 100 s after the trigger. An example of such thermal component is shown on the right panel in Figure 2.8. The calculation is done using an expression presented in Ruffini et al. (2018b). Namely,

$$\frac{\beta^5}{4[\ln(1+\beta)-(1-\beta)\beta]^2}\left(\frac{1+\beta}{1-\beta}\right)^{1/2} = \frac{D_L(z)}{1+z}\frac{1}{t_2-t_1}\left(\sqrt{\frac{F_{\rm bb,obs}(t_2)}{\sigma T^4_{\rm obs}(t_2)}}-\sqrt{\frac{F_{\rm bb,obs}(t_1)}{\sigma T^4_{\rm obs}(t_1)}}\right), \tag{2.19}$$

where $\beta = v/c$ is the expansion velocity of the SN ejecta, $D_L(z)$ is the luminosity distance for the redshift z, $F_{\rm bb,obs}$ is the observed thermal flux at times t_1 and t_2 (as it arrives to the detector) and $T_{\rm obs}$ is the corresponding temperature. The left hand-side term is only a function of velocity (β) and the right-hand side term is only function of observables. This equation assumes uncollimated emission and considers only the radiation coming from the line of sight. It is model-independent and valid in both Newtonian and relativistic regimes. The inferred expansion velocities are in the range of $\beta \sim 0.6$–0.9, which corresponds to Lorentz gamma factors $\Gamma < 5$ (e.g., see the analysis of GRB 151027A in Ruffini et al. 2018g). Together with Episode 1 and the P-GRB, this is the third thermal emission that can be observed during the same burst. Within the IGC model, it is referred to as the extended thermal emission (ETE). Other bursts that have been analyzed are GRB 090618 with $\beta \sim 0.8$ (Ruffini et al. 2014c), GRB 081008 with $\beta \sim 0.9$ (Ruffini et al. 2018b) and GRB 130427A, where the average velocity was found to be $\beta = 0.94$ at average radius of $\sim 10^{13}$ cm (Ruffini et al. 2018a). The optical signal after 10–15 days reveals a further slowing down of the ejecta, with $\beta \sim 0.1$ (Xu et al. 2013a; Cano et al. 2017). The mildly relativistic regime and the small emitting radii agree with the predictions of the (updated) BdHNe model. They do not agree, however, with the fireball model where the ultra-relativistic shock wave is expanding with $\Gamma \sim 500$, producing the X-ray afterglow at the radius of $r > 10^{16}$ cm (see Section 1.4). Therefore, here the X-ray flares play a fundamental role as their time-resolved analysis supports the predictions made by the IGC paradigm, singling it out from the rest of the models. As it was mentioned earlier, Ruffini et al. (2018a) demonstrated that the mildly relativistic ejecta can also account for the non-thermal component (in the early thousands of seconds) powered by its kinetic energy. After this, the afterglow is powered by a release of the rotational energy of the millisecond νNS.

The occurrence of X-ray flares is exclusive to BdHNe alone, although there have been claims for their existence in short bursts and XRFs (see Section 1.2 and references within). Still, short GRB flare

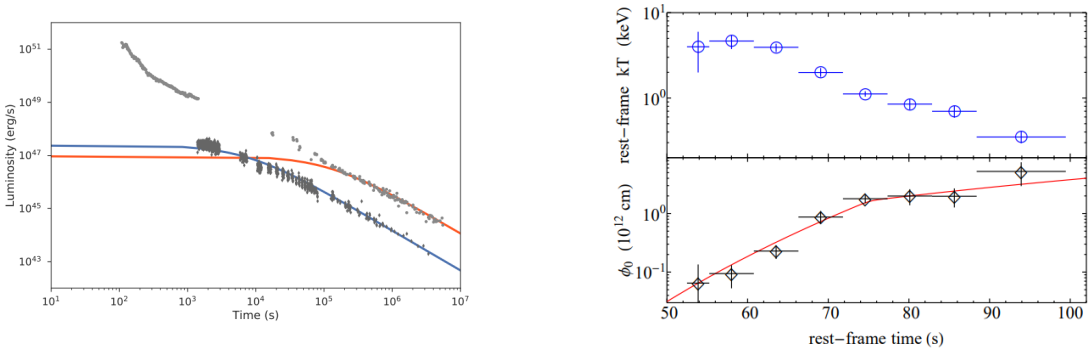

Figure 2.8. *Left panel:* Light-curves of GRB 1340427A (orange line) and GRB 180728A (blue line) afterglow, fitted assuming that the bolometric luminosity required by the synchrotron model equals to the energy loss of the pulsar. Figure reproduced from Wang et al. (2019). *Right panel:* The rest-frame evolution of kT and ϕ_0 found in the hard X-ray flare of GRB 151027A. Quantity ϕ_0 is related the radius R of the emitter, where for non-relativistic limit ($\beta \to 0$) $R \to \phi_0$ and for ultra-relativistic limit ($\beta \to 1$) $R \to 1.92\,\Gamma\,\phi_0$. Figure reproduced from Ruffini et al. (2018g).

candidates are ~ 100 times dimmer than the long ones (Margutti et al. 2011). In addition, the fluence of an X-ray flare is on average ten times dimmer than the prompt emission fluence (Chincarini et al. 2007; Falcone et al. 2007). X-ray flares also need to be distinguished from the late gamma-ray flares, which can often be prominent in the lower energy band. Here, the soft X-ray component is only a manifestation of the low-energy part of the gamma-ray flare. The difference is also visible in the Lorentz factor Γ, which has a much higher value. Therefore, the occurrence of X-ray flares in short GRBs is often claimed while using a low data quality (Ruffini et al. 2018b).

Not all BdHNe have a well-determined early X-ray flare, despite having complete *Swift*-XRT observations ($\approx 8\%$, Ruffini et al. 2018b). From these, only half will have a confident thermal component (meaning that the addition of a BB spectrum improves a single power-law fit). How prominent this component is depends on two factors. First, a low BB flux with respect to the non-thermal one makes the identification of the thermal component challenging. Second, the observable temperature must be within the range of the satellite bandpass, which is not always the case. Future observations may improve this statistics and validate if the X-ray flares are exclusive solely to BDHNe. Ruffini et al. (2018b) analyzed the early X-ray emission of BdHNe that satisfy these conditions, yielding a sample that spreads over a wide redshift ($0.84 \leq z \leq 4.11$) and energy ($10^{52} < E_{\rm iso} < 10^{55}$ erg) range. Analysis of the parameters that are used to characterize the flares revealed their correlation with $E_{\rm iso}$. Namely, L_p and E_f (t_p and Δt) are highly (anti)correlated with $E_{\rm iso}$. Here, t_p is the flare peak time (with respect to the BAT trigger), L_p is the corresponding peak luminosity, E_f is the flare energy and Δt is flare duration, calculated as the time interval during which the flare luminosity is above $0.5 L_p$.

3

PROMPT EMISSION ANALYSIS: A SAMPLE OF LONG GRBs

Determining the prompt emission energetics, and the parameters that describe it, is a necessary first step of every GRB-related study. This chapter presents the prompt (UPE) phase analysis within the fireshell frame-work for selected BdHNe-I. The *Fermi* observatory and its energy span showed to be crucial for the identification of different episodes in the UPE phase, including the P-GRB. The P-GRB identification is essential in order to characterize a given burst within the fireshell model. Its temperature and energy (in terms of $E_{\rm iso}$) are used to determine the baryon load (Eq. 2.8) and consequently set the dynamics of the e^+e^- plasma in motion. From this, a set of different quantities can be identified, one of them being the CBM distribution which gives rise to the variable prompt light-curve.

Section 3.1 describes the procedure that was used throughout this work in order to obtain these quantities. The identification of P-GRB required the time-integrated and time-resolved prompt emission analysis. Thus, the focus here is on the *Fermi*/GBM light-curves. Data preparation, that was applied to each GRB presented here, is also summarized in Section 3.1. Section 3.2 presents the properties of 11 long GRBs whose prompt emission was broke down to find the P-GRB signature. This section deals with the `rmfit`-part of the analysis. The observed GeV emission and the large energy of the prompt phase place these GRBs in the BdHNe-I subclass (with two possible exceptions, see GRB 130702A and GRB 120729A). Further analysis of GRB 110731A and GRB 151027A is presented in Section 3.3. New interpretation of the multiple prompt emission components presented in Ruffini et al. (2018b;g) motivated the revisit of GRB 090618. Due to the extent of its analysis and obtained data, GRB 090618 deserved a section of its own (Section 3.4). In these two sections, the CBM densities were determined from the prompt emission light-curves. Furthermore, the e^+e^- plasma propagation up to the transparency point can be utilized in order to approximate the GRB redshift. The application of this method is explained in Section 3.5 on the example of short GRB 160829A. Final remarks and future perspectives can be found in Chapter 4.

In the last few years, the IGC model went through several changes. The most severe ones occurred in 2019, during which this thesis was being written (see Chapter 2). Thus, this chapter utilizes the version of the model that was actual at the time of the analyses here presented. That is, developed up to 2018. It invokes an EMBH (Section 2.2), which birth is signalized by the high-energy GeV emission (if the viewing angle is $< 60^\circ$ from the normal to the plane of the binary). Although the way vacuum polarization is induced differs from the case of a Kerr BH immersed into a magnetic field, the conceptual idea remains the same.

3.1 INTRODUCTION TO GRB ANALYSIS

Obtaining the fireshell parameters and CBM densities

The process of obtaining the fireshell model parameters ($E^{\rm tot}_{e^+e^-}$, B and $E_{\rm P-GRB}$), which are in return used to simulate the light-curve and the corresponding spectrum, begun with determining the observed isotropic energy $E_{\rm iso}$ from the gamma-ray prompt light-curve. This value was then assumed to be equal to $E^{\rm tot}_{e^+e^-}$ (which is, in return, determined by the BH parameters). Although, $E_{\rm iso}$ actually represents its lower limit: no process is perfectly adiabatic/fully radiative, not all energy will be detected by the instruments and some of the energy will also be emitted in lower wavelengths. Next, the correct identification of the P-GRB was in order. It was done through the time-resolved spectral analysis performed at the beginning of the prompt emission. The P-GRB duration and energetics were determined by the thermal component found in the spectrum, though a non-thermal component was found as well (due to the early onset of baryon interaction with the CBM). In the case of dyadotorus (Section 2.3), the spectral shape is expected to arise from the convolution of thermal spectra. This results in a power-law with an exponential cut-off (Compton or COMP, see Section 1.3). If the remaining part of the emission was also well-fitted by COMP, the time interval of a constant $E_{\rm p}$ was taken as the P-GRB. As it was explained in Section 2.3, the relative energetics of the $E^{\rm tot}_{e^+e^-}$ and the P-GRB is determined by the baryon load B (see Figure 2.3 or the bottom right panel in Figure 3.1). If there is no baryon contamination, no energy will be transformed into the kinetic energy and all of it will be radiated at the transparency point.

Knowing the baryon load and $E_{\rm iso}$ also makes it possible to set the simulation of the expanding fireshell in motion. The simulation then results in a number of parameters, including the Lorentz factor at transparency, the fireshell temperature and the P-GRB energy expressed in terms of $E^{\rm tot}_{e^+e^-}$ (see Figure 3.1). Therefore, through a trial-and-error procedure, a cross-check was done in order to see if the baryon load input gave back the correct P-GRB temperature ($kT^{\rm obs} = kT\,(1+z)^{-1}$) and energy. If the P-GRB spectrum is well fitted by COMP model, the effective temperature[1] was obtained using $kT = E_{\rm p}/3.92$. In that case, the error interval for kT was estimated by adopting the $E_{\rm p}$ errors provided by the `rmfit` analysis and dividing them by the factor of 3.92. The P-GRB energy was required to be within the error bars of the ratio $R = E_{\rm P-GRB}/E_{\rm iso}$. The error σ_R was calculated using the propagation formula:

$$\sigma_R = \sqrt{\left(\frac{\partial R}{\partial E_{\rm iso}}\right)^2 \sigma^2_{E_{\rm iso}} + \left(\frac{\partial R}{\partial E_{\rm P-GRB}}\right)^2 \sigma^2_{E_{\rm P-GRB}}} = \sqrt{\left(-\frac{E_{\rm P-GRB}}{E^2_{\rm iso}}\right)^2 \sigma^2_{E_{\rm iso}} + \left(\frac{1}{E_{\rm iso}}\right)^2 \sigma^2_{E_{\rm P-GRB}}}\,, \qquad (3.1)$$

where $\sigma_{E_{\rm iso}}$ and $\sigma_{E_{\rm P-GRB}}$ errors were scaled to match the corresponding mean flux (erg cm^{-2} s^{-1}) errors of the $E_{\rm iso}$ and $E_{\rm P-GRB}$ time intervals. These were in return obtained from the spectral fits during `rmfit` analysis (see further below). A match of the simulated values and the ones obtained through the `rmfit` analysis would be considered as positive if the P-GRB energy was within the interval defined with Eq. 3.1 and the $kT_{\rm sim}$ would be within the errors provided by the `rmfit`. Naturally, the redshift of the source needs to be known or approximated through other means (e.g., see Section 3.5). The relation between these B, kT and R cannot be expressed analytically. They need to be obtained through numerical integration of the entire set of fireball equations of motion.

Once the simulation of transparency confirmed the quantities in question, the second phase of the simulation was set in motion. This phase starts with the evolution of ultra-relativistic baryons from the transparency point. The multi-peak structure of the light-curve was modeled by assuming that the CBM medium is distributed in the form of thin shell-clouds, with each pulse of the light-curve corresponding to

[1] The BB temperature and the peak of its $\nu F(\nu)$ spectrum $E_{\rm p}$ are correlated as $E_{\rm p} = 3.92\,kT$. This also applies to quasi-thermal GRB spectral models (e.g., see Bellm 2010).

one cloud. The CBM density distribution was hence obtained through a trial and error technique until the simulated light-curve matched the observed one. Finally, the simulated spectrum was produced to see how well it matched the observed one. Parameters that govern the light-curve and spectral fitting process are:

CBM DENSITY PROFILE The CBM density profile $n_{\rm CBM}$ (number of particles per cubic centimeter) primarily determines the temporal behavior of the light-curve and it is radius-dependent.

SURFACE FILLING FACTOR Another quantity that is associated with the environment is the fireshell surface filling factor $\mathcal{R} = A_{eff}/A_{vis}$, where A_{eff} is the effective emitting area of the fireshell and A_{vis} is its total visible area (Ruffini et al. 2002; 2005a). As a result, this definition takes into account the CBM inhomogeneities and its filamentary structure (Ruffini et al. 2004). Only the parts of the fireshell that hit the (inhomogeneously) distributed CBM will heat up and radiate. As the $n_{\rm CBM}$, $\mathcal{R}$ is a function of distance. Increasing its value increases the peak of the spectrum. The higher concentration of the CBM when it is distributed in a clump-like way will result in higher temperatures. Typical values are in the range of $10^{-12} \lesssim \mathcal{R} \lesssim 10^{-8}$ (also see Shara et al. 1997; Ducci et al. 2009).

MODIFIED THERMAL SPECTRUM As it was explained in Section 2.4, the observed non-thermal spectrum is produced by convolution over EQTSs of a number of modified thermal spectra with different Lorentz and Doppler factors, and different temperatures. The introduced phenomenological parameter $\alpha_{\rm BB}$ (Patricelli et al. 2012) modifies the low-energy part of the spectrum and it is constant for a specific GRB in question. The values of $\alpha_{\rm BB}$ obtained by comparing the numerical simulations with the observed prompt emission spectra were found to be in the range $-2.0 \lesssim \alpha_{\rm BB} \lesssim -1.8$. It is usually taken to be equal to $\alpha - 1$ if this value does not exceed -2, Here, α is the (low-energy) spectral index of the Band or COMP model that describes the prompt emission (excluding the P-GRB).

The fitting was done pulse-by-pulse, consequently adding the values of $n_{\rm CBM}$ and $\mathcal{R}$ at the corresponding distances. The emission produced by each succeeding pulse (for a multi-pulse light-curve) depends not only on the added parameters but also on all the previous ones, i.e., on the entire fireshell evolution. Because of EQTSs, the emission produced at a given distance will also influence all the light-curve shape fitted after it. The light-curve fitting is therefore a complex procedure, where all the parameters and their values are intervened with the ones that come after them through the equations that describe the fireshell and baryon dynamics. These equations are a direct link between the two phases of the fireshell model, the one before and the one after the point when transparency condition has been reached. Their agreement with data can not be independently optimized. An arbitrary light-curve with some given values of P-GRB and $E^{\rm tot}_{e^+e^-}$ can not be fitted with the simulated one. In addition, as the simulation progresses, the assumptions made regarding the equations of motions presented in Section 2.4 may cease to be valid and the simulation can become increasingly inaccurate (e.g., Dainotti et al. 2007).

Retrieving the data

The *Fermi* observatory was launched in June 2008 in low Earth orbit, which enables it to scan the sky about 16 times per day. It harbors two instruments: the Gamma-Ray Burst Monitor (GBM, Meegan et al. 2009) and the Large Area Telescope (LAT, Atwood et al. 2009). Specially designed for GRB studies, GBM covers the energy range from 8 keV to 40 MeV. It observes the whole unocculted sky with total of 12 sodium iodide (NaI) detectors sensitive to energies between 8 keV and $\sim$ 1 MeV, and with two bismuth germanate detectors (BGO) covering the range from 250 keV to 40 MeV[2]. The GBM provides a

[2] The mentioned 8 keV–40 MeV energy window refers to the one obtained after data preparation. The raw data is spread over a much larger energy range.

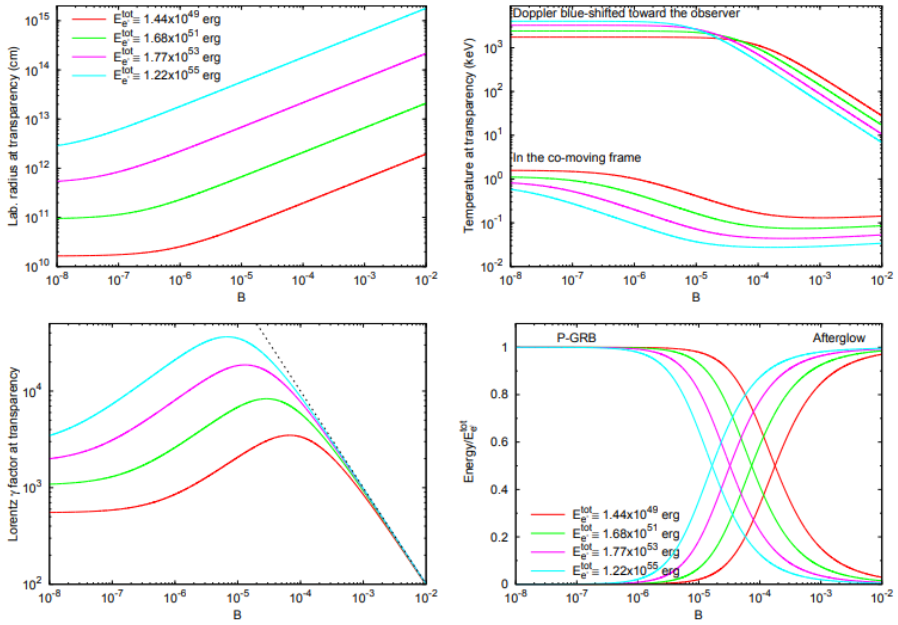

Figure 3.1. Main parameters of the fireshell at the point of transparency as functions of baryon load B: the laboratory radius (upper-left), the fireshell temperature (upper-right), the Lorentz gamma factor (bottom-left) and the P-GRB energy in the units od $E^{\rm tot}_{e^+e^-}$ (bottom-right). Different lines correspond to different values of energy ($E^{\rm tot}_{e^+e^-}$). Figure reproduced from Muccino et al. (2013a).

rough localization (10° uncertainty) within one second using the cosine-like angular response of the NaI detectors. LAT is sensitive to the higher complementary energy range, from 20 MeV up to more than 300 GeV. However, if the observed GRB is located > 65° off the detector axis, the upper energy limit drops to ≈ 100 MeV. Covering seven decades in energy, the *Fermi* observatory offers an unprecedented energy and sensitivity for the study of high-energy emission in GRBs. It also enriched the GRB science with a dozen of thermal signature detections and high-energy observations. These properties make it ideal for sub-classifying the long GRBs into BdHNe-I or BdHNe-II/III (XRFs).

For each burst, the *Fermi*/GBM data was downloaded from the online *Fermi* burst catalog (Narayana Bhat et al. 2016) that can be found on the NASA HEASARC website[3]. Each of the twelve NaI detectors (n0–n9, na, nb) views a different portion of the sky; signals therefore differ from one detector to another. For the majority of GRBs presented here, the downloaded data consists of the time-tagged event (TTE) files of the triggering NaI detectors and the BGO detectors that share their field of view. The TTE data contain individual photon events with arrival time and the energy channel tags. It is an un-binned list of counts divided in 128 energy channels. Prior to 2012, now a continuous version of TTE data had a shorter time window. It started 15–30 seconds before the burst (depending on the number of events) and lasted for 300 seconds after the trigger time. Since the GRB duration in this work does not exceed this value, the TTE data were chosen over the CSPEC data; an option with a larger time-window (≈ 8000 s) but lower time-resolution (1.024 s). In order to see which detector triggered, the `quicklook` and `glg_trigdat_all_bn` files were consulted. Usually, selecting more than two or three NaI detectors will not significantly improve the fit. For each event file of the NaI/BGO detectors, a corresponding detector response file was also chosen. A detector response is a function of the detector sensitivity by energy channel and its current

[3] `https://heasarc.gsfc.nasa.gov/W3Browse/fermi/fermigbrst.html`

off-axis cosine respond. These files map the input energy to the visible count energy for each detector in all of 128 energy channels. Therefore, the response files with the CSPEC binning were taken, which corresponds to the maximum (128 channel). Response files can be recalculated if a better burst position became available due to additional (e.g., *Swift*) observations. In that case, the updated version of the response file was downloaded. If available, files with extension `var2` were selected, which provide new detector response values for every 5 degrees of spacecraft slew.

Time-integrated and time-resolved spectral analysis was performed using the software package `rmfit`[4] (version 4.3.2). Before the fitting process, for each GRB the standard data reduction was applied. From the available 128 energy channels, the ones below ~ 8 keV (for NaI detectors) and ~ 250 keV (for BGO detectors). The variable GBM background (BG) was subtracted by fitting different order polynomials using a user-defined interval, before and after the prompt emission. The regions were selected following instruction in the thread for `rmfit` data analysis[5] and roughly corresponded to a [-20 s, -3 s] interval (before the source counts) and [100 s, 200 s] interval (after the source counts). After the analysis, the BG intervals would be changed and the analysis repeated. This was done in order to see if the first selection of BG intervals and choice of the polynomial influenced the final parameter values. The results were consistent with the previously obtained parameter errors. The data was also screened for overflow effects and other artifacts[6]. Here. the systematic residuals around the k-edge energies were also considered to see how they influence the fitting results. This "P-Cygni"-type effect can be observed in the spectrum at ~ 33 keV, extending 4–6 channels within the channel space. This roughly corresponds to 5–10 keV interval in the energy space. Repeating the analysis in which these channels were excluded did not significantly change the model parameters and their errors.

Time-integrated spectral fits of the *Fermi*/GBM data were performed using the built-in power-law (PL), the power-law with exponential cutoff (COMP) and the Band function (see Section 1.3) in order to determine the best fit model. The time-resolved spectral analysis (i.e., the P-GRB search) was done using the three already mentioned models and PL+BB. This equals to four different models compared and contrasted with each other for every selected bin. Sometimes, the COMP+BB model was also compared. More details on the time-resolved analysis for individual GRBs are given in Section 3.2 and Section 3.4. The Castor statistics (C-STAT, Cash 1979) was used as a measure of the goodness of the fit, with the best fit model having the lowest C-stat value. Following the statistical analysis for nested[7] models in Nava et al. (2011b) or Guiriec et al. (2010), for every degree of freedom (DOF) an improvement of $\Delta C - STAT \approx 9$ was required. This value is equivalent to an improvement accepted with the 3σ confidence level. Otherwise, the simpler model (i.e., the one with fewer parameters) was chosen as a better fit. Here, $\Delta C - STAT$ is the difference between the C-STAT values of the two comparable models. For bright bursts, the χ^2 statistics was applied due to the high number of counts. Finally, the calibration constant EAC (effective area correction) among the different detectors was allowed to be free (it is usually fixed to 1). If not stated otherwise, no significant difference was found when comparing the C-STAT and parameter values between these two cases.

[4] Program for GBM analysis, developed by the GBM Team and publicly available at `fermi.gsfc.nasa.gov/ssc/data/analysis`.
[5] `https://fermi.gsfc.nasa.gov/ssc/data/analysis/scitools/rmfit_tutorial.html`
[6] `https://fermi.gsfc.nasa.gov/ssc/data/analysis/GBM_caveats.html`
[7] The significance of the fit improvement between the two nested models (e.g., PL and PL+BB, COMP and COMP+BB, and so on) can be calculated from their C-STAT values (e.g., see Muccino et al. 2013a or Muccino et al. 2013b and the probability values reported there). As in the limit of $\beta \to \infty$ Band function turns to COMP, the C-STAT of these two models can also be compared (e.g., Nava et al. 2011b; Ruffini et al. 2015b). A similar argument can be applied to the relationship between the PL and the COMP model.

Isotropic and P-GRB energy calculation

Once the correct model was identified, the isotropic-equivalent energy was calculated using

$$E_{\rm iso} = \frac{4\pi d_{\rm l}^2}{1+z} S_{\rm bol}, \tag{3.2}$$

where $d_{\rm l}$ is the luminosity distance to the source at redshift z. Factor $(1+z)^{-1}$ corrects for the cosmic time dilatation and $S_{\rm bol}$ is the total "bolometric" fluence (energy per unit area) in the $1/(1+z)$–$10^4/(1+z)$ frame. It is not possible to observe the bolometric fluence directly. Instead, it is typically measured in some bandpass of the detector ($S_{\rm obs}$). The same GRB placed at different redshift would have a different fluence measurement (that might be for the extreme cases completely shifted to X-rays). Therefore, in order to determine the energies of a GRB sample in a consistent way, it would not be enough to use some common energy detector span. Instead, one needs to extrapolate the observed spectrum outside the detectors bandpass by using a function that best describes the GRB spectral shape[8] (k-correction, Bloom et al. 2001). The fluence was then calculated using

$$S_{\rm bol} = S_{\rm obs} \frac{\int_{1/(1+z)}^{10^4/(1+z)} E\,\phi(E)\,dE}{\int_{E_{\rm min}}^{E_{\rm max}} E\,\phi(E)\,dE}, \tag{3.3}$$

where $\phi(E)$ is the best fit model from the time-integrated spectral analysis and $S_{\rm obs} = \Delta t\, F_{\rm obs}$. Here, $F_{\rm obs}$ is the mean energy flux in the $E_{\rm min}$–$E_{\rm max}$ detection band and Δt is the time interval of the spectral fit. If not stated otherwise, the GBM-T_{90} interval provided by the *Fermi* burst catalog (in the 50–300 keV energy band) was used in order to calculate the isotropic energy. The P-GRB energy was calculated in a similar manner, where $\phi(E)$ was either a BB component or a COMP model and where Δt was the P-GRB duration. Throughout the analysis, the ΛCDM cosmological model was adopted, with $\Omega_{\rm m} = 0.27$, $\Omega_\Lambda = 0.73$ and $H_0 = 71\ {\rm km\,s^{-1}\,Mpc^{-1}}$.

3.2 SAMPLE OF TYPE I BINARY-DRIVEN HYPERNOVAE

A list of 11 BdHNe-I is given in Table 2. For these sources, the time-resolved analysis was done in order to find a possible P-GRB that occurs at the beginning of the UPE phase (indicated by a star in the last column). The first eight GRBs are a result of the selection rules that were applied to long bursts within the *Fermi*/LAT catalog (Ajello et al. 2019). They are long, LAT-detected bursts with a known redshift and for which $E_{\rm iso} \gtrsim 10^{52}$ erg could be found in the literature (Ruffini et al. 2018e). There is one exception, however, a low-energy GRB 130702A with LAT detection. Within the IGC/BdHNe model, the LAT detection signals the BH birth and automatically classifies the observed GRB as a BdhN-I. This GRB was classified as an XRFs (BdHNe-II) in Ruffini et al. (2016b) on the basis of its low energy. Here, it is classified as BdHNe-I. The low-energy BdHNe-I are possible in a specific case of the binary progenitor separation and companion mass (see Section 2.7). From the remaining three GRBs, only GRB 110731A was detected by LAT. From the remaining two, GRB 090618 was not in the optimal position for high-energy detection. However, GRB 151027A was. The lack of high-energy photons was hence contributed to the line-of-sight angle larger than 60° from the normal to the plane of the binary (Ruffini et al. 2018g).

A list of BdHNe-I with a given redshift can be found in Ruffini et al. (2016b). There, $E_{\rm iso}$ was calculated using the fit parameters provided by the GCN notices. If one of the GRBs in Table 2 was already

[8] This step, although necessary for the GRB sample analysis, is not always applied in the current literature (e.g., see Chincarini et al. 2007; Falcone et al. 2007; Margutti et al. 2010).

GRB	z	θ(LAT)	Model	$E_{\rm iso}$(erg)	$E_{\rm iso,OLD}$(erg)	P
090323(002)	3.57	53°	COMP	$3.833(\pm0.277)\times10^{54}$	$4.38(\pm0.53)\times10^{54}$	
100414A(097)	1.368	65°	Band	$6.2283(\pm0.0465)\times10^{53}$	$5.50(\pm0.55)\times10^{53}$	
100728A(095)	1.567	59°	COMP	$7.256(\pm0.293)\times10^{53}$	$8.68(\pm0.87)\times10^{53}$	*
120624B(933)	2.197	71°	Band	$3.4792(\pm0.1640)\times10^{54}$	$3.19(\pm0.32)\times10^{54}$	
120729A(456)	0.8	83°	PL(+BB)	$3.2034(\pm0.1025)\times10^{52}$	-	
130518A(580)	2.488	48°	Band	$1.9396(\pm0.0116)\times10^{54}$	$1.93(\pm0.19)\times10^{54}$	
130702A(004)	0.145	75°	PL	$6.724(\pm0.249)\times10^{50}$	-	
141028A(455)	2.332	19°	Band	$7.6224(\pm0.0064)\times10^{53}$	$6.890(\pm0.002)\times10^{53}$	*
110731A(465)	2.83	3°	Band	$6.05(\pm0.09)\times10^{53}$	$4.95(\pm0.49)\times10^{53}$	*
151027A(166)	0.81	10°	Band	$7.26(\pm0.36)\times10^{51}$	-	*
090618(353)	0.54	133°	Band	$1.94(\pm0.02)\times10^{53}$	$2.49(\pm0.02)\times10^{53}$	*

Table 2. List of 11 BdHNe-I (column 1), where numbers in the parentheses refer to the fraction of the day at which the GRB was detected. These numbers were assigned by pipeline processing and help to differentiate bursts that happened within the same day (similar to suffixes 'A' or 'B' within the name). Redshift (column 2), *Fermi*/LAT boresight angle (column 3) and the best-fitting model (column 4) are also listed for each GRB. Marginal BB component within the time-integrated spectrum is indicated by (+BB). Column 5 provides $E_{\rm iso}$ calculated using best-fit parameters obtained from this work. The fitting interval approximately corresponds to T_{90} (50–300 keV), taken from the *Fermi*/GBM burst catalog. This energy differs from the $E_{\rm iso}$ in column 6. These values can be found in Ruffini et al. (2016b). They were obtained using preliminary parameters and time intervals found in GCN notices. If this column is empty, the GRB was not enlisted as a BdHN-I up to this work. For GRB 151029A, the energy of the first pulse is given. The old $E_{\rm sio}$ of GRB 090618 was taken from the work of Izzo et al. (2012b). Asterisk in column 7 indicates that a P-GRB was found within the time-resolved analysis.

classified as BdHNe-I, Columns 5 and 6 compare the values of $E_{\rm iso}$ obtained from this work and ones from the Ruffini et al. (2016b). For each of GRBs listed in Table 2, a more detailed description of the analysis is given further below. This includes:

(i) a summary of detections and best-fit models reported via GCN notices by different observatories,

(ii) the best-fit model parameters used for the $E_{\rm iso}$ calculation, obtained through the analysis in this work,

(iii) and the summary of the time-resolved analysis (i.e., the P-GRB search).

Due to the extent of the produced data, the results for GRB 090618 are separately outlined in Section 3.4.

GRB 090323

GRB 090323 triggered the GBM onboard *Fermi* which observed a multi-peak light-curve with duration of ~ 150 s (Ohno et al. 2009). After ~ 70 s following the trigger time, *Fermi* executed a maneuver due to the Earth-angle constraints. Because of this inconvenience, the reported GCN analysis was restricted to the first 70 s of the emission which consists of two main peaks (e.g., see Figure 3.2). The best fit model for this time interval was said to be COMP with $\alpha = -0.89(\pm0.03)$ and $E_{\rm p} = 697(\pm51)$ keV (van der Horst & Xin 2009). Softening of the emission can be observed between the two peaks since both of them are also best fitted by COMP but with different spectral peak energies, namely $E_{\rm p,1} = 1173(\pm175)$ keV and $E_{\rm p,2} = 574(\pm34)$ keV. A similar light-curve was observed by KONUS/*Wind*. Here, the entire burst interval was best fitted with Band function, where $\alpha = -0.96$, $\beta = -2.09$ and $E_{\rm p} \approx 416^{+76}_{-73}$ keV (Golenetskii et al. 2009b). The *Fermi*/LAT detection was significant. Emission up to a few GeV started a few seconds after the GBM trigger time and continued up to $\sim$ kilo-seconds. *Swift*/XRT observed the afterglow which

followed a simple power-law decay with no evident jet break (Perri & Stratta 2009). The burst was also observed in optical wavelengths by multiple observatories (e.g., Guidorzi et al. 2009; Perley et al. 2009; Kann et al. 2009c), which detected one of the most luminous afterglows ever detected (Kann et al. 2009b). During these observations a flattening of the light-curve was indicated, followed by a possible steepening (Rumyantsev & Pozanenko 2009; Kann et al. 2009a). However, steepening matched the extrapolation of the earlier decay, suggesting that the plateau may rebrightened or that an optical flare spanned for a few days. Spectrum showed multiple absorption lines and a strong absorption blueward of 5580 Å, consistent with the redshift of $z = 3.57$ (Chornock et al. 2009). The burst was also detected in radio wavelengths ~ 5 days after the GBM trigger (Harrison et al. 2009; van der Horst 2009).

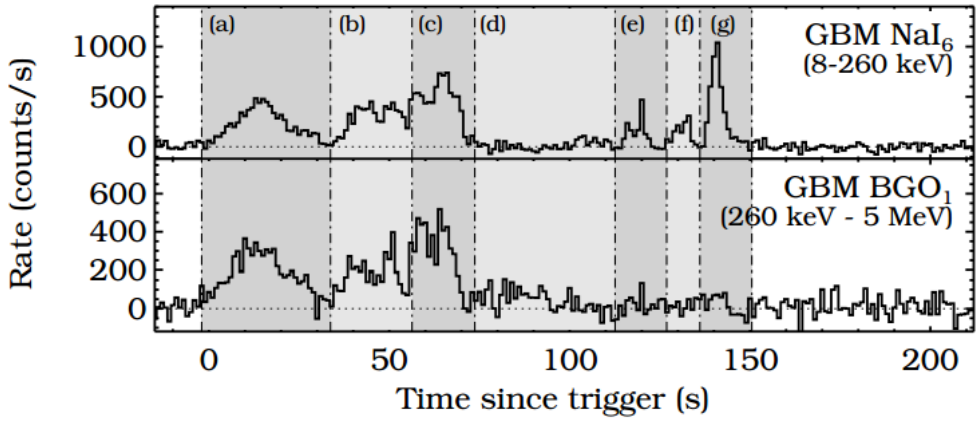

Figure 3.2. Light-curve of GRB 090323 observed with GBM detectors (1 s binning), as indicated in the top right corner. Intervals marked with dashed lines correspond to the ones used in the analysis. In this work, the last three intervals were fitted as one. Figure reproduced from Bissaldi (2010).

The `rmfit` analysis and the choice of detectors needed to be done with special care. Different time intervals required different detectors due to the executed spacecraft maneuver. The maneuver caused rapid changes in the source angles of various detectors as well as the rapid changes in the BG behavior. Therefore, the time-integrated spectral analysis could not be done by simply taking the parameter values for the first 70 s (given by GCN report) and applying it to the rest of the burst. Hence, the procedure and the choice of the detectors was done following Bissaldi (2010). Detectors NaI-n9, nb and BGO-b1 were used for fits that encompassed time intervals up to 71.68 seconds. For times after ≈ 114 seconds, NaI-n6,n7,n9 and BGO-b1 were used. The time-integrated analysis (Table 3) was done using only NaI-n9 and BGO-b1.

The obtained results are consistent with the analysis within the paper, i.e. first three peaks are best fitted by Band, COMP and COMP, respectively (see intervals indicated in Figure 3.2). Sub-pulse resolved analysis was consistent with these results. There are slight deviations in the $E_{\rm p}$ temperature between the two fits, probably due to the user-defined BG intervals. The last three peaks are also best fitted by COMP while the quiescence interval is best fitted with a PL. Table 3 also shows HTS evolution of the $E_{\rm p}$ with each succeeding pulse. This can be also be seen from the comparison of the NaI and BGO light-curves in Figure 3.2.

Model	$T_{\rm start}$(s)	$T_{\rm stop}$(s)	E_p(keV)	α	F (erg cm^{-2}s^{-1})	C-STAT/DOF
COMP	8.19	143.36	644(±156)	-0.8741	$8.57(\pm0.62)\times10^{-7}$	268.15/237

Interval (s)	[-2,05, 33.79]	[33.79, 56.32]	[56.32, 71.68]	[113.66, 150.53]
$E_{\rm p}$ (keV)	722.2(±139.0)	514.4(±55.0)	490.1(±29.4)	127.9(±21.7)

Table 3. Best-fit model parameters for GRB 090323. The GBM catalog T_{90} and $T_{\rm start}$ values were 135.17 s and 8.192 s, respectively. Bissaldi (2010) and KONUS/*Wind* report Band as the best fit with similar $E_{\rm p} \approx 591$ keV. Evolution of $E_{\rm p}$ is also showed for different burst intervals.

GRB 100414A

On 10 April 2010, the *Fermi*/GBM triggered and located GRB 100414A (Foley 2010). The light-curve consisted of one main pulse with a duration of about 26 seconds (in 50–300 keV range). The time-averaged spectrum was well fitted by COMP, where $\alpha = -0.58(\pm0.01)$ and $E_{\rm p} = 627.6^{12.5}_{12.1}$keV. Although the angle from the LAT boresight was 65° (close the edge of the LAT field of view), a significant emission was detected as late as 300 seconds after the GBM trigger, where the highest energy photon (4 GeV) was observed at 40 seconds after the trigger. Observations of *Swift*/XRT two and five days after set a lower limit on the decay slope $\alpha > 1.5$ (where $F \propto t^{-\alpha}$, Page et al. 2010a;b). The detected optical light-curve is well described with a simple power-law decay, having a temporal index ≈ 2.5 (Filgas et al. 2010; Landsman & Cannizzo 2010; Urata & Huang 2010). Here, a series of metal absorption lines were identified on a common redshift of $z = 1.368$ (Cucchiara & Fox 2010). The burst was also detected in radio-wavelengths by multiple observatories (Kamble et al. 2010; Frail et al. 2010).

The best-fit model for the time-integrated fit was Band (see Table 4 and Figure 3.3), although COMP fitted equally well, with parameters similar to ones reported by Foley (2010). When EAC was allowed to be free, the fit was bother-line improved but parameter values did not change significantly. Band function was also found to be the best-fitting model by KONUS/*Wind* and *Suzaku*/WAM analyses (Frederiks 2010; Uehara et al. 2010). One-second time-resolved analysis was done up to 11.264 s after the GBM trigger, as explained in Section 3.1. This was followed by the 3.5-second time-resolved analysis over the total GRB duration. From all of the fitted models (see Section 3.1), the best fits were COMP and Band. Both models fitted equally well for all the time bins and different time intervals, including T_{90}. No significant difference was observed, with Band having a slight C-STAT advantage ($\gtrsim 9$) for the T_{90} interval and the [17.5 s, 24.5 s] interval when the flux was at its highest. Within the 3.5 s binning, there is no evolution in $E_{\rm p}$ temperature, which remains constant for both models ($E_{\rm p} \approx$ 570–650 keV). Within 1.024 s batch-fit analysis, $E_{\rm p}$ evolution exhibits intensity tracking behavior. Each of the described analyses was done using NaI-n6,n7,na and BGO-b1 detectors.

Model	$T_{\rm start}$(s)	$T_{\rm stop}$(s)	E_p(keV)	α	β	F (erg cm^{-2}s^{-1})	C-STAT/DOF
Band	1.024	27.648	678.8(±15.6)	-0.5373	-2.854	$3.349(\pm0.025)\times10^{-6}$	2590.1/478

Table 4. Best-fit model parameters for GRB 100414A. The GBM catalog T_{90} and $T_{\rm start}$ values were 26.497 s and 1.856 s, respectively. Both Band and COMP ($E_{\rm p} \approx 690$ keV, $\alpha \approx -0.55$) model provide a good fit for the T_{90} interval.

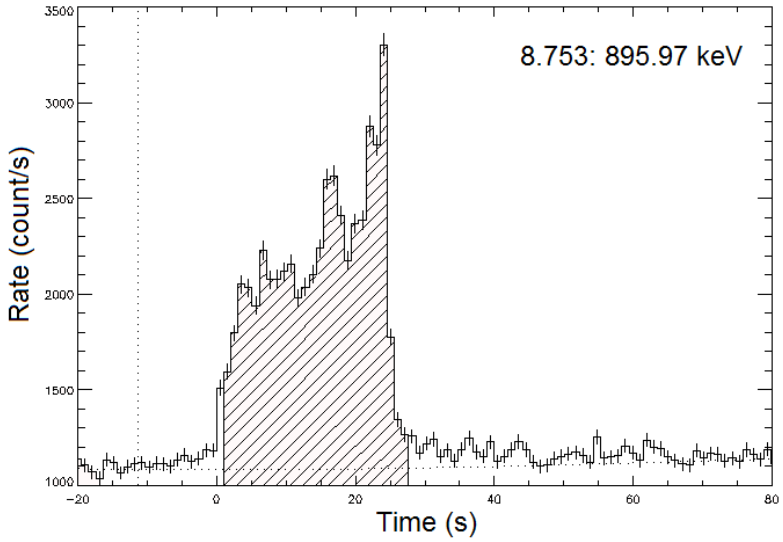

Figure 3.3. GRB 100414A (NaI-nb detector) light-curve, with the selected T_{90} interval that was used in $E_{\rm iso}$ calculation.

GRB 100728A

The *Fermi*/GBM detected GRB 100728A at 02:17:30.61 (UT) on 28 July 2010 (von Kienlin 2010). The burst duration is substantial ($\approx$ 163 s in the 50–300 keV band), where the time-averaged spectrum is best fitted by COMP ($\alpha = -0.76(\pm0.01)$, $E_{\rm p} = 353.7(\pm6.7)$ keV), or equally, with Band ($\alpha = -0.75^{+0.01}_{-0.01}$, $\beta = -3.04^{+0.23}_{-0.57}$, $E_{\rm p} = 344.3^{+9.7}_{-7.9}$ keV). Similar results were found by KONUS/*Wind* and *Suzaku*/WAM (Golenetskii et al. 2010; Tsai et al. 2010). The burst was also detected by the *Swift*/BAT (Cannizzo et al. 2010; Ukwatta et al. 2010a), triggering 55 seconds after the *Fermi*/GBM. It showed a multi-peaked light-curve extending for more than 700 seconds. A series of overlapping peaks starting around 120 s after the BAT trigger (corresponding to the end of the GBM emission) coincides with the considerable flaring activity observed by *Swift*/XRT (see Figure 3.4, Evans & Cannizzo 2010). The best-fit model is reported to be a simple PL. Therefore, GRB 100728A is yet another example of a single GRB that can be characterized with quite a different set of parameter values, stressing out the need for standardized analysis and data treatment. The X-ray light-curve follows a broken PL decay, with two breaks. The final decay was found to lie within the error bars of the initial decay. The LAT high-energy emission was previously unreported and found only when the observations were revisited (Abdo et al. 2011; Rubtsov et al. 2012). Bright X-ray emission and faint red/NIR afterglow (Ivarsen et al. 2010; Oates & Cannizzo 2010) suggests a dust-extinguished event that occurred at $z = 1.567$.

Details of the time-integrated analysis, done by using NaI-n0,n1,n2,n5 and BGO-b0 detectors, are presented in Table 5. Parameters are consistent with the ones reported by (von Kienlin 2010). Large C-STAT values and large C-STAT variations, on the order of 10^5, are possibly caused by a large data sample (long burst duration). Due to the brightness of the burst and quality of the data, χ^2-fit was performed. The fitted interval is shown in Figure 3.5 - left panel and it is best fitted by the COMP model. For shorter intervals, C-STAT analysis was used. Time interval extending up to 38.9 s (the first broad peak) was best fitted with a Band model. Interval was then reduced to the first 24.6 seconds, giving a similar result. On the other hand, the first 12.3 seconds was best fitted with a PL (Figure 3.5 - right panel). For that reason, a time-resolved analysis on the 1.024 s bin basis was performed. Starting from 8.192 s, up to 11.264 s, a PL+BB component was found with $\Gamma = -1.596(\pm0.0869)$ and kT = 53.71($\pm$3.39) keV (Figure 3.6). This

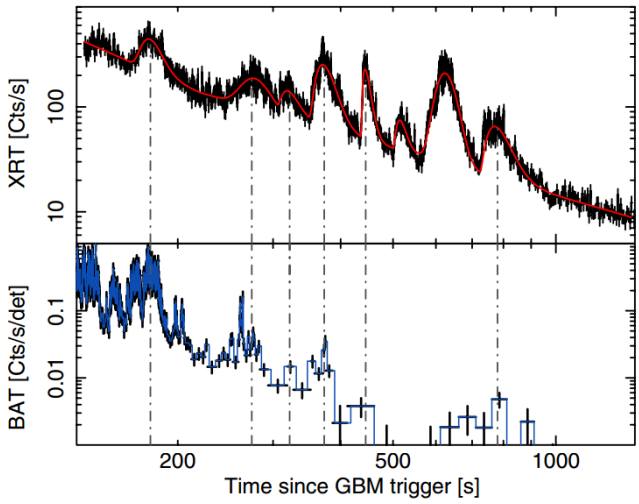

Figure 3.4. Light-curve of GRB 100728A, as observed by XRT (upper panel) and BAT (bottom panel) onboard the *Swift* observatory. Several peaks in the BAT light-curve are seen in coincidence with the X-ray flares. Figure reproduced from Abdo et al. (2011).

would suggest an extremely low P-GRB energy when compared to the total $E_{\rm iso}$, which is in agreement with the dust-obscured GRB environment.

Model	$T_{\rm start}$(s)	$T_{\rm stop}$(s)	E_p(keV)	α	F (erg cm^{-2}s^{-1})	CHIQ/DOF
COMP	13.31	178.176	324.9(±24.2)	−0.635	$6.698(\pm0.270)\times10^{-7}$	747.64/603

Table 5. Best-fit model parameters for GRB 100728A. The GBM catalog T_{90} and $T_{\rm start}$ values were 165.378 s and 13.312 s, respectively. The χ^2 test was used to calculate $E_{\rm iso}$, with CHISQ value given in the last column.

GRB 120624B

The extremely bright GRB 120624B triggered by all of the main GRB observatories: KONUS/*Wind* (Golenetskii et al. 2012), *Suzaku*/WAM (Sakamoto et al. 2012a), *Swift*/BAT (Barthelmy et al. 2012) and finally, *Fermi*/GBM (Gruber et al. 2012). The GBM light-curve consists of three bright pulses, starting ∼ 250 seconds before the trigger and lasting for about 270 seconds (50–300 keV). The trigger delay happened due to the momentary position of the *Fermi* satellite in the orbit, where the triggering function is disabled due to the high particle activity. The time-averaged spectrum is best fitted with a Band function which can be parametrized with: $\alpha = -0.85(\pm0.01)$, $\beta = -2.36(\pm0.08)$ and $E_{\rm p} = 566(\pm20)$ keV. Similar parameters were obtained by other observatories, except for *Swift*/BAT data, which are best fitted with a simple PL due to the energy window of the detector (Sakamoto et al. 2012b). For the whole duration of the prompt emission, the GRB was outside the LAT field of view (∼ 70°) but the high energy emission was still detected (Vianello & Kocevski 2012). Considering the afterglow, only the detection in radio wavelengths was reported with high certainty (Bremer et al. 2012; Bathurst et al. 2012). The *Swift*/XRT observation remained inconclusive (Littlejohns et al. 2012). Optical afterglow was undetected by the majority of the observatories (Sanchez-Caso & Castro-Tirado 2012; Xu et al. 2012; Schady et al. 2012; Breeveld et al. 2012). This pointed towards a highly obscured GRB hosted by a compact luminous galaxy with intense SFR. Spectroscopic observations were carried out between 17 and 19 days after the burst (de

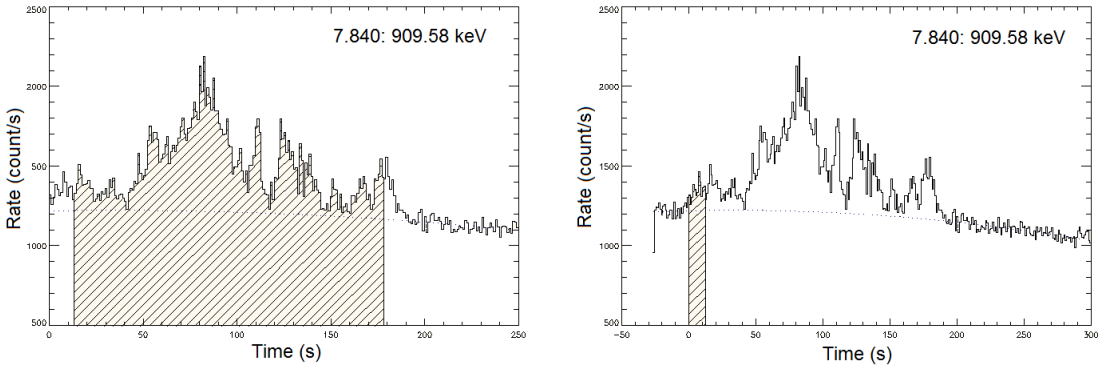

Figure 3.5. GRB 100728A (NaI-n5 detector) light-curve. *Left panel:* The T_{90} interval used for fitting $E_{\rm iso}$ is shown dashed. *Right panel:* Last three seconds of a 11.3 s interval marked dashed (best fitted by a PL as a whole) had a PL+BB as the best-fit model.

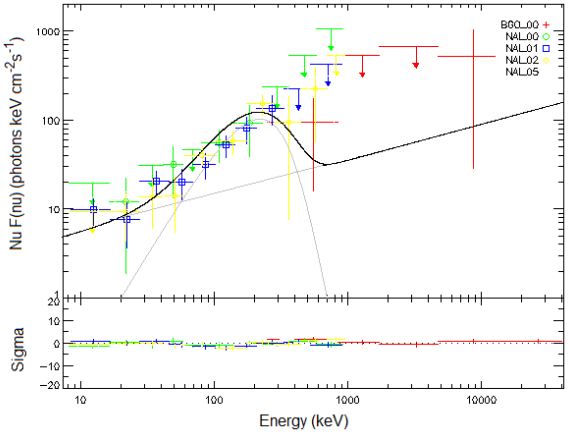

Figure 3.6. *Fermi*/GBM $\nu F(\nu)$ P-GRB spectrum of GRB 100728A. The time-integrated interval lasts from 8.192 s to 11.264 s. Best fit was PL+BB with $kT = 53.71(\pm 3.39)$ keV and $\Gamma = -1.596(\pm 0.087)$.

Ugarte Postigo et al. 2013) using the X-shooter spectrograph (Vernet et al. 2011). A redshift of $z = 1.197$ was determined. The host was observed to be compact and one of the most luminous galaxies ever to be associated with a GRB.

The calculated isotropic energy is in agreement with the one obtained by de Ugarte Postigo et al. (2013). Band model was found to provide the best fit (using χ^2 statistic), with parameters given in Table 6. Data from the NaI-1,2,9,1a and BGO-b0,b1 detectors were used and divided in the time-resolved analysis as depicted in Figure 3.7. All intervals have Band as the best fit model. Intervals 3–5 were found to be also well described by a PL+BB model. However, the P-GRB is expected to be found at the beginning of the prompt emission. Still, the first four segments may be interpreted as the Episode 1 (Section 2.8), where the BB component can arise from the convection instabilities. The P-GRB that follows this emission would then correspond to segment number 5. Nevertheless, the beginning of Episode 1 is not expected to be well fitted with a Band function, which acts as a prompt emission beacon. The possibility that the segment number 5 is, in fact, a P-GRB was not pursued further in this work and remains the subject of further studies.

Model	T_{start}(s)	T_{stop}(s)	E_P(keV)	α	β	F (erg cm^{-2}s^{-1})	CHIQ/DOF
Band	-258.05	14.34	435(±111)	−0.7093	−1.928	$7.00(\pm0.33)\times10^{-7}$	869.83/718

Table 6. Best-fit model parameters for the T_{90} interval of GRB 120624B. The GBM catalog T_{90} and T_{start} values were 271.364 s and -257.028 s, respectively.

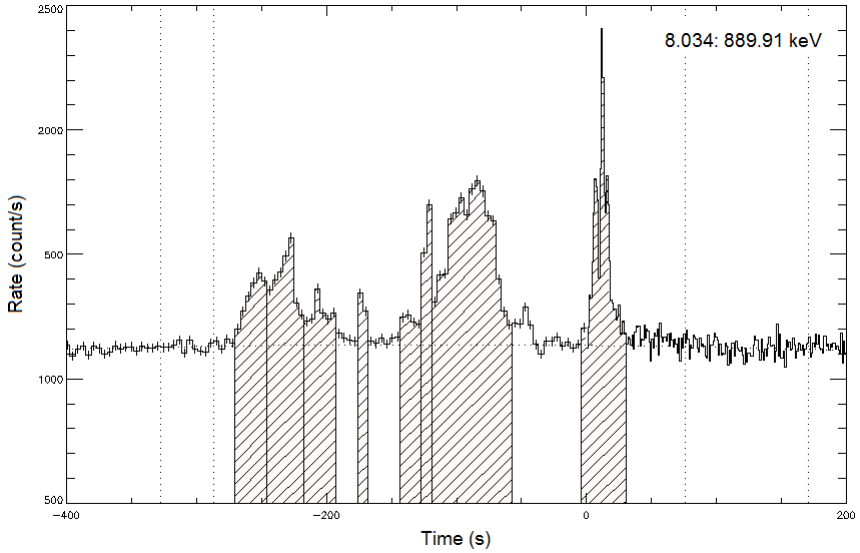

Figure 3.7. GRB 120624B (NaI-n9 detector) light-curve. Eight different intervals used in the time-resolved analysis shown dashed. All intervals have Band as the best fit model, from which segments 3–5 have a PL+BB fitting equally well.

GRB 120729A

On 29 July 2012, both *Fermi*/GBM and *Swift*/BAT triggered and located GRB 120729A (Rau 2012; Ukwatta et al. 2012), which has a redshift of $z = 0.8$ (Tanvir & Ball 2012). Due to its proximity, the burst has an associated SN (e.g., Cano et al. 2014). The GBM light-curve consists of a single FRED pulse lasting ≈ 25 s, best fitted with a simple PL function (with the PL index $\Gamma = -1.49(\pm0.05)$, where $PL(E) =\sim (\frac{E}{100\,\mathrm{keV}})^{\Gamma}$). The same model also fitted well the BAT data (Palmer et al. 2012). Although the angle from the *Fermi*/LAT boresight was 83°, high energy photons were still detected within the time-resolved LAT analysis (Ackermann et al. 2013b). However, the time-delay of the LAT emission was large (400 s), and contained only 3 photons. The *Swift*/XRT light-curve exhibited a break at ≈ 8200 s, where the power-law decay index changed from $\alpha = 1.12$ to $\alpha = 2.9$ (Maselli et al. 2012). The break was also observed in the optical light-curve, although earlier than it was seen in X-rays (D'Avanzo et al. 2012), On the contrary, a single power-law decay was also reported by other optical observations (Wang et al. 2015a). No radio emission was detected, despite multiple conducted observations (Smith et al. 2012; Laskar et al. 2012).

As expected, the time-integrated spectrum was found to be well fitted with a simple PL (using NaI-n1,n2,na and BGO-b0,b1 detectors, Figure 3.8). Among the different models that were fitted on the complete burst duration, a PL+BB model showed an improvement (Table 7). The comparison of the

two fits is shown in Figure 3.9. Following Rau (2012), which started their analysis at -3.6 seconds, time-resolved fits were done for two intervals: [-7.168 s, -2.048 s] and [-4.096 s, -1.024 s]. No P-GRB was found nor excluded due to poor data quality at these early times, which resulted in negative count-rate models and unconstrained parameters. Considering the low isotropic energy of GRB 120729A (within the BdHNe-I group) and the late onset of the LAT emission that contained only 3 photons (found within the time-resolved analysis), the possibility that GRB 120729A is an energetic member of an XRF subclass can not be excluded.

Model	$T_{\rm start}$(s)	$T_{\rm stop}$(s)	kT(keV)	Γ	F (erg cm^{-2}s^{-1})	C-STAT/DOF
PL	-1.024	24.576	-	$-1.398(\pm0.019)$	$2.499(\pm0.080)\times10^{-7}$	2046.0/598
PL+BB	-1.024	24.576	$15.95(\pm1.54)$	$-1.325(\pm0.028)$	$2.294(\pm0.089)\times10^{-7}$	2017.6/596

Table 7. Best-fit model parameters for GRB 120729A. The GBM catalog T_{90} and $T_{\rm start}$ values were 25.472 s and -1.024 s, respectively. A PL+BB model gives a better fit.

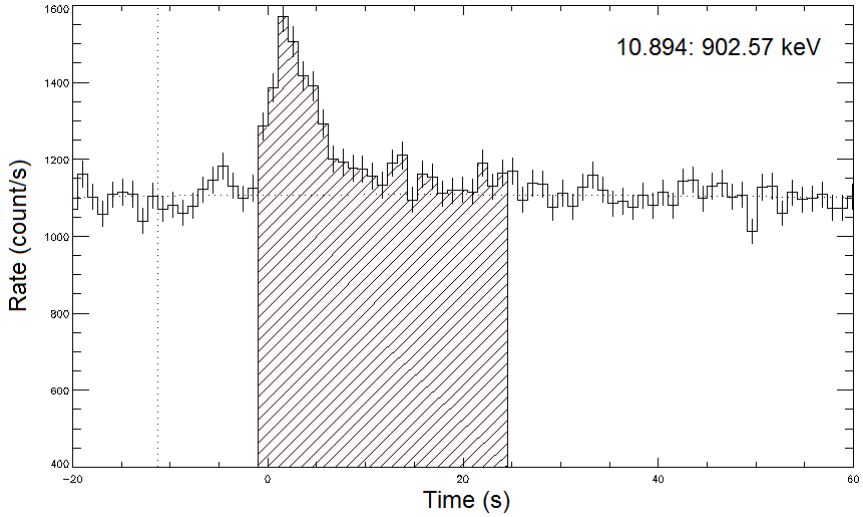

Figure 3.8. GRB 120729A light-curve (NaI-n2 detector) which depicts the T_{90} interval used for fitting (dashed).

GRB 130518A

The long GRB 130518A was bright enough to catch the attention of all the main GRB observatories: *Fermi*/GBM (Xiong 2013), *Swift*/BAT (Cummings 2013), KONUS/*Wind* (Golenetskii et al. 2013b) and *Suzaku*/WAM (Kawano et al. 2013). The *Fermi*/GBM light-curve consists of two overlapping peaks with a duration of about 50 seconds (50–300 keV). The time-integrated spectrum encompassing this time was best fitted with a Band function with $\alpha = -0.86(\pm0.01)$, $\beta = -2.27(\pm0.04)$ and $E_{\rm p} = 396(\pm9)$ keV. At the time of the trigger, the angle from the *Fermi*/LAT boresight was 43 degrees (Omodei & McEnery 2013). The emission lasted approximately from 40 to 100 seconds, depending on the type of data considered. Similar values were obtained by Golenetskii et al. (2013b) and Kawano et al. (2013). The *Swift*/XRT located the GRB 130518A afterglow (Evans et al. 2013a;b). The afterglow was also observed in optical and radio wavelengths (Cenko 2013; Castro-Tirado et al. 2013). Several absorption features, including the broad Lyα dampening (see Section 1.5), placed GRB 130518A at $z = 2.488$ (Sanchez-Ramirez et al. 2013; Cucchiara & Cenko 2013).

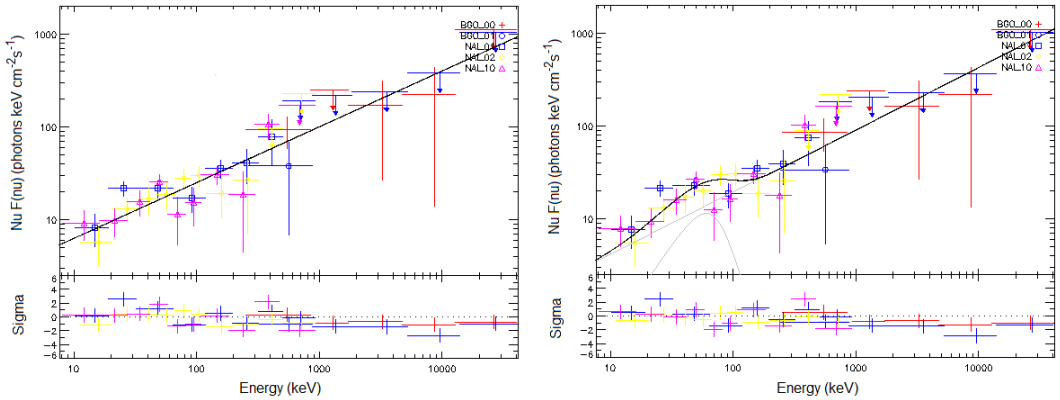

Figure 3.9. *Fermi*/GBM $\nu F(\nu)$ spectrum of GRB 120729A for the T_{90} time interval. PL fit is shown on the left while the PL+BB fit is shown on the right.

Analysis was done using NaI-n3,n6,n7 and BGO-b0,b1 detectors. Parameters of the time-integrated spectral fit (Figure 3.10) are similar to ones obtained by Xiong (2013) and are listed in Table 8. The time-resolved analysis was divided into three intervals: the weak pulse [0.0 s, 19.46 s], the large peak [19.46 s, 34.82 s] and the long tail [34.82 s, 68.81 s]. All segments are visible in all of the detector light-curves. Neither PL+BB or COMP provided a good fit. For all fits, the Band model was the best-fitted one, with $E_{\rm p}$ showing HIT behavior.

Model	$T_{\rm start}$(s)	$T_{\rm stop}$(s)	$E_{\rm p}$(keV)	α	β	F (erg cm^{-2}s^{-1})	C-STAT/DOF
BAND	9.22	59.39	412.4(±11.9)	−0.8848	−2.012	$1.845(\pm0.011)\times10^{-6}$	6413.8/602

Table 8. Best-fit model parameters for the time-integrated analysis of GRB 130518A. GBM catalog T_{90} and $T_{\rm start}$ values were 48.577 s and 9.920 s, respectively. All GCN circulars related to the prompt emission report BAND as the best-fit model with $E_{\rm p} \approx 400$keV.

GRB 130702A

On 2 July 2013, at 00:05:23.08 (UT), the *Fermi*/GBM triggered and located GRB 130702A (Collazzi & Connaughton 2013). A FRED-like light-curve has a ∼ 60 s duration. The brightest part of the emission (the first ∼ 17 s) it is best fitted with a simple PL, where $\Gamma = -1.65(\pm0.02)$. The same spectral shape was also observed by KONUS/*Wind* (Golenetskii et al. 2013a). At the time of the trigger, the angle from the *Fermi*/LAT boresight is 75° (Cheung et al. 2013b). The burst entered the LAT nominal field of view 250 seconds after the trigger, only to exit again at 2200 seconds. In this time interval, more than 5 photons with energies > 100 MeV were observed. The *Swift*/XRT and *Swift*/UVOT detected a fading counterpart at burst location (D'Avanzo et al. 2013c; Porterfield et al. 2013). The X-ray light-curve decayed as a PL with $\alpha = 0.57^{+0.21}_{-0.20}$ (D'Avanzo et al. 2013b), in a similar manner as its (extremely bright) optical counterpart (e.g., Schulze et al. 2013). However, a significant flattening of the optical light-curve was observed 4 days after the burst, which then rebrightened on the 6.6th day (Butler et al. 2013; Pozanenko et al. 2013). The emerging SN was later spectroscopically confirmed (Cenko et al. 2013; D'Elia et al. 2013). Radio emission was also detected by Perley & Kasliwal (2013), van der Horst (2013), Corsi et al. (2013) and Chandra (2013). The redshift that was inferred from the spectrum of the optical afterglow was the same as the one

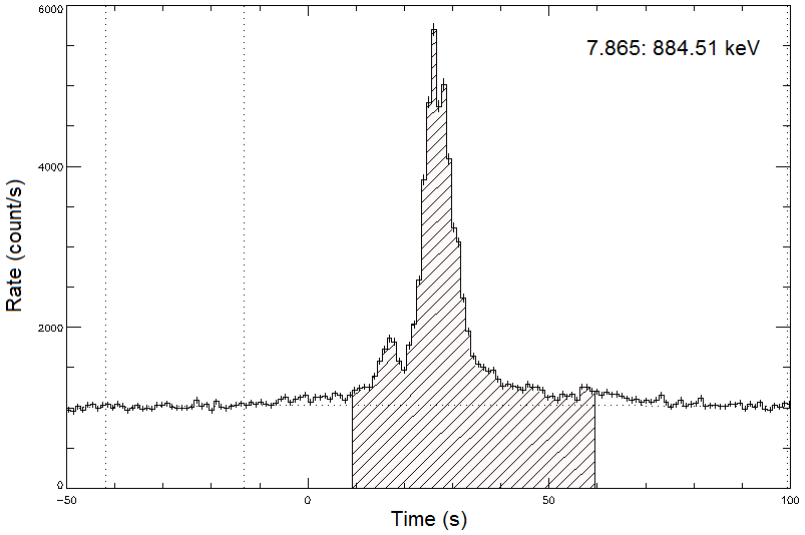

Figure 3.10. NaI-n3 detector light-curve of GRB 130518A. The T_{90} interval used for fitting is shown dashed.

obtained for the nearby SDSS galaxy (Leloudas et al. 2013), namely $z = 0.145$ (D'Avanzo et al. 2013a). The burst was located at a large offset from the host, which was observed to be a relatively passive galaxy.

Similar as reported in *Konus*-Wind and *Fermi*/GBM circulars, the best-fit model for the total duration of the burst was found to be a simple PL (with $\Gamma = -2.218(\pm 0.029)$, see Table 9). Throughout the analysis, NaI-n6,n7,n8 and BGO-b1 were used. The obtained isotropic energy is the same as the one reported by Golenetskii et al. (2013a) and Amati et al. (2013). The time-integrated interval (T_{90}) was adopted from the GBM catalog as for the rest of the bursts (Figure 3.11). However, the value of the PL index is harder if one considers only the bright portion of the event (Collazzi & Connaughton 2013). This indicates that the spectral peak energy may lie just below the instrument threshold. Amati et al. (2013) fitted the spectrum using the Band function while fixing the low-energy spectral index at different values. The obtained $E_{\rm p}$ was in the range of 15–20 keV. In this case (and keeping in mind that $E_{\rm iso} \sim 10^{50}$ erg) GRB 130702A obeys the Amati relation. Despite the efforts, these results could not be reproduced (obtained results included fits that could not converge or parameters that are not constrained).

Time-resolved analysis was performed starting with the [-1.024 s, 1.024 s] interval. Fitted models included a simple PL and a PL+BB (since fitting COMP or Band would be redundant). The interval would then be enlarged for 1.024 s and the fitting was repeated (keeping the -1.024 s as the starting time). Up to ≈ 10 s, the two models give a comparably good fit. The C-STAT was smaller for a PL+BB, but the C-STAT difference was < 9. After ≈ 10 s and up to 13.312 s, the PL+BB becomes the best-fitting model (with $kT = 6.59(\pm 0.48)$ keV and $\Gamma = -1.579$, see Figure 3.12). Since the P-GRB is expected at the beginning of the emission, the interval was gradually increased while keeping the same -1.024 s starting time. In this way, the signal to noise ratio also gradually increased, as did the possibility to detect a BB component (assuming one is present). This spectral profile also fits the observational properties of Episode 1, as does the isotropic energy of this GRB. However, due to the undoubtable LAT detection, the subclassification of this GRB remains difficult.

Model	T_{start}(s)	T_{stop}(s)	Γ	F (erg cm^{-2}s^{-1})	C-STAT/DOF
PL	1.024	59.392	$-2.218(\pm0.029)$	$1.026(\pm0.038)\times10^{-7}$	2667.6/482

Table 9. Best-fit model parameters for the T_{90} duration of GRB 130702A. The GBM catalog T_{90} and T_{start} values were 58.881 s and 0.768 s, respectively.

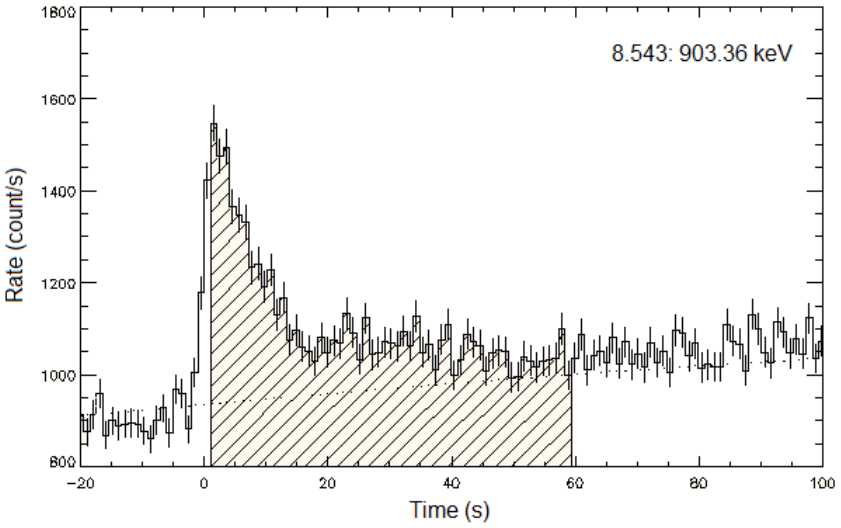

Figure 3.11. The light-curve of GRB 130702A (NaI-n6 detector). The T_{90} interval used for fitting is shown dashed.

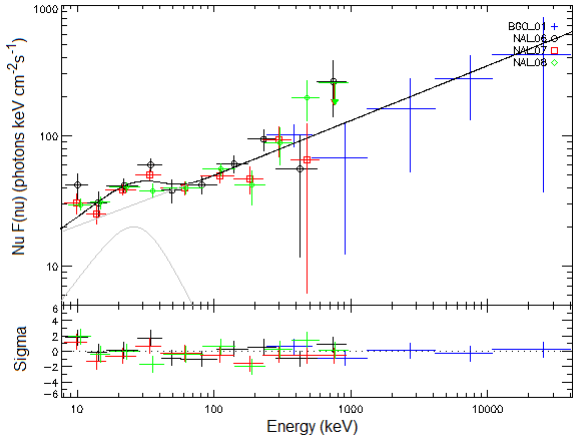

Figure 3.12. *Fermi*/GBM $\nu F(\nu)$ spectrum of GRB 130702A. The time-integrated interval lasts from -1.024 s to 13.312 s. Best fit was a PL+BB with kT = 6.59(±0.48) keV and $\Gamma = -1.579$.

GRB 141028A

GRB 141028A triggered *Fermi*/GBM at 10:54:46.78 (UT) on 28 October 2014 (Roberts 2014), causing an Autonomous Repoint Request (ARR). The emission lasted for about 30 seconds (50–300 keV), for which the time-averaged spectrum was found to be well described with a Band function ($\alpha = -0.71(\pm0.03)$, $\beta = -1.93(\pm0.03)$ and $E_{\rm p} = 249.9(\pm12.6)$ keV). The angle from the *Fermi*/LAT boresight was about 19 degrees, which detected a significant number of events until the burst exited the LAT field of view (around 600 s). The highest-energy photon (1.9 GeV) was observed 160 seconds after the GBM trigger (Bissaldi et al. 2014). Although the burst did not trigger the BAT detector onboard *Swift* observatory, an XRT follow-up was requested upon the *Fermi* detection. The *Swift*/XRT detected an afterglow which light-curve can be modelled with a PL decay where $\alpha = 2.0(\pm1.0)$ (Kennea et al. 2014; Pagani et al. 2014). The optical afterglow was also detected, fading with a PL decay of index $\alpha \sim 0.9$ (Troja et al. 2014b;a; Cenko & Perley 2014). The afterglow did not exhibit any evident break. Several absorption lines in the optical afterglow shared a common redshift of $z = 1.82$. However, these lines originated from a strong intervening system located between the GRB and the detectors. The identification of metal features at $z = 2.332$ helped to determine the correct redshift of the burst (Xu et al. 2014).

The parameters and the time interval used to calculate $E_{\rm sio}$ (given in Table 2) are listed in Table 10. The light-curve contains a single episode (Figure 3.13). The analysis was done using the data from NaI-n6,n7,n9 and BGO-b1 detectors. The time-resolved analysis was performed on four intervals, starting at 0.0 s, and ending at 5.120 s, 6.144 s, 8.192 s, and 9.216 s. Intervals up to 6.144 s have Band function unconstrained and COMP is by far the best-fit model. Interval ending at 8.192 s is still best fitted by COMP, although now the Band high-energy power-law index is constrained ($\beta \approx -4$) and C-STAT has the same value as the COMP model. ΔC-STAT for the (0.0 s, 9.216 s) interval between the COMP and the Band model is -7. Since the time-integrated spectrum is best fitted with a Band function, this suggests that the onset of the high-energy GBM component starts around 8 seconds post-trigger. Figure 3.14 shows the selected time interval corresponding to the possible P-GRB (left panel) and its spectrum. The best-fit was shown to be the COMP model, where $\alpha = -0.986(\pm0.057)$ and $E_{\rm p} = 721.4(\pm127)$ keV (right panel).

Model	$T_{\rm start}$(s)	$T_{\rm stop}$(s)	$E_{\rm p}$(keV)	α	β	F (erg cm^{-2}s^{-1})	C-STAT/DOF
Band	6.144	37.888	233.0(±13.9)	-0.7996	-1.779	$1.183(\pm0.010)\times10^{-6}$	1874.3/479

Table 10. Best-fit model parameters for the T_{90} duration of GRB 141028A. GBM catalog T_{90} and $T_{\rm start}$ values were 31.489 s and 6.656 s, respectively. GCN reported that *Fermi*/GBM data were also best fitted with a Band model, where $E_{\rm p} \approx 250$keV.

GRB 110731A

As many bright long bursts presented so far, bright GRB 110731A was also detected by numerous observatories. At 11:09:29.94 (UT) on 31 July 2011. It triggered the *Fermi*/GBM and caused an ARR (Gruber 2011). Burst was also detected by *Fermi*/LAT. With GRB being already in the LAT field of view (3.4° off-axis), repointing had little impact on the observation. The LAT followed the burst continuously from the initial trigger time up to 1400 s, when *Fermi* passed into the SAA. Although the observation continued up to 7400 s after *Fermi* exited the SAA at 3150 s, no significant signal was detected. The GBM light-curve was reported via GCN to consists of one pulse with a duration of about 7 seconds (50–300 keV). The corresponding time-integrated spectrum was best fitted by COMP model (with $\alpha = -0.82^{0.03}_{0.03}$ and $E_{\rm p} = 317^{10}_{10}$ keV), although it was reported that the Band function describes the spectrum equally well ($\alpha = -0.80^{0.03}_{0.03}$, $\beta = -2.98^{0.30}_{0.3^0}$ and $E_{\rm p} = 304^{13}_{13}$ keV).

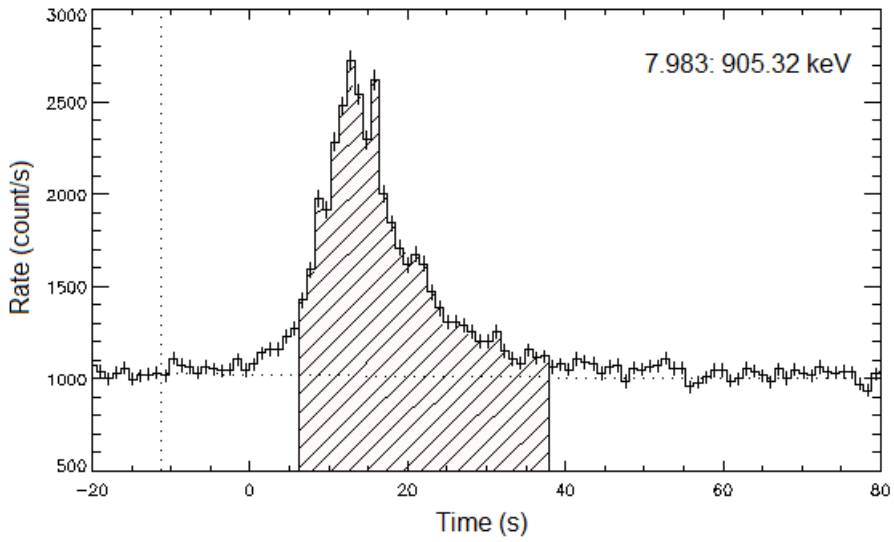

Figure 3.13. GRB 141028A (NaI-n9 detector) light-curve. The T_{90} interval used for fitting is marked dashed.

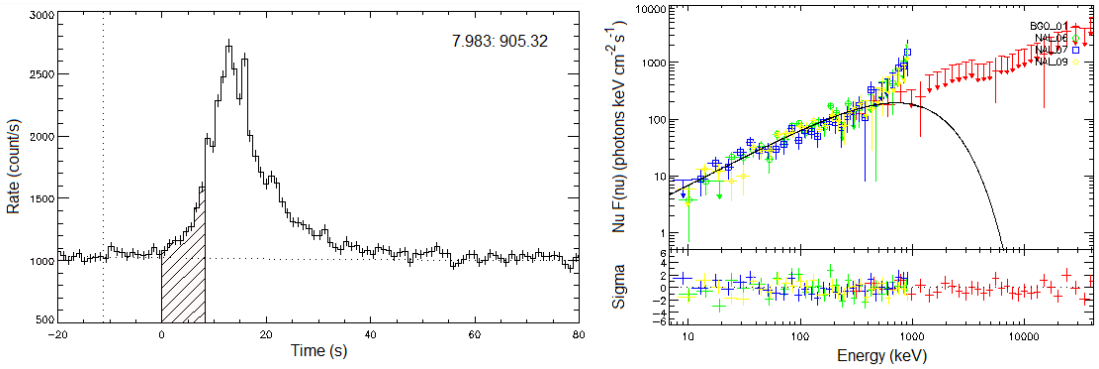

Figure 3.14. *Left panel:* Candidate P-GRB interval of GRB 141028A, starting at 0.0 s and ending at 8.192 s. *Right panel:* The $\nu F(\nu)$ *Fermi*/GBM spectrum of the same time interval, where the best-fit COMP model is parameterized with $E_{\rm p} = 721.4(\pm127)$ keV and $\alpha = -0.986(\pm0.057)$.

The *Swift*/BAT was also triggered by GRB 110731A and slew immediately to the burst (Oates et al. 2011; Krimm et al. 2011). The BAT light-curve showed a multiple-peaked structure with a long exponential decay lasting up 80 s (which is a significantly larger duration than the one reported in *Fermi*/GBM notice). As many BAT-observed bursts, GRB 110731A was best fitted with a simple PL with $\Gamma = -1.15(\pm0.05)$. The *Swift*/XRT began observations 56 s after the BAT trigger, while the spacecraft was still settling at the end of the initial slew. Two breaks were reported within the X-ray afterglow light-curve (Littlejohns et al. 2011). The initial PL decay ($\alpha = 1.04$) steepens after ~ 500 s ($\alpha = 1.183$) before breaking again at 29.0 ks ($\alpha = 4.2$). The burst was also observed in optical wavelengths by multiple observatories (e.g., Bersier 2011; Malesani et al. 2011), from which a decay PL index of $\alpha = 1$ was inferred (with no observed breaks). No radio signal was detected at the location of the afterglow (Zauderer et al. 2011). The progenitor system was located at the redshift of $z = 2.83$ (Tanvir et al. 2011). Other gamma-ray observatories also reported the detection of GRB 110731A, including the KONUS/*Wind* and the *Suzaku*/WAM (Golenetskii et al.

2011; Hanabata et al. 2011). While Suzaku/WAM measured a similar burst duration as the GBM, the KONUS/*Wind* detected the low-level, soft emission lasting up to 40 s post-trigger (as the *Swift*/BAT).

This burst is a part of the subgroup of three GRBs for which the next step was taken in order to give a fully comprehensive analysis within the fireshell model. This includes the simulations of the P-GRB, the light-curve and the matching spectrum. Therefore, a more detailed outline of the `rmfit` analysis is here presented. The selected detectors are the same as in Ackermann et al. (2013a), namely, the triggering detectors NaI-n0, n3 and the BGO-b0 detector. Figure 3.15 presents the reproduced LAT and BG-subtracted GBM light-curves of the prompt emission phase in several energy bands. Top two panels show data from the NaI-n0 (8–260 keV, top panel) and BGO-b0 (0.26–40 MeV, middle panel) detectors with 0.2 s binning. As it was mentioned in the *Fermi* GCN notice (Gruber 2011), GRB 110731A exhibits a complex single-peak structure starting around T_0-0.4 s with a sudden decrease in emission after $\sim T_0$+7.3 s, followed by an exponential decay up to ∼10 s. Here, T_0 refers to the GBM trigger time. The observed decay and the difference in T_{90} duration reported by the *Swift* team (Krimm et al. 2011) are consistent with the soft nature of the long GRBs. Since BAT (15–350 keV) is more sensitive to softer energies than GBM, it can detect fainter, softer emission, which results in longer T_{90} times. This possible sampling of only the hardest and brightest part of the spectrum by GBM can affect the derivation of the isotropic energy (e.g., see Virgili et al. 2012 for the comparison of the T_{90} values between the GBM and the BAT band). If the emission is interpreted as a single-pulse, the peak of the high-energy BGO emission occurs after the one visible on the beginning of the NaI light-curve. This means that the GRB 110731A has a negative lag (see Section 1.3).

Over the course of the *Fermi* mission, the event-level analysis software has been periodically updated. Bottom panel in Fig. 3.15 shows LAT 'P8R2_TRANSIENT020'-class events light-curve with 0.5 s binning. This latest Pass 8 release (P8R2) introduces significant changes to the event-level reconstruction, yielding to a substantial gain in instrument performance. As a result, sensitivity was improved over the whole LAT energy range and P8R2 contains many more events than Pass7 for a given time span. The 'P8R2_TRANSIENT020'-class events with energies 100 MeV–100 GeV were extracted from a circular region of 10° radius. Front and back-converting events were considered, with zenith angles less than 100°, in order to reduce the number of gamma rays from the Earth's limb. Although using P8R2 data resulted in a higher number of counts when compared to GRB 110731A light-curve in Ackermann et al. (2013a), the two observed features are still present: a delay of high energy emission (∼2.5 s) with respect to the prompt phase and the peak count rate after ∼ 5.5 seconds.

.

The time-integrated spectral analysis of the prompt emission was done using the interval starting at T_0+0.19 s, up to T_0+7.81 s, corresponding to the *Fermi* T_{90} interval. In order to determine the best fit model for the prompt emission, three different models were used: a simple PL, a PL with an exponential cut-off (COMP) and a Band function. Following Ackermann et al. (2013a), the spectrum of the prompt emission was also fitted using composite models, namely COMP+PL and Band+PL. In some GRBs, an additional PL component extrapolated from the GeV energies was found in the sub-MeV range (overpowering the Band model below ∼ 50 keV, see Section 1.2). The best-fit parameters for the time-integrated analysis are given in Table 12. The COMP fit showed significant improvement over the PL fit, while the Band function, having one parameter more, improved the fit by $\Delta C - STAT \approx 4$. Similar conclusions were reached by *Fermi*/GBM (Gruber 2011), Konus/*Wind* (Golenetskii et al. 2011) and *Suzaku*/WAM (Hanabata et al. 2011) team in their preliminary analysis. When compared to the Band model alone, adding a power-law reduced the C-stat value by ≈ 40, but the high energy photon index β=-9.64 was unconstrained. The COMP+PL had the same ΔC-stat as the Band+PL model, suggesting the possibility that the low energy LAT photons contribute to the GBM spectrum. The time-integrated spectrum corresponding to COMP and COMP+PL is shown in Fig. 3.16.

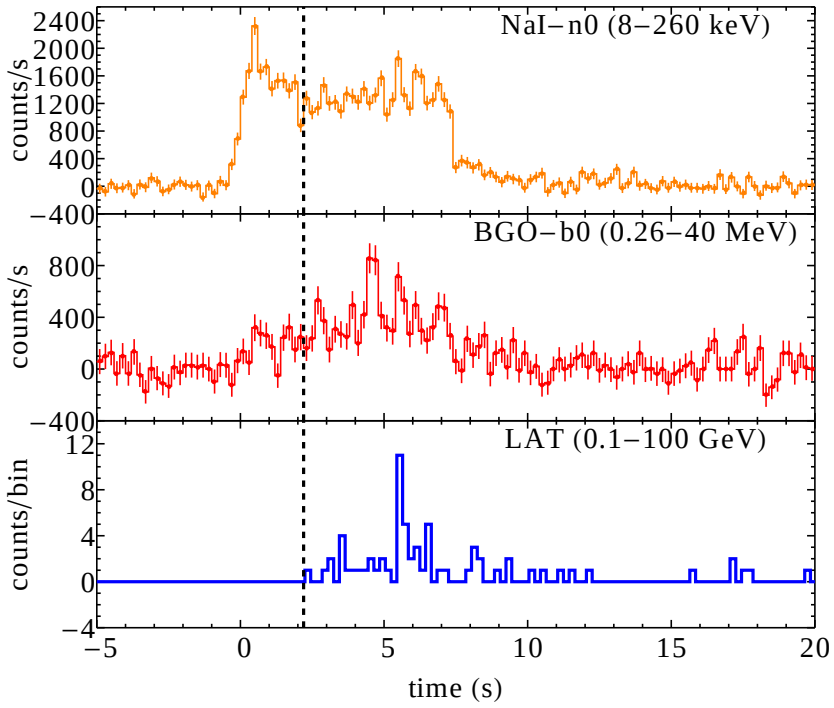

Figure 3.15. LAT and BG-subtracted GBM (NaI & BGO) light-curves of GRB 110731A. The top two panels have 0.2 s binning. The vertical dashed line indicates the onset of high energy emission observed by LAT. The LAT light-curve was generated using 'P8R2_TRANSIENT020'-class events with 0.5 s binning.

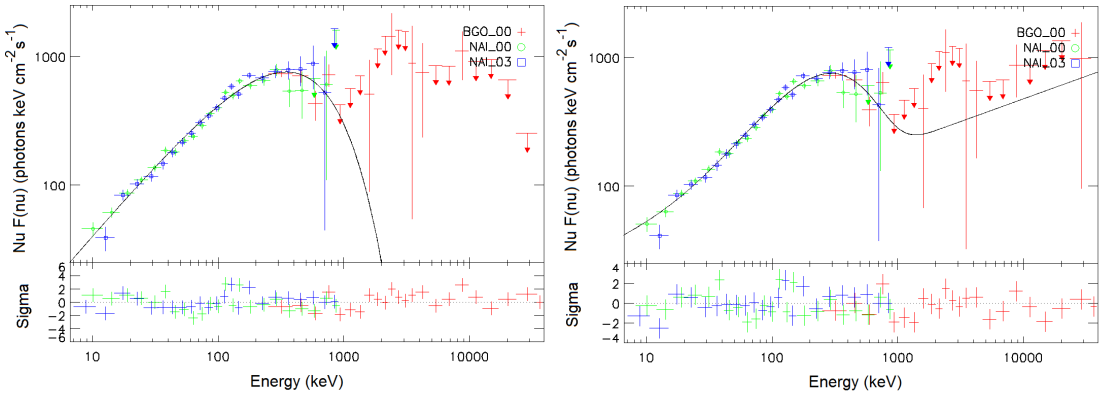

Figure 3.16. *Fermi*/GBM $\nu F(\nu)$ spectrum of GRB 110731A for the T_{90} time interval. Two out of five fitted models are shown: COMP model on the left panel and COMP+PL on the right panel.

So far, the T_{90} value provided by the *Fermi*/GBM catalog was used in order to estimate the isotropic energy of different bursts. However, since here the $E_{\rm iso}$ is used as an input parameter for the simulation of the fireshell expansion, the approach has been slightly adjusted. Keeping in mind that $E_{\rm iso}$ is actually an equivalent to the lower limit of $E^{\rm tot}_{e^+e^-}$ and that the emission was observed to last much longer than the T_{90} (Krimm et al. 2011; Golenetskii et al. 2011), the fitted interval included the long tail up to ~ 10 s that can be seen on the *Fermi*/GBM light-curve. In addition, Virgili et al. (2012) showed that a systematic underestimation of $E_{\rm iso}$ can occur for fits performed using a COMP model instead of Band (for the cases where both models fit equally well). On that account, the equally-well fitting Band function was fitted to the entire burst interval, starting at 0.0 s and ending at 10.56 s. The best-fit parameters were: $\alpha = -0.91^{+0.03}_{-0.03}$, $\beta = 2.19^{+0.07}_{-0.09}$ and $E_{\rm p} = 319.4^{+18.9}_{-16.8}$ keV, with an energy flux (10–1000 keV) of $F = 2.159(\pm0.032)\times10^{-6}$erg s^{-1} cm^{-2}. The isotropic equivalent energy was found to be $E_{\rm iso} = 6.05(\pm0.09)\times10^{53}$ erg.

In order to find a P-GRB, a time-resolved analysis was performed. Here, one expects to find either a spectrum described by a single thermal component or by a COMP model with the constant $E_{\rm p}$. depending on the geometry of the fireshell. In order to optimize the quality of the data, the light-curve interval before the GeV emission was binned using criteria of the constant signal to noise ratio (S/N). The criterion of S/N=20 was applied to the [0.00 s, 2.48 s] interval. Spectra of the six resulting bins were fitted to each of the following six models: a simple PL, the COMP model, Band and the same three empirical models with an added black body (BB) component. These fits were then compared for each time interval of interest. The time intervals and the best-fit results are showed in Table 13. For all bins, spectra were best described with the COMP model. The same result was obtained by Ackermann et al. (2013a, interval 'a'). The $E_{\rm p}$ evolution is plotted in the left panel of Figure 3.17. The first two bins were identified as the P-GRB interval. After the second bin, the $E_{\rm p}$ drops and then continues to monotony increase. Interestingly, the cut-off PL index α follows this pattern: after the second bin, it rises to an approximately constant value of $\alpha = -0.6$.

The binning is not uniquely defined just by the selected S/N value. The S/N criterion is applied to a signal of a certain duration as seen with only one of the (NaI) detectors loaded into the `rmfit` software. The resulting bin distribution is then applied to the rest of the detectors. Then, the length of the bins, and consequently the values of the computed parameters, also depend on the selected detector, the S/N value, and the time interval. The process was therefore repeated in order to check if the obtained $E_{\rm p}$ evolution (and the P-GRB duration) changes with a new binning. The S/N=15 was applied to a different detector. The time interval was also slightly changed. The first bin starts at -0.38 s while the last one ends at 2.40 s. Eleven bins were obtained in this way. Each of them was again fitted to six different models. The results are consistent with the previous analysis and are summarized in Table 14. The $E_{\rm p}$ evolution obtained with the S/N=15 binning criterion is shown in the right panel of Figure 3.17.

The interval starting at -0.384 s and ending at 0.686 s was taken as the P-GRB. The best-fit parameters of the COMP model are given in Table 11. They were used to obtain the P-GRB energy of $E_{\rm PGRB} = 3.7\times10^{52}$ erg.

Model	$T_{\rm start}$(s)	$T_{\rm stop}$(s)	$E_{\rm p}$ (keV)	α	F (erg cm^{-2}s^{-1})	C-STAT/DOF
COMP	-0.384	0.686	171.4(±16.4)	$-1.082(\pm0.079)$	$1.758(\pm0.085)\times10^{-6}$	443.6/361

Table 11. P-GRB spectral parameters used as a simulation input for GRB 110731A.

As for the GRBs described before, a (more robust) time-resolved analysis of the entire burst interval was carried out. In this way, best-fitting models could be compared between the different intervals. This consistency check is needed in order to confirm that a BB component does not appear in the prompt phase of the burst. This would pose a significant challenge to the fireshell model. Still, a BB can be found mid-emission if the GRB belongs to the BdHNe-II subclass. In this case, the observed gamma-ray light-curve is entirely made out of Episode 1 (see Section 2.8). As expected for the case of GRB 110731A (BdHNe-I), no BB was found. Following Ackermann et al. (2013a), the light-curve was divided into four different intervals. Results were consistent with the ones presented in Ackermann et al. (2013a), to which the reader is referred for more details. Namely, the first interval is best fitted with a COMP model (up to 2.44 s), while the rest is best-fitted by Band. $E_{\rm p}$ does not follow HTS nor the HIT pattern.

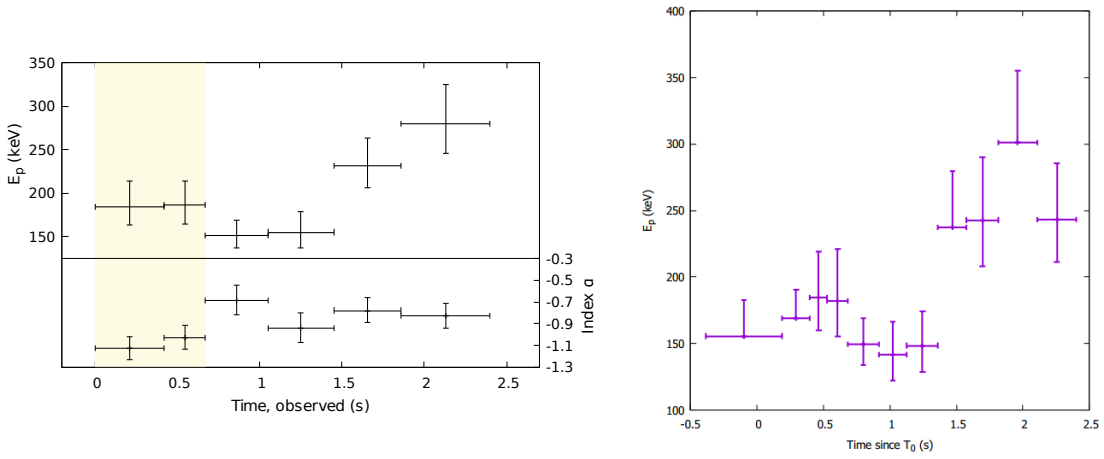

Figure 3.17. *Left panel:* Temporal evolution of the $E_{\rm p}$ spectral parameter within the COMP model (with $\pm 1\sigma$ error bars) for GRB 110731A. Time is given in the observer frame, starting with 0.0 s and ending at 2.48 s, with the binning criterion of S/N=20. The corresponding power-law index α is also given in the bottom. The P-GRB interval, consisting of the first two bins, is highlighted in red. *Right panel:* The same GRB 110731A $E_{\rm p}$ evolution, where a different NaI detector light-curve was binned to S/N=15. The interval was also slightly changed, here starting at -0.384 s and ending at 2.404 s.

Model	$E_{\rm p}$ (keV)	α	β	Γ	F (erg cm^{-2}s^{-1})	C-STAT/DOF
PL	-	-	-	$-1.509^{+0.006}_{-0.005}$	$2.607(\pm0.027)\times10^{-6}$	1926.6/360
Compton	$348.1^{+13.2}_{-12.3}$	$-0.859^{+0.026}_{-0.026}$	-	-	$2.848(\pm0.047)\times10^{-6}$	618.8/359
Band	$330.7^{+16.4}_{-15.9}$	$-0.850^{+0.030}_{-0.028}$	$-2.548^{+0.161}_{-0.291}$	-	$2.835(\pm0.043)\times10^{-6}$	614.1/358
Compton+PL	$282.2^{+12.9}_{-12.0}$	$-0.320^{+0.132}_{-0.124}$	-	$-1.647^{+0.031}_{-0.032}$	$2.744(\pm0.046)\times10^{-6}$	574.2/357
Band+PL	$282.9^{+12.1}_{-12.7}$	$-0.326^{+0.138}_{-0.115}$	$-9.638^{+23.400}_{-\infty}$	$-1.647^{+0.031}_{-0.032}$	$2.747(\pm0.048)\times10^{-6}$	574.2/356

Table 12. Summary of best-fit parameters obtained from the time-integrated spectral analysis of GRB 110731A. Each column lists: the spectral model, the peak energy in the $\nu F(\nu)$ spectrum $E_{\rm p}$, the low-energy α and the high-energy β photon indices, the power-law photon index Γ, the energy flux F and the C-STAT value over the number of DOF. The reference energy is fixed to 100 keV. The energy flux is evaluated for the 10–1000 keV range.

Time bins (s)	Best-fit COMP				STAT/DOF (other models)				
	$E_{\rm p}$ (keV)	α	F (erg cm^{-2}s^{-1})	C-STAT/DOF	PL	PL+BB	Compt+BB	Band	Band+BB
[0.00,0.42]	$184.5^{+29.0}_{-20.9}$	$-1.125^{+0.103}_{-0.102}$	$2.08(\pm0.15)\times10^{-6}$	390.3/359	439.5/360	393.0/358	382.8/357	390.3/358	383.2/356
[0.42,0.67]	$186.4^{+27.9}_{-21.4}$	$-1.027^{+0.111}_{-0.106}$	$3.16(\pm0.22)\times10^{-6}$	381.0/359	436.9/360	391.0/358	379.3/357	380.5/358	379.1/356
[0.67,1.05]	$151.8^{+17.6}_{-14.4}$	$-0.687^{+0.144}_{-0.133}$	$2.22(\pm0.13)\times10^{-6}$	370.6/359	463.4/360	369.9/358	365.6/357	363.4/358	363.1/356
[1.05,1.45]	$155.3^{+23.9}_{-18.4}$	$-0.942^{+0.117}_{-0.129}$	$1.86(\pm0.13)\times10^{-6}$	424.0/359	477.6/360	426.3/358	421.9/357	422.6/358	422.0/356
[1.45,1.86]	$231.6^{+31.6}_{-25.3}$	$-0.779^{+0.118}_{-0.110}$	$2.60(\pm0.17)\times10^{-6}$	360.7/359	461.4/360	380.4/358	354.9/357	360.1/358	354.9/356
[1.86,2.40]	$279.9^{+45.1}_{-34.2}$	$-0.827^{+0.118}_{-0.110}$	$2.25(\pm0.16)\times10^{-6}$	437.6/359	514.3/360	439.5/358	436.6/357	437.3/358	435.1/356

Table 13. Results of the time-resolved spectral analysis for GRB 110731A. Bins correspond to portions of the light-curve for which S/N=20. The best fit was a COMP model for all the time intervals. The C-STAT values of other (rejected) models are given for comparison.

Time bins (s)	Best-fit COMP		STAT/DOF (other models)				
	$E_{\rm p}$ (keV)	C-STAT/DOF	PL	PL+BB	COMP+BB	Band	Band+BB
[−0.38.0.19]	$155.7^{+26.9}_{-0.0}$	413.2/361	429.7/362	413.8/360	412.5/359	413.2/360	413.1/358
[0.19, 0.40]	$168.9^{+21.6}_{-0.0}$	368.3/361	403.0/362	366.7/360	361.9/359	368.3/360	-NaN/358
[0.40, 0.53]	$184.7^{+34.5}_{-24.6}$	319.1/361	361.8/362	332.7/360	314.9/359	319.0/360	315.1/358
[0.53, 0.67]	$181.9^{+38.9}_{-26.9}$	331.6/361	359.8/362	332.4/360	331.1/359	330.0/360	329.8/358
[0.67, 0.92]	$149.3^{+19.8}_{-15.3}$	362.3/361	421.3/362	364.5/360	362.2/359	361.7/360	360.1/358
[0.92, 1.13]	$141.7^{+24.8}_{-19.7}$	373.7/361	425.8/362	369.1/360	361.4/359	362.0/360	361.2/358
[1.13, 1.36]	$148.5^{+25.8}_{-19.5}$	357.7/361	393.2/362	359.3/360	357.2/359	358.1/360	358.7/358
[1.36, 1.58]	$237.3^{+42.3}_{-0.0}$	365.1/361	391.8/362	368.9/360	363.4/359	364.4/360	363.9/358
[1.58, 1.81]	$242.8^{+47.3}_{-34.5}$	366.9/361	429.5/362	380.3/360	361.6/359	365.0/360	361.5/358
[1.81, 2.11]	$301.0^{+54.2}_{-0.0}$	431.8/361	455.8/362	433.8/360	425.9/359	430.2/360	424.1/358
[2.11, 2.40]	$243.2^{+42.4}_{-31.6}$	421.6/361	487.5/362	419.6/360	418.7/359	421.8/360	418.6/358

Table 14. Results of the repeated time-resolved spectral analysis for GRB 110731A. Bins correspond to portions of the light-curve for which S/N=15. The best fit was COMP for all the time intervals. The C-STAT values of other (rejected) models are given for comparison.

GRB 151027A (and the case of GRB 140206A)

The *Fermi*/GBM triggered at 3:58:24.03 (UT) and located GRB 151027A on 27 October 2015 (Toelge et al. 2015). Although the angle from the *Fermi*/LAT was 10 degrees, no high-energy emission was observed. Hence, it was suggested that this GRB should be a part of a sample that would probe the angular distribution of the high energy emission (Ruffini et al. 2015c). Three different pulses are visible in the GBM light-curve, with a duration of about ~ 130 seconds. The time-averaged spectrum up to ~ 133 s was reported to be best fitted by COMP, with $\alpha = -1.41(\pm 0.04)$ and $E_{\rm p} = 340(\pm 63)$ keV. Similar duration was reported by the KONUS/*Wind* notice (Golenetskii et al. 2015), but with a much softer spectral peak energy $E_{\rm p} = 178^{+135}_{-46}$ keV. The $E_{\rm p}$ near the maximum count rate (first pulse) was found to be even softer, with $E_{\rm p} = 91^{+14}_{-11}$ keV, suggesting that this burst does not obey either the HIT or HTS evolution patterns. The burst was also observed with all three detectors onboard the *Swift* spacecraft (Maselli et al. 2015). Only two different peaks are resolved in the BAT light-curve, lasting around 170 seconds, including the quiescent period. The last of the two is best-fitted with a PL model (Palmer et al. 2015). The XRT light-curve can be modeled with a series of power-law decays, with two flares superimposed at early times (Page et al. 2015). These breaks add up to a classical FPA light-curve. The first flare was observed at the very beginning of the light-curve, starting 80 seconds after the BAT trigger. The *Swift*/UVOT began observing the field 96 s after the BAT trigger (Balzer et al. 2015). A chaotic light-curve was reported by the initial observations (Wren et al. 2015). At later times the emission decayed with a power-law index of ~ 1.9 (Cenko & Perley 2015). Other observatories also detected optical and radio transient coinciding with the location of the GRB 151027A (e.g., Cano 2015; Wiggins 2015; Moskvitin 2015; Zheng & Filippenko 2015; Chandra & Nayana 2015a;b; Laskar et al. 2015). The burst occurred at the redshift of $z = 0.81$ (Perley et al. 2015; Zhang et al. 2015), which is still in the limit of the possible SN detection. Tentative evidence of an emerging SN was indeed found in the late-time optical observations (e.g., see Nappo et al. 2017).

Comparing the reported T_{90} values with an actual summed duration of the three pulses (≈ 75 s), GRB 151027A is an example of how the T_{90} definition can cause an overestimation of duration. However, the last observed pulse coincides with the hard X-ray flare observed with the *Swift*/XRT. Therefore, within the fireshell model and the IGC paradigm, the prompt emission (UPE) duration of GRB 151027A is much shorter. It encompasses the first 25 seconds, as shown on the left panel in Figure 3.18. The two peaks can

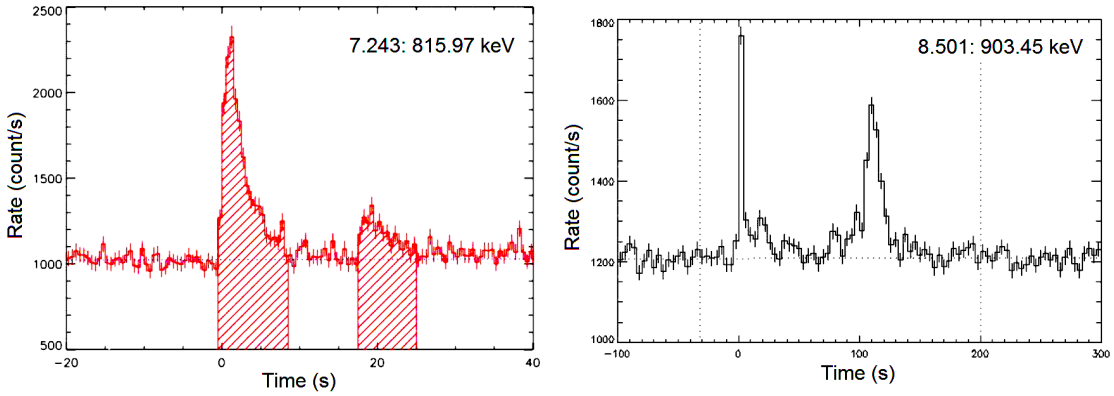

Figure 3.18. *Left panel:* UPE phase of GRB 151027A (NaI-n0 detector light-curve). It consists of two peaks separated by a quiescent period. Each bin has a 0.5 second duration. *Right panel:* Entire observed *Fermi*/GBM emission (NaI-n1 detector light-curve), including the X-ray flare at ~ 100 s. Each bin has a 4 second duration.

be seen, each lasting for about ~ 8 seconds. Ruffini et al. (2018g) considered a possibility that the two peaks are directly connected to the central engine activity. This view was extended to the two X-ray flares observed at the beginning of the FPA phase. These are then also a reflection of the same mechanism. If that is the case, then the time difference between the UPE double component and the flares is set by the propagation of the e^+e^- plasma through the SN ejecta and the rotational period of the system.

Detectors NaI-n0,n1,n3 and BGO-b0 were used in the time-integrated and the time-resolved analysis. Both pulses in the UPE phase are best fitted by COMP, as reported by the *Fermi* team (see Figure 3.19). However, PL+BB also gave a satisfying fit, with the $\Delta C - STAT = 7$ when compared to COMP. Following the GCN-reported analyses, the COMP model was chosen. Since the fireshell propagation was simulated only for the case of the first pulse, their isotropic energies were calculated separately. Best-fit parameters and E_{iso} are given in Table 15. A full, multiwavelength analysis of GRB 151027A within the IGC/BdHNe can be found in Ruffini et al. (2018g).

Model	T_{start}(s)	T_{stop}(s)	E_p(keV)	α	E_{iso} (erg)
COMP	-0.1	8.4	172.5(±19.3)	−1.296(±0.056)	$7.26(\pm0.36)\times10^{51}$
COMP	17.5	25.0	147.4(±46.2)	−1.356(±0.162)	$4.99(\pm0.60)\times10^{51}$

Table 15. Best-fit model parameters for GRB 151027A. For both pulses, here analyzed separately, the COMP model was shown to provide the best fit. Last column lists the isotropic equivalent energy for each pulse.

The time-resolved analysis of 0.1 seconds was done for the two peaks. While the second peak appears to be featureless, an extra BB component was found in the first second of the first peak, superimposed on the previous Compton model. This corresponds to the P-GRB emission when the e^+e^- plasma reaches the point of transparency. The best fit model for the [-0.1 s, 0.9 s] interval was therefore a COMP+BB, with kT = 36.6(±5.2) keV, and an energy of E_{BB} = 0.074(±0.038) $E_{iso,1}$ (see Figure 3.20). Here, $E_{iso,1}$ is the isotropic energy of the first peak. Since a BB component was directly observed, the P-GRB energy is in this case equal to E_{BB}.

Ruffini et al. (2018g) made a parallel between GRB 151027A and GRB 140206A. The light-curve of this burst also contains multiple pulses separated by a quiescent period. GRB 140206A was observed by multiple detectors on various spacecrafts, including the *INTEGRAL* (Gotz et al. 2014), the *Swift*/BAT

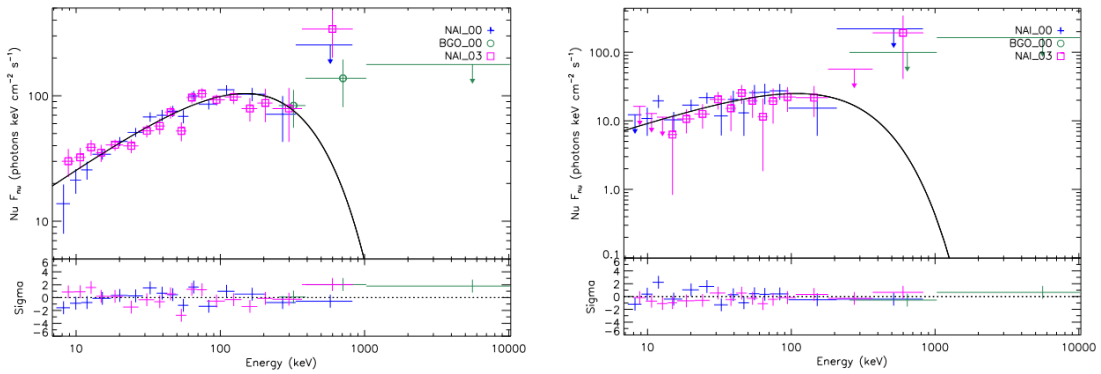

Figure 3.19. *Left panel:* Observed spectrum of the first pulse found in the light-curve of GRB 151027A and its best-fit model. The time-integrated analysis corresponds to the [-0.1 s, 8.4 s] interval. *Right panel:* The observed spectrum of the second pulse and its best-fit model, corresponding to the [17.5 s, 25.0 s] interval.

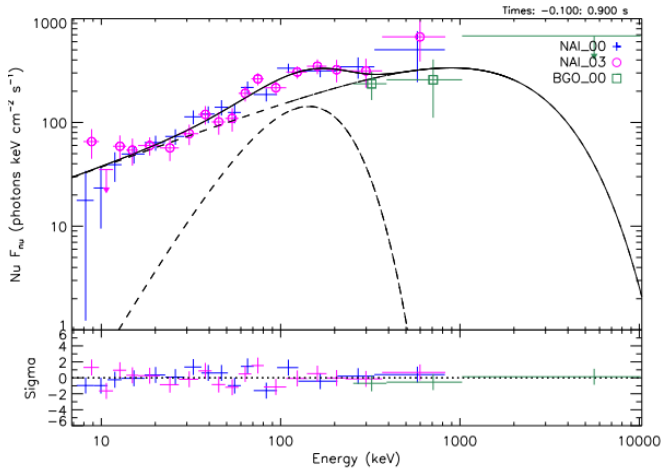

Figure 3.20. COMP+BB spectrum found within the first second of GRB 151027A. The dashed line shows the BB component with $kT = 36.6(\pm 5.2)$ keV.

(Lien et al. 2014) and the *Fermi*/GBM (von Kienlin & Bhat 2014). Redshift was reported to be z=2.73 (Malesani et al. 2014b). Unfortunately, *INTEGRAL* observations encountered technical difficulties. The detection time coincided with the very beginning of the *INTEGRAL's* orbit, just outside the radiation belts, making the data polluted by a high particle BG. The *Fermi*/GBM did not have more luck. Only the second peak of the GRB has been detected in the GBM data because, during the first peak, the source was occulted by Earth. Therefore, a joined BAT/GBM analysis is needed in the future in order to repeat the procedure as for GRB 151027A. The angle from the *LAT* boresight was 123 degrees, too far for a meaningful detection of high energy photons. Nevertheless, BAT observed a multi-peaked structure with a duration of about 90 seconds (Figure 3.21). The first pulse duration starts at ~ -15 s and ends at ~ 25 s, containing roughly three to four peaks. The second one starts at around ~ 50 s and ends at ~ 90 *rms* and it also contains multiple peaks. There is also a hint of a third, weaker pulse peaking at ~ 210 seconds

(Sakamoto et al. 2014). The *Swift*/XRT began observations 44 s after the BAT trigger. Light-curve showed an initial flaring activity consisting of two spikes at about 61 s and 223 s after the trigger. These flares coincide with the second and the third observed in gamma-rays. As noted in Section 2.8, this shows that the so-called classical prompt emission and the X-ray afterglow can not always be easily distinguished. This calls for an occasional redefinition of the burst duration.

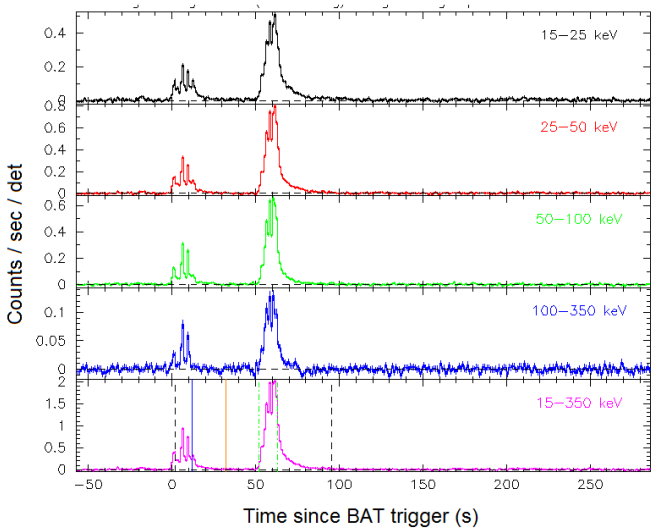

Figure 3.21. *Swift*/BAT light-curve in different energy bands of GRB 140206A. Two pulses with the separation of ∼ 50 s are visible. The image was obtained from the NASA database site `https://swift.gsfc.nasa.gov`.

If the parallel between the two GRBs is drawn, the first (occulted) spike should correspond to the double peak in GRB 151027A, making it the UPE phase of GRB 140206A. A time-resolved analysis was performed for the second spike which corresponds to the flaring activity. Starting at 1.024 s before the GBM trigger, three intervals separated at 4.096 s and 8.192 s were fitted to different models. The third interval encompassed the long decay and ended at 26.624 s after the trigger. The detectors No BB component was found, but this does not exclude that it exists in the X-ray domain. The best-fitting model for all three segments was found to be the Band function. Figure 3.22 (left panel) shows the GRB 140206A light-curve as observed by *Fermi*/GBM. The interval used for the time-integrated analysis is marked dashed. As expected, the best fit was a Band function (right panel), with parameters listed in Table 16.

Model	$T_{\rm start}$(s)	$T_{\rm stop}$(s)	$E_{\rm p}$(keV)	α	β	F (erg cm^{-2}s^{-1})	C-STAT/DOF
BAND	0.00	26.62	123.4(±6.4)	−0.075	2.328	$6.12(\pm0.16)\times10^{-7}$	664.8/358

Table 16. Best-fit model parameters for the time-integrated analysis of GRB 140206A. GBM catalog T_{90} and $T_{\rm start}$ values were 27.264 s and 0.512 s, respectively. The indicated times encompass only the second pulse, since *Fermi*/GBM could not detect the first one due to the observational constraints.

Here, I will take the opportunity to note that an equally good parallel can be drawn using GRB 180728A, a member of the BdHNe-II subclass already discussed in Section 2.9. As GRB 151027A, it was in the optimal position for high-energy detection. The angle from the LAT boresight was 35° degrees. Still, no GeV photons were observed. The light-curve also consists of two, well-separated spikes where the brighter one is well-fitted with a PL+BB. The energy of the brighter pulse has the same order of magnitude

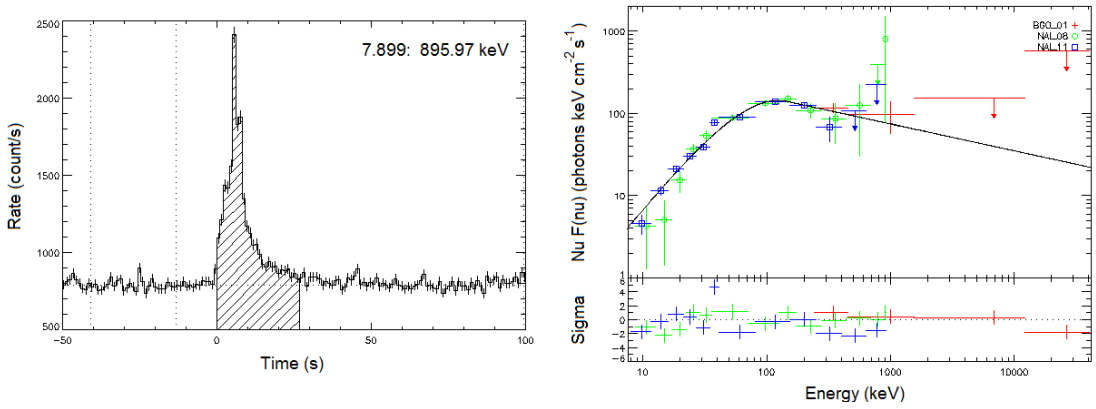

Figure 3.22. *Fermi*/GBM (NaI-n11 detector) light-curve of GRB 140206A is shown on the left. The time-integrated spectrum, corresponding to the dashed interval, is best fitted with a Band function (shown on the right).

as the one found in GRB 151027A. In addition, the total energy of GRB 151027A lies on the $\sim 10^{52}$ erg separation limit for the BdHNe-I and BdHNe-II subclasses. Considering all of the above, a possibility that GRB 151027A is an XRF should not be discarded. However, if the X-ray flares originate from the interaction of the e^+e^- plasma with the SN remnant (Section 2.9), they signal the BH birth in a similar manner as the LAT detection does. This, on the other hand, means that GRB 151027A belongs in the BdHNe-I class. Unfortunately, the *Swift*/XRT observations of GRB 180728A started quite late (Perri et al. 2018), making it impossible to determine if the X-ray flares were present.

3.3 LIGHT-CURVE AND SPECTRAL SIMULATIONS

In the former section it was shown how different quantities were obtain through the means of `rmfit` analysis. These quantities, namely $E_{\rm iso}$, $E_{\rm BB}$ (or $E_{\rm P-GRB}$) and kT ($E_{\rm p}$), are needed for the next step, the simulation of the UPE light-curve and its spectrum (see Section 3.1). This is done solving the equations of the dynamics of the e^+e^--baryon plasma and its interaction with the CBM (as explained in Section 2.4). This section summarizes the main results of the fireshell simulation for two bursts: GRB 110731A and GRB 151027A.

GRB 110731A

The value of $E_{\rm iso}$ (Section 3.2), together with the some arbitrary value of baryon load B, served as an input for the numerical code. The observed peak energy $E_{\rm p} = 171.9$ keV corresponds to the effective temperature of $kT^{\rm RF} = E_{\rm p}(1+z)/3.92 = 167.9$ keV (in the reference frame of GRB 110731A). A match of the observed and simulated quantities was obtained for the baryon load $B = 4.35\times10^{-4}$. At the transparency point, the laboratory radius was 8.33×10^{13} cm. Here, the Lorentz factor was $\Gamma \sim 2.17\times10^{3}$ and the rest-frame temperature was $kT^{\rm RF}_{\rm sim} = 168$ keV. The simulated light-curve and the corresponding spectrum are showed in Figure 3.23 and Figure 3.24. The simulation starts after the P-GRB (solid red line in Figure 3.23) and ends at the point marked with the black dashed line, after which the simulation becomes inaccurate (see

Section 3.1). The resulting CBM distribution is showed in Figure 3.25, with an average value of ~ 0.03 particles per cm^3. Two surface filling factors values were used: $\mathcal{R} = 3.0 \times 10^{-10}$ and $\mathcal{R} = 4.6 \times 10^{-9}$, for distances smaller and larger than 16.4×10^{16} cm, respectively.

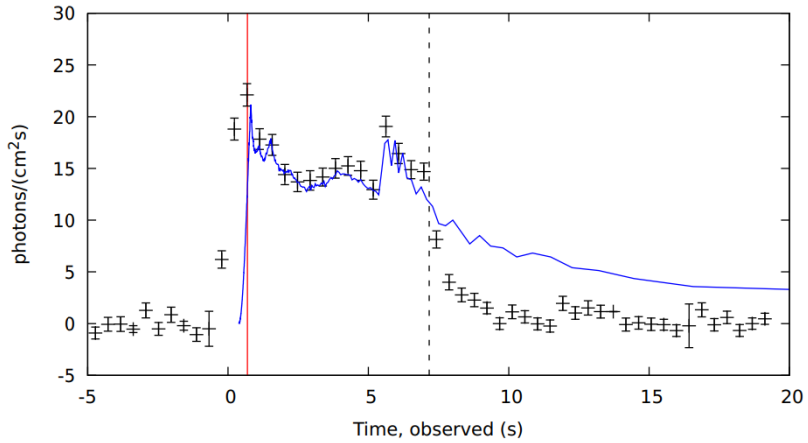

Figure 3.23. Simulated and NaI-n3 detector (0.2 s binning) light-curve of GRB 110731A. Red vertical line at 0.69 s marks the end of P-GRB. The dashed line marks the end of the time interval used to simulate the spectrum.

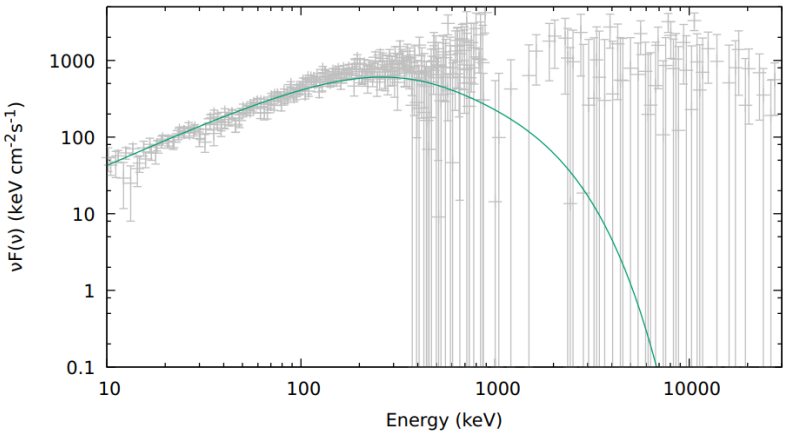

Figure 3.24. Simulated $\nu F(\nu)$ prompt emission spectrum of GRB 110731A (solid line), superimposed on the joined NaI-n0,n3 and BGO-b0 (observed) spectrum.

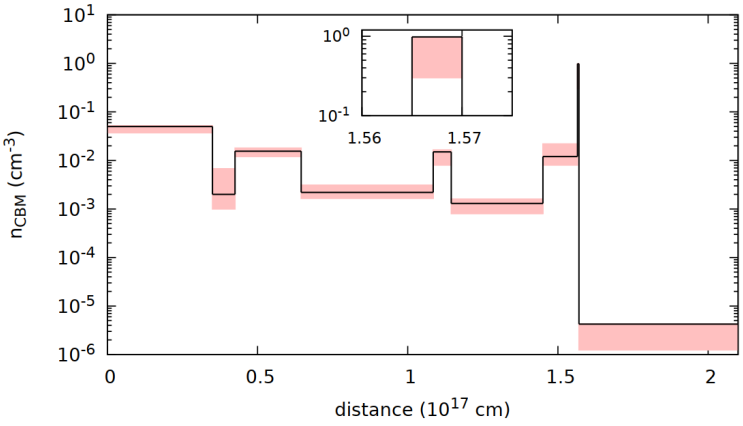

Figure 3.25. Density profile of the CBM derived for GRB 110731A. Here, the $n_{\rm CBM}$ errors were determined by the means of light-curve simulation (indicated in red).

GRB 151027A

The initial e^+e^- plasma energy was assumed equal to the isotropic equivalent energy of the first pulse. The P-GRB temperature in the reference frame of the burst is equal to: $kT^{\rm RF} = 36.6(1+z)$ keV = 66.24 keV. The ratio between the isotropic and the P-GRB energy was found to be 0.074(±0.038). These values were also obtained in the simulation for a baryon load $B = 1.92\times10^{-3}$, where the $E_{\rm iso}/E_{\rm P-GRB}$ was within 1σ limit (≈ 0.037). For GRB 151027A, the fireshell reaches transparency at the radius of 1.92×10^{13} cm. Here, a flash of thermal radiation was emitted, with $kT^{\rm RF}_{\rm sim} = 66.15$ keV the fireshell reached the ultra-relativistic speeds, with Lorentz factor $\Gamma \sim 503$. The first-pulse of GRB 151025A has a simple, FRED shape. This was reflected in the CBM density distribution. An agreement with the observed light-curve (from 0.9 s to 9.44 s, see Figure 3.26) and spectrum (Figure 3.27 - left panel) was achieved for the CBM distribution showed in the right panel of Figure 3.27. An average CBM density is therefore ~ 15 cm^{-3} (ignoring the part that extends to infinity). This is consistent with a typical value of the long GRB host galaxies at 10^{16} cm radii. Due to the simplicity of the light-curve, a constant value of $\mathcal{R} = 1.5\times10^{-8}$ was sufficient to make the fit.

3.4 CASE OF GRB 090618

The debut of the IGC paradigm happened with GRB 090618 (Izzo et al. 2012a), As the model progressed and evolved, GRB 090618 was revisited two additional times. Both of these analyses are presented in this work. This is the third, final burst which has been given a full treatment within the fireshell model.

Observations of GRB 090618

GRB 090618 was detected by numerous gamma-ray observatories, all of which observed a complex light-curve that lasted for ~ 150 s. The *Fermi*/GBM resolved four different pulses (McBreen 2009). The time-averaged spectrum is best described with a Band function (in which $\alpha = -1.26^{+0.06}_{-0.02}$, $\beta = -2.50^{+0.15}_{-0.33}$ and $E_{\rm p} = 155.5^{+11.1}_{-10.5}$ keV). The angle from the LAT boresight was 133°, too far for a significant high-energy

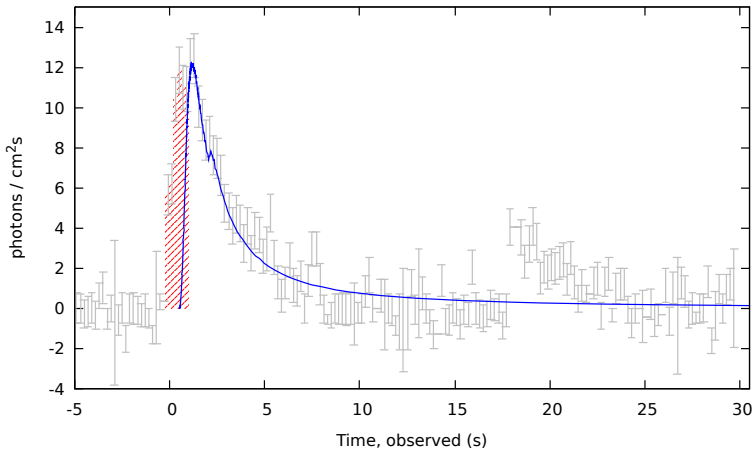

Figure 3.26. Observed and the simulated light-curve for the [0.9 s, 9.4 s] interval of GRB 151027A. The dashed red area marks the P-GRB interval.

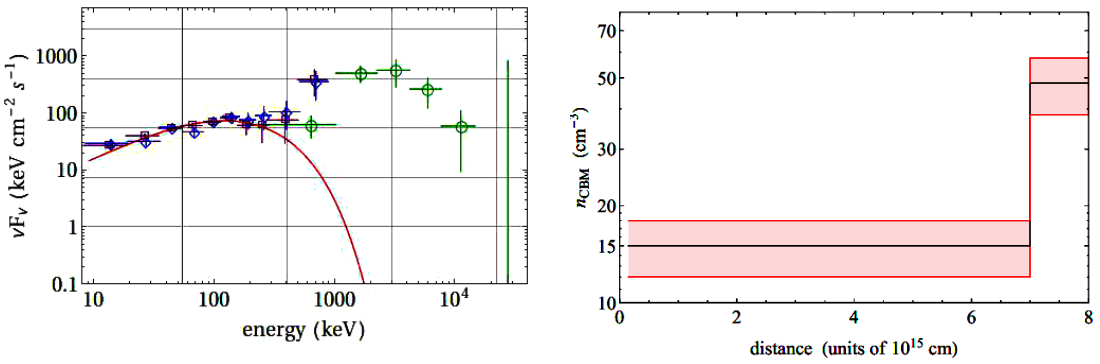

Figure 3.27. *Left panel:* The simulated spectrum of GRB 151027A for the [0.9 s, 9.4 s] interval, together with the observed *Fermi*/GBM spectrum. The interval corresponds to the simulated UPE phase. Spectral peaks coincide at 122 keV. *Right panel:* Density profile of the CBM derived for GRB 151027A. For this GRB, $n_{\rm CBM}$ errors were also determined through the light-curve simulation and are indicated in red.

detection. Still, AGILE also did not detect any emission above 30 MeV, despite covering the energy range up to 60 GeV (Longo et al. 2009). The KONUS/*Wind* and the *Suzaku*/WAM both obtained time-integrated spectral parameters similar to the ones reported by *Fermi*/GBM (Golenetskii et al. 2009a; Kono et al. 2009). Although, a significant spectral hardening was seen at the peak of the emission. Similar to the case of GRB 151027A, all of the detectors onboard *Swift* observed GRB 090618 (Schady et al. 2009). The BAT light-curve had a duration of about ~ 300 seconds (Sakamoto et al. 2009a). The peak spectral energy was soft enough to fall within the *Swift*/BAT range. The time-integrated spectrum was therefore also best described with a COMP model. The X-ray light-curve initially decayed with a slope of ~ 6, before breaking at 310 s to a shallower decay of 0.71. After ~ 1 h, the decay steepened again, with the power-law index of 1.22 (Beardmore & Schady 2009). The light-curve follows the canonical X-ray behavior described in Section 1.2.

The complexity of prompt emission was also reflected in the optical afterglow, which rebrightened after ~ 90 s and then declined again 120 seconds post-trigger. As in the X-ray wavelengths, two breaks were observed. However, not at the same times. The first one happened at 600 s. The power-law index changed from 1.08 to 0.70 (Li et al. 2009; Melandri et al. 2009). Another break happened 14.6 hours after the trigger, where the decay index steepened to the value of 1.4 (Cenko 2009). A series of other telescopes also observed the afterglow in radio wavelengths (Updike et al. 2009; Kamble et al. 2009; Chandra & Frail 2009). The redshift of this GRB was determined to be $z = 0.54$ (Cenko et al. 2009; Fatkhullin et al. 2009). Upon a closer inspection, an underlying SN was detected in the optical afterglow (Cano et al. 2011).

`Rmfit` analysis - the P-GRB search

The P-GRB search was somewhat alleviated since the BB component was already found in the work of Izzo et al. (2012b). Gamma-ray light-curve consists of four distinct pulses. The first pulse is well separated from the other three, which overlap to some extent (Figure 3.28). Izzo et al. (2012b) showed that the first pulse corresponds to Episode 1, rarely identified in BdHNe-I. In this work, three consequent pulses after the Episode 1 are refereed to as the first, the second and the third pulse. According to the new developments in the IGC paradigm, the third pulse was not anymore interpreted as a part of the prompt emission, but as the onset of the X-ray afterglow. Hence, the analysis of Izzo et al. (2012b) was repeated in order to see how the changes in $E_{\rm iso}$ influence the final results (and if they can be reproduced at all). As it was mentioned in Section 3.1, the fitting process is governed by the equations that describe the fireshell and the baryon dynamics. These equations form a direct link between the P-GRB analysis and the light-curve simulation. Their agreement with data can not be independently optimized in a way that allows some arbitrary, but well-fitted light-curve. For example, Izzo et al. (2012b) initially considered the PL+BB found in the first ~ 50 s (now Episode 1) as the P-GRB. In this attempt the whole observed GBM emission corresponded to the UPE phase. They found that this interpretation was not sustainable due to the source energetics, the P-GRB duration and its temperature. A comparison of the results obtained in this work with the one of Izzo et al. (2012b) is given further below.

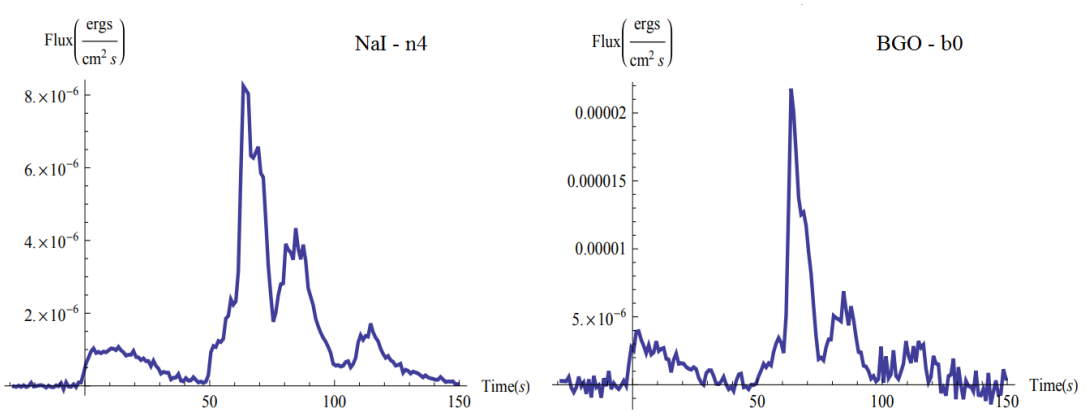

Figure 3.28. Light-curve of GRB 090618 as seen by the NaI (left panel) and the BGO (right panel) detector onboard the *Fermi* observatory. Four different pulses are visible. Figure taken from Izzo et al. (2012b).

Keeping in mind that the third pulse is now viewed as the high-energy end of the X-ray emission, the prompt phase begins at $T_0 + 50.0$ s and ends at $T_0 + 105$ s. This is equal to the B-C-D-E time interval in Izzo et al. (2012b). The goodness of the fit was estimated using χ^2-statistic. Band was the best-fitting model, in which $\alpha = -1.21(\pm 0.04)$, $\beta = -2.57(\pm 0.18)$ and $E_{\rm p} = 237.8(\pm 11.7)$ keV. The new isotropic equivalent energy of GRB 090618 was now equal to $E_{\rm iso} = 1.94(\pm 0.02) \times 10^{53}$ erg.

Izzo et al. (2012b) found a BB signature in the early seconds of the prompt emission: the 50–59 s interval was equally well fitted with Band and with PL+BB. This pointed towards a different emission mechanism. The P-GRB duration was confined to the first 4 seconds based on the time variability of the thermal component. Following their analysis, the beginning of the first pulse (starting at $T_0 + 50$ s) was divided into 12 one-second duration intervals (up to $T_0 + 62$ s). The Cash statistic was used because time-resolved intervals can contain a low number of counts. These counts were observed with NaI-n4 and BGO-b0 detectors. The C-STAT values were compared for five different models: a simple PL, PL+BB. COMP, COMP+BB, and Band. In the first two seconds, the COMP model provided the best fit. The composite PL+BB model had similar C-STAT value, with the observed temperature of $kT = 34.9(\pm 6.4)$ keV (for the first second) and $kT = 22.5(\pm 2.7)$ keV (for the second second). After second 52, until second 54, the PL+BB became an equally good or bother-line better fit than the COMP model. The observed BB temperatures for these two bins were $kT = 17.4(\pm 2.5)$ keV and $kT = 29.6(\pm 3.9)$ keV. For the time bins that followed, the PL+BB fit got progressively worse. No BB component was observed up to $T_0 + 59$ s as in the work of Izzo et al. (2012b). In addition, the C-STAT values did not show that the Band function and the PL+BB were best-fitting models. The data was always described better with the COMP model rather than Band. Adding a BB component to the COMP model also did not improve any of these fits. Next, a two-second time-resolved analysis was carried out, up to 74 seconds after the trigger time. No BB component was found. Therefore, it was concluded that the first prompt peak is featureless and that the P-GRB (possibly) lasts up to 54 s. Details of the time-resolved analysis up to 62 s are given in Table 17. Spectra of COMP and PL+BB models for the first four seconds are compared in Figure 3.29.

Time bins (s)	COMP/BB parameters		STAT/DOF				
	$E_{\rm p}$ (keV)	kT (keV)	PL	PL+BB	COMP	COMP+BB	Band
[50.0, 51.0]	188.2(±48.3)	34.9(±6.4)	299.5/241	284.6/239	282.2/240	281.9/238	282.3/239
[51.0, 52.0]	176.8(±29.5)	22.5(±2.7)	328.1/241	297.4/239	294.5/240	290.8/238	291.7/239
[52.0, 53.0]	204.8(±52.3)	17.4(±2.5)	284.5/241	268.6/239	275.4/240	268.3/238	267.1/239
[53.0, 54.0]	175.4(±25.2)	29.6(±3.5)	333.4/241	295.9/239	303.4/240	302.2/238	301.6/239
[54.0, 55.0]	197.4(±32.6)	33.9(±4.4)	282.5/241	251.3/239	242.7/240	241.7/238	242.7/239
[55.0, 56.0]	155.9(±24.6)	30.9(±4.0)	291.0/241	259.9/239	260.1/240	258.5/238	259.7/239
[56.0, 57.0]	218.0(±31.5)	40.3(±4.1)	325.7/241	276.0/239	260.9/240	260.9/238	260.6/239
[57.0, 58.0]	223.2(±23.7)	40.3(±3.1)	414.2/241	327.5/239	294.4/240	284.4/238	294.2/239
[58.0, 59.0]	230.1(±24.8)	33.7(±2.7)	374.5/241	284.6/239	263.4/240	261.1/238	260.4/239
[59.0, 60.0]	205.1(±21.8)	31.6(±2.6)	374.8/241	293.4/239	283.2/240	281.4/238	277.0/239
[60.0, 61.0]	160.3(±14.3)	28.1(±2.0)	366.0/241	266.5/239	249.0/240	247.5/238	248.6/239
[61.0, 62.0]	249.1(±18.3)	41.7(±2.1)	512.1/241	311.8/239	276.6/240	272.8/238	271.3/239

Table 17. Results of the time-resolved analysis for GRB 090618. Listed are the first twelve (one-second resolved) bins. Each row gives the values of $E_{\rm p}$ (COMP fit), kT (PL+BB fit) and C-STAT (all models).

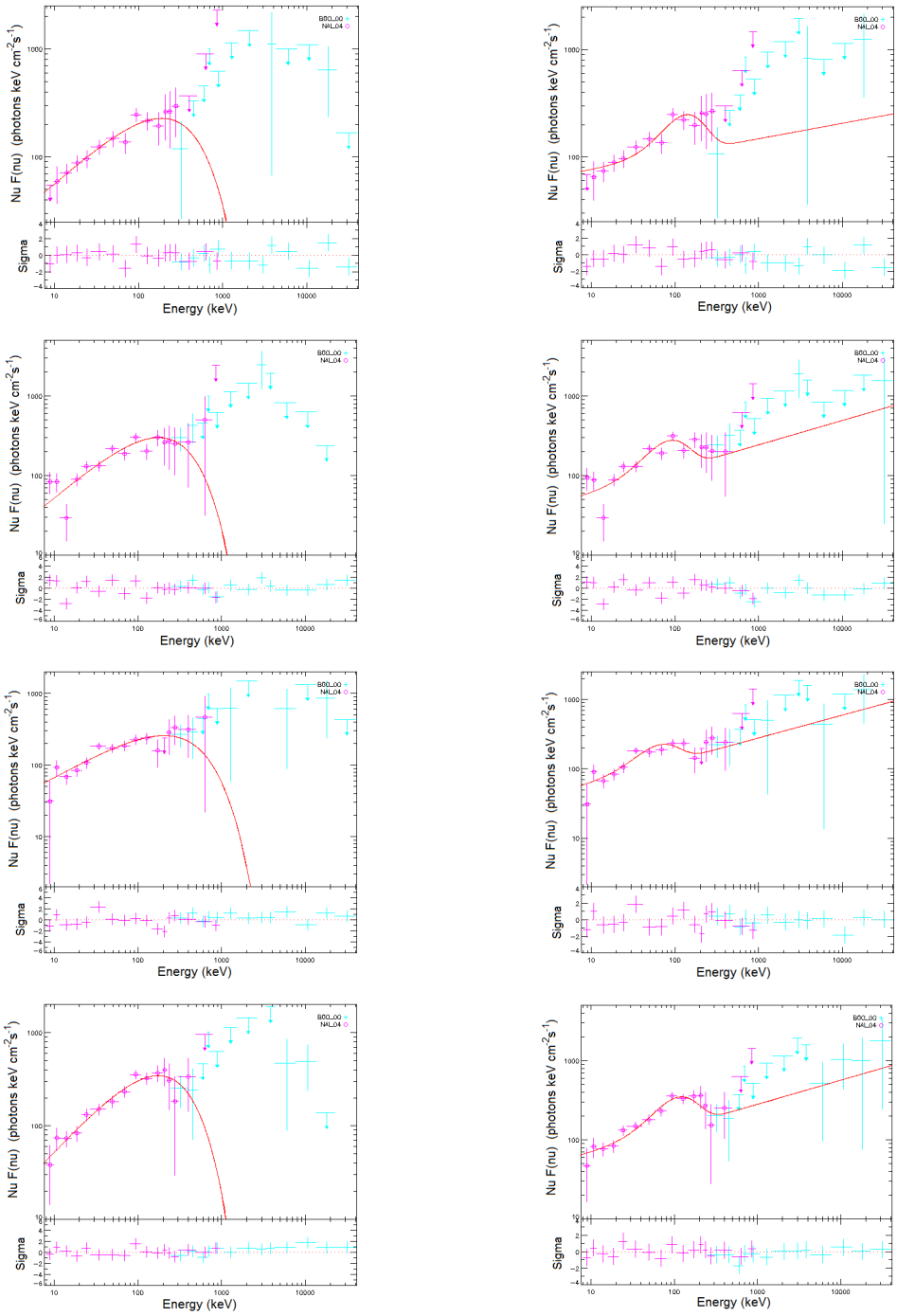

Figure 3.29. Comparison between COMP (left panels) and PL+BB (right panels) models found in the first four seconds of GRB 090618. This interval corresponds to the P-GRB found in Izzo et al. (2012b). Each row present the fit for a one-second time interval (starting at $T_0 + 50$ s).

For testing their entire data-fitting procedure, Izzo et al. (2012b) considered the χ^2-statistic rather than the Castor statistic. For this reason, the whole analysis was repeated in order to see if the BB component would emerge in the 50–59 second interval like it did in the previous analysis. These results could not be reproduced. The PL+BB showed to be a better fit only for the first, second and fourth bin. Temperature evolution (all bins included) is given in the left panel of Figure 3.30. The decrease of temperature lasts for 3 seconds, as it does in the C-STAT case (see Table 17). The interval from 50.0 s up to 53.0 seconds was therefore chosen as the P-GRB. The fitted PL+BB model is shown in the right panel of Figure 3.30. Here, the corresponding P-GRB temperature is $kT = 21.75(\pm 2.14)$ keV, while the PL index has a value of $\Gamma = -1.680(\pm 0.034)$. Placing these parameters into the Eq. 3.2 gives an energy of $E_{\rm BB} = 5.42(\pm 2.16) \times 10^{50}$ erg.

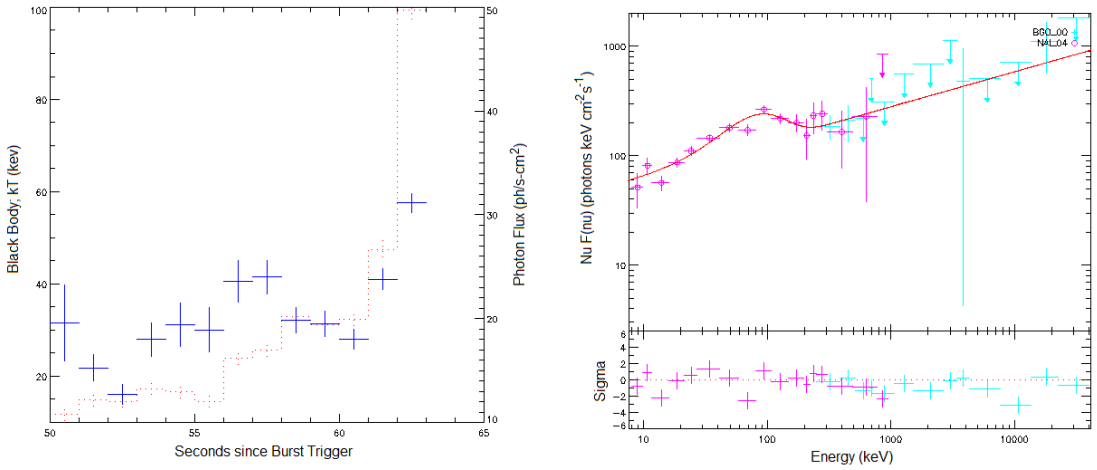

Figure 3.30. *Left panel:* Evolution of the BB temperature found in the prompt emission of GRB 090618. Plot contains the first 12 seconds of the time-resolved analysis using χ^2-statistic. *Right panel:* The P-GRB spectrum (corresponding to the 50–53 s interval) and its PL+BB fit.

Light-curve and spectral simulations

As it was explained for all of the previous cases, obtained $E_{\rm iso}$, $E_{\rm BB}$ and kT were used to simulate the fireshell expansion up to the transparency point and the collision of accelerated baryons with the CBM. Starting with $E_{\rm iso} = E^{\rm tot}_{e^+e^-}$, a match of the simulated and the observed temperature was obtained for a baryon load $B = 2.8 \times 10^{-3}$. The fireshell reached the transparency condition at the distance of $\sim 10^{14}$ cm from the source. The Lorentz factor at this point was $\Gamma \sim 352$. However, the radiated P-GRB energy ($E_{\rm P-GRB,sim}$) did not match the one obtained by the `rmfit` analysis ($E_{\rm P-GRB} = E_{\rm BB}$). Namely, $E_{\rm P-GRB,sim} = 0.01696\ E_{\rm iso}$ while $E_{\rm BB} = 0.00279(\pm 0.00111)\ E_{\rm iso}$ (see Eq. 3.1). Similar difference was obtained by Izzo et al. (2012b) (see column 1 in Table 18). Since it was then accepted and judged satisfactory, it was also accepted here. The results of light-curve simulation are shown in Figure 3.31. The CBM distribution for which the simulated light-curve imitates the observed one is showed in the left panel of Figure 3.32. The CBM density has an average value of ~ 0.24 particles/cm^{-3}. This value is lower than 1 particle/cm^{-3} (obtained by Izzo et al. 2012b). The data were simulated with the surface filling factor value of $\mathcal{R} = 9.8 \times 10^{-10}$ up to 7.8×10^{16} cm while the data from this distance was simulated with $\mathcal{R} = 2.0 \times 10^{-8}$. Izzo et al. (2012b)

obtained a similar trend, namely $\mathcal{R} = 3.0 \times 10^{-9}$ and $\mathcal{R} = 9.0 \times 10^{-9}$ with separation at 8.5×10^{16} cm, respectively. The time-integrated spectrum was simulated for interval starting after the P-GRB ($T_0 + 53$ s). The interval ended with the last data point for which the light-curves still coincided ($T_0 + \sim 90$ s). The result is shown in the right panel of Figure 3.32. The simulated spectrum (blue line) does not match the observed one (gray points). Marked with the dashed line is the simulated $E_{\rm p,sim}$ at 86.05 keV. Much lower than the observed $E_{\rm p} = 277.3$ keV (in the same time interval).

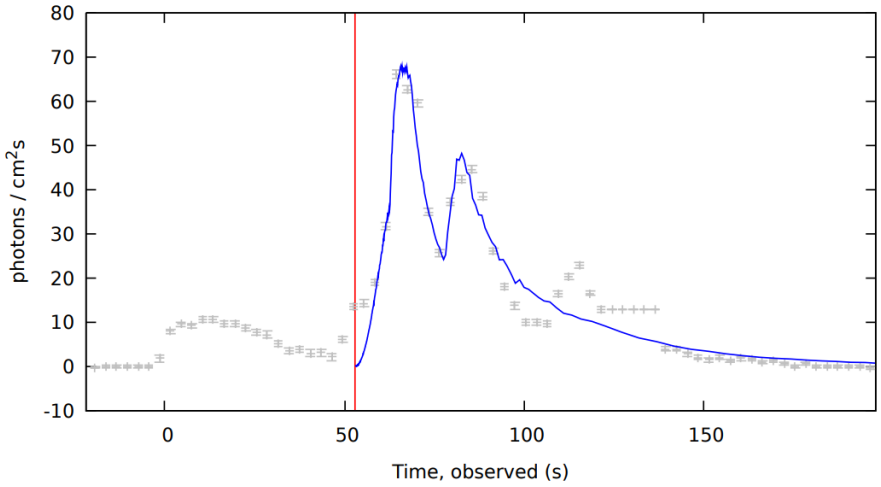

Figure 3.31. Observed and the simulated light-curves of GRB 090618. The red line marks the end of P-GRB and the beginning of prompt emission.

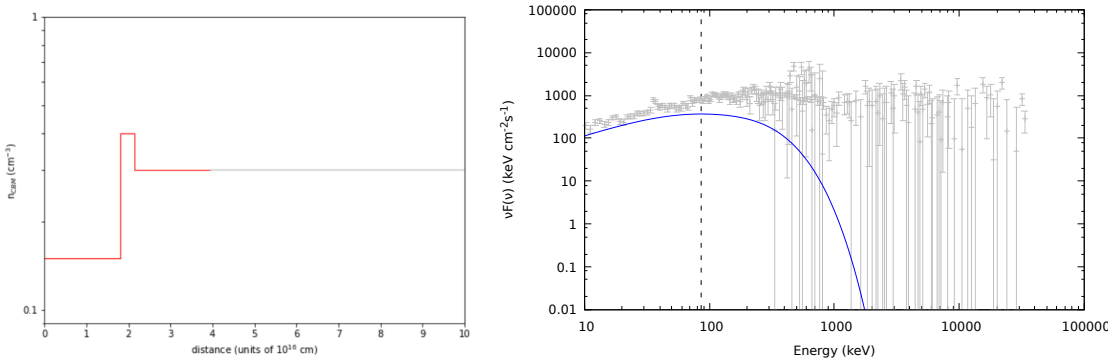

Figure 3.32. *Left panel:* Density profile of the CBM derived for GRB 090618. The gray line indicated the distance for which CBM densities remain unknown. This is due to the finite GRB energy (adding any density value after this point does not influence the light-curve shape). *Right panel:* Simulated spectrum of GRB 090618 for the [3.0 s, 90.0 s] interval. The dashed line marks the $E_{\rm p,sim}$ at 86.05 keV.

Alternative interpretation of the prompt emission

At one point during the development of the model, duration of the prompt emission was reconsidered. If the second pulse (starting at $T_0 + 75$ s) is actually a gamma-ray flare (similar to an X-ray flare, only harder), the new prompt emission interval would only last 25 seconds (from $T_0 + 50$ s to $T_0 + 75$ s). This called for $E_{\rm iso}$ recalculation. The new interval was also best fitted with a Band model. Best-fit parameters were: $\alpha = -1.105(\pm 0.034)$, $\beta = -2.562(\pm 0.0894)$ and $E_{\rm p} = 296.6(\pm 13.7)$ keV. The new isotropic energy was now reduced, namely $E_{\rm iso} = 1.306(\pm 0.015) \times 10^{53}$ erg. The P-GRB parameters remained the same. To maintain the match between the simulated and observed P-GRB temperature, the baryon load was slightly increased to the value of $B = 2.93 \times 10^{-3}$. Changes in $E_{\rm iso}$ and B parameters resulted in a slightly lower Lorentz factor $\Gamma \sim 336$. The fireshell became transparent at the distance of 1.004×10^{14} cm, similar as before. P-GRB energy at this point was still considerably lower (see Table 18). Note how a slightly lower $E^{\rm tot}_{e^+e^-}$ caused an equivalently small decrease of the Lorentz factor.

Results of the light-curve simulation are showed in Figure 3.33. The CBM distribution for which the simulated light-curve shape tracks the observed one is showed in the left panel of Figure 3.34. The CBM density has an average value of ~ 4.33 particles/cm^3, an order of magnitude higher when compared to the previous analysis. Values of the surface filling factor are approximately one order of magnitude lower, namely $\mathcal{R} = 2.0 \times 10^{-10}$ and $\mathcal{R} = 3 \times 10^{-9}$, for distances smaller and larger than 3.3×10^{16} cm, respectively. The time-integrated spectrum was simulated for the [53.0 s, 75.0 s] time interval. The result is shown in the right panel of Figure 3.34. It matches the observed spectrum much better than the one showed in Figure 3.32. The dashed line marks the simulated $E_{\rm p,sim}$ at 148.7 keV. The GBM-observed peak spectral energy for the same time interval was $E_{\rm p} = 290.0$ keV. The main results of this work and the work of Izzo et al. (2012b) can be found, side by side, in Table 18.

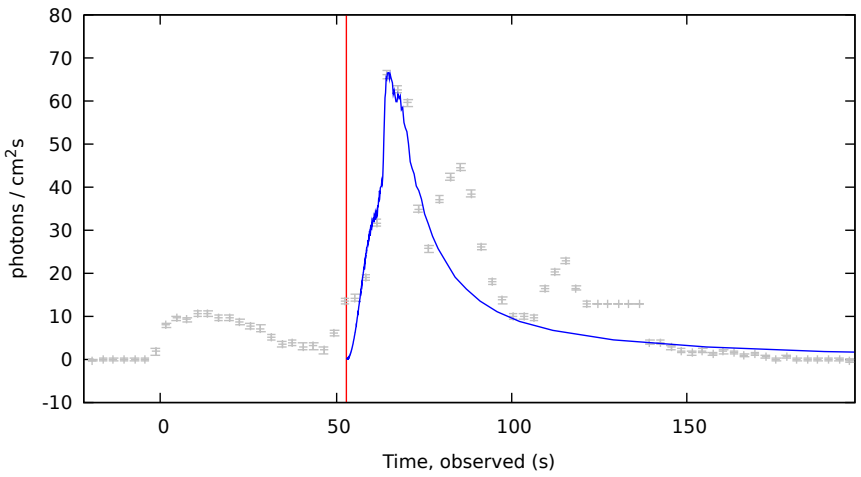

Figure 3.33. Observed and simulated light-curves of GRB 90618 (second case). The red line marks the end of P-GRB and the beginning of the prompt emission (which here ends at $T_0 + 75$ s).

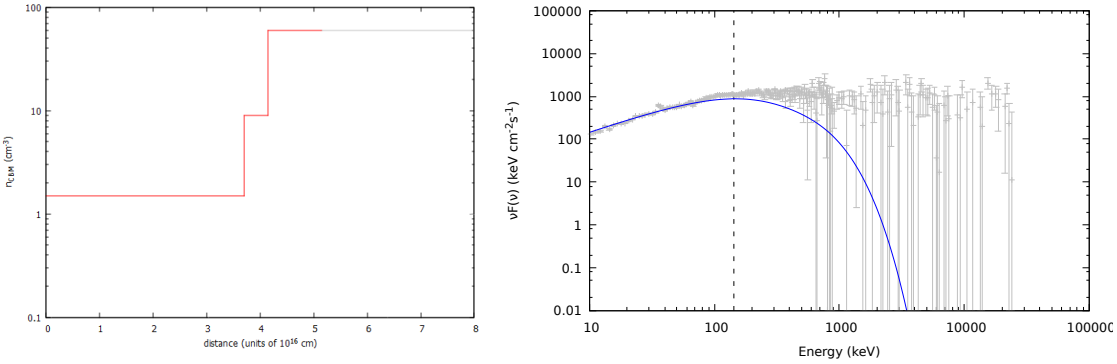

Figure 3.34. *Left panel:* Density profile of the CBM derived for GRB 090618 (second case). The gray line indicated the distance for which CBM densities remain unknown. This is due to the finite GRB energy (adding any density value after this point does not influence the light-curve shape). *Right panel:* Simulated spectrum of GRB 090618 for the [3.0 s, 75.0 s] interval. The dashed line marks the $E_{\rm p,sim}$ at 148.7 keV.

Quantity	Izzo et al. (2012)	this work-1	this work-2
$\Delta t_{\rm prompt}$	50–151	50–105	50–75
$\Delta t_{\rm P-GRB}$	50–54	50–53	50–53
$E_{\rm BB}(10^{50})$ erg	9.24(±0.5)	5.42(±2.16)	5.42(±2.16)
$kT^{\rm obs}$ (keV)	29.22(±2.21)	21.75(±2.14)	21.75(±2.14)
$E_{\rm iso}(10^{53})$ erg	2.49(±0.02)	1.94(±0.02)	1.306(±0.015)
R	0.00371	0.00279(±0.00111)	0.00415(±0.00166)
$R_{\rm sim}$	0.017389	0.01696	0.0175
B(10^{-3})	1.98	2.8	2.93
r(10^{14}) cm	1.46	1.20	1.004
Γ	495	352	336

Table 18. Comparison of the results obtained in this work with the ones found in Izzo et al. (2012b). Parameter R refers to the ratio between the $E_{\rm P-GRB}$ and $E_{\rm iso}$. Second column refers to the prompt emission analysis which included the second pulse. Values listed in the third column apply to the prompt emission consisting of the first pulse only. Here, the first, second and third pulse refer to the peaks observed after Episode 1.

`Rmfit` analysis - the last two pulses

With two different BB components visible within the time-resolved analysis[9], spectral complexity of GRB 090618 matches the one of its light-curve. If one adopts the possibility that the last two pulses are an X-ray and a gamma-ray flare, a BB component may be observed here as well. Although, if there is one, it is more likely to be found in the X-ray band (e.g., see Section 1.2 and Section 2.9). Still, a time-resolved analysis of the last two pulses was done in order to see if a BB component would emerge. In addition, (a colorful) Figure 3.35 summarizes the time-integrated results separately for each pulse, with parameter values adjusted to the reference frame of the burst.

As before, the Castor statistic was used for the time-resolved analysis. The second pulse was divided into intervals of 5-second duration. Band was showed to be the best fit for each bin in the 75–100 s interval.

[9] The first BB component can be found in Episode 1 that lasts up to $T_0 + 50$ s (see Izzo et al. 2012b)

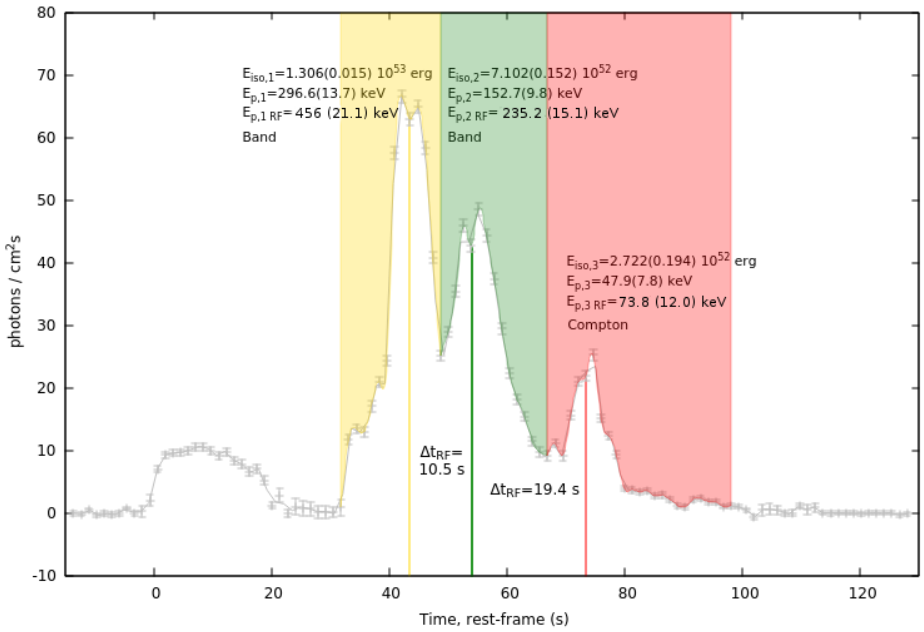

Figure 3.35. Light-curve of GRB 090618 with emphasized prompt emission phase (and flares, depending on the interpretation). For each pulse, the best fit model is also written, together with the corresponding $E_{\rm iso}$ and $E_{\rm p}$ in the reference frame of the burst. The time difference between two consequent peaks is indicated as well. The prompt emission in the work of Izzo et al. (2012b) would include all three colors. The first analysis presented here applies to the interval marked with yellow and green while the prompt emission in the second analysis only applies to the yellow interval.

Last bin, ending at 105 seconds, was best fitted with a COMP model. This can be anticipated as the BGO signal vanishes at that point (see Figure 3.28). The C-STAT values for the PL+BB model were improving with each consequent bin but never exceeded the goodness of the fit of the other models. In the last bin, PL+BB had the same C-STAT as the COMP model (but also 1 DOF less). The spectral fit residuals were also less scattered, exhibiting a trend when compared to the ones of the COMP and Band.

The same process was repeated for the third pulse (105–151 s). In every bin, COMP had the best C-STAT value and the best looking residuals. For the first two bins (up to 115 s), Band function fitted equally well. Again, this result coincides with the lack of high energy signal in BGO after ≈ 90s. A simple PL was not the best-fitting model for any of the intervals in the time-resolved or time-integrated third pulse analysis. This result differs from the one obtained by Izzo et al. (2012b), where the last pulse was best-fitted with a simple PL model ($\Gamma = 2.20(\pm 0.03)$). The composite PL+BB was not the best-fitting model for any of the time intervals either. Still, a more refined time-resolved analysis was done in order to further investigate the improving PL+BB fit in the last bins of the second pulse.

Here, the 76–114 s time interval was divided into bins of 2-second duration. Again. the COMP and Band models were proven to give the best C-STAT values and the best-looking residuals, depending on the time bin. In the bin starting at 96 seconds, the PL+BB fit started to improve. In the 98–100 s bin it had better (lower by 8) C-STAT than the COMP model, but still higher than Band with the same DOF (kT was 12.2 ± 1.3 keV). Fit residuals also did not show any sinusoidal pattern. This trend continued to the next bin ($kT = 17.7$ keV), all the way up to 110 seconds. After 110 s the residuals and C-STAT values

for PL+BB model started to be progressively worse. Still, the C-STAT values were only comparable to other models, never lower. Therefore, these results remain inconclusive. A comparison between C-STAT values of different models can be found in Table 19. It is interesting to note that the second pulse shows HIT behavior of $E_{\rm p}$ while the third shows a HTS evolution pattern.

It was suggested that a Band+BB fit could show a BB component at the beginning of the second peak. The analysis was therefore repeated. Here, only the general conclusion is outlined. No significant BB component was found at the beginning of the second peak. At least not to the extent where the BB component is more likely than it is in some random bin located in the middle of the prompt emission. Accepting these probabilities would hence influence the entire analysis and the fireshell model itself. Therefore, it can be concluded that this pulse is featureless.

3.5 REDSHIFT EVALUATION FOR GRB 171120A AND GRB 160829A

Not all GRBs have a determined redshift. Without it, the isotropic energy can not be calculated. As a consequence of their undetermined energetics, the redshift-less bursts can not be correctly placed in one of the subclasses described in Section 2.6. In addition, the propagation of the fireshell can not be simulated as well. However, there are means to estimate the redshift through the spectral analysis of the prompt emission light-curve. This section describes two different techniques of redshift estimation. The first one involves the well know Amati relation (Amati et al. 2002, also see Section 1.3) and it was applied on GRB 171120A. The second one relies on the simulation of the fireshell dynamics up to the transparency point and it was applied to GRB 160829A.

GRB 171120A

GRB 171120A was detected by *Fermi*/GBM at 20 November 2017 (Longo et al. 2017). The GBM light-curve consists of two, well-separated pulses with a total duration of about ~ 45 s (Figure 3.36). These well-separated pulses were individually used to evaluate the redshift. The pulse-wise Amati correlation was shown to be more robust than the original one. It is also unaffected by the hardness difference between pulses that appear in the same burst (e.g., Basak & Rao 2013, but also see Collazzi et al. 2012). The applied method is straightforward. Two peaks were analyzed separately using the `rmfit` software. The best-fitting models are given in Table 20. Isotropic energy $E_{\rm iso}$ and the reference frame $E_{\rm p}$ were calculated for different values of z. The results are plotted in Figure 3.37. Starting with $z = 0.1$, each of the 20 consequent points correspond to a redshift increase of 0.1 (the difference between the other points is equal to the redshift of 0.2). Redshift of $0.6 < z < 1.2$ was inferred from the requirement that these two peaks originate from the same GRB.

GRB 160829A

GRB 160829A was identified as a member of the S-GRB (BM-II) subclass (Table 1) based on its duration and associated high-energy photons (Racusin et al. 2016; Hamburg et al. 2016). It is also the only member of the BM class processed in this work. Ruffini et al. (2018f) reproduced a joint 0.1–100 GeV isotropic luminosity light-curve using a sample of S-GRBs (with a similar result as the one obtained by Nava et al. 2014). However, the sample size was limited to a few short GRBs that had a precisely determined redshift. For that reason, other short bursts without a redshift were considered in order to expand the number of

Time bins (s)	COMP/Band/BB parameters		STAT/DOF				
	$E_{\rm p}$ (keV)	kT (keV)	PL	PL+BB	COMP	COMP+BB	Band
[75.0, 80.0]	95.7(±5.9)	21.6(±0.6)	864.8/241	390.8/239	349.5/240	328.6/238	314.3/239
[80.0, 85.0]	150.1(±6.5)	28.3(±0.6)	1578.6/241	523.6/239	297.8/240	286.5/238	295.5/239
[85.0, 90.0]	137.2(±6.7)	27.8(±0.7)	1455.7/241	512.4/239	364.6/240	356.4/238	348.1/239
[90.0, 95.0]	95.7(±6.0)	21.4(±0.7)	772.4/241	430.7/239	367.9/240	350.1/238	349.4/239
[95.0, 100.0]	67.5(±6.8)	16.4(±0.9)	449.5/241	330.2/239	318.7/240	308.2/238	308.6/239
[100.0, 105.0]	64.0(±6.2)	17.7(±1.4)	372.2/241	319.1/239	319.0/240	316.7/238	318.0/239
[105.0, 110.0]	85.9(±6.6)	15.4(±1.1)	420.3/241	351.4/239	340.4/240	334.8/238	337.4/239
[110.0, 115.0]	67.7(±2.6)	16.5(±0.7)	564.0/241	359.6/239	315.8/240	314.4/238	313.2/239
[115.0, 120.0]	51.0(±2.5)	14.8(±0.8)	411.1/241	307.9/239	284.3/240	284.3/238	282.7/239
[120.0, 125.0]	45.2(±2.8)	–	428.5/241	351.4/239	352.2/240	249.0/238	352.2/239
[125.0, 130.0]	32.6(±2.7)	–	332.8/241	292.4/239	285.5/240	283.5/238	285.0/239
[130.0, 135.0]	28.2(±3.4)	–	358.0/241	332.4/239	331.9/240	-Nan	331.9/239
[135.0, 140.0]	27.7(±7.3)	–	332.5/241	314.5/239	313.9/240	313.2/238	318.0/239
[76.0, 78.0]	96.0(±9.5)	21.6(±1.1)	439.9/241	261.2/239	251.0/240	242.1/238	239.5/239
[78.0, 80.0]	90.2(±7.7)	20.9(±0.9)	637.1/241	386.7/239	359.3/240	338.5/238	330.2/239
[80.0, 82.0]	122.4(±9.1)	25.7(±0.9)	745.3/241	329.9/239	272.0/240	261.3/238	259.2/239
[82.0, 84.0]	162.8(±7.3)	30.1(±1.1)	748.9/241	348.3/239	240.4/240	237.0/238	240.3/239
[84.0, 86.0]	192.8(±8.2)	32.0(±1.1)	891.4/241	409.1/239	290.8/240	288.2/238	290.8/239
[86.0, 88.0]	145.6(±10.3)	28.9(±1.0)	814.4/241	392.3/239	308.8/240	305.9/238	303.7/239
[88.0, 90.0]	116.8(±10.1)	25.0(±1.0)	608.4/241	300.8/239	290.0/240	278.5/238	272.8/239
[90.0, 92.0]	107.2(±10.3)	22.7(±1.1)	464.7/241	293.9/239	264.0/240	255.1/238	252.8/239
[92.0, 94.0]	(c)100.0(±5.9)	21.0(±1.1)	470.6/241	326.9/239	298.5/240	287.2/238	294.3/239
[94.0, 96.0]	(c)114.9(±10.5)	(20.6 ± 1.7)	379.9/241	320.3/239	306.7/240	299.9/238	301.4/239
[96.0, 98.0]	(c)83.3(±6.5)	17.4(±1.2)	406.4/241	325.4/239	321.0/240	316.7/238	318.9/239
[98.0, 100.0]	(c)84.7(±11.7)	12.2(±1.3)	306.2/241	279.8/239	287.7/240	277.3/238	275.1/239
[100.0, 102.0]	(c)66.5(±7.1)	17.7(±1.8)	303.8/241	272.1/239	269.5/240	268.9/238	269.4/239
[102.0, 104.0]	(c)56.0(±6.6)	15.9(±2.3)	310.9/241	395.1/239	291.8/240	290.0/238	291.6/239
[104.0, 106.0]	(c)78.2(±10.9)	17.0(±2.2)	298.0/241	278.2/239	282.4/240	278.2/238	279.9/239
[106.0, 108.0]	(c)78.8(±14.7)	13.5(±2.6)	273.0/241	264.0/239	266.5/240	259.4/238	260.7/239
[108.0, 110.0]	(c)100.3(±9.9)	16.3(±1.4)	356.6/241	305.5/239	305.5/240	366.2/238	297.3/239
[110.0, 112.0]	(c)76.2(±5.2)	19.4(±1.3)	398.1/241	317.6/239	294.5/240	291.6/238	294.1/239
[112.0, 114.0]	(c)61.2(±3.6)	14.9(±0.9)	368.3/241	279.8/239	278.8/240	278.1/238	275.2/239

Table 19. Results of the time-resolved analysis for the last two pulses of GRB 090618. The table is divided in two parts. These show the results of the 5-s (first part) and 2-s (second part) time-resolved analysis. For the time bins corresponding to the second (third) pulse, the $E_{\rm p}$ was taken from the Band (COMP) fit. In the second part of the table this is indicated with '(c)'. The kT value is listed regardless of the goodness of the PL+BB fit, except for the cases of a negative count rate model. The last five columns compare C-STAT values of different models.

Model	$T_{\rm start}$(s)	$T_{\rm stop}$(s)	$E_{\rm p}$ (keV)	α	β	C-STAT/DOF
Band	-0.32	4.80	194.4(±18.8)	−0.803(±0.060)	−1.991(±0.061)	394.5/360
Band	37.5	50.1	100.0(±8.7)	−1.006(±0.073)	−2.224(±0.083)	502.6/362

Table 20. Best-fit parameters for two pulses observed in GRB 171120A.

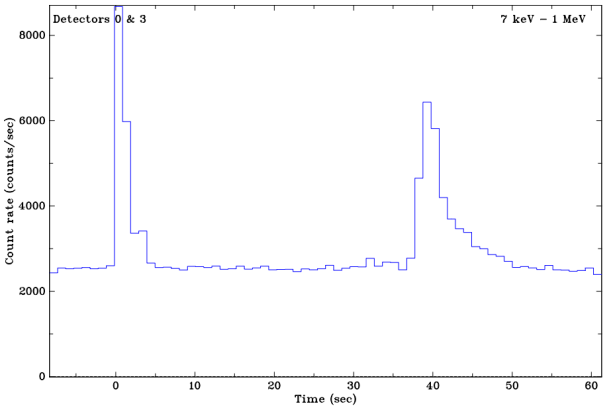

Figure 3.36. NaI light-curve of GRB 171120A. Two well-separated peaks are visible. Figure reproduced from the online *Fermi*/GBM burst catalog (Narayana Bhat et al. 2016).

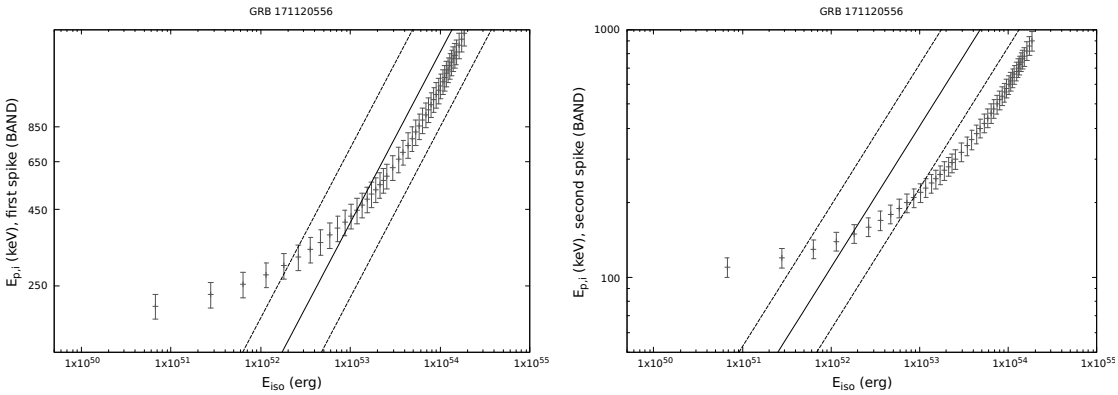

Figure 3.37. $E_{\rm p}^{\rm RF}$-$E_{\rm iso}$ plot for the first (left panel) and the second (right panel) pulse of GRB 171120A. Each point corresponds to a different value of z. Amati relation is indicated with a full line. Dashed lines represent the 1σ confidence interval.

sources and improve the poor data statistics. For these GRBs, including GRB 160829A, redshift was evaluated through the means of fireshell simulation (also see Muccino et al. 2013a).

As always, the P-GRB duration needed to be found through the time-resolved analysis. Although the redshift was unknown, $R = E_{\rm P-GRB}/E_{\rm iso}$ ratio was approximated using the observed fluences. Namely,

$$R = \frac{E_{\rm P-GRB}}{E_{\rm iso}} = \frac{4\pi d_l^2\, F_{\rm P-GRB}\, \Delta t_{\rm P-GRB}/\,(1+z)}{4\pi d_l^2\, F_{\rm tot}\, \Delta t_{\rm tot}/\,(1+z)} = \frac{S_{\rm P-GRB}}{S_{\rm tot}}, \tag{3.4}$$

where $(1+z)$ factors cancel out. Knowing the ratio, one can then start the simulation process for an arbitrary value of $E_{\rm iso}$ (or equivalently, z). This would result in a standard set of parameters, including the $E_{\rm P-GRB}/E_{\rm iso}$ (already known from Eq. 3.4) and the reference-frame P-GRB temperature. The temperature can be correctly transformed to the observed one using the z defined by the selected $E_{\rm iso}$ value. These quantities can then be compared and the process repeated until the match is found. However, the *user* is also free to choose the baryon load value. This means that parameter B also needed to be varied with each selected z. The higher the B, the lower the P-GRB temperature will be at the transparency point. The methodology can be summarized as follows:

(i) starting from the redshift of $z = 0.1$, the simulation was initiated with the corresponding $E_{\rm iso}$

(ii) the parameter B was varied until the match between the correct $E_{\rm P-GRB}/E_{\rm iso}$ ratio was found (Eq. 3.4)

(iii) the simulated P-GRB temperature was then transformed to the observed frame and compared with the one obtained from the analysis.

(iv) if the temperatures did not match, the process was repeated for a higher value of z.

Coming back to the case of GRB 160819A, the entire prompt emission interval (from $T_0 - 0.064$ s to $T_0 + 0.448$) was best fitted with COMP model. The associated parameters were $\alpha = -1.402(\pm 0.146)$ and $E_{\rm p} = 3247(\pm 795)$ keV. The P-GRB could only be constrained to an interval starting at $T_0 - 0.064$ s and ending anywhere up to $T_0 + 0.128$ s. This was due to the poor S/N ratio of the data. Resolution under 0.192 seconds lead to unconstrained parameters and negative count rate models (if the fitting procedure converged at all). Three P-GRB durations were selected. That is, 1-bin, 2-bin and 3-bin intervals starting at T_0, where one bin corresponds to 0.064 seconds. The obtained R were 0.419, 0.278 and 0.064, respectively. The redshift estimation for the 1-bin case did not converge for a meaningful value of z. In other words, the burst would need to be in an extreme proximity if one expects the (simulated and the observed) transparency temperatures to coincide. The 3-bin option, for which the P-GRB lasts up to 0.128 seconds, gave a redshift of $z \sim 9$. This would be the farthest S-GRB observed up to date. The 3-bin option was therefore comfortably discarded. The remaining, 2-bin case was best fitted by a PL+BB model. Although the COMP model had a better C-STAT value, the low-energy power-law index was positive and poorly constrained. The BB component had a temperature of $114.3(\pm 16.6)$ keV. The trial and error procedure for the remaining, 2-bin case converged at the redshift of $z = 5.8(\pm 1.0)$. At this redshift, GRB 160819A has an isotropic equivalent energy $E_{\rm iso} = 3.76(\pm 0.32) \times 10^{52}$ erg. The simulated temperature, transformed into the detectors reference frame, was 115.135 keV. The baryon load was $B = 1.0025 \times 10^{-4}$. In the following order, Figure 3.38, Figure 3.39, and Figure 3.40 depict the evolution of the P-GRB temperature, burst energy, and baryon load with z for the 2-bin case. Figure 3.41 shows GRB 160819A on the joint 0.1–100 GeV isotropic luminosity light-curve.

Note how the $E_{\rm iso}$ errors in Figure 3.39 increase with redshift (i.e., remain approximately the same since the y-axis is logarithmic). These errors were estimated using the flux error obtained from the `rmfit` analysis. As the redshift gets larger, the energy associated with these errors also grows. The redshift errors correspond to the interval for which the match in the temperature would still be within the kT errors derived from the P-GRB analysis. For example, a lower limit of $z = 4.8$ obtained for the 2-bin case would imply that the simulated temperature at that redshift is equal to a higher limit of $114.3(\pm 16.6)$ keV. Since the kT errors transform in the same way as their values (i.e., $kT^{\rm RF} = kT\,(1+z)$), the redshift error grows as well. As a result, the inaccuracy of this method increases with higher redshifts. It is important to note that the redshift of ~ 5.8 should solely be taken as an upper limit. The P-GRB interval was only approximated and can last anything from $0.064\ {\rm s} < \Delta t_{\rm P-GRB} < 0.128$ s. The values of baryon load (Figure 3.40) are consistent with the ones expected for short GRBs.

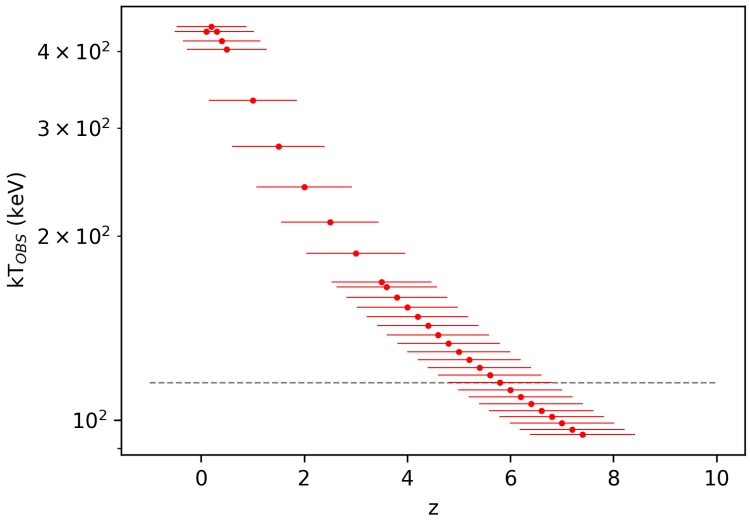

Figure 3.38. Evolution of simulated P-GRB temperature with redshift for the 2-bin case of GRB 160819A. The dashed line marks the temperature of 115.14 keV.

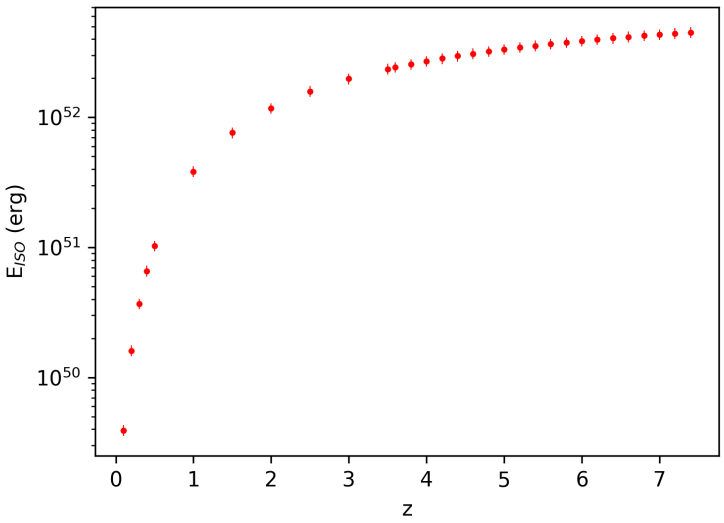

Figure 3.39. Isotropic equivalent energy of GRB 160819A for different redshifts.

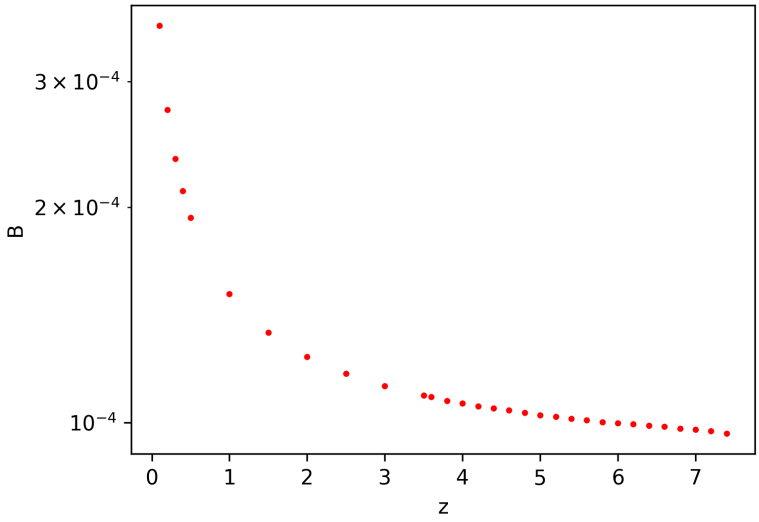

Figure 3.40. Baryon load B at different redshifts for which the simulated ratio R corresponded to the one of the fluence.

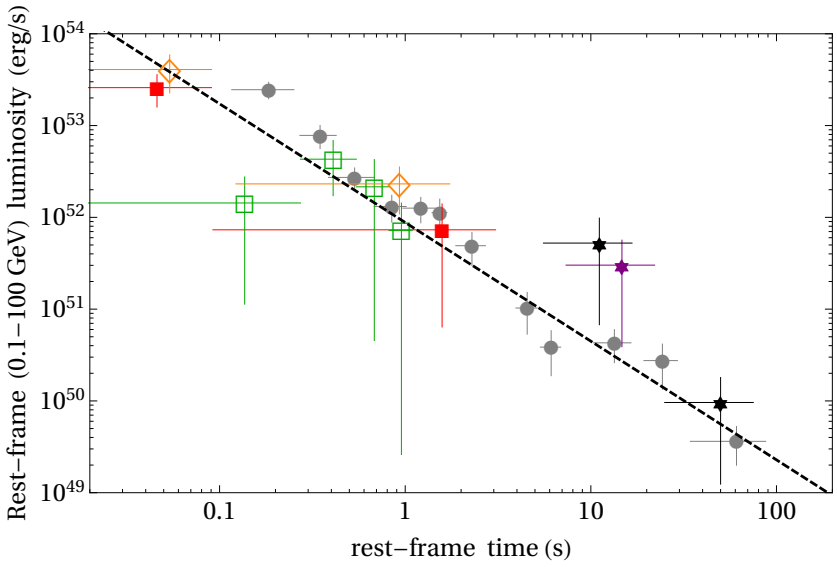

Figure 3.41. GRB 160819A showed on the joint 0.1–100 GeV isotropic luminosity light-curve. The purple star marks the 2-bin case ($z = 5.8$). Black stars mark the luminosity of GRB 160819A on a hypothetical redshift of $z = 8.0$ (upper star) and $z = 1.0$ (lower star). Figure adapted from Ruffini et al. (2018e).

4

CONCLUSION AND ONGOING WORK

In this work, the time-resolved and the time-integrated spectroscopy was performed on the sample of 11 long GRBs, classified as BdHNe-I within the IGC paradigm. Within this framework, the richness and diversity of GRBs is a result of binary system parameters, viewing angle of the orbital plane, and rotation period of the system.

Thermal (BB) component was identified in six GRBs: GRB 100728A, GRB 120624B, GRB 120729A, GRB 130702A, GRB151027A and GRB 090618. Ghirlanda et al. (2013b) presented a classification of GRBs based on the thermal component in their spectra. Following this classification, GRB 120729A is a Class-III burst. These bursts have a BB plus a non-thermal component throughout their entire duration. A T_{90}-long thermal emission can not be interpreted as a P-GRB. In addition, GRB 120729A had low BdHNe-I energy ($\sim 10^{52}$ erg) and a weak evidence of GeV emission. Therefore, it can not be excluded that this burst is a member of an XRF subclass. Other GRB classes in Ghirlanda et al. (2013b) involve a pure BB component, either at the beginning or during the entire prompt emission. None of the remaining GRBs had their time-resolved spectra described solely with a BB. The thermal component was always superimposed on an underlying spectrum, as in GRB 130702A. For this GRB, the prompt emission was best fitted with a PL (although low $E_{\rm p}$ can not be excluded) while the BB component was found in the first 13 seconds. This was another burst with a questionable classification due to its low energetics, a PL spectrum and (therefore conflicting) LAT detection. As a result, P-GRB identification was dubious. Excluding GRB 120729A and GRB 130702A, which may belong to the XRF subclass, the rest of GRBs have (redshift-corrected) $E_{\rm p,i}$ well above 0.2 MeV, which is the limiting value for the BdHNe-I subclass. In the case of GRB 120624B, thermal component was found mid-emission. Time intervals before and after were best fitted with a Band function. This configuration is hard to interpret within the fireshell model. The thermal component was accepted as the P-GRB for the remaining three bursts: GRB 100728A, GRB151027A and GRB 090618. It is interesting to note that the kT evolution in GRB 090618 follows the behavior described by Ryde & Pe'er (2009), i.e., a decrease of temperature accompanied by an increase of flux.

For GRB 110731A and GRB 141028A, COMP fit was accepted as the P-GRB since it could be distincted from the rest of the prompt emission. This adds up to 5 bursts with an identified P-GRB episode. High baryon load or an unfavorable orientation of the binary may be possible explanations for the lack of P-GRB in other bursts. From these five bursts, three were further analyzed using the simulation of fireshell propagation: GRB 110731A, GRB 151027A and GRB 090618. All three bursts occurred in quite different environments. An average value of the CBM density was ~ 0.03 cm^{-3}, ~ 15 cm^{-3} and ~ 1 cm^{-3}, respectively. CBM density values that span over a wide range of values point to different regions of the host galaxies. Value of 1 particle per cm^3 or more is typically found in inner-galaxy regions. The averaged value of this small sample is consistent with the one usually inferred for GRBs; 1 particle per cm^3, as noted in Ruffini (2011). Values of the surface filling factor $\mathcal{R}$ increased with distance for GRB 090618 and

GRB 110731A. This is in an agreement with conclusions reached by Ducci et al. (2009). In addition, a small trend has been noticed in the difference between the low-energy PL indices reported by *Fermi* GCN and the ones obtained in this analysis. In order of their occurrence, GCN bursts before GRB 130518A had a slightly harder α than the ones obtained by `rmfit`. This behaviour reversed for the bursts that followed after GRB 130518A. Somewhat similar trend up to 2008 was pointed out by Nava et al. (2011b).

Redshift was estimated for two GRBs, GRB 171120A and GRB 160829A. In the case of GRB 160829A, the accuracy was severely limited by the low S/N ratio. However, the method is generally lacking an accuracy estimation. This means that it should be tested on a sample of GRBs with known redshifts in order to determine its reliability and hence the reliability of the fireshell model. For example, the redshift of GRB 171120A could also be estimated in the same way as the redshift of GRB 160829A in order to compare the results. The other way around would not be advisable since short GRBs do not obey the Amati relation. It would also be interesting to see if the simulation of the fireshell propagation can reproduce the complex $E_{\rm p}$ evolution patterns (and for which cases). This can be done by employing the time-resolved spectral fitting once a correct light-curve has been obtained. Baryon load inferred for short GRB 160829A was $B \approx 1 \times 10^{-4}$, order of magnitude less than the ones of the three long BdHNe-I.

New developments in the IGC model were not necessarily confirmed with the revisit of GRB 090618. The P-GRB was found in the first three seconds following Episode 1. Still, as it can be seen from Table 17, the PL+BB model for this time interval only provided a fit that was equally good as the other ones, not better. At best, this allowed for it to be chosen in the view of theoretical understanding of the fireshell model. In addition, while the GRB 090618 energy differed among the three analyses, the final set of fireshell parameters remained similar (see Table 18). Although, this can be contributed to the similar P-GRB energy and to the differences in $E_{\rm iso}$ that never exceeded an order of magnitude. Furthermore, many of the results presented in Izzo et al. (2012b) that do not depend on our theoretical understanding could not be reproduced. For example, the BB component was not observed up to 59 seconds. In the same interval, Band function did not provide the best fit for some bins. Lastly, the third pulse was best-fitted with a COMP model, not a simple PL. This happened despite following the same procedure as much as it was possible (e.g., the choice of the detector and binning). It follows that results can often be influenced by the statistical approach, the choice of BG intervals, and energy channels. The first reduced UPE of GRB 090618 (first and second pulse) did not provide an acceptable fit. The second fit, where the UPE lasts only 25 seconds gave a more adequate spectrum. All considering, the Izzo et al. (2012b) interpretation can not be completely abandoned. The time-resolved analysis excluded any other BB component in this phase, at least in the gamma-ray band. The 5-second time-resolved analyses of the last two pulses showed that they are well fitted by Band and COMP models, depending on how strongly the BGO emission was present. The 2-second time-resolved analysis did not find a confident BB as well. Only one bin (98 s–100 s) had a PL+BB with a better (COMP) or equally good (Band) C-STAT value when compared to other models. For future assignments, it would be interesting to check if the interpretation of Episode 1 can change due to the new view on the prompt emission duration. In other words, would it be possible to simulate the light-curve and the spectrum if the Episode 1 was now considered to be the P-GRB while the prompt emission remains shortened? A successful simulation would, however, imply that a single GRB in multiple rearrangements can be fitted to the model, limiting by that its use (and calling in question all of the previously derived results). Problems that emerged during these analyses placed the fireshell model to the test and drove its further development.

Nevertheless, the analysis of GRB 090618 (and the one of GRB 110731A) certainly demonstrated the complexity of this process. Approximately five different models needed to be fitted and contrasted for each of the time-integrated and time-resolved intervals. In the case of GRB 090618, this adds up to more than ~ 300 individual spectra. For GRB 110731A, the number of fitting results revolves around 100. The equally time-consuming is the trial and error procedure applied throughout the simulation. It

is done by hand. This means that each value of baryon load or CBM density needs to be readjusted for a small value until the match is eye-validated. The more complex the light-curve is, the longer is the process. Final tweaks are also out of the question since any change in the parameters that govern the light-curve shape will affect all of the fits that come after it (see Section 3.1). Once the light-curve is fitted to a satisfactory level, the simulated spectrum often does not correspond to the observed one. In that case, a new configuration of parameters needs to be found. The explained process can sometimes take weeks to complete.

Thus, a naturally imposing idea is the one of a graphic user interface with a background Monte Carlo algorithm that would fit the P-GRB and the light-curve automatically. This is currently a work in progress. From the user-selected BG interval, distribution of the oscillations is fitted to a normal function. The obtained variance will help to determine which local maxima (or minima) are to be ignored and which ones are to be included in the fitting process. The number of 'real' local maxima and their position will set the number of CBM density values and $\mathcal{R}$ factors that are to be used in the simulation. This should give necessary directions to Monte Carlo algorithm and significantly speed up the process. Allowing the algorithm to blindly fit the data while demanding a match with every BG oscillation would be unnecessary and time-consuming. When to accept the data point as a peak and when to average it out would also depend on the general behavior of that interval. The fit, or some stage of the fit, will be accepted if they fall between the error bars of the (non-ignored) data points. The GUI will then repeatably call the `GRB8Sim` program until the light-curve fit is found. When the final spectrum is produced, the user will be able to repeat the fitting process if deemed necessary. Although this may take a substantial amount of time as well, the user's only effort would consist of loading the appropriate files and choosing the BG intervals. His or her presence will not be demanded for every iteration of the program (one program execution can take several minutes). In the final stage the program should be tested on the old, already analyzed GRBs. If successful, it would present a step toward the development of a more complete BdHNe-I catalog. Then, in addition to $E_{\rm iso}$, values of the average CBM density, baryon load B, and Lorentz factor at transparency should also be available with the help of this initiative. All this could lead toward a more complete population analysis.

Work in progress - exploitation of GRB catalogs

Although the existence of long and short GRBs is by now well established, classification based solely on T_{90} may not be sufficient (proving this point is the content of GCN notices summarized in Section 3.2). Firstly, there is a large overlap between the two distributions showed in the right panel of Figure 1.1 (e.g., Lü et al. 2010). Furthermore, Zhao et al. (2004) showed that T_{50} distribution is still bimodal, but with ≈3% of GRBs exchanging classes (where short GRBs are now classified as long ones and vice versa). While for the short GRBs this is due to the boundary effect, the long ones mostly have an unsuitably fitted BG. This can also be caused by the T_{90} definition. The quiescent interval will be accounted for if the burst did not accumulate 95% of counts before that time. Long GRBs in Zhao et al. (2004) sample that changed class also have the hardness ratio closer to ones found in short bursts. These bursts were found to have properties of Norris-Bonnell sources discussed in Section 2.5.

Ideally, the GRB classification method should be free from the potential biases introduced by data analysis, detector sensitivity, redshift measurements, and many more. Often this is not the case and prompt emission quantities are very sensitive to the instrument's detection threshold (Butler et al. 2010). Therefore, a GRB sample from a given mission will be only a representative of a smaller part of the (possibly evolving) GRB fluence distribution. As it was noted many times in Section 3.2, long bursts observed by *Fermi*/GBM have much longer duration when observed with *Swift*/BAT (Virgili et al. 2012). If more short GRBs were analyzed in this work, one would see that for them the trend reverses; short GRBs last longer when observed with *Fermi*/GBM. Shahmoradi & Nemiroff (2015) found that the ratio of

the observed $E_{\rm p}$ to T_{90} is the least biased GRB classification method. Others find that the ratio of $E_{\rm iso}$ and the rest-frame peak spectral energy is a more suitable parameter for distinguish between the GRBs that originate from the collapsar and the ones that originate from the mergers (Zhang 2006, Gehrels et al. 2006, also see GRB 060614 in Zhang 2007b). For example, long GRB 080913 at $z = 6.7$ is intrinsically short although it was classified as a long event based on its observed duration (Pérez-Ramírez et al. 2010, also see Jakobsson et al. 2007). Hints of a third peak within the T_{90} distribution were reported in various papers, suggesting a separate, intermediate class of GRBs (e.g., Horváth 1998; Mukherjee et al. 1998). In addition to this intermediate class, it was proposed that ultra-long GRBs, lasting for hours, may form a distinct population with a blue supergiant as its progenitor (Levan et al. 2014). Let us not forget to mention the open question regarding the X-ray afterglow and whether it should be included (and which part) in the prompt duration and isotropic energy calculation. This decision should be based on the knowledge of the central engine that powers the burst (Ghisellini et al. 2007). Therefore, there is still an ongoing discussion in the scientific community regarding the GRB classification. This is of particular interest for the IGC paradigm, as explained further below.

The analyses of BdHNe-I described in Section 3.2 motivated another work now left in progress. It was noticed how spectral parameters differ, duration in particular, from one GCN report to another for the same GRB. This was more of a rule than an exception (as one can expect due to instrumental biases, as explained earlier). However, the IGC classification, as well as the fireshell simulation, is $E_{\rm iso}$ sensitive. Furthermore, not all GRBs are detected with the *Fermi* satellite. In that case, one turns to one of the alternative options, which is usually the *Swift* observatory. Since the values of $E_{\rm iso}$ and T_{90} are detector sensitive, a methodological approach is needed in order to consistently classify GRBs within the IGC paradigm. This initiated an effort to devise a way to build a coherent sample of temporal and spectral properties of BdHNe, with an emphasis on their energetics. Similar as in Virgili et al. (2012), a starting point was the analysis of GRBs observed both with *Fermi* and *Swift* satellites in order to determine the relations between their observables. Software `TOPCAT` (Tool for OPerations on Catalogues And Tables, Taylor 2005) was found to be suitable for this analysis. It is an interactive graphical viewer and editor for tabular data that enables the manipulation of source catalogs. However, the *Fermi* catalog offers more than T_{90} and spectral fit parameters. More precisely, T_{90} and T_{50} start and end times can be regarded as T_{05}, T_{95}, T_{25} and T_{75}, keeping in mind that their interval starts at T_0. Six different temporal quantities are therefore available and can be used to quantitatively describe the burst shape and its variability. Various options are available from this point onward. Different ratios can be constructed, and from them, different color-color diagrams (or time-time diagrams in this case). This can uncover the existence of possible subgroups of long and short GRBs, at least based on their temporal properties. $E_{\rm iso}$ and $E_{\rm p}$ can be investigated for these subgroups, including the correlations listed in Section 1.3. It would also be interesting to see how these quantities relate (and for which bursts) to the ones found in the *Swift* catalog and what is their relation (if any) with the subclasses in the IGC paradigm.

BIBLIOGRAPHY

Aartsen, M. G., Ackermann, M., Adams, J., et al. 2015, ApJ, 805, L5

Aartsen, M. G., Ackermann, M., Adams, J., et al. 2017a, ApJ, 843, 112

Aartsen, M. G., Ackermann, M., Adams, J., et al. 2017b, Journal of Instrumentation, 12, P03012

Aartsen, M. G., Ackermann, M., Adams, J., et al. 2019, PhRvL, 122, 051102

Abbott, B. P., Abbott, R., Abbott, T. D., et al. 2016a, PhRvD, 93, 122003

Abbott, B. P., Abbott, R., Abbott, T. D., et al. 2016b, The Astrophysical Journal Supplement Series, 227, 14

Abbott, B. P., Abbott, R., Abbott, T. D., et al. 2016c, ApJ, 833, L1

Abbott, B. P., Abbott, R., Abbott, T. D., et al. 2016d, ApJ, 832, L21

Abbott, B. P., Abbott, R., Abbott, T. D., et al. 2017, PhRvL, 119, 161101

Abbott, B. P., Abbott, R., Abbott, T. D., et al. 2018, arXiv e-prints

Abbott, B. P., et al. 2018, arXiv e-prints, arXiv:1811.12907

Abbott, B. P., Abbott, R., Abbott, T. D., et al. 2019, Physical Review X, 9, 011001

Abbott, D. C., & Conti, P. S. 1987, ARA&A, 25, 113

Abdo, A. A., Ackermann, M., Ajello, M., et al. 2009a, Nature, 462, 331

Abdo, A. A., Ackermann, M., Ajello, M., et al. 2009b, ApJ, 706, L138

Abdo, A. A., Ackermann, M., Arimoto, M., et al. 2009c, Science, 323, 1688

Abdo, A. A., Ackermann, M., Ajello, M., et al. 2011, ApJL, 734, L27

Acciari, V. A., Ansoldi, S., Antonelli, L. A., et al. 2019, Nature, 575, 455

Acernese, F., Agathos, M., Agatsuma, K., et al. 2015, Classical and Quantum Gravity, 32, 024001

Achterberg, A., Gallant, Y. A., Kirk, J. G., & Guthmann, A. W. 2001, MNRAS, 328, 393

Ackermann, M., Asano, K., Atwood, W. B., et al. 2010a, ApJ, 716, 1178

Ackermann, M., Ajello, M., Baldini, L., et al. 2010b, ApJ, 717, L127

Ackermann, M., Ajello, M., Asano, K., et al. 2011, ApJ, 729, 114

Ackermann, M., Ajello, M., Asano, K., et al. 2013a, ApJ, 763, 71

Ackermann, M., Ajello, M., Asano, K., et al. 2013b, ApJS, 209, 11

Adrián-Martínez, S., Samarai, I. A., Albert, A., et al. 2013a, Journal of Cosmology and Astro-Particle Physics, 2013, 008

Adrián-Martínez, S., Albert, A., Samarai, I. A., et al. 2013b, A&A, 559, A9

Ajello, M., Arimoto, M., Axelsson, M., et al. 2019, ApJ, 878, 52

Aksenov, A. G., Bianco, C. L., Ruffini, R., & Vereshchagin, G. V. 2008, in American Institute of Physics Conference Series, Vol. 1000, American Institute of Physics Conference Series, ed. M. Galassi, D. Palmer, & E. Fenimore, 309–312

Aksenov, A. G., Ruffini, R., & Vereshchagin, G. V. 2007, PhRvL, 99, 125003

Amati, L. 2006, MNRAS, 372, 233

Amati, L., & Della Valle, M. 2013, International Journal of Modern Physics D, 22, 1330028

Amati, L., Dichiara, S., Frontera, F., et al. 2013, GRB Coordinates Network, 15025, 1

Amati, L., Frontera, F., Tavani, M., et al. 2002, A&A, 390, 81

Amelino-Camelia, G., Ellis, J., Mavromatos, N. E., Nanopoulos, D. V., & Sarkar, S. 1998, Nature, 393, 763

Antoniadis, J. 2015, in Gravitational Wave Astrophysics, Vol. 40, 1

Aptekar, R. L., Frederiks, D. D., Golenetskii, S. V., et al. 1995, SSRv, 71, 265

Arcavi, I., Hosseinzadeh, G., Howell, D. A., et al. 2017, Nature, 551, 64

Arnett, D. 1996, Supernovae and Nucleosynthesis: An Investigation of the History of Matter from the Big Bang to the Present

Asano, K., Guiriec, S., & Mészáros, P. 2009, ApJL, 705, L191

Atwood, W. B., Abdo, A. A., Ackermann, M., et al. 2009, ApJ, 697, 1071

Balzer, B. G., Siegel, M. H., & Maselli, A. 2015, GRB Coordinates Network, 18502, 1

Band, D., Matteson, J., Ford, L., et al. 1993, ApJ, 413, 281

Band, D. L. 1997, ApJ, 486, 928

Band, D. L., Axelsson, M., Baldini, L., et al. 2009, ApJ, 701, 1673

Barkana, R., & Loeb, A. 2000, ApJ, 531, 613

Barkana, R., & Loeb, A. 2004, ApJ, 601, 64

Barthelmy, S. D., Butterworth, P., Cline, T. L., & Gehrels, N. 1998, in American Institute of Physics Conference Series, Vol. 428, Gamma-Ray Bursts, 4th Hunstville Symposium, ed. C. A. Meegan, R. D. Preece, & T. M. Koshut, 139–143

Barthelmy, S. D., Butterworth, P., Cline, T. L., et al. 1995, Ap&SS, 231, 235

Barthelmy, S. D., Kennea, J., & Racusin, J. 2012, GRB Coordinates Network, 13381, 1

Barthelmy, S. D., Chincarini, G., Burrows, D. N., et al. 2005a, Nature, 438, 994

Barthelmy, S. D., Barbier, L. M., Cummings, J. R., et al. 2005b, SSRv, 120, 143

Basak, R., & Rao, A. R. 2013, MNRAS, 436, 3082

Bathurst, C., Frail, D. A., & Cenko, S. B. 2012, GRB Coordinates Network, 13474, 1

Beardmore, A. P., & Schady, P. 2009, GRB Coordinates Network, 9528, 1

Becerra, L., Bianco, C. L., Fryer, C. L., Rueda, J. A., & Ruffini, R. 2016, ApJ, 833, 107

Becerra, L., Cipolletta, F., Fryer, C. L., Rueda, J. A., & Ruffini, R. 2015, ApJ, 812, 100

Becerra, L., Ellinger, C. L., Fryer, C. L., Rueda, J. A., & Ruffini, R. 2019, ApJ, 871, 14

Becerra, L., Guzzo, M. M., Rossi-Torres, F., et al. 2018, ApJ, 852, 120

Becker, G. D., Rauch, M., & Sargent, W. L. W. 2007, ApJ, 662, 72

Becker, R. H., Fan, X., White, R. L., et al. 2001, AJ, 122, 2850

Bekenstein, J. D. 1971, PhRvD, 4, 2185

Belczynski, K., Perna, R., Bulik, T., et al. 2006, ApJ, 648, 1110

Bellm, E. C. 2010, ApJ, 714, 881

Belvedere, R., Boshkayev, K., Rueda, J. A., & Ruffini, R. 2014, NuPhA, 921, 33

Berger, E. 2009, ApJ, 690, 231

Berger, E. 2011, New Astronomy Reviews, 55, 1

Berger, E. 2014a, Annual Review of Astronomy and Astrophysics, 52, 43

Berger, E. 2014b, ARA&A, 52, 43

Berger, E., Fong, W., & Chornock, R. 2013, ApJL, 774, L23

Berger, E., Kulkarni, S. R., Pooley, G., et al. 2003, Nature, 426, 154

Berger, E., Price, P. A., Cenko, S. B., et al. 2005, Nature, 438, 988

Berger, E., Zauderer, B. A., Chary, R. R., et al. 2014, ApJ, 796, 96

Bernardini, M. G., Bianco, C. L., Caito, L., et al. 2007, A&A, 474, L13

Bernardini, M. G., Bianco, C. L., Caito, L., et al. 2008, in American Institute of Physics Conference Series, Vol. 966, Relativistic Astrophysics, ed. C. L. Bianco & S.-S. Xue, 7–11

Bernardini, M. G., Bianco, C. L., Chardonnet, P., et al. 2005, ApJL, 634, L29

Bernardini, M. G., Margutti, R., Mao, J., Zaninoni, E., & Chincarini, G. 2012, A&A, 539, A3

Bernardini, M. G., Ghirlanda, G., Campana, S., et al. 2015, MNRAS, 446, 1129

Bersier, D. 2011, GRB Coordinates Network, 12216, 1

Bersier, D., McLeod, B., Garnavich, P. M., et al. 2003, ApJL, 583, L63

Bianco, C. L., & Ruffini, R. 2004, ApJL, 605, L1

Bianco, C. L., & Ruffini, R. 2005a, ApJL, 633, L13

Bianco, C. L., & Ruffini, R. 2005b, ApJL, 620, L23

Bianco, C. L., & Ruffini, R. 2006, ApJL, 644, L105

Bianco, C. L., Ruffini, R., & Xue, S. S. 2001, A&A, 368, 377

Bianco, C. L., Bernardini, M. G., Caito, L., et al. 2008, in The Eleventh Marcel Grossmann Meeting On Recent Developments in Theoretical and Experimental General Relativity, Gravitation and Relativistic Field Theories, 1974–1976

Bildsten, L., & Cutler, C. 1992, ApJ, 400, 175

Bisnovatyi-Kogan, G. S., & Murzina, M. V. A. 1995, PhRvD, 52, 4380

Bissaldi, E. 2010, arXiv e-prints, arXiv:1002.4194

Bissaldi, E., Racusin, J. L., Longo, F., et al. 2014, GRB Coordinates Network, 16969, 1

Blandford, R. D., & McKee, C. F. 1976, Physics of Fluids, 19, 1130

Blandford, R. D., & Znajek, R. L. 1977, MNRAS, 179, 433

Bloom, J. S., Fox, D., van Dokkum, P. G., et al. 2003a, ApJ, 599, 957

Bloom, J. S., Frail, D. A., & Kulkarni, S. R. 2003b, ApJ, 594, 674

Bloom, J. S., Frail, D. A., & Sari, R. 2001, AJ, 121, 2879

Bloom, J. S., Kulkarni, S. R., & Djorgovski, S. G. 2002, AJ, 123, 1111

Bloom, J. S., Kulkarni, S. R., Djorgovski, S. G., et al. 1999, Nature, 401, 453

Bloom, J. S., Prochaska, J. X., Pooley, D., et al. 2006, ApJ, 638, 354

Bloom, J. S., Giannios, D., Metzger, B. D., et al. 2011, Science, 333, 203

Boella, G., Butler, R. C., Perola, G. C., et al. 1997, A&AS, 122, 299

Boër, M., Gendre, B., & Stratta, G. 2015, ApJ, 800, 16

Bondi, H. 1952, MNRAS, 112, 195

Bondi, H., & Hoyle, F. 1944, MNRAS, 104, 273

Bonnell, I. A., Bate, M. R., Clarke, C. J., & Pringle, J. E. 1997, MNRAS, 285, 201

Bonnell, I. A., Bate, M. R., Clarke, C. J., & Pringle, J. E. 2001, MNRAS, 323, 785

Bošnjak, Ž., Daigne, F., & Dubus, G. 2009, A&A, 498, 677

Brainerd, J. J. 1992, Nature, 355, 522

Breeveld, A. A., Marshall, F. E., & Racusin, J. 2012, GRB Coordinates Network, 13397, 1

Bremer, M., Winters, J. M., Konig, S., de Ugarte Postigo, A., & Castro-Tirado, A. J. 2012, GRB Coordinates Network, 13421, 1

Bromm, V. 2013, Reports on Progress in Physics, 76, 112901

Bromm, V., Coppi, P. S., & Larson, R. B. 2002, ApJ, 564, 23

Bromm, V., & Larson, R. B. 2004, Annual Review of Astronomy and Astrophysics, 42, 79

Bromm, V., & Loeb, A. 2002, ApJ, 575, 111

Bromm, V., & Loeb, A. 2003, ApJ, 596, 34

Bromm, V., & Loeb, A. 2006, ApJ, 642, 382

Bufano, F., Pian, E., Sollerman, J., et al. 2012, ApJ, 753, 67

Burgess, J. M., Preece, R. D., Connaughton, V., et al. 2014, ApJ, 784, 17

Burlon, D., Ghirlanda, G., Ghisellini, G., Greiner, J., & Celotti, A. 2009, A&A, 505, 569

Burlon, D., Ghirlanda, G., Ghisellini, G., et al. 2008, ApJ, 685, L19

Burrows, D. N., Romano, P., Falcone, A., et al. 2005a, Science, 309, 1833

Burrows, D. N., Hill, J. E., Nousek, J. A., et al. 2005b, SSRv, 120, 165

Butler, N., Watson, A. M., Kutyrev, A., et al. 2013, GRB Coordinates Network, 14993, 1

Butler, N. R., Bloom, J. S., & Poznanski, D. 2010, The Astrophysical Journal, 711, 495

Butler, N. R., & Kocevski, D. 2007, ApJ, 663, 407

Butler, N. R., Kocevski, D., Bloom, J. S., & Curtis, J. L. 2007, ApJ, 671, 656

Bykov, A., Gehrels, N., Krawczynski, H., et al. 2012, SSRv, 173, 309

Cabrera, J. I., Firmani, C., Avila-Reese, V., et al. 2007, MNRAS, 382, 342

Cadelano, M., Pallanca, C., Ferraro, F. R., et al. 2015, ApJ, 812, 63

Caito, L., Amati, L., Bernardini, M. G., et al. 2010, A&A, 521, A80

Caito, L., Bernardini, M. G., Bianco, C. L., et al. 2009, A&A, 498, 501

Calderone, G., Ghirlanda, G., Ghisellini, G., et al. 2015, MNRAS, 448, 403

Campana, S., Mangano, V., Blustin, A. J., et al. 2006, Nature, 442, 1008

Campisi, M. A., Maio, U., Salvaterra, R., & Ciardi, B. 2011, MNRAS, 416, 2760
Cannizzo, J. K., Baumgartner, W. H., Evans, P. A., et al. 2010, GRB Coordinates Network, 11004, 1
Cano, Z. 2015, GRB Coordinates Network, 18552, 1
Cano, Z., Wang, S.-Q., Dai, Z.-G., & Wu, X.-F. 2017, Advances in Astronomy, 2017, 8929054
Cano, Z., Bersier, D., Guidorzi, C., et al. 2011, MNRAS, 413, 669
Cano, Z., de Ugarte Postigo, A., Pozanenko, A., et al. 2014, A&A, 568, A19
Cash, W. 1979, ApJ, 228, 939
Castro-Tirado, A. J., Bremer, M., & Winters, J. M. 2013, GRB Coordinates Network, 14689, 1
Castro-Tirado, A. J., de Ugarte Postigo, A., Gorosabel, J., et al. 2008, Nature, 455, 506
Cavallo, G., & Rees, M. J. 1978, MNRAS, 183, 359
Cen, R. 2003, ApJ, 591, 12
Cenko, S. B. 2009, GRB Coordinates Network, 9513, 1
Cenko, S. B. 2013, GRB Coordinates Network, 14680, 1
Cenko, S. B., Gal-Yam, A., Kasliwal, M. M., et al. 2013, GRB Coordinates Network, 14998, 1
Cenko, S. B., & Perley, D. A. 2014, GRB Coordinates Network, 16989, 1
Cenko, S. B., & Perley, D. A. 2015, GRB Coordinates Network, 18537, 1
Cenko, S. B., Perley, D. A., Junkkarinen, V., et al. 2009, GRB Coordinates Network, 9518, 1
Chandra, P. 2013, GRB Coordinates Network, 15002, 1
Chandra, P., & Frail, D. A. 2009, GRB Coordinates Network, 9533, 1
Chandra, P., & Frail, D. A. 2012, ApJ, 746, 156
Chandra, P., & Nayana, A. J. 2015a, GRB Coordinates Network, 18620, 1
Chandra, P., & Nayana, A. J. 2015b, GRB Coordinates Network, 18608, 1
Charlot, S., & Fall, S. M. 1993, ApJ, 415, 580
Cheng, L. X., Ma, Y. Q., Cheng, K. S., Lu, T., & Zhou, Y. Y. 1995, A&A, 300, 746
Cherubini, C., Geralico, A., Rueda, H. J. A., & Ruffini, R. 2009, PhRvD, 79, 124002
Cherubini, C., Ruffini, R., & Vitagliano, L. 2002, Physics Letters B, 545, 226
Cheung, T., Vianello, G., Zhu, S., et al. 2013a, GRB Coordinates Network, 14971, 1
Cheung, T., Vianello, G., Zhu, S., et al. 2013b, GRB Coordinates Network, 14971, 1
Chevallier, M., & Polarski, D. 2001, International Journal of Modern Physics D, 10, 213
Chincarini, G., Moretti, A., Romano, P., et al. 2007, ApJ, 671, 1903
Chincarini, G., Mao, J., Margutti, R., et al. 2010, MNRAS, 406, 2113
Chornock, R., Berger, E., Fox, D. B., et al. 2014, arXiv e-prints, arXiv:1405.7400
Chornock, R., Berger, E., Fox, D. B., et al. 2013, ApJ, 774, 26
Chornock, R., Perley, D. A., Cenko, S. B., & Bloom, J. S. 2009, GRB Coordinates Network, 9028, 1
Christodoulou, D., & Ruffini, R. 1971, PhRvD, 4, 3552
Ciardi, B., & Loeb, A. 2000, ApJ, 540, 687
Ciardi, B., Inoue, S., Abdalla, F. B., et al. 2015, MNRAS, 453, 101
Cobb, B. E., Bailyn, C. D., van Dokkum, P. G., & Natarajan, P. 2006, ApJL, 645, L113
Cobb, B. E., Bloom, J. S., Perley, D. A., et al. 2010, ApJL, 718, L150
Cohen, E., Katz, J. I., Piran, T., et al. 1997, ApJ, 488, 330
Colgate, S. A. 1968, Canadian Journal of Physics, 46, S476
Colgate, S. A. 1974, ApJ, 187, 333
Collazzi, A. C., & Connaughton, V. 2013, GRB Coordinates Network, 14972, 1
Collazzi, A. C., Schaefer, B. E., Goldstein, A., & Preece, R. D. 2012, ApJ, 747, 39
Corsi, A., Perley, D. A., & Cenko, S. B. 2013, GRB Coordinates Network, 14990, 1
Costa, E., Frontera, F., Heise, J., et al. 1997, Nature, 387, 783
Crowther, P. A. 2006, arXiv e-prints, astro
Crowther, P. A. 2007, ARA&A, 45, 177
Cucchiara, A., & Cenko, S. B. 2013, GRB Coordinates Network, 14687, 1
Cucchiara, A., & Fox, D. B. 2010, GRB Coordinates Network, 10606, 1

Cucchiara, A., Levan, A. J., Fox, D. B., et al. 2011, ApJ, 736, 7
Cummings, J. R. 2013, GRB Coordinates Network, 14676, 1
Curran, P. A., van der Horst, A. J., & Wijers, R. A. M. J. 2008, MNRAS, 386, 859
Dado, S., Dar, A., & De Rújula, A. 2004, A&A, 422, 381
Dai, X., Halpern, J. P., Morgan, N. D., et al. 2007, ApJ, 658, 509
Dai, Z. G., & Cheng, K. S. 2001, ApJ, 558, L109
Dainotti, M. G., Bernardini, M. G., Bianco, C. L., et al. 2007, A&A, 471, L29
Dainotti, M. G., Cardone, V. F., & Capozziello, S. 2008, MNRAS, 391, L79
Dainotti, M. G., Hernandez, X., Postnikov, S., et al. 2017, ApJ, 848, 88
Dainotti, M. G., Willingale, R., Capozziello, S., Fabrizio Cardone, V., & Ostrowski, M. 2010, ApJ, 722, L215
D'Alessio, V., Piro, L., & Rossi, E. M. 2006, A&A, 460, 653
Damour, T., & Ruffini, R. 1975, PhRvL, 35, 463
D'Avanzo, P., D'Elia, V., Tagliaferri, G., et al. 2013a, GRB Coordinates Network, 14984, 1
D'Avanzo, P., Melandri, A., & Evans, P. A. 2013b, GRB Coordinates Network, 14982, 1
D'Avanzo, P., Melandri, A., Steele, I., Mundell, C. G., & Palazzi, E. 2012, GRB Coordinates Network, 13551, 1
D'Avanzo, P., Porterfield, B., Burrows, D. N., et al. 2013c, GRB Coordinates Network, 14973, 1
de Barros, G., Amati, L., Bernardini, M. G., et al. 2011, A&A, 529, A130
De Pasquale, M., Piro, L., Perna, R., et al. 2003, ApJ, 592, 1018
de Ugarte Postigo, A., Campana, S., Thöne, C. C., et al. 2013, A&A, 557, L18
D'Elia, V., D'Avanzo, P., Melandri, A., et al. 2013, GRB Coordinates Network, 15000, 1
Della Valle, M., Chincarini, G., Panagia, N., et al. 2006, Nature, 444, 1050
Della Valle, M., Guetta, D., Cappellaro, E., et al. 2018, MNRAS, 481, 4355
Demianski, M., Piedipalumbo, E., Rubano, C., & Scudellaro, P. 2012, MNRAS, 426, 1396
Demianski, M., Piedipalumbo, E., Sawant, D., & Amati, L. 2017, A&A, 598, A112
Dermer, C. D. 1998, ApJ, 501, L157
Dermer, C. D. 2004, ApJ, 614, 284
Dermer, C. D., Chiang, J., & Böttcher, M. 1999, ApJ, 513, 656
Dermer, C. D., Chiang, J., & Mitman, K. E. 2000, ApJ, 537, 785
Dermer, C. D., & Holmes, J. M. 2005, ApJL, 628, L21
Di Matteo, T., Perna, R., & Narayan, R. 2002, ApJ, 579, 706
Dijkstra, M. 2014, Publications of the Astronomical Society of Australia, 31, e040
Dingus, B. L. 1995, Ap&SS, 231, 187
Djorgovski, S. G., Frail, D. A., Kulkarni, S. R., et al. 2001, ApJ, 562, 654
Djorgovski, S. G., Kulkarni, S. R., Frail, D. A., et al. 2003, in Proc. SPIE, Vol. 4834, Discoveries and Research Prospects from 6- to 10-Meter-Class Telescopes II, ed. P. Guhathakurta, 238–247
Doctor, Z., Kessler, R., Chen, H. Y., et al. 2017, ApJ, 837, 57
Ducci, L., Sidoli, L., Mereghetti, S., Paizis, A., & Romano, P. 2009, MNRAS, 398, 2152
Duncan, R. C., & Thompson, C. 1992, ApJ, 392, L9
Dyks, J., Zhang, B., & Fan, Y. Z. 2005, arXiv e-prints, astro
Edgar, R. 2004, NewAR, 48, 843
Eichler, D., & Levinson, A. 2004, ApJ, 614, L13
Eichler, D., Livio, M., Piran, T., & Schramm, D. N. 1989, Nature, 340, 126
Eichler, D., & Manis, H. 2008, ApJ, 689, L85
Eichler, D., & Waxman, E. 2005, ApJ, 627, 861
Euler, H., & Kockel, B. 1935, Naturwissenschaften, 23, 246
Evans, P. A., & Cannizzo, J. K. 2010, GRB Coordinates Network, 11014, 1
Evans, P. A., de Pasquale, M., Stroh, M. C., & Siegel, M. H. 2013a, GRB Coordinates Network, 14678, 1
Evans, P. A., Stroh, M. C., & Siegel, M. H. 2013b, GRB Coordinates Network, 14681, 1
Evans, P. A., Beardmore, A. P., Page, K. L., et al. 2009, MNRAS, 397, 1177

Falcone, A. D., Burrows, D. N., Lazzati, D., et al. 2006, ApJ, 641, 1010

Falcone, A. D., Morris, D., Racusin, J., et al. 2007, ApJ, 671, 1921

Fan, X., White, R. L., Davis, M., et al. 2000, AJ, 120, 1167

Fan, Y. Z., & Wei, D. M. 2005, MNRAS, 364, L42

Fan, Y.-Z., Zhang, B.-B., Xu, D., Liang, E.-W., & Zhang, B. 2011, ApJ, 726, 32

Fargion, D., & Oliva, P. 2016, arXiv e-prints, arXiv:1605.00177

Fatkhullin, T., Moskvitin, A., Castro-Tirado, A. J., & de Ugarte Postigo, A. 2009, GRB Coordinates Network, 9542, 1

Felten, J. E., & Rees, M. J. 1972, A&A, 17, 226

Fenimore, E. E., Epstein, R. I., & Ho, C. 1993, A&AS, 97, 59

Fenimore, E. E., in 't Zand, J. J. M., Norris, J. P., Bonnell, J. T., & Nemiroff, R. J. 1995, ApJ, 448, L101

Fenimore, E. E., & Ramirez-Ruiz, E. 2000, arXiv e-prints, astro

Filgas, R., Kruehler, T., & Greiner, J. 2010, GRB Coordinates Network, 10607, 1

Fiore, F., Guetta, D., Piranomonte, S., D'Elia, V., & Antonelli, L. A. 2007, A&A, 470, 515

Firmani, C., Ghisellini, G., Avila-Reese, V., & Ghirland a, G. 2006, MNRAS, 370, 185

Fishman, G. J., & Meegan, C. A. 1995, ARA&A, 33, 415

Fishman, G. J., Meegan, C. A., Wilson, R. B., et al. 1994, ApJS, 92, 229

Foley, S. 2010, GRB Coordinates Network, 10595, 1

Fong, W., Berger, E., & Fox, D. B. 2010, ApJ, 708, 9

Fong, W., Metzger, B. D., Berger, E., & Özel, F. 2016, ApJ, 831, 141

Ford, L. A., Band, D. L., Matteson, J. L., et al. 1995, ApJ, 439, 307

Fox, D. B., Frail, D. A., Price, P. A., et al. 2005, Nature, 437, 845

Fox, D. W., Price, P. A., Soderberg, A. M., et al. 2003, ApJ, 586, L5

Frail, D. A., Chandra, P., Cenko, S. B., & Harrison, F. 2010, GRB Coordinates Network, 10698, 1

Frail, D. A., Goss, W. M., & Whiteoak, J. B. Z. 1994, ApJ, 437, 781

Frail, D. A., Kulkarni, S. R., Nicastro, L., Feroci, M., & Taylor, G. B. 1997, Nature, 389, 261

Frail, D. A., Soderberg, A. M., Kulkarni, S. R., et al. 2005, ApJ, 619, 994

Frail, D. A., Kulkarni, S. R., Sari, R., et al. 2001a, ApJ, 562, L55

Frail, D. A., Kulkarni, S. R., Sari, R., et al. 2001b, ApJL, 562, L55

Frail, D. A., Yost, S. A., Berger, E., et al. 2003, ApJ, 590, 992

Frederiks, D. 2010, GRB Coordinates Network, 10598, 1

Friedman, A. S., & Bloom, J. S. 2005, ApJ, 627, 1

Friis, M., & Watson, D. 2013, ApJ, 771, 15

Frontera, F., Costa, E., dal Fiume, D., et al. 1997, A&AS, 122, 357

Fruchter, A. S., Thorsett, S. E., Metzger, M. R., et al. 1999, ApJ, 519, L13

Fruchter, A. S., Levan, A. J., Strolger, L., et al. 2006, Nature, 441, 463

Fryer, C. L. 2009, ApJ, 699, 409

Fryer, C. L., Herwig, F., Hungerford, A., & Timmes, F. X. 2006a, ApJL, 646, L131

Fryer, C. L., Oliveira, F. G., Rueda, J. A., & Ruffini, R. 2015, PhRvL, 115, 231102

Fryer, C. L., Rockefeller, G., & Warren, M. S. 2006b, ApJ, 643, 292

Fryer, C. L., Rueda, J. A., & Ruffini, R. 2014, ApJL, 793, L36

Fryer, C. L., Woosley, S. E., & Hartmann, D. H. 1999a, ApJ, 526, 152

Fryer, C. L., Woosley, S. E., Herant, M., & Davies, M. B. 1999b, ApJ, 520, 650

Furlanetto, S. R., & Loeb, A. 2003, ApJ, 588, 18

Fynbo, J. P. U., Watson, D., Thöne, C. C., et al. 2006, Nature, 444, 1047

Fynbo, J. U., Jensen, B. L., Gorosabel, J., et al. 2001, A&A, 369, 373

Gal-Yam, A., Fox, D. B., Price, P. A., et al. 2006, Nature, 444, 1053

Galama, T. J., Vreeswijk, P. M., van Paradijs, J., et al. 1998, Nature, 395, 670

Galante, D., & Horvath, J. E. 2007, International Journal of Astrobiology, 6

Gao, H., Lei, W.-H., Zou, Y.-C., Wu, X.-F., & Zhang, B. 2013a, NewAR, 57, 141

Gao, S., Kashiyama, K., & Mészáros, P. 2013b, ApJ, 772, L4

Gao, W.-H., Mao, J., Xu, D., & Fan, Y.-Z. 2009, ApJ, 706, L33

Gehrels, N., & Cannizzo, J. K. 2015, Journal of High Energy Astrophysics, 7, 2

Gehrels, N., Laird, C. M., Jackman, C. H., et al. 2003, ApJ, 585, 1169

Gehrels, N., Ramirez-Ruiz, E., & Fox, D. B. 2009, ARA&A, 47, 567

Gehrels, N., Chincarini, G., Giommi, P., et al. 2004, ApJ, 611, 1005

Gehrels, N., Sarazin, C. L., O'Brien, P. T., et al. 2005a, Nature, 437, 851

Gehrels, N., Sarazin, C. L., O'Brien, P. T., et al. 2005b, Nature, 437, 851

Gehrels, N., Norris, J. P., Barthelmy, S. D., et al. 2006, Nature, 444, 1044

Ghirlanda, G., Celotti, A., & Ghisellini, G. 2002, A&A, 393, 409

Ghirlanda, G., Celotti, A., & Ghisellini, G. 2003, A&A, 406, 879

Ghirlanda, G., Ghisellini, G., & Lazzati, D. 2004, ApJ, 616, 331

Ghirlanda, G., Nava, L., Ghisellini, G., Celotti, A., & Firmani, C. 2009, A&A, 496, 585

Ghirlanda, G., Pescalli, A., & Ghisellini, G. 2013a, MNRAS, 432, 3237

Ghirlanda, G., Pescalli, A., & Ghisellini, G. 2013b, Monthly Notices of the Royal Astronomical Society, 432, 3237

Ghisellini, G., Celotti, A., & Lazzati, D. 2000, MNRAS, 313, L1

Ghisellini, G., Ghirlanda, G., Nava, L., & Celotti, A. 2010, MNRAS, 403, 926

Ghisellini, G., Ghirlanda, G., Nava, L., & Firmani, C. 2007, The Astrophysical Journal, 658, L75

Goldstein, A., Veres, P., Burns, E., et al. 2017, ApJ, 848, L14

Golenetskii, S., Aptekar, R., Pal'Shin, V., et al. 2013a, GRB Coordinates Network, 14986, 1

Golenetskii, S., Aptekar, R., Mazets, E., et al. 2009a, GRB Coordinates Network, 9553, 1

Golenetskii, S., Aptekar, R., Mazets, E., et al. 2009b, GRB Coordinates Network, 9030, 1

Golenetskii, S., Aptekar, R., Frederiks, D., et al. 2010, GRB Coordinates Network, 11021, 1

Golenetskii, S., Aptekar, R., Mazets, E., et al. 2011, GRB Coordinates Network, 12223, 1

Golenetskii, S., Aptekar, R., Frederiks, D., et al. 2012, GRB Coordinates Network, 13382, 1

Golenetskii, S., Aptekar, R., Frederiks, D., et al. 2013b, GRB Coordinates Network, 14677, 1

Golenetskii, S., Aptekar, R., Frederiks, D., et al. 2015, GRB Coordinates Network, 18516, 1

Goodman, J. 1986, ApJL, 308, L47

Gotz, D., Mereghetti, S., Bozzo, E., et al. 2014, GRB Coordinates Network, 15785, 1

Graham, J. F., & Fruchter, A. S. 2013, ApJ, 774, 119

Granot, J., & Kumar, P. 2006, MNRAS, 366, L13

Granot, J., Piran, T., & Sari, R. 1999a, ApJ, 513, 679

Granot, J., Piran, T., & Sari, R. 1999b, ApJ, 527, 236

Granot, J., & Sari, R. 2002, ApJ, 568, 820

Graziani, C., Lamb, D. Q., Sakamoto, T., Donaghy, T., & Hete-2 Science Team. 2004, in American Institute of Physics Conference Series, Vol. 727, Gamma-Ray Bursts: 30 Years of Discovery, ed. E. Fenimore & M. Galassi, 42–46

Groot, P. J., Galama, T. J., van Paradijs, J., et al. 1998, ApJ, 493, L27

Gruber, D. 2011, GRB Coordinates Network, 12221, 1

Gruber, D., Burgess, J. M., & Connaughton, V. 2012, GRB Coordinates Network, 13377, 1

Guetta, D., & Della Valle, M. 2007, ApJL, 657, L73

Guetta, D., & Piran, T. 2005, A&A, 435, 421

Guetta, D., & Piran, T. 2006, A&A, 453, 823

Guetta, D., Piran, T., & Waxman, E. 2005, ApJ, 619, 412

Guetta, D., Rahin, R., Bartos, I., & Della Valle, M. 2020, MNRAS, 492, 843

Guidorzi, C., Monfardini, A., Gomboc, A., et al. 2006, Publications of the Astronomical Society of the Pacific, 118, 288

Guidorzi, C., Steele, I. A., Melandri, A., et al. 2009, GRB Coordinates Network, 9039, 1

Guilbert, P. W., Fabian, A. C., & Rees, M. J. 1983, MNRAS, 205, 593

Guiriec, S., Gonzalez, M. M., Sacahui, J. R., et al. 2016, ApJ, 819, 79

Guiriec, S., Briggs, M. S., Connaugthon, V., et al. 2010, ApJ, 725, 225

Guiriec, S., Connaughton, V., Briggs, M. S., et al. 2011, ApJ, 727, L33

Gunn, J. E., & Peterson, B. A. 1965, ApJ, 142, 1633

Haiman, Z., & Loeb, A. 2001, ApJ, 552, 459

Hakkila, J., Giblin, T. W., Norris, J. P., Fragile, P. C., & Bonnell, J. T. 2008, ApJ, 677, L81

Hakkila, J., & Preece, R. D. 2011, ApJ, 740, 104

Hamburg, R., Meegan, C., & Roberts, O. 2016, GRB Coordinates Network, 19882, 1

Hanabata, Y., Uehara, T., Takahashi, T., et al. 2011, GRB Coordinates Network, 12244, 1

Hancock, P. J., Gaensler, B. M., & Murphy, T. 2013, ApJ, 776, 106

Harrison, F., Cenko, B., Frail, D. A., Chandra, P., & Kulkarni, S. 2009, GRB Coordinates Network, 9043, 1

Harrison, F. A., Yost, S. A., Sari, R., et al. 2001, ApJ, 559, 123

Harrison, F. A., Craig, W. W., Christensen, F. E., et al. 2013, ApJ, 770, 103

Hawking, S. W. 1974, Nature, 248, 30

Hawking, S. W. 1975, Communications in Mathematical Physics, 43, 199

Heise, J. 2003, in American Institute of Physics Conference Series, Vol. 662, Gamma-Ray Burst and Afterglow Astronomy 2001: A Workshop Celebrating the First Year of the HETE Mission, ed. G. R. Ricker & R. K. Vanderspek, 229–236

Heise, J., Zand, J. I., Kippen, R. M., & Woods, P. M. 2001, in Gamma-ray Bursts in the Afterglow Era, ed. E. Costa, F. Frontera, & J. Hjorth, 16

Heisenberg, W., & Euler, H. 1936, Zeitschrift fur Physik, 98, 714

Higdon, J. C., Matz, S. M., Share, G. H., Messina, D. C., & Iadicicco, A. 1992, in American Institute of Physics Conference Series, Vol. 265, American Institute of Physics Conference Series, ed. W. S. Paciesas & G. J. Fishman, 89–93

Hjorth, J., Sollerman, J., Møller, P., et al. 2003, Nature, 423, 847

Hjorth, J., Malesani, D., Jakobsson, P., et al. 2012, ApJ, 756, 187

Horváth, I. 1998, The Astrophysical Journal, 508, 757

Hoyle, F., & Lyttleton, R. A. 1939, Proceedings of the Cambridge Philosophical Society, 35, 405

Hulse, R. A., & Taylor, J. H. 1975, ApJ, 195, L51

Hurley, K., Dingus, B. L., Mukherjee, R., et al. 1994, Nature, 372, 652

Imamura, J. N., & Epstein, R. I. 1987, ApJ, 313, 711

Ivarsen, K., Haislip, J., Reichart, D., et al. 2010, GRB Coordinates Network, 11008, 1

Izzo, L., Muccino, M., Zaninoni, E., Amati, L., & Della Valle, M. 2015, A&A, 582, A115

Izzo, L., Rueda, J. A., & Ruffini, R. 2012a, A&A, 548, L5

Izzo, L., Ruffini, R., Penacchioni, A. V., et al. 2012b, A&A, 543, A10

Izzo, L., Thöne, C. C., Schulze, S., et al. 2017, MNRAS, 472, 4480

Izzo, L., Thöne, C. C., García-Benito, R., et al. 2018, A&A, 610, A11

Izzo, L., de Ugarte Postigo, A., Maeda, K., et al. 2019, Nature, 565, 324

Jager, R., Mels, W. A., Brinkman, A. C., et al. 1997, A&AS, 125, 557

Jakobsson, P., Hjorth, J., Fynbo, J. P. U., et al. 2004a, ApJ, 617, L21

Jakobsson, P., Vreeswijk, P. M., Hjorth, J., et al. 2007, GRB Coordinates Network, 6952, 1

Jakobsson, P., Hjorth, J., Fynbo, J. P. U., et al. 2004b, A&A, 427, 785

Jakobsson, P., Levan, A., Fynbo, J. P. U., et al. 2006, A&A, 447, 897

Jansen, F., Lumb, D., Altieri, B., et al. 2001, A&A, 365, L1

Japelj, J., Kopač, D., Kobayashi, S., et al. 2014, ApJ, 785, 84

Jin, Z.-P., Li, X., Cano, Z., et al. 2015, ApJL, 811, L22
Kamble, A., van der Horst, A. J., & Wijiers, R. 2009, GRB Coordinates Network, 9538, 1
Kamble, A. P., van der Horst, A. J., Wijers, R. A. M. J., et al. 2010, GRB Coordinates Network, 10697, 1
Kanbach, G., Bertsch, D. L., Fichtel, C. E., et al. 1988, SSRv, 49, 69
Kaneko, Y., Preece, R. D., Briggs, M. S., et al. 2006, ApJS, 166, 298
Kann, D. A., Laux, U., Ludwig, F., & Stecklum, S. 2009a, GRB Coordinates Network, 9063, 1
Kann, D. A., Laux, U., & Stecklum, S. 2009b, GRB Coordinates Network, 9033, 1
Kann, D. A., Laux, U., & Stecklum, S. 2009c, GRB Coordinates Network, 9041, 1
Kann, D. A., Schulze, S., & Updike, A. C. 2008, GRB Coordinates Network, 7627, 1
Kasen, D., Metzger, B., Barnes, J., Quataert, E., & Ramirez-Ruiz, E. 2017, Nature, 551, 80
Katz, J. I. 1994, ApJ, 422, 248
Katz, J. I. 1997, ApJ, 490, 633
Katz, J. I., & Piran, T. 1997, ApJ, 490, 772
Kawanaka, N., Piran, T., & Krolik, J. H. 2013, ApJ, 766, 31
Kawano, T., Ohno, M., Takaki, K., et al. 2013, GRB Coordinates Network, 14725, 1
Kennea, J. A., Racusin, J. L., & Pagani, C. 2014, GRB Coordinates Network, 16978, 1
Kerr, R. P. 1963, PhRvL, 11, 237
King, A., O'Brien, P. T., Goad, M. R., et al. 2005, ApJ, 630, L113
Kippen, R. M., Woods, P. M., Heise, J., et al. 2003, in American Institute of Physics Conference Series, Vol. 662, Gamma-Ray Burst and Afterglow Astronomy 2001: A Workshop Celebrating the First Year of the HETE Mission, ed. G. R. Ricker & R. K. Vanderspek, 244–247
Kitayama, T., Yoshida, N., Susa, H., & Umemura, M. 2004, ApJ, 613, 631
Klebesadel, R. W., Strong, I. B., & Olson, R. A. 1973, ApJL, 182, L85
Klose, S., Schmidl, S., Kann, D. A., et al. 2019, A&A, 622, A138
Kobayashi, S., Piran, T., & Sari, R. 1997, ApJ, 490, 92
Kocevski, D., & Liang, E. 2003, ApJ, 594, 385
Kono, K., Daikyuji, A., Sonoda, E., et al. 2009, GRB Coordinates Network, 9568, 1
Kopač, D., D'Avanzo, P., Melandri, A., et al. 2012, MNRAS, 424, 2392
Koshut, T. M., Kouveliotou, C., Paciesas, W. S., et al. 1995, ApJ, 452, 145
Kouveliotou, C., Meegan, C. A., Fishman, G. J., et al. 1993, ApJL, 413, L101
Kouveliotou, C., Dieters, S., Strohmayer, T., et al. 1998, Nature, 393, 235
Krimm, H. A., Barthelmy, S. D., Baumgartner, W. H., et al. 2011, GRB Coordinates Network, 12217, 1
Kulkarni, S. R. 2005, arXiv e-prints, astro
Kulkarni, S. R., Djorgovski, S. G., Ramaprakash, A. N., et al. 1998, Nature, 393, 35
Kumar, P., & Barniol Duran, R. 2009, MNRAS, 400, L75
Kumar, P., & Panaitescu, A. 2000, Astrophys. J., 541, L51
Kumar, P., & Zhang, B. 2015, PhR, 561, 1
La Parola, V., Mangano, V., Fox, D., et al. 2006, A&A, 454, 753
Lamb, D. Q. 2003, in American Institute of Physics Conference Series, Vol. 662, Gamma-Ray Burst and Afterglow Astronomy 2001: A Workshop Celebrating the First Year of the HETE Mission, ed. G. R. Ricker & R. K. Vanderspek, 433–437
Lamb, D. Q., & Reichart, D. E. 2000, ApJ, 536, 1
Lamb, D. Q., Ricker, G. R., Atteia, J. L., et al. 2004, NewAR, 48, 423
Landsman, W., & Cannizzo, J. 2010, GRB Coordinates Network, 10609, 1
Laskar, T., Alexander, K., & Berger, E. 2015, GRB Coordinates Network, 18508, 1
Laskar, T., Zauderer, A., & Berger, E. 2012, GRB Coordinates Network, 13547, 1
Lazarus, P., Tauris, T. M., Knispel, B., et al. 2014, MNRAS, 437, 1485
Lazzati, D. 2005, MNRAS, 357, 722
Lazzati, D., Morsony, B. J., Margutti, R., & Begelman, M. C. 2013, ApJ, 765, 103
Le Floc'h, E., Duc, P. A., Mirabel, I. F., et al. 2003, A&A, 400, 499

Lee, W. H., Ramirez-Ruiz, E., & López-Cámara, D. 2009, ApJL, 699, L93
Leloudas, G., Fynbo, J. P. U., Schulze, S., et al. 2013, GRB Coordinates Network, 14983, 1
Levan, A. J., Cenko, S. B., Perley, D. A., & Tanvir, N. R. 2013, GRB Coordinates Network, 14455, 1
Levan, A. J., Tanvir, N. R., Starling, R. L. C., et al. 2014, ApJ, 781, 13
Li, L.-X. 2007, MNRAS, 379, L55
Li, L.-X., & Paczyński, B. 1998, ApJL, 507, L59
Li, T.-P., Qu, J.-L., Feng, H., et al. 2004, ChJA&A, 4, 583
Li, W., Perley, D. A., & Filippenko, A. V. 2009, GRB Coordinates Network, 9517, 1
Li, Y., & Zhang, B. 2015, ApJ, 810, 41
Liang, E., & Kargatis, V. 1996, Nature, 381, 49
Liang, E., & Zhang, B. 2005, ApJ, 633, 611
Liang, E. W., Dai, Z. G., & Wu, X. F. 2004, ApJ, 606, L29
Liang, E.-W., Racusin, J. L., Zhang, B., Zhang, B.-B., & Burrows, D. N. 2008a, ApJ, 675, 528
Liang, N., Xiao, W. K., Liu, Y., & Zhang, S. N. 2008b, ApJ, 685, 354
Lien, A., Sakamoto, T., Barthelmy, S. D., et al. 2016, ApJ, 829, 7
Lien, A. Y., Barthelmy, S. D., Chester, M. M., et al. 2014, GRB Coordinates Network, 15784, 1
LIGO Scientific Collaboration, Aasi, J., Abbott, B. P., et al. 2015, Classical and Quantum Gravity, 32, 074001
Linder, E. V. 2003, PhRvL, 90, 091301
Lithwick, Y., & Sari, R. 2001, ApJ, 555, 540
Littlejohns, O. M., Evans, P. A., Beardmore, A. P., & Oates, S. R. 2011, GRB Coordinates Network, 12224, 1
Littlejohns, O. M., Evans, P. A., Page, K. L., et al. 2012, GRB Coordinates Network, 13394, 1
Liu, T., Gu, W.-M., Xue, L., Weng, S.-S., & Lu, J.-F. 2008, ApJ, 676, 545
Lloyd, N. M., Petrosian, V., & Mallozzi, R. S. 2000, ApJ, 534, 227
Lloyd-Ronning, N. M., Fryer, C. L., & Ramirez-Ruiz, E. 2002, ApJ, 574, 554
Longo, F., Vianello, G., Kocevski, D., & Arimoto, M. 2017, GRB Coordinates Network, 22136, 1
Longo, F., Moretti, E., Barbiellini, G., et al. 2009, GRB Coordinates Network, 9524, 1
Lü, H.-J., Liang, E.-W., Zhang, B.-B., & Zhang, B. 2010, The Astrophysical Journal, 725, 1965
Lü, H.-J., Zhang, B., Lei, W.-H., Li, Y., & Lasky, P. D. 2015, ApJ, 805, 89
Lu, R., & Liang, E. 2010, Science China Physics, Mechanics, and Astronomy, 53, 163
Lu, R. J., Hou, S. J., & Liang, E.-W. 2010, ApJ, 720, 1146
Lu, R. J., Qin, Y. P., Zhang, Z. B., & Yi, T. F. 2006, MNRAS, 367, 275
Lu, R.-J., Wei, J.-J., Liang, E.-W., et al. 2012, ApJ, 756, 112
Lyman, J. D., Bersier, D., James, P. A., et al. 2016, MNRAS, 457, 328
Lyne, A. G., & Lorimer, D. R. 1994, Nature, 369, 127
MacFadyen, A. I., & Woosley, S. E. 1999, ApJ, 524, 262
Mackey, J., Bromm, V., & Hernquist, L. 2003, ApJ, 586, 1
Maeda, K., & Nomoto, K. 2003, ApJ, 598, 1163
Maeder, A., & Meynet, G. 2001, A&A, 373, 555
Malesani, D., Leloudas, G., Xu, D., et al. 2011, GRB Coordinates Network, 12220, 1
Malesani, D., Tagliaferri, G., Chincarini, G., et al. 2004, ApJL, 609, L5
Malesani, D., Xu, D., Fynbo, J. P. U., et al. 2014a, GRB Coordinates Network, 15800, 1
Malesani, D., Xu, D., Fynbo, J. P. U., et al. 2014b, GRB Coordinates Network, 15800, 1
Malhotra, S., & Rhoads, J. E. 2004, ApJ, 617, L5
Mangano, V., Holland, S. T., Malesani, D., et al. 2007, A&A, 470, 105
Mao, S., & Paczynski, B. 1992, ApJ, 388, L45
Margutti, R., Guidorzi, C., Chincarini, G., et al. 2010, MNRAS, 406, 2149
Margutti, R., Chincarini, G., Granot, J., et al. 2011, MNRAS, 417, 2144
Maselli, A., D'Ai, A., Lien, A. Y., et al. 2015, GRB Coordinates Network, 18478, 1
Maselli, A., Burrows, D. N., Kennea, J. A., et al. 2012, GRB Coordinates Network, 13541, 1
Maselli, A., Melandri, A., Nava, L., et al. 2014, Science, 343, 48

Matsumoto, T., Ioka, K., Kisaka, S., & Nakar, E. 2018, ApJ, 861, 55
Mazets, E. P., Golenetskii, S. V., Aptekar, R. L., Gurian, I. A., & Ilinskii, V. N. 1981a, Nature, 290, 378
Mazets, E. P., Golenetskii, S. V., Ilinskii, V. N., et al. 1981b, Ap&SS, 80, 3
Mazzali, P. A., Deng, J., Nomoto, K., et al. 2006, Nature, 442, 1018
McBreen, S. 2009, GRB Coordinates Network, 9535, 1
Meegan, C., Lichti, G., Bhat, P. N., et al. 2009, ApJ, 702, 791
Meegan, C. A., Fishman, G. J., Wilson, R. B., et al. 1992, Nature, 355, 143
Melandri, A., Guidorzi, C., Bersier, D., et al. 2009, GRB Coordinates Network, 9520, 1
Melandri, A., Pian, E., D'Elia, V., et al. 2014, A&A, 567, A29
Melott, A. L., Thomas, B. C., Hogan, D. P., Ejzak, L. M., & Jackman, C. H. 2005, Geophys. Res. Lett., 32, L14808
Melott, A. L., Lieberman, B. S., Laird, C. M., et al. 2004, International Journal of Astrobiology, 3, 55
Mesinger, A. 2010, MNRAS, 407, 1328
Mesler, R. A., Pihlström, Y. M., Taylor, G. B., & Granot, J. 2012, ApJ, 759, 4
Mészáros, P. 2006, Reports on Progress in Physics, 69, 2259
Meszaros, P., Laguna, P., & Rees, M. J. 1993, ApJ, 415, 181
Meszaros, P., & Rees, M. J. 1993a, ApJ, 418, L59
Meszaros, P., & Rees, M. J. 1993b, ApJ, 405, 278
Mészáros, P., & Rees, M. J. 1997, ApJ, 476, 232
Mészáros, P., & Rees, M. J. 2001, ApJ, 556, L37
Meszaros, P., Rees, M. J., & Papathanassiou, H. 1994, ApJ, 432, 181
Metzger, A. E., Parker, R. H., Gilman, D., Peterson, L. E., & Trombka, J. I. 1974, ApJ, 194, L19
Metzger, B. D., Martínez-Pinedo, G., Darbha, S., et al. 2010, MNRAS, 406, 2650
Metzger, M. R., Djorgovski, S. G., Kulkarni, S. R., et al. 1997, Nature, 387, 878
Meynet, G., Mowlavi, N., & Maeder, A. 2006, arXiv e-prints, astro
Mignone, A., Zanni, C., Tzeferacos, P., et al. 2012, ApJS, 198, 7
Minaev, P. Y., & Pozanenko, A. S. 2017, Astronomy Letters, 43, 1
Mirabal, N., & Halpern, J. P. 2006, GRB Coordinates Network, 4792, 1
Miralda-Escudé, J. 1998, ApJ, 501, 15
Mitsuda, K., Bautz, M., Inoue, H., et al. 2007, PASJ, 59, S1
Mochkovitch, R., Heussaff, V., Atteia, J. L., Boçi, S., & Hafizi, M. 2016, A&A, 592, A95
Mochkovitch, R., Loiseau, S., Hernanz, M., & Isern, J. 1994, in American Institute of Physics Conference Series, Vol. 307, Gamma-Ray Bursts, ed. G. J. Fishman, 537
Modjaz, M., Kewley, L., Kirshner, R. P., et al. 2008, AJ, 135, 1136
Moskvitin, A. 2015, GRB Coordinates Network, 18521, 1
Muccino, M., Ruffini, R., Bianco, C. L., Izzo, L., & Penacchioni, A. V. 2013a, ApJ, 763, 125
Muccino, M., Ruffini, R., Bianco, C. L., et al. 2013b, ApJ, 772, 62
Mukherjee, S., Feigelson, E. D., Jogesh Babu, G., et al. 1998, The Astrophysical Journal, 508, 314
Mundell, C. G., Melandri, A., Guidorzi, C., et al. 2007, ApJ, 660, 489
Murakami, T., Inoue, H., Nishimura, J., van Paradijs, J., & Fenimore, E. E. 1991, Nature, 350, 592
Murakami, T., Yonetoku, D., Izawa, H., & Ioka, K. 2003, PASJ, 55, L65
Nakar, E., Piran, T., & Granot, J. 2002, ApJ, 579, 699
Nappo, F., Pescalli, A., Oganesyan, G., et al. 2017, A&A, 598, A23
Narayan, R., Paczynski, B., & Piran, T. 1992, ApJL, 395, L83
Narayan, R., & Popham, R. 1989, ApJ, 346, L25
Narayana Bhat, P., Meegan, C. A., von Kienlin, A., et al. 2016, ApJS, 223, 28
Nava, L., Ghirlanda, G., Ghisellini, G., & Celotti, A. 2011a, MNRAS, 415, 3153
Nava, L., Ghirlanda, G., Ghisellini, G., & Celotti, A. 2011b, A&A, 530, A21

Nava, L., Ghirlanda, G., Ghisellini, G., & Firmani, C. 2008, MNRAS, 391, 639

Nava, L., Ghisellini, G., Ghirlanda, G., Tavecchio, F., & Firmani, C. 2006, A&A, 450, 471

Nava, L., Vianello, G., Omodei, N., et al. 2014, MNRAS, 443, 3578

Nemiroff, R. J. 1994, Comments on Astrophysics, 17, 189

Nomoto, K., Yamaoka, H., Pols, O. R., et al. 1994, Nature, 371, 227

Nomoto, K. I., Iwamoto, K., & Suzuki, T. 1995, PhR, 256, 173

Nordström, G. 1918, Koninklijke Nederlandse Akademie van Wetenschappen Proceedings Series B Physical Sciences, 20, 1238

Norris, J. P. 2002, ApJ, 579, 386

Norris, J. P., & Bonnell, J. T. 2006, ApJ, 643, 266

Norris, J. P., Bonnell, J. T., Kazanas, D., et al. 2005, ApJ, 627, 324

Norris, J. P., Cline, T. L., Desai, U. D., & Teegarden, B. J. 1984, Nature, 308, 434

Norris, J. P., Marani, G. F., & Bonnell, J. T. 2000a, ApJ, 534, 248

Norris, J. P., Marani, G. F., & Bonnell, J. T. 2000b, ApJ, 534, 248

Norris, J. P., Nemiroff, R. J., Bonnell, J. T., et al. 1996, ApJ, 459, 393

Nousek, J. A., Kouveliotou, C., Grupe, D., et al. 2006, ApJ, 642, 389

Nysewander, M., Fruchter, A. S., & Pe'er, A. 2009, ApJ, 701, 824

Oates, S. R., & Cannizzo, J. K. 2010, GRB Coordinates Network, 11016, 1

Oates, S. R., Beardmore, A. P., Holland, S. T., et al. 2011, GRB Coordinates Network, 12215, 1

O'Brien, P. T., Willingale, R., Osborne, J., et al. 2006, ApJ, 647, 1213

Oesch, P. A., Brammer, G., van Dokkum, P. G., et al. 2016, ApJ, 819, 129

Ofek, E. O., Cenko, S. B., Gal-Yam, A., et al. 2007, ApJ, 662, 1129

Ogasaka, Y., Murakami, T., Nishimura, J., Yoshida, A., & Fenimore, E. E. 1991, ApJL, 383, L61

Ohno, M., Cutini, S., McEnery, J., Chiang, J., & Koerding, E. 2009, GRB Coordinates Network, 9021, 1

Omodei, N., & McEnery, J. 2013, GRB Coordinates Network, 14675, 1

Omukai, K. 2000, ApJ, 534, 809

Paczynski, B. 1986, ApJ, 308, L43

Paczynski, B. 1990, ApJ, 363, 218

Paczyński, B. 1998a, ApJ, 494, L45

Paczyński, B. 1998b, in American Institute of Physics Conference Series, Vol. 428, Gamma-Ray Bursts, 4th Hunstville Symposium, ed. C. A. Meegan, R. D. Preece, & T. M. Koshut, 783–787

Pagani, C., Page, K. L., & Evans, P. A. 2014, GRB Coordinates Network, 16986, 1

Page, K. L., Evans, P. A., & Goad, M. R. 2010a, GRB Coordinates Network, 10605, 1

Page, K. L., Racusin, J. L., Kennea, J. A., & Cannizzo, J. K. 2010b, GRB Coordinates Network, 10601, 1

Page, K. L., D'Avanzo, P., D'Elia, V., et al. 2015, GRB Coordinates Network, 18490, 1

Palmer, D. M., Barthelmy, S. D., Baumgartner, W. H., et al. 2012, GRB Coordinates Network, 13536, 1

Palmer, D. M., Barthelmy, S. D., Cummings, J. R., et al. 2015, GRB Coordinates Network, 18496, 1

Panagia, N., & Laidler, V. G. 1988, Type-Ib Supernovae - what they may BE and what they are not, ed. W. Kundt, Vol. 316, 187

Panaitescu, A. 2006, MNRAS, 367, L42

Panaitescu, A., & Kumar, P. 2001, ApJ, 554, 667

Panaitescu, A., & Mészáros, P. 1998, ApJL, 493, L31

Panaitescu, A., & Mészáros, P. 2000, ApJ, 544, L17

Panaitescu, A., Mészáros, P., Burrows, D., et al. 2006a, MNRAS, 369, 2059

Panaitescu, A., Mészáros, P., Gehrels, N., Burrows, D., & Nousek, J. 2006b, MNRAS, 366, 1357

Parmar, A. N., Martin, D. D. E., Bavdaz, M., et al. 1997, A&AS, 122, 309

Patel, M., Warren, S. J., Mortlock, D. J., & Fynbo, J. P. U. 2010, A&A, 512, L3

Patricelli, B., Bernardini, M. G., Bianco, C. L., et al. 2012, ApJ, 756, 16
Penacchioni, A. V., Ruffini, R., Bianco, C. L., et al. 2013, A&A, 551, A133
Penacchioni, A. V., Ruffini, R., Izzo, L., et al. 2012, A&A, 538, A58
Penrose, R., & Floyd, R. M. 1971, Nature Physical Science, 229, 177
Pérez-Ramírez, D., de Ugarte Postigo, A., Gorosabel, J., et al. 2010, Astronomy and Astrophysics, 510, A105
Perley, D. A., Hillenbrand, L., & Prochaska, J. X. 2015, GRB Coordinates Network, 18487, 1
Perley, D. A., & Kasliwal, M. 2013, GRB Coordinates Network, 14979, 1
Perley, D. A., Klein, C. R., Morgan, A. N., & Petigura, E. 2009, GRB Coordinates Network, 9036, 1
Perna, R., Armitage, P. J., & Zhang, B. 2006, ApJL, 636, L29
Perri, M., Evans, P. A., Osborne, J. P., et al. 2018, GRB Coordinates Network, 23049, 1
Perri, M., & Stratta, G. 2009, GRB Coordinates Network, 9031, 1
Pian, E., Mazzali, P. A., Masetti, N., et al. 2006, Nature, 442, 1011
Piran, T. 1999, PhR, 314, 575
Piran, T. 2004, Reviews of Modern Physics, 76, 1143
Piran, T., & Jimenez, R. 2014, PhRvL, 113, 231102
Piran, T., Nakar, E., Mazzali, P., & Pian, E. 2019, Astrophys. J., 871, L25
Piran, T., & Shemi, A. 1993, ApJ, 403, L67
Piran, T., Shemi, A., & Narayan, R. 1993, MNRAS, 263, 861
Piro, L., Frail, D. A., Gorosabel, J., et al. 2002, ApJ, 577, 680
Piro, L., De Pasquale, M., Soffitta, P., et al. 2005, ApJ, 623, 314
Pisani, G. B., Izzo, L., Ruffini, R., et al. 2013, A&A, 552, L5
Podsiadlowski, P., Rees, M. J., & Ruderman, M. 1995, MNRAS, 273, 755
Popham, R., Woosley, S. E., & Fryer, C. 1999, ApJ, 518, 356
Porterfield, B., Siegel, M., & D'Avanzo, P. 2013, GRB Coordinates Network, 14991, 1
Postnov, K. A., & Yungelson, L. R. 2014, Living Reviews in Relativity, 17, 3
Pozanenko, A., Volnova, A., Burhonov, O., & Molotov, I. 2013, GRB Coordinates Network, 15003, 1
Preece, R. D., Briggs, M. S., Giblin, T. W., et al. 2002, ApJ, 581, 1248
Preece, R. D., Briggs, M. S., Mallozzi, R. S., et al. 1998a, ApJ, 506, L23
Preece, R. D., Briggs, M. S., Mallozzi, R. S., et al. 2000, ApJS, 126, 19
Preece, R. D., Pendleton, G. N., Briggs, M. S., et al. 1998b, ApJ, 496, 849
Preparata, G., Ruffini, R., & Xue, S.-S. 1998, A&A, 338, L87
Proga, D., & Zhang, B. 2006, MNRAS, 370, L61
Racusin, J. L., Vianello, G., Kocevski, D., Bissaldi, E., & Desiante, R. 2016, GRB Coordinates Network, 19879, 1
Racusin, J. L., Karpov, S. V., Sokolowski, M., et al. 2008, Nature, 455, 183
Racusin, J. L., Liang, E. W., Burrows, D. N., et al. 2009, ApJ, 698, 43
Ramirez-Ruiz, E., Celotti, A., & Rees, M. J. 2002, MNRAS, 337, 1349
Rau, A. 2012, GRB Coordinates Network, 13560, 1
Rees, M. J., & Meszaros, P. 1992, MNRAS, 258, 41
Rees, M. J., & Meszaros, P. 1994, ApJ, 430, L93
Rees, M. J., & Mészáros, P. 1998, ApJL, 496, L1
Reichart, D. E. 1999, ApJL, 521, L111
Reichart, D. E., Lamb, D. Q., Fenimore, E. E., et al. 2001, ApJ, 552, 57
Reid, G. C., McAfee, J. R., & Crutzen, P. J. 1978, Nature, 275, 489
Reissner, H. 1916, Annalen der Physik, 355, 106
Rhoads, J. E. 1999, ApJ, 525, 737
Ricker, G., Hurley, K., Lamb, D., et al. 2002, ApJL, 571, L127
Roberts, O. J. 2014, GRB Coordinates Network, 16971, 1
Roming, P. W. A., Hunsberger, S. D., Mason, K. O., et al. 2004, in Society of Photo-Optical Instrumentation Engineers (SPIE) Conference

Series, Vol. 5165, X-Ray and Gamma-Ray Instrumentation for Astronomy XIII, ed. K. A. Flanagan & O. H. W. Siegmund, 262–276

Rosswog, S., Ramirez-Ruiz, E., & Davies, M. B. 2003, MNRAS, 345, 1077

Rubtsov, G. I., Pshirkov, M. S., & Tinyakov, P. G. 2012, MNRAS, 421, L14

Ruderman, M. 1975, in Annals of the New York Academy of Sciences, Vol. 262, Seventh Texas Symposium on Relativistic Astrophysics, ed. P. G. Bergman, E. J. Fenyves, & L. Motz, 164–180

Rueda, J. A., & Ruffini, R. 2012, ApJL, 758, L7

Rueda, J. A., Ruffini, R., & Wang, Y. 2019a, Universe, 5, 110

Rueda, J. A., Ruffini, R., Wang, Y., et al. 2018, JCAP, 2018, 006

Rueda, J. A., Ruffini, R., Wang, Y., et al. 2019b, JCAP, 2019, 044

Ruffert, M. 1999, A&A, 346, 861

Ruffert, M., & Arnett, D. 1994, ApJ, 427, 351

Ruffini, R. 1998, arXiv e-prints, astro

Ruffini, R. 1999, A&AS, 138, 513

Ruffini, R. 2011, International Journal of Modern Physics D, 20, 1797

Ruffini, R., Bernardini, M. G., Bianco, C. L., et al. 2005a, in American Institute of Physics Conference Series, Vol. 782, XIth Brazilian School of Cosmology and Gravitation, ed. M. Novello & S. E. Perez Bergliaffa, 42–127

Ruffini, R., Bernardini, M. G., Bianco, C. L., et al. 2006, in The Tenth Marcel Grossmann Meeting. On recent developments in theoretical and experimental general relativity, gravitation and relativistic field theories, 369

Ruffini, R., Bianco, C. L., Chardonnet, P., et al. 2003, in American Institute of Physics Conference Series, Vol. 668, Cosmology and Gravitation, ed. M. Novello & S. E. Perez Bergliaffa, 16–107

Ruffini, R., Bianco, C. L., Chardonnet, P., Fraschetti, F., & Xue, S.-S. 2002, ApJL, 581, L19

Ruffini, R., Bianco, C. L., Fraschetti, F., Xue, S.-S., & Chardonnet, P. 2001a, ApJL, 555, L113

Ruffini, R., Bianco, C. L., Fraschetti, F., Xue, S.-S., & Chardonnet, P. 2001b, ApJL, 555, L107

Ruffini, R., Bianco, C. L., Xue, S.-S., et al. 2004, International Journal of Modern Physics D, 13, 843

Ruffini, R., Bianco, C. L., Xue, S.-S., et al. 2005b, International Journal of Modern Physics D, 14, 97

Ruffini, R., Karlica, M., Sahakyan, N., et al. 2018a, ApJ, 869, 101

Ruffini, R., Melon Fuksman, J. D., & Vereshchagin, G. V. 2019a, arXiv e-prints, arXiv:1904.03163

Ruffini, R., Salmonson, J. D., Wilson, J. R., & Xue, S. S. 1999, A&A, 350, 334

Ruffini, R., Salmonson, J. D., Wilson, J. R., & Xue, S. S. 2000, A&A, 359, 855

Ruffini, R., Vereshchagin, G., & Xue, S.-S. 2010, PhR, 487, 1

Ruffini, R., & Vitagliano, L. 2002, Physics Letters B, 545, 233

Ruffini, R., & Wheeler, J. A. 1971, Physics Today, 24, 30

Ruffini, R., & Wilson, J. 1973, PhRvL, 31, 1362

Ruffini, R., Aksenov, A. G., Bernardini, M. G., et al. 2008, in American Institute of Physics Conference Series, Vol. 1065, American Institute of Physics Conference Series, ed. Y.-F. Huang, Z.-G. Dai, & B. Zhang, 219–222

Ruffini, R., Bianco, C. L., Enderli, M., et al. 2013a, GRB Coordinates Network, 14526, 1

Ruffini, R., Bianco, C. L., Enderli, M., et al. 2013b, GRB Coordinates Network, 15576, 1

Ruffini, R., Bianco, C. L., Enderli, M., et al. 2014a, GRB Coordinates Network, 15794, 1

Ruffini, R., Izzo, L., Muccino, M., et al. 2014b, A&A, 569, A39

Ruffini, R., Muccino, M., Bianco, C. L., et al. 2014c, A&A, 565, L10

Ruffini, R., Wang, Y., Enderli, M., et al. 2015a, ApJ, 798, 10

Ruffini, R., Muccino, M., Kovacevic, M., et al. 2015b, ApJ, 808, 190

Ruffini, R., Aimuratov, Y., Barres, U., et al. 2015c, GRB Coordinates Network, 18555, 1

Ruffini, R., Izzo, L., Bianco, C. L., et al. 2015d, Astronomy Reports, 59, 626

Ruffini, R., Muccino, M., Aimuratov, Y., et al. 2016a, ApJ, 831, 178

Ruffini, R., Rueda, J. A., Muccino, M., et al. 2016b, ApJ, 832, 136
Ruffini, R., Wang, Y., Aimuratov, Y., et al. 2018b, ApJ, 852, 53
Ruffini, R., Aimuratov, Y., Bianco, C. L., et al. 2018c, GRB Coordinates Network, 23066, 1
Ruffini, R., Moradi, R., Rueda, J. A., et al. 2018d, arXiv e-prints, arXiv:1812.00354
Ruffini, R., Moradi, R., Rueda, J. A., et al. 2018e, arXiv e-prints, arXiv:1803.05476
Ruffini, R., Muccino, M., Aimuratov, Y., et al. 2018f, arXiv e-prints, arXiv:1802.07552
Ruffini, R., Becerra, L., Bianco, C. L., et al. 2018g, ApJ, 869, 151
Ruffini, R., Rueda, J. A., Moradi, R., et al. 2018h, arXiv e-prints, arXiv:1811.01839
Ruffini, R., Moradi, R., Aimuratov, Y., et al. 2019b, GRB Coordinates Network, 23715, 1
Ruffini, R., Li, L., Moradi, R., et al. 2019c, arXiv e-prints, arXiv:1904.04162
Ruffini, R. J. 2002, in Quantum Aspects of Beam Physics, 387–409
Rumyantsev, V., & Pozanenko, A. 2009, GRB Coordinates Network, 9324, 1
Rybicki, G. B., & Lightman, A. P. 1979, Radiative processes in astrophysics (New York, Wiley-Interscience, 1979. 393 p.)
Ryde, F. 2004, ApJ, 614, 827
Ryde, F. 2005a, A&A, 429, 869
Ryde, F. 2005b, ApJL, 625, L95
Ryde, F., & Pe'er, A. 2009, The Astrophysical Journal, 702, 1211
Ryde, F., Axelsson, M., Zhang, B. B., et al. 2010, ApJ, 709, L172
Ryde, F., Pe'er, A., Nymark, T., et al. 2011, MNRAS, 415, 3693
Sahu, K. C., Livio, M., Petro, L., et al. 1997, Nature, 387, 476
Sakamoto, A., Tashiro, M., Terada, Y., et al. 2012a, GRB Coordinates Network, 13413, 1
Sakamoto, T., Ukwatta, T. N., & Barthelmy, S. D. 2009a, GRB Coordinates Network, 9534, 1
Sakamoto, T., Lamb, D. Q., Graziani, C., et al. 2004, ApJ, 602, 875
Sakamoto, T., Lamb, D. Q., Kawai, N., et al. 2005, ApJ, 629, 311
Sakamoto, T., Barbier, L., Barthelmy, S. D., et al. 2006, ApJ, 636, L73
Sakamoto, T., Sato, G., Barbier, L., et al. 2009b, ApJ, 693, 922
Sakamoto, T., Barthelmy, S. D., Baumgartner, W. H., et al. 2012b, GRB Coordinates Network, 13384, 1
Sakamoto, T., Barthelmy, S. D., Baumgartner, W. H., et al. 2014, GRB Coordinates Network, 15805, 1
Salmonson, J. D., & Galama, T. J. 2002, ApJ, 569, 682
Salmonson, J. D., & Wilson, J. R. 2002, ApJ, 578, 310
Salvaterra, R., Campana, S., Chincarini, G., Tagliaferri, G., & Covino, S. 2007, MNRAS, 380, L45
Salvaterra, R., Della Valle, M., Campana, S., et al. 2009, Nature, 461, 1258
Sanchez-Caso, A., & Castro-Tirado, A. J. 2012, GRB Coordinates Network, 13385, 1
Sanchez-Ramirez, R., Gorosabel, J., Castro-Tirado, A. J., Cepa, J., & Gomez-Velarde, G. 2013, GRB Coordinates Network, 14685, 1
Sander, A., Hamann, W. R., & Todt, H. 2012, A&A, 540, A144
Sari, R. 1998, ApJL, 494, L49
Sari, R., Narayan, R., & Piran, T. 1996, ApJ, 473, 204
Sari, R., & Piran, T. 1997, MNRAS, 287, 110
Sari, R., & Piran, T. 1999, ApJ, 520, 641
Sari, R., Piran, T., & Halpern, J. P. 1999, ApJ, 519, L17
Sari, R., Piran, T., & Narayan, R. 1998, ApJ, 497, L17
Sato, G., Yamazaki, R., Ioka, K., et al. 2007, ApJ, 657, 359
Sauter, F. 1931, Zeitschrift fur Physik, 69, 742
Savaglio, S., Fall, S. M., & Fiore, F. 2003, ApJ, 585, 638
Savaglio, S., Glazebrook, K., & Le Borgne, D. 2009, ApJ, 691, 182
Schady, P., Nicuesa Guelbenzu, A., Klose, S., et al. 2012, GRB Coordinates Network, 13393, 1
Schady, P., Mason, K. O., Osborne, J. P., et al. 2006, ApJ, 643, 276

Schady, P., Baumgartner, W. H., Beardmore, A. P., et al. 2009, GRB Coordinates Network, 9512, 1

Schaefer, B. E. 2001, arXiv Astrophysics e-prints

Schaefer, B. E. 2003, ApJ, 583, L71

Schaefer, B. E. 2007, ApJ, 660, 16

Scheuer, P. A. G. 1965, Nature, 207, 963

Schmidt, M., Higdon, J. C., & Hueter, G. 1988, ApJ, 329, L85

Schmidt, W. K. H. 1978, Nature, 271, 525

Schulze, S., Xu, D., Kann, D. A., et al. 2013, GRB Coordinates Network, 14978, 1

Schulze, S., Klose, S., Björnsson, G., et al. 2011, A&A, 526, A23

Schwinger, J. 1951, Physical Review, 82, 664

Shahmoradi, A., & Nemiroff, R. J. 2015, Monthly Notices of the Royal Astronomical Society, 451, 126

Shao, L., Zhang, B.-B., Wang, F.-R., et al. 2017, ApJ, 844, 126

Shara, M. M., Zurek, D. R., Williams, R. E., et al. 1997, AJ, 114, 258

Sharma, V., Iyyani, S., Bhattacharya, D., et al. 2019, ApJL, 882, L10

Shemi, A., & Piran, T. 1990, ApJL, 365, L55

Shima, E., Matsuda, T., Takeda, H., & Sawada, K. 1985, MNRAS, 217, 367

Sibgatullin, N. R., & Sunyaev, R. A. 2000, Astronomy Letters, 26, 772

Smartt, S. J. 2009, ARA&A, 47, 63

Smartt, S. J., Chen, T. W., Jerkstrand, A., et al. 2017, Nature, 551, 75

Smith, I. A., Tilanus, R. P. J., Tanvir, N. R., & Frail, D. A. 2012, GRB Coordinates Network, 13554, 1

Smith, N., Li, W., Filippenko, A. V., & Chornock, R. 2011, MNRAS, 412, 1522

Soderberg, A. M., Kulkarni, S. R., Nakar, E., et al. 2006, Nature, 442, 1014

Soderberg, A. M., Berger, E., Page, K. L., et al. 2008, Nature, 453, 469

Sommer, M., Bertsch, D. L., Dingus, B. L., et al. 1994, ApJL, 422, L63

Sonbas, E., MacLachlan, G. A., Shenoy, A., Dhuga, K. S., & Parke, W. C. 2013, ApJ, 767, L28

Starling, R. L. C., Page, K. L., Pe'Er, A., Beardmore, A. P., & Osborne, J. P. 2012, MNRAS, 427, 2950

Stern, B. E., & Poutanen, J. 2004, MNRAS, 352, L35

Strong, I. B., Klebesadel, R. W., & Evans, W. D. 1975, in Seventh Texas Symposium on Relativistic Astrophysics, ed. P. G. Bergman, E. J. Fenyves, & L. Motz, Vol. 262, 145–158

Tagliaferri, G., Goad, M., Chincarini, G., et al. 2005, Nature, 436, 985

Takahashi, T., Abe, K., Endo, M., et al. 2007, PASJ, 59, 35

Tanga, M., Krühler, T., Schady, P., et al. 2018, A&A, 615, A136

Tanvir, N. R., & Ball, J. 2012, GRB Coordinates Network, 13532, 1

Tanvir, N. R., Levan, A. J., Fruchter, A. S., et al. 2013, Nature, 500, 547

Tanvir, N. R., Wiersema, K., Levan, A. J., Cenko, S. B., & Geballe, T. 2011, GRB Coordinates Network, 12225, 1

Tanvir, N. R., Fox, D. B., Levan, A. J., et al. 2009, Nature, 461, 1254

Tanvir, N. R., Levan, A. J., Fruchter, A. S., et al. 2012, ApJ, 754, 46

Taub, A. H. 1948, Physical Review, 74, 328

Tauris, T. M., Langer, N., Moriya, T. J., et al. 2013, ApJL, 778, L23

Tauris, T. M., Langer, N., & Podsiadlowski, P. 2015, MNRAS, 451, 2123

Tauris, T. M., van den Heuvel, E. P. J., & Savonije, G. J. 2000, ApJL, 530, L93

Tavani, M., Barbiellini, G., Argan, A., et al. 2009, A&A, 502, 995

Taylor, G. B., Frail, D. A., Berger, E., & Kulkarni, S. R. 2004, ApJL, 609, L1

Taylor, M. B. 2005, in Astronomical Society of the Pacific Conference Series, Vol. 347, Astronomical Data Analysis Software and Systems XIV, ed. P. Shopbell, M. Britton, & R. Ebert, 29

Tegmark, M., Silk, J., Rees, M. J., et al. 1997, ApJ, 474, 1

Thomas, B. C. 2009, International Journal of Astrobiology, 8, 183

Thomas, B. C., Neale, P. J., & Snyder, Brock R., I. 2015, Astrobiology, 15, 207

Thomas, B. C., Melott, A. L., Jackman, C. H., et al. 2005, ApJ, 634, 509

Thompson, C., Mészáros, P., & Rees, M. J. 2007, ApJ, 666, 1012

Toelge, K., Yu, H. F., & Meegan, C. A. 2015, GRB Coordinates Network, 18492, 1

Totani, T., Kawai, N., Kosugi, G., et al. 2006, PASJ, 58, 485

Totani, T., & Panaitescu, A. 2002, ApJ, 576, 120

Totani, T., Aoki, K., Hattori, T., et al. 2014, PASJ, 66, 63

Troja, E., Rosswog, S., & Gehrels, N. 2010, ApJ, 723, 1711

Troja, E., Butler, N., Watson, A. M., et al. 2014a, GRB Coordinates Network, 16991, 1

Troja, E., Cucchiara, A., Butler, N., et al. 2014b, GRB Coordinates Network, 16980, 1

Tsai, P., Urata, Y., Lin, H. M., et al. 2010, GRB Coordinates Network, 11037, 1

Turley, C. F., Fox, D. B., Keivani, A., et al. 2018, ApJ, 863, 64

Uehara, T., Hanabata, Y., Takahashi, T., et al. 2010, GRB Coordinates Network, 10610, 1

Uhm, Z. L., & Zhang, B. 2014, Nature Physics, 10, 351

Ukwatta, T. N., Barthelmy, S. D., Baumgartner, W. H., et al. 2010a, GRB Coordinates Network, 11018, 1

Ukwatta, T. N., Stamatikos, M., Dhuga, K. S., et al. 2010b, ApJ, 711, 1073

Ukwatta, T. N., Burrows, D. N., Chester, M. M., et al. 2012, GRB Coordinates Network, 13530, 1

Updike, A., Brittain, S., Hartmann, D., et al. 2009, GRB Coordinates Network, 9575, 1

Urata, Y., & Huang, K. Y. 2010, GRB Coordinates Network, 10641, 1

Usov, V. V. 1992, Nature, 357, 472

Valan, V., Larsson, J., & Ahlgren, B. 2018, MNRAS, 474, 2401

van der Horst, A. J. 2009, GRB Coordinates Network, 9047, 1

van der Horst, A. J. 2013, GRB Coordinates Network, 14987, 1

van der Horst, A. J., & Xin, L. P. 2009, GRB Coordinates Network, 9035, 1

van Paradijs, J., Kouveliotou, C., & Wijers, R. A. M. J. 2000, ARA&A, 38, 379

van Paradijs, J., Groot, P. J., Galama, T., et al. 1997, Nature, 386, 686

Vanderspek, R., Sakamoto, T., Barraud, C., et al. 2004, ApJ, 617, 1251

Varela, K., Graham, J., Greiner, J., & Kann, D. A. 2013, GRB Coordinates Network, 15586, 1

Vernet, J., Dekker, H., D'Odorico, S., et al. 2011, A&A, 536, A105

Vianello, G., & Kocevski, D. 2012, GRB Coordinates Network, 13379, 1

Vietri, M. 1995, ApJ, 453, 883

Villasenor, J. S., Lamb, D. Q., Ricker, G. R., et al. 2005, Nature, 437, 855

Virgili, F. J., Qin, Y., Zhang, B., & Liang, E. 2012, MNRAS, 424, 2821

von Kienlin, A. 2009, GRB Coordinates Network, 9251, 1

von Kienlin, A. 2010, GRB Coordinates Network, 11006, 1

von Kienlin, A., & Bhat, P. N. 2014, GRB Coordinates Network, 15796, 1

Vreeswijk, P. M., Ellison, S. L., Ledoux, C., et al. 2004, A&A, 419, 927

Wald, R. M. 1974, PhRvD, 10, 1680

Wanderman, D., & Piran, T. 2010, MNRAS, 406, 1944

Wang, X., Zheng, W., Filippenko, A. V., & Cenko, S. B. 2015a, GRB Coordinates Network, 18184, 1

Wang, X.-G., Zhang, B., Liang, E.-W., et al. 2015b, ApJS, 219, 9

Wang, Y., Rueda, J. A., Ruffini, R., et al. 2019, ApJ, 874, 39

Wang, Z., Chakrabarty, D., & Kaplan, D. L. 2006, Nature, 440, 772

Waxman, E. 1995, PhRvL, 75, 386

Waxman, E. 1997a, ApJ, 489, L33

Waxman, E. 1997b, ApJ, 485, L5

Waxman, E., & Katz, B. 2017, Shock Breakout Theory (Handbook of Supernovae, ISBN 978-3-319-21845-8. Springer International Publishing AG), 967

Waxman, E., Kulkarni, S. R., & Frail, D. A. 1998, ApJ, 497, 288

Weisberg, J. M., & Taylor, J. H. 1981, General Relativity and Gravitation, 13, 1

Weisskopf, M. C., Tananbaum, H. D., Van Speybroeck, L. P., & O'Dell, S. L. 2000, in Society of Photo-Optical Instrumentation Engineers (SPIE) Conference Series, Vol. 4012, X-Ray Optics, Instruments, and Missions III, ed. J. E. Truemper & B. Aschenbach, 2–16

Wick, S. D., Dermer, C. D., & Atoyan, A. 2004, Astroparticle Physics, 21, 125

Wiersema, K., Covino, S., Toma, K., et al. 2014, Nature, 509, 201

Wiggins, P. 2015, GRB Coordinates Network, 18539, 1

Willingale, R., O'Brien, P. T., Osborne, J. P., et al. 2007, ApJ, 662, 1093

Wilson, J. R., Salmonson, J. D., & Mathews, G. J. 1998, in American Institute of Physics Conference Series, Vol. 428, Gamma-Ray Bursts, 4th Hunstville Symposium, ed. C. A. Meegan, R. D. Preece, & T. M. Koshut, 788–792

Wiltshire, D. L., Visser, M., & Scott, S. M. 2009, The Kerr Spacetime (Cambridge, UK: Cambridge University Press)

Winkler, C., Courvoisier, T. J. L., Di Cocco, G., et al. 2003, A&A, 411, L1

Wolf, C. J. E., & Rayet, G. 1867, Academie des Sciences Paris Comptes Rendus, 65, 292

Woosley, S. E. 1993, ApJ, 405, 273

Woosley, S. E., & Heger, A. 2006, in American Institute of Physics Conference Series, Vol. 836, Gamma-Ray Bursts in the Swift Era, ed. S. S. Holt, N. Gehrels, & J. A. Nousek, 398–407

Wren, J., Vestrand, W. T., Wozniak, P., & Davis, H. 2015, GRB Coordinates Network, 18495, 1

Xiong, S. 2013, GRB Coordinates Network, 14674, 1

Xu, D., de Ugarte Postigo, A., Malesani, D., Gandolfi, D., & Leloudas, G. 2012, GRB Coordinates Network, 13387, 1

Xu, D., Levan, A. J., Fynbo, J. P. U., et al. 2014, GRB Coordinates Network, 16983, 1

Xu, D., de Ugarte Postigo, A., Leloudas, G., et al. 2013a, ApJ, 776, 98

Xu, D., de Ugarte Postigo, A., Kruehler, T., et al. 2013b, GRB Coordinates Network, 14597, 1

Yamaoka, K., Endo, A., Enoto, T., et al. 2009, PASJ, 61, S35

Yamazaki, R., Ioka, K., & Nakamura, T. 2002, ApJ, 571, L31

Yang, B., Jin, Z.-P., Li, X., et al. 2015, Nature Communications, 6, 7323

Yi, T., Liang, E., Qin, Y., & Lu, R. 2006, MNRAS, 367, 1751

Yonetoku, D., Murakami, T., Nakamura, T., et al. 2004, ApJ, 609, 935

York, D. G., Adelman, J., Anderson, Jr., J. E., et al. 2000, AJ, 120, 1579

Yoshida, A., Murakami, T., Itoh, M., et al. 1989, PASJ, 41, 509

Yoshida, N., Sokasian, A., Hernquist, L., & Springel, V. 2003, ApJ, 591, L1

Yost, S. A., Frail, D. A., Harrison, F. A., et al. 2002, ApJ, 577, 155

Yu, H.-F., Greiner, J., van Eerten, H., et al. 2015, A&A, 573, A81

Zauderer, A., Berger, E., & Frail, D. A. 2011, GRB Coordinates Network, 12227, 1

Zel'dovich, Y. B., Ivanova, L. N., & Nadezhin, D. K. 1972, Soviet Ast., 16, 209

Zhang, B. 2006, Nature, 444, 1010

Zhang, B. 2007a, Advances in Space Research, 40, 1186

Zhang, B. 2007b, Chinese Journal of Astronomy and Astrophysics, 7, 1

Zhang, B. 2011, Comptes Rendus Physique, 12, 206

Zhang, B., Fan, Y. Z., Dyks, J., et al. 2006a, ApJ, 642, 354

Zhang, B., & Mészáros, P. 2004, International Journal of Modern Physics A, 19, 2385

Zhang, B., Zhang, B.-B., Liang, E.-W., et al. 2007a, ApJ, 655, L25

Zhang, B., Zhang, B.-B., Virgili, F. J., et al. 2009, ApJ, 703, 1696

Zhang, B.-B., Liang, E.-W., & Zhang, B. 2007b, ApJ, 666, 1002

Zhang, C. M., Wang, J., Zhao, Y. H., et al. 2011, A&A, 527, A83

Zhang, F.-W., Shao, L., Yan, J.-Z., & Wei, D.-M. 2012, ApJ, 750, 88

Zhang, J., Mao, J., & Bai, J. 2015, GRB Coordinates Network, 18493, 1
Zhang, Z., Xie, G. Z., Deng, J. G., & Jin, W. 2006b, MNRAS, 373, 729
Zhao, X.-H., Qin, Y.-P., Dong, Y.-M., & Peng, Z.-Y. 2004, Chinese Journal of Astronomy and Astrophysics, 4, 349
Zheng, W., & Filippenko, A. V. 2015, GRB Coordinates Network, 18479, 1
Zitouni, H., Guessoum, N., & Azzam, W. J. 2016, Ap&SS, 361, 383